Multi-scale deep-marine stratigraphic expressions in the Cretaceous Magallanes Basin, Chile: Implications for depositional architecture and basin evolution

Sebastian Andres Kaempfe Droguett

Dissertation submitted to the faculty of the Virginia Polytechnic Institute and State University in partial fulfillment of the requirements for the degree of

Doctor of Philosophy
In
Geosciences

Brian W. Romans, Chair
Stephen M. Hubbard
Kenneth A. Eriksson
Benjamin C. Gill

May 6, 2022
Blacksburg, Virginia

Keywords: Magallanes Basin, submarine channels, deep-marine sedimentation, channel-levee systems

Multi-scale deep-marine stratigraphic expressions in the Cretaceous Magallanes Basin, Chile: Implications for depositional architecture and basin evolution

Sebastian Andres Kaempfe Droguett

ABSTRACT

Submarine channel-levee systems represent one of the most significant features of sediment transfer on Earth and one of the final segments in source-to-sink routing systems. As such, they serve as conduits as well as intermediate or final storage for large volumes of sediment, paleoenvironmental signals, and pollutants on their way to the deep ocean. Over the years, these systems have been studied through a variety of methods, including: (i) outcropping analogs; (ii) seismic data, occasionally integrated with core analysis; (iii) numerical modeling and physical experiments, and more recently; (iv) repeated multibeam bathymetry and (v) direct measurement of sediment gravity flows. However, as we are able to show in this study, there are still questions about the inherent evolution of these systems that need to be addressed.

In this study, we focus on the sedimentary processes and depositional products of submarine channel-levee systems through the characterization, analysis and interpretation at different scales of outcropping analog systems of the Upper Cretaceous Tres Pasos and Cerro Toro Formations in the Magallanes-Austral Basin.

In the first research-chapter, ***Chapter 2***, we analyze the transition between laterally offset and vertically stacked channels on a previously undocumented, seismic-scale outcrop of the Tres Pasos Formation. This change in stacking pattern has been widely recognized in submarine channel systems, however, the stratigraphic and sedimentologic details and implications to general conceptual models have not been addressed in the past. Our observations indicate that in between these two depositional architecture styles there is a significant phase of erosion and bypass at a complex-scale (or larger) and that the relief achieved via this deep incision of one or multiple simultaneously active conduits was the necessary condition to promote flow stripping processes and associated overbank deposition. In addition, we discuss the presence of an unusual intra-channel lithofacies association observed directly overlying one of these incisions, which we interpret to represent the along-strike expression of bedforms associated with supercritical flow processes that are found in modern channels and some ancient channel-fill successions.

In the next research chapter, ***Chapter 3***, we characterize a 500 m thick fine-grained dominated sedimentary succession interpreted as overbank deposits of the Cerro Toro Formation that have been affected by synsedimentary faulting and crosscut by an extensive injectite network. The scale of this outcrop allows us to resolve the relationship between sedimentary packages and structural features that are commonly overlooked or beyond the resolution of datasets derived from other sources by using high-resolution measurements and quantitative analysis at a cm scale. The orientation of synsedimentary normal faults, paleocurrent directions, and characteristics of 10-36 m thick sandstone-prone intervals suggest a model of overspilling turbidity currents (from the main axial channel belt to the west) on a large levee-slope that might share deformational mechanisms with other depositional slopes.

Finally, in ***Chapter 4***, we use detrital zircon U-Pb geochronology to determine maximum depositional ages of seven sandstone samples attributed to the axial channel-belt of the Cerro Toro Formation and shallow-marine deposits of the Dorotea Formation, which extend the chronostratigraphic framework for Ultima Esperanza 55 km southward to help reduce the gap between field sites in the Ultima Esperanza and Magallanes provinces. Based on these new data, we hypothesize that the conglomeratic-rich deposits at this location, which have generally similar lithofacies and large-scale stratigraphic architecture to the Cerro Toro Formation, are unlikely to represent the southward extension of the well-studied axial channel belt deposits to the north, and therefore they potentially represent their own sediment routing system emanating from erosional catchments in the fold-thrust belt to the west. This chapter highlights the value of establishing a chronostratigraphic framework to reconstruct ancient paleogeography in addition to interpretation based purely on observable sedimentary parameters.

Multi-scale deep-marine stratigraphic expressions in the Cretaceous Magallanes Basin, Chile: Implications for depositional architecture and basin evolution

Sebastian Andres Kaempfe Droguett

GENERAL AUDIENCE ABSTRACT

Turbidity currents are one of the most common processes in in deep-marine environments, they are sediment-laden flows that move downslope due to an excess of density caused by the sediment they carry. They occur under a wide range of geomorphologic configurations, one of such are submarine channel-levees systems. A submarine channel-levee system is a composite geomorphologic feature in the ocean floor consisting of a concave, long-lived sedimentary conduit flanked by parallel depositional highs that is orders of magnitude longer in its downslope longitude than its width. These systems have a worldwide distribution and can be found in every tectonic setting. They represent one of the final segments in sedimentary routing systems and their study is of great importance for numerous reasons, including (i) as hydrocarbon reservoirs, (ii) to mitigate submarine geological hazards that might affect human infrastructure, (iii) their role in the carbon cycle as they transport and bury organic carbon, (iv) their impact to the marine environment as they disperse human-sourced pollutants, and (v) their capacity to preserve geochemical proxies that record past climate and tectonic history.

This dissertation is divided in three research chapters focused on different aspects of the processes and depositional products of submarine channel-levee systems through the characterization, analysis and interpretation at different scales of analog ancient systems now exposed in the mountains of Southern Chile. The use of outcropping sedimentary successions is a common practice to characterize and understand modern environments, as they provide an accessible record of their evolution through temporal scales of hundreds of thousands or even millions of years. From a geologic point of view, this study is located in the Chilean part of the Magallanes-Austral Basin, which in the past was an ocean that reached paleowater depths of ~2,000 m during the Late Cretaceous and that was subsequently filled with sediments that form the different geologic units of the area. Here, we focus on two geologic units that represent deep-marine sedimentation in this ancient ocean, known as the Tres Pasos and the Cerro Toro formations. Our study ranges from the detailed stratigraphic characterization of the transition between two different styles of stacking patterns widely recognized in submarine channel systems and its implications, to the influence of sedimentary structures on hundreds of meters of fine-grained sediments deposited in a large levee

subjected to failure, and the use of tiny minerals known as zircons to constrain the depositional age and paleogeography associated to coarse-grained deposits historically attributed to a >150 km long axial channel-belt.

The results presented here do not only serve to better understand the configuration of ancient deep-marine deposits in this part of the world, but also have implications to improve our understanding of the fundamental sedimentary processes and the depositional products in deep-marine environments worldwide.

DEDICATION

I dedicate this work to my family. My mother, Ximena, who has been a crucial emotional support through my life and especially in the moments when I have found myself at my lowest. My sister, Paz, who I admire for her resilience and bravery, and for giving me a niece and nephew (soon another nephew) that always put a smile in face. And to those who are not here anymore, like my father, Erwin, who since I can remember encouraged me to follow my passion and to admire and care for my natural surroundings. I wish you were here.

I may be the one doing this work, but they are the ones who in one way or another helped me to get here.

ACKNOWLEDGEMENTS

Funding for this research was provided by the **Chile Slope Systems Joint Industry Project** (CSS-JIP), a collaboration between the University of Calgary, Colorado State University, Virginia Tech and industrial partners, which aims to better understand the processes of sediment transfer across deep-water slopes through analysis of channel deposits that crop out in the Magallanes Basin of southern Chile.

Over the past five years, there has been a growing list of amazing people that were directly and indirectly involved in the successful conclusion of this Ph.D. **Chilean mentors** who believed in me when I was applying to this graduate program: Salvador Harambour, Marcelo Leppe and Constantino Mpodozis. My **CSS friends**, with whom I collectively spend hundreds of hours working in my dream field site, my remote, beautiful and windy Patagonia and unearthing (sometimes literally) its geologic secrets: Benjamin Daniels (more machine than human), Neal Auchter, Sarah Jancuska, Sarah Southern, Aaron Reimchen, Daniel Niquet, Rebecca Englert, Sophie Hage, Paul Nesbitt, (young) Tom Peploe, Daniel Bell, Adam Nielson, Casey Meirovitz, Noah Vento, Andrew Reutten, Zane Jobe, Sean Fletcher and Erin Pemberton, I have nothing but wonderful things to say about each one of you. The **friendly people and landowners from Última Esperanza**: Mr. Ciro Solabarrieta at Estancia Montserrat (I'm sorry I didn't find gold); Alejandro, Lucy and the Cardenas family at Estancia Rincon Negro; Armando Alvarez at Laguna Figueroa; Francisco Buzolic for sharing is toponymic knowledge of Última Esperanza; Ivo Goic at Monte Rotunda; Hella Roehrs, Mauricio Álvarez and the staff at the Hotel Posada 3 Pasos; Jose Luis and Manuel Cardenas at Estancia San Luis; Alejandrina Mac Leod and Gerardo Muñoz – *¡espero volver a verlos y contarles todas las maravillas geológicas que tiene Magallanes!*

People working in the **Virginia Tech Geoscience Department**, Mary Jane Smith, April Newcomer, Sharon Collins, Mark Lemon and Jim Langridge for making my life easier as an international student and always being there when I needed. **Geo-friends** Sylvain Pasquet, Morrison Nolan, Cody Wiersma, Ali Namayandeh, Amin Abbasi, Priya Bose, Jess DePaolis, Aly Hoeher, Andrew Parent, Codi Mason, Natalia Varela, Rui Sierra, Emmanuel Njinju, Khanh To, Yezi Yang, Kira Dickey.

My **friends from Blacksburg and around the globe** who made me feel at home: Martin Scavone (pizza dealer), my dear Renatas (Carneiro and Reis), neighbors Andrew and Ali-Sha, Kenneth Velez, the Italians Fabrizio Meroni, Beatrice Castellani, Federico and Micaela, Esther Lisozain, Aldo Gargiulo,

Vanesa and MiguelAndrés Guerra, Juanjo Monsalve, Roberto Marivela and Seba Andrade. I really hope I'm not leaving anyone outside this list.

I would also like to thank **committee members** Ken Eriksson and Ben Gill for their help to consolidate this work. I really wish I had the time to take their courses, as I have no doubts of their qualities as researchers and human beings.

A special mention goes for these brilliant scientists that I also consider my **friends and mentors**: my advisors Brian Romans and Steve Hubbard (University of Calgary). I remember my early years as a geoscientist in Magallanes (southern Chile) reading their publications and being amazed by the quality of their research and wondering if I would ever be close to produce anything like that. I saw it as something so far away that when my friend Marcelo Leppe called me to have some beers with these geoscientists in early 2013 I didn't realize it was them, but after a few beers I was joking about going to grad school in the US and being part of the CSS team. For the next couple of years I worked with them and their students as a field assistant in each of their field seasons, and my admiration just grew bigger. They both lead by example, their dedication and pursuit of knowledge, the efforts to disseminate it, and critical thinking are research qualities that I aspire to attain, but I have also learned a lot from them at a human level. Being part of the CSS team also gave the opportunity to meet and work with other scientists like Lisa Stright of Colorado State University, who's also co-director of the CSS-JIP. Her understanding of geologic models takes field-based research to a whole new level, William Matthews, who taught me that geochronology is much more than just an age and Miquel Poyatos-Moré, who was the last to join this list, but quickly became another friend and mentor. I look forward for future collaborations and new opportunities to keep learning from them.

TABLE OF CONTENTS

LIST OF FIGURES

LIST OF TABLES

ABBREVIATIONS

AdT:	Cerro Aleta de Tiburón
CC:	Channel complex
CP:	Cerro Pelario
ECB-:	El Chingue Bluff (N: North; C: Central; S: South)
LF:	Lithofacies
LFA:	Lithofacies association
MAB:	Magallanes-Austral Basin
MDA:	Maximum depositional age
MTD:	Mass-transport deposit
MR:	Monte Rotunda
RVB:	Rocas Verdes Basin
SPI:	Sandstone-prone Interval
YMAG:	Youngest multiple ablated grain
YGC:	Youngest grain cluster

1 | INTRODUCTION

This dissertation consists of three main research chapters (Chapters 2-4) that summarize three independent research projects. These chapters are designed and formatted to facilitate future submission to peer-reviewed journals. The common theme connecting the three research chapters is the investigation of sedimentary processes and depositional products of submarine channel-levee systems through the characterization, analysis, and interpretation at different scales of analog ancient systems now exposed in the mountains of the Magallanes Region in Southern Chile.

The geologic record outcropping in this part of the world is the Magallanes-Austral Basin and its associated fold-thrust belt, comprising the southern region of Patagonia in Argentina and Chile (**Figure 1.2A**). The Magallanes-Austral Basin (MAB) is a retroarc foreland basin formed in response to the Andean Orogenesis in a compressive tectonic setting during Late Cretaceous to Paleogene (Katz, 1963; Bruhn and Dalziel, 1977; Dalziel, 1981; Wilson, 1991; Fosdick *et al*., 2011). Unlike most retroarc foreland basins, which are typically dominated by shallow-marine and nonmarine strata, the MAB accumulated more than ~4,000 m of deep-marine strata during a period of ~20 to 25 Myr of its depositional evolution. This long-lived deep-marine foredeep was the result of a predecessor extensional phase associated with the break-up of Gondwana during mid-late Jurassic and Early Cretaceous that culminated in the opening of the Rocas Verdes back-arc basin (RVB) and the development of an attenuated crust (Natland et al., 1974; Dalziel, 1981; Biddle *et al.*, 1986; Wilson, 1991; Pankhurst *et al.*, 2000; Stern and De Witt, 2003; Fildani and Hessler, 2005; Romans *et al*., 2010).

The studied strata are located between 50°S and 52°10'S and are part of the deep-marine Cerro Toro and Tres Pasos Formations, which have been interpreted to represent the peak in subsidence and initial fill of the MAB during the Late Cretaceous (**Figure 1.2B**) (Katz, 1963; Scott, 1966; Smith, 1977; Winn and Dott, 1979; Shultz *et al*., 2005; Romans *et al*., 2011).

Chapter 2, ***The stratigraphic expression of early channel-fill deposits during the evolution of submarine slope channels in the Upper Cretaceous Tres Pasos Formation, Magallanes Basin, Chile,*** provides new insights into the evolution of submarine channel systems by analyzing the stratigraphic and sedimentologic details of the transition from highly amalgamated and laterally offset to aggradational and vertically stacked submarine channels. This change in stacking pattern has been widely recognized in

similar systems around the world and with various types of data (Labourdette, 2007; Deptuck *et al.*, 2007; Hodgson *et al.*, 2011; Englert *et al.*, 2020), however the bed-scale details and implications to general conceptual models have not been addressed in the past.

In this study, we characterize a previously undocumented, seismic-scale outcrop that features those widely recognized aspects of submarine channel evolution systems. The boundary between the underlying laterally offset and the overlying vertically stacked stacking patterns is defined by a composite erosional surface (up to ~35 m relief) with two adjacent element-scale channelized incisions with contrasting sedimentary infills: (1) an eastern incision consisting of typical channel-fill deposits and (2) a western incision filled with a distinctive mudstone dominated thinning- and fining-upward succession with mudclast-rich sandstones at its base.

Our observations indicate that in between these two depositional architecture styles there is a significant phase of erosion and bypass at a complex-scale (or larger) and that the relief achieved via this deep incision of one or multiple simultaneously active conduits was the necessary condition to promote flow stripping processes and associated overbank deposition. We also document an unusual intra-channel lithofacies association observed directly overlying the western incision is interpreted to represent the stratigraphic expression of the earliest deposits of an active submarine channel. These strata were preserved due to the abrupt abandonment of this specific channel pathway (as the adjacent pathway became the main active channel), which resulted in these deposits that record the early stages of channel filling being covered with fine-grained overbank deposits. Finally, we discuss the possibility that these early-stage channel-fill deposits represent the along-strike expression of bedforms and similar features associated with supercritical flow processes that are found in modern channels and some ancient channel-fill successions.

Chapter 3, ***Stratigraphy and syn-depositional faulting of an overbank succession in a large submarine channel-levee system, Upper Cretaceous Cerro Toro Formation at El Chingue Bluff, Southern Chile***, highlights the influence that syndepositional deformational structures can have on otherwise uniform overbank deposits. An aspect that has been largely overlooked and that has the potential to cause misleading interpretations if not considered.

Here, we use high-resolution measurements and quantitative analysis at a cm scale to characterize an extensive fine-grained dominated sedimentary succession (~500 m thick and 2 km across) affected by

synsedimentary normal faulting. The scale of this outcrop allows us to integrate high-resolution sedimentologic parameters into a spatial scale comparable to seismic-reflection data and levees associated with submarine channels observed on continental margins. Objectives of this study are to: (1) Characterize sedimentary parameters of a mostly thin-bedded turbiditic succession coeval to axial channel-belt deposits of the Cerro Toro Formation at a location where erosion by sediment gravity flows is interpreted to be minimal; (2) Integrate stratigraphic and sedimentologic features and trends into an outcrop with dimensions comparable to seismic-reflection data; and (3) Resolve the relationship between sedimentary packages and structural features that are commonly overlooked or beyond the resolution of datasets derived from other sources. The orientation of synsedimentary normal faults, paleocurrent directions, and characteristics of 10-36 m thick sandstone-prone intervals within the ~500 m thick succession suggest a model of overspilling turbidity currents (from the main axial channel belt to the west). Finally, the relationship between sediments and extensional features in the context of levee-slope dynamics and foreland basin evolution is discussed.

Finally, in contrast to previous chapters, chapter 4 ***Deciphering the depositional age of coarse-grained deep-marine sedimentation in a previously undocumented location in the Magallanes Foreland Basin, Southern Chile***, relies on detrital zircon U-Pb geochronology to determine maximum depositional ages and extend the chronostratigraphic framework of Daniels *et al.* (2019) 55 km southward to help reduce the gap between the field sites in the Ultima Esperanza and Magallanes provinces. The focus of this study is a conglomeratic-rich succession historically assumed to be the southward extension of the axial channel belt of the Cerro Toro Formation. We also provide maximum depositional ages for the shallow-marine Dorotea Formation, which serves an upper boundary for the Tres Pasos Formation, which is not exposed in this region.

We report maximum depositional age data for 9 samples, using an analytical technique that reablates the youngest zircon grains in a sample in order to improve accuracy of the statistical determination of a maximum depositional age. Based on these new data, we hypothesize that the conglomeratic-rich deposits at this location, which have generally similar lithofacies and large-scale stratigraphic architecture to the Cerro Toro Formation, are unlikely to represent the southward extension of the well-studied axial channel belt deposits to the north, and therefore they potentially represent their own sediment routing system emanating from erosional catchments in the fold-thrust belt to the west. In addition, our maximum depositional ages from the overlying Dorotea Formation show that these shallow-marine units are

generally coeval to similar deposits to the north. Our results highlight the value of establishing a chronostratigraphic framework to reconstruct ancient paleogeography in addition to interpretation based purely on observable sedimentary parameters.

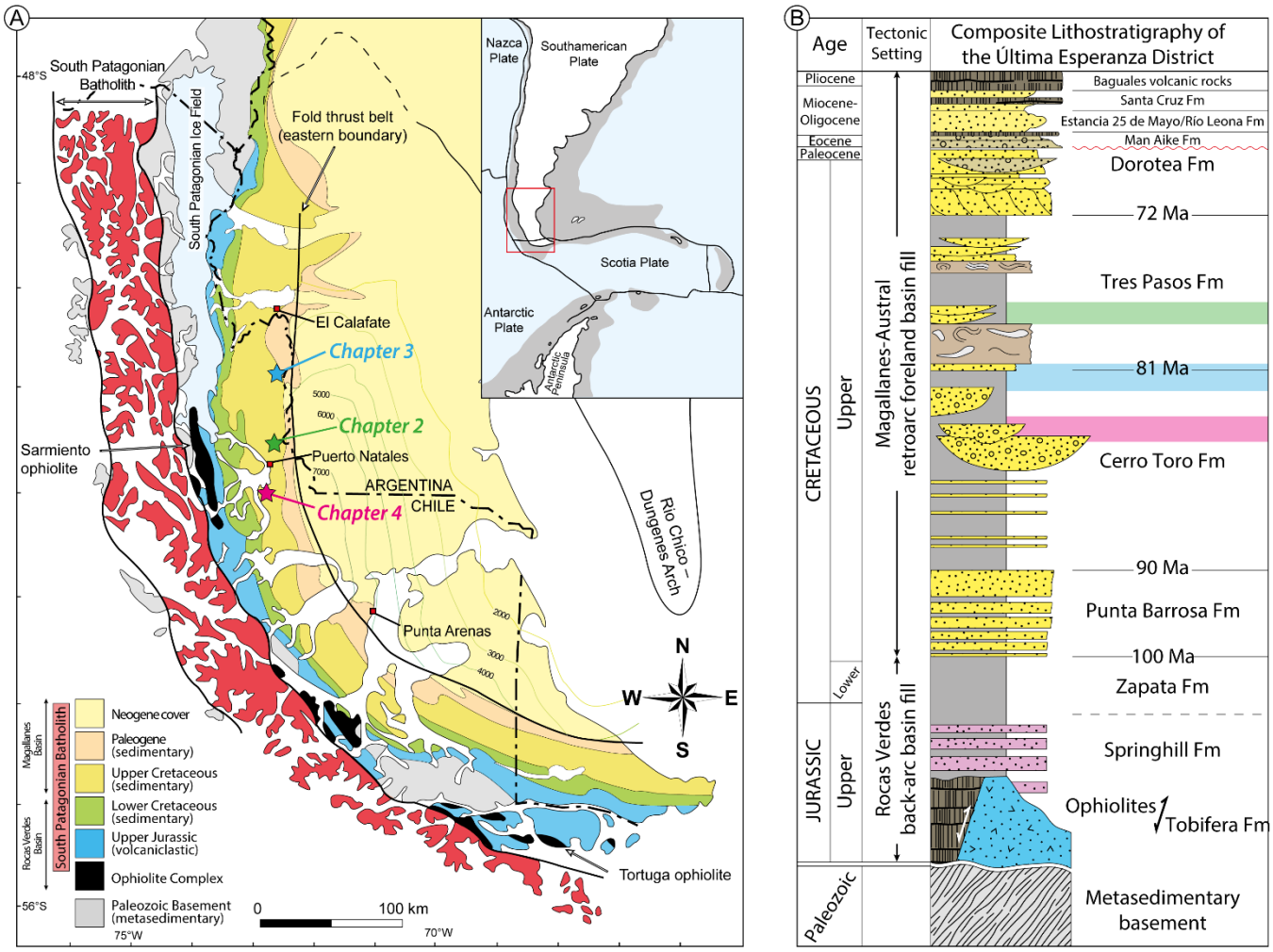

Figure 1.1: **(A)** Geographic location of the research chapters in the context of the Magallanes-Austral Basin (based on Wilson *et al.*, 1991; modified from Romans *et al.*, 2010; Malkowski *et al.*, 2017b). **(B)** Location of the research chapters in the lithostratigraphic context of the Magallanes-Austral Basin in the Ultima Esperanza Province (modified from Wilson, 1991; Fildani *et al.*, 2003; Fosdick *et al.*, 2011; Schwartz *et al.*, 2017; George *et al.*, 2020).

REFERENCES

Biddle, K.T., Uliana, M.A., Mitchum, R.M., Fitzgerald, M.G., Wright, R.C., 1986. The stratigraphic and structural evolution of the central and eastern Magallanes Basin, southern South America. Forel. basins 41–61. https://doi.org/10.1002/9781444303810.ch2

Bruhn, R.L., Dalziel, I.W.D., 1977. Destruction of the Early Cretaceous marginal basin in the Andes of Tierra del Fuego. In: Island Arcs, Deep SeaTrenches, and Back-arc Basins (Ed. by M. Talwani &W.C. Pitman III), Am. Geophys. Union, Maurice Ewing Ser., 1, 395^405.

Dalziel, I.W.D., 1981. Back-arc extension in the southern Andes: a review and critical reappraisal. Royal Society of London Philosophical Transactions, ser. A, 300, 319-335.

Daniels, B.G., Hubbard, S.M., Romans, B.W., Malkowski, M.A., Matthews, W.A., Bernhardt, A., Kaempfe, S.A., Jobe, Z.R., Fosdick, J.C., Schwartz, T.M., Fildani, A., Graham, S.A., 2019. Revised chronostratigraphic framework for the Cretaceous Magallanes-Austral Basin, Última Esperanza Province, Chile. J. South Am. Earth Sci. 94, 102209. https://doi.org/10.1016/j.jsames.2019.05.025

Deptuck, M.E., Sylvester, Z., Pirmez, C., O'Byrne, C., 2007. Migration-aggradation history and 3-D seismic geomorphology of submarine channels in the Pleistocene Benin-major Canyon, western Niger Delta slope. Mar. Pet. Geol. 24, 406–433. https://doi.org/10.1016/j.marpetgeo.2007.01.005

Englert, R.G., Hubbard, S.M., Matthews, W.A., Coutts, D.S., Covault, J.A., 2020. The evolution of submarine slope-channel systems: Timing of incision, bypass, and aggradation in late cretaceous nanaimo group channel-system strata, British Columbia, Canada. Geosphere 16, 281–296. https://doi.org/10.1130/GES02091.1

Fildani, A., Hessler, A.M., 2005. Stratigraphic record across a retroarc basin inversion: Rocas Verdes-Magallanes Basin, Patagonian Andes, Chile. Bull. Geol. Soc. Am. 117, 1596–1614. https://doi.org/10.1130/B25708.1

Fosdick, J.C., Romans, B.W., Fildani, A., Bernhardt, A., Calderón, M., Graham, S.A., 2011. Kinematic evolution of the Patagonian retroarc fold-and-thrust belt and Magallanes foreland basin, Chile and Argentina, 51°30's. Bull. Geol. Soc. Am. 123, 1679–1698. https://doi.org/10.1130/B30242.1

Hodgson, D.M., Di Celma, C.N., Brunt, R.L., Flint, S.S., 2011. Submarine slope degradation and aggradation and the stratigraphic evolution of channel-levee systems. J. Geol. Soc. London. 168, 625–628. https://doi.org/10.1144/0016-76492010-177

Katz, H., 1963. Revision of Cretaceous Stratigraphy in Patagonian Cordillera of Ultima Esperanza, Magallanes Province, Chile. Am. Assoc. Pet. Geol. Bull. 47. https://doi.org/10.1306/bc743a5d-16be-11d7-8645000102c1865d

Labourdette, R., 2007. Integrated three-dimensional modeling approach of stacked turbidite channels. Am. Assoc. Pet. Geol. Bull. 91, 1603–1618. https://doi.org/10.1306/06210706143

Natland, M.L., Eduardo, G.P., Cañon, A., 1974. Introduction. Mem. Geol. Soc. Am. 139, 1–117. https://doi.org/10.1130/MEM139-p1

Pankhurst, R.J., Riley, T.R., Fanning, C.M., Kelley, S.P., 2000. Episodic silicic volcanism in Patagonia and the Antarctic Peninsula: Chronology of magmatism associated with the break-up of Gondwana. J. Petrol. 41, 605–625. https://doi.org/10.1093/petrology/41.5.605

Romans, B.W., Fildani, A., Graham, S.A., Hubbard, S.M., Covault, J.A., 2010. Importance of predecessor basin history on sedimentary fill of a retroarc foreland basin: provenance analysis of the Cretaceous Magallanes basin, Chile (50-52°S). Basin Res. 22, 640–658. https://doi.org/10.1111/j.1365-2117.2009.00443.x

Romans, B.W., Fildani, A., Hubbard, S.M., Covault, J.A., Fosdick, J.C., Graham, S.A., 2011. Evolution of deep-water stratigraphic architecture, Magallanes Basin, Chile. Mar. Pet. Geol. 28, 612–628. https://doi.org/10.1016/j.marpetgeo.2010.05.002

Scott, K.M., 1966, Sedimentology and dispersal pattern of a Cretaceous flysch sequence, Patagonian Andes, southern Chile. AAPG Bull., 50, 72-107

Shultz, M.R., Fildani, A., Cope, T.D., Graham, S.A., 2005. Deposition and stratigraphic architecture of an outcropping ancient slope system: Tres Pasos Formation, Magallanes Basin, southern Chile. Geol. Soc. London, Spec. Publ. 244, 27–50. https://doi.org/10.1144/GSL.SP.2005.244.01.03

Smith, C., 1977. Sedimentology of the Late Cretaceous (Santonian–Maastrichtian) Tres Pasos Formation, Ultima Esperanza District, southern Chile. M.Sc Thesis, University of Wisconsin, Madison, WI, 129 p.

Stern, C.R., De Wit, M.J., 2004. Rocas Verdes ophiolites, southernmost South America: Remnants of progressive stages of development of oceanic-type crust in a continental margin back-arc basin. Geol. Soc. Spec. Publ. 218, 665–683. https://doi.org/10.1144/GSL.SP.2003.218.01.32

Winn, R.D., Dott, R.H., 1979. Deep-water fan-channel conglomerates of Late Cretaceous age, southern Chile. Sedimentology 26, 203–228. https://doi.org/10.1111/j.1365-3091.1979.tb00351.x

Wilson, T.J., 1991. Transition from back-arc to foreland basin development in the southernmost Andes: stratigraphic record from the Ultima Esperanza District, Chile. Geol. Soc. Am. Bull. 103, 98–111. https://doi.org/10.1130/0016-7606(1991)103<0098:TFBATF>2.3.CO;2

2 | THE STRATIGRAPHIC EXPRESSION OF EARLY CHANNEL-FILL DEPOSITS DURING THE EVOLUTION OF SUBMARINE SLOPE CHANNELS IN THE UPPER CRETACEOUS TRES PASOS FORMATION, MAGALLANES BASIN, CHILE

Sebastian A. Kaempfe[1], Brian W. Romans[1], Stephen M. Hubbard[2], Benjamin G. Daniels[3], Lisa Stright[4], and Sarah Southern[2]

[1] Department of Geosciences, Virginia Tech, 926 West Campus Drive, Blacksburg, VA, 24061, USA

[2] Department of Geoscience, University of Calgary, 2500 University Drive NW, Calgary, AB, T2N1N4, Canada

[3] Department of Earth and Environmental Sciences, Mount Royal University, 4825 Mount Royal Gate SW, Calgary, AB, T3E 6K6, Canada.

[4] Department of Geosciences, Colorado State University, 1482 Campus Delivery, Fort Collins, Colorado 80523-1482, USA

ABSTRACT

The transition from highly amalgamated and laterally offset to aggradational and vertically stacked submarine channels is a pattern that has been widely recognized in seismic reflection datasets as well as in outcrop belts of channel systems around the globe. However, the sedimentary and stratigraphic details of such an important part of channel evolution and its implications have not been discussed.

In this study, we address that gap by characterizing a previously undocumented, seismic-scale, outcrop of the Upper Cretaceous Tres Pasos Formation that features those key aspects of submarine channel evolution systems. The 750 m long by 300 m thick outcrop records the transition between a laterally offset/low-aggradational channel complex and a vertically stacked aggradational complex associated with the development of an internal levee that further enhanced aggradation. The boundary between both complexes is defined by a composite erosional surface (up to ~35 m relief) with two adjacent element-scale channelized incisions with contrasting sedimentary infills (an eastern incision consisting of typical channel-fill deposits and a western incision filled with a distinctive mudstone dominated thinning- and fining-upward succession with mudclast-rich sandstones at its base).

These observations indicates that, in between these two depositional architecture styles there is a significant phase of erosion and bypass at a complex-scale (or larger). The relief achieved via this deep incision of one or multiple simultaneously active conduits is interpreted to be necessary to set up the conditions for flow stripping and subsequently overbank deposition. In addition, the unusual intra-channel lithofacies association observed directly overlying the western incision is interpreted to represent the

stratigraphic expression of the earliest deposits of an active submarine channel preserved due to the abrupt abandonment of this pathway and the development of an adjacent conduit (the eastern channel), which resulted in the former being covered with fine-grained overbank deposits. We also discuss the possibility that these deposits represent the along-strike expression of bedforms, cyclic steps, and similar features found in modern channels.

Keywords: Channel architecture, channel early evolution, slope channels, Tres Pasos Formation

2.1 | INTRODUCTION

Submarine channels are sedimentary pathways characterized by a downslope longitude orders of magnitude greater than their width (Mutti, 1977; Mutti and Normark, 1987). They represent one of the most significant features of sediment transfer on Earth and one of the final segments in source-to-sink routing systems (Covault *et al.*, 2011; Normark *et al.*, 1993). As such, they serve as conduits as well as intermediate or final storage for large volumes of sediment, paleoenvironmental signals, and pollutants on their way to the deep ocean (Blum *et al.*, 2018; Castelltort *et al.*, 2017; Fildani *et al.*, 2016; Romans *et al.*, 2016). Over the years, these systems have been studied through a variety of methods, including: (i) outcropping analogs (Bernhardt *et al.*, 2011; Casciano *et al.*, 2019; Englert *et al.*, 2020); (ii) seismic data, occasionally integrated with core analysis (Deptuck *et al.*, 2003; Posamentier and Kolla, 2003; Mayall *et al.*, 2006; Hubbard *et al.*, 2009; Janocko *et al.*, 2013; Qin *et al.*, 2016); (iii) numerical modeling and physical experiments (Straub *et al.*, 2008; Sylvester *et al.*, 2011; De Leeuw *et al.*, 2018) and more recently; (iv) repeated multibeam bathymetry (Hage *et al.*, 2018; Heijnen *et al.*, 2020; Hughes Clarke, 2016) and (v) direct measurement of sediment gravity flows (Khripounoff *et al.*, 2003; Vangriesheim *et al.*, 2009; Paull *et al.*, 2018; Stacey *et al.*, 2019; Maier *et al.*, 2019; Bailey *et al.*, 2021). Each one has served to reveal distinct aspects of these systems, for example, the protracted and complex history of sediment bypass, erosion, and deposition in intra- and out-of-channel deposits, as shown by abrupt changes in lithofacies in outcropping successions (Schwartz and Arnot, 2007; Di Celma *et al.*, 2011; Kane and Hodgson, 2011; Macauley and Hubbard, 2013; Bain and Hubbard, 2016; Bell *et al.*, 2021); the changes in depositional architecture reflected by the transition from lateral to vertical stacking patterns and composite basal surfaces (*i.e.* diachronous incisional surfaces) seen at numerous scales in seismic-reflection datasets and large-scale outcrops (Labourdette, 2007; Deptuck *et al.*, 2007; Hodgson *et al.*, 2011; Englert *et al.*, 2020) (**Figure 2.1**); or by direct monitoring, the mechanisms by which event-scale

processes shape and fill active submarine channels (Hage *et al.*, 2018; Paull *et al.*, 2018; Vendettuoli *et al.*, 2019).

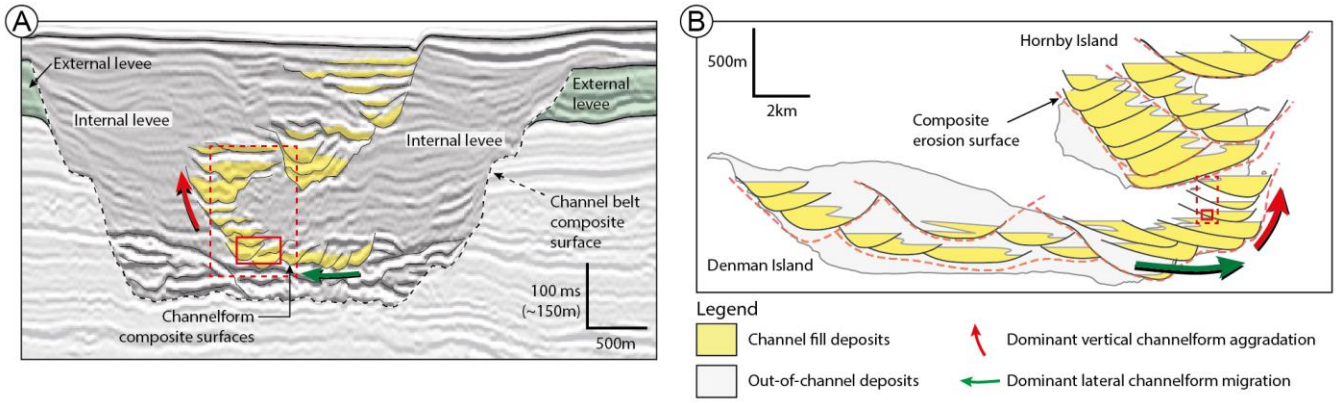

Figure 2.1: Examples from the transition from laterally offset to vertically stacked channels in different types of datasets. **(A)** Strike-oriented seismic reflection profile across the Benin-Major channel-levee system, offshore Nigeria (adapted from Deptuck *et al.*, 2007). **(B)** Strike oriented cross-section of the Upper Cretaceous Nanaimo Group, British Columbia, Canada (adapted from Englert *et al.*, 2020). Note that, despite the different scales and data type, both systems show a similar transition from laterally offset to vertically stacked channel pattern. Dashed and continuous red squares represent the scale of figures 2.5 and 2.14 respectively.

However, despite all the advances, each method has inherent limitations resulting in gaps: the depositional products observed in outcrops commonly represent only the final stages of channel evolution, and therefore a small, and potentially biased, fraction of the actual history of the channel system (McHargue *et al.*, 2011; Stevenson *et al.*, 2014; Hubbard *et al.*, 2014; Bain and Hubbard, 2016; Li *et al.*, 2018; Englert *et al.*, 2020); seismic datasets lack the stratigraphic and sedimentologic details provided by outcrops (Labourdette, 2007; Hubbard *et al.*, 2020); and seafloor surveys, direct observation and monitoring of turbidity current conducted daily over weeks/months, seasonally, or even over the course of years might still miss the more rare and large magnitude events, which also may exceed the monitored area (Vangriesheim *et al.*, 2009; Vendettuoli *et al.*, 2019).

In this study, we approach these limitations by characterizing an exceptional, previously undocumented outcrop of the Upper Cretaceous submarine slope channel system of the Tres Pasos Formation in the Magallanes retroarc foreland basin of Chile that provides the opportunity to discuss the sedimentological and stratigraphic expressions of: **(i)** the transition from laterally offset channels to aggradational channels in the context of a seismic-scale channel system and **(ii)** the depositional products during the early phases of channel evolution.

2.2 | GEOLOGIC SETTING

2.2.1 | The Magallanes-Austral retroarc foreland basin

The Magallanes-Austral Basin (MAB) contains more than ~4,000 m of deep-water stratigraphy. Its origin is attributed to rapid convergence and consequent inception of the Andean orogeny during the Late Cretaceous coupled with attenuated lithosphere derived from mid-late Jurassic to Early Cretaceous extension (Bruhn *et al.*, 1978; Pankhurst *et al.*, 2000; Fildani and Hessler, 2005; Calderon *et al.*, 2007), resulting in the development of a fold-thrust belt linked with a narrow N-S elongated retroarc foreland basin that subsided to bathyal water depths (Fosdick *et al.*, 2011). The onset of deep-water sedimentation in the MAB is defined by laterally extensive tabular sand-rich turbidites of the Punta Barrosa Formation (~100-90 Ma; <1000 m), deposited in unconfined to weakly confined submarine fan systems (Fildani *et al.*, 2003; Romans *et al.*, 2011, Daniels *et al.*, 2019). Ongoing convergence and subsidence resulted in the transition to the fine-grained deposits of the Cerro Toro Formation (~90-80 Ma; ~2000 m), which in its upper section is characterized by a >400 m thick conglomeratic-rich interval, informally called the "Lago Sofia Member", interpreted to be part of an axial channel-belt system (Katz, 1963; Winn and Dott; 1979; Romans *et al.*, 2011; Bernhardt *et al.*, 2011; Malkowski *et al.*, 2018). As basin subsidence diminished, accommodation was eventually outpaced by sediment deposition, beginning the filling stage of the deep-marine phase of the MAB, recorded by the Tres Pasos (~81-72 Ma; 1200 – 1500 m) and the shallow-water Dorotea Formations (~73-63 Ma; ~1250 m thick) (Katz, 1963; Natland *et al.*, 1974; Smith, 1977; Romans *et al.*, 2010; Hubbard *et al.*, 2010; Daniels *et al.*, 2018, 2019; George *et al.*, 2020) (**Figure 2.2**).

2.2.2 | The Tres Pasos slope system

Fold-thrust belt tectonics and Pleistocene glaciations resulted in the superb exposure of Late Cretaceous sedimentary units in southernmost Chile (**Figure 2.2C**) (Fogwill and Kubik, 2005; García *et al.*, 2018, 2015, 2014). Here, the Tres Pasos Formation is exposed for >100 km along a north-south, east-dipping monocline that crops out intermittently from the town of El Calafate (Argentina) to the north, to the town of Puerto Natales (Chile) to the south. The lithostratigraphic base of the Tres Pasos Formation is defined by the first significant sandstone succession overlying shale-dominated deposits of the Cerro Toro Formation, whereas its top is marked by the transition into sandstone-dominated deposits of the Dorotea Formation (Katz, 1963; Smith, 1977; Macellari *et al.*, 1989; Shultz *et al.*, 2005; Covault *et al.*, 2009; Romans *et al.*, 2009).

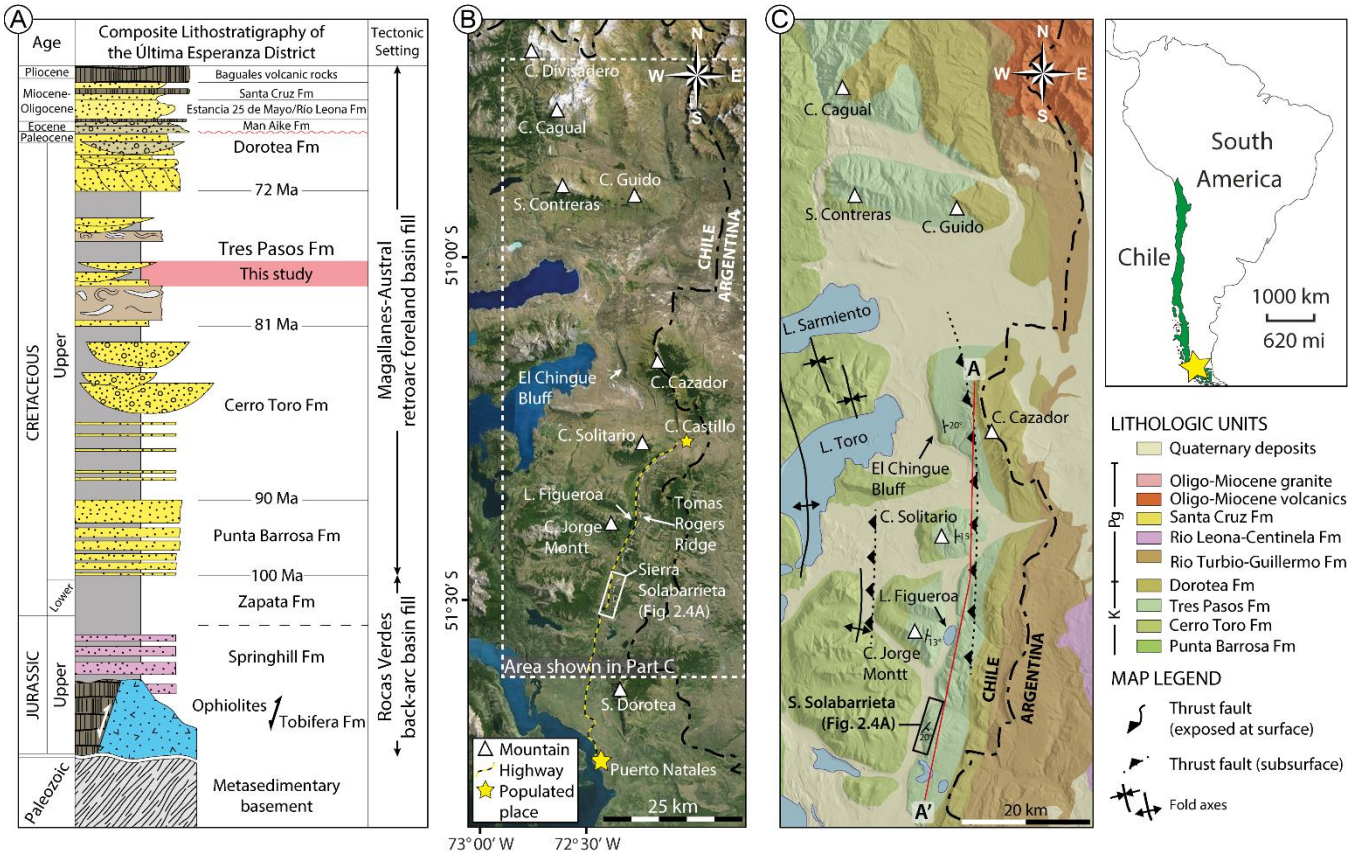

Figure 2.2: Geologic and stratigraphic context. **(A)** Generalized lithostratigraphic column for the Magallanes Basin in Última Esperanza Province, southern Chile. Modified from Wilson (1991), Fildani and Hessler (2005), Fosdick *et al.* (2011), Schwartz *et al.* (2017); Age constraints from Daniels *et al.* (2019). **(B)** Geographic location of the studied area and other known outcrops of the Tres Pasos Formation (yellow stars point out populated areas; Satellite image from Google Earth). **(C)** Geologic map of the studied area (modified from Fosdick *et al.*, 2011). Cross-section A-A' is shown in figure 2.3.

Lithologically, this unit is characterized by a basal succession of up to ~800 m of amalgamated mass-transport deposits (MTD) with lenticular to tabular sandstone-prone intercalations, interpreted as lobe deposits, that onlap onto unstratified MTD deposits at Cerro Divisadero, Cerro Cagual, Sierra Contreras, and Cerro Jorge Montt (Shultz *et al.*, 2005; Shultz and Hubbard, 2005; Armitage *et al.*, 2009; Romans *et al.*, 2009; Auchter *et al.*, 2016). The middle portion of the formation consists of a ~600 m thick succession of fine-grained turbidite deposits with 100s m thick sandstone-rich successions interpreted as stacked slope channel and local MTDs (5-30 m thick) deposits exposed in the area of Arroyo Picana, Laguna Figueroa, and Sierra Solabarrieta (Shultz *et al.*, 2005; Macauley and Hubbard, 2013; Hubbard *et al.*, 2014; Pemberton *et al.*, 2016), whereas the upper part is dominated by silt-dominated turbidite successions that transition into thick and coarse-grained deltaic strata of the Dorotea Formation (Covault *et al.*, 2009; Bauer *et al.*, 2020) (**Figure 2.2A**).

From a paleogeographic perspective, the Tres Pasos and Dorotea formations form a partially coeval high-relief shelf and slope depositional system that records the axial filling of the Magallanes-Austral Basin through southward prograding clinoform systems. These clinoforms are represented by a series of resistant ridges of turbiditic sandstones or conglomeratic sandstone (*i.e.* slope channels) that developed in paleo-water depths that reached >1000 m during the early fill of the basin (**Figure 2.3**) (Natland, *et al.*, 1974; Covault *et al.*, 2009; Romans *et al.*, 2009; Hubbard *et al.*, 2010; Macauley and Hubbard, 2013; Bauer *et al.*, 2020). A thorough geochronologic analysis carried out by Daniels *et al.* (2018) determined four distinct phases of slope evolution based on clinoform architecture and linked to basin-scale controls, confirming also the diachronous fill of the basin to the south.

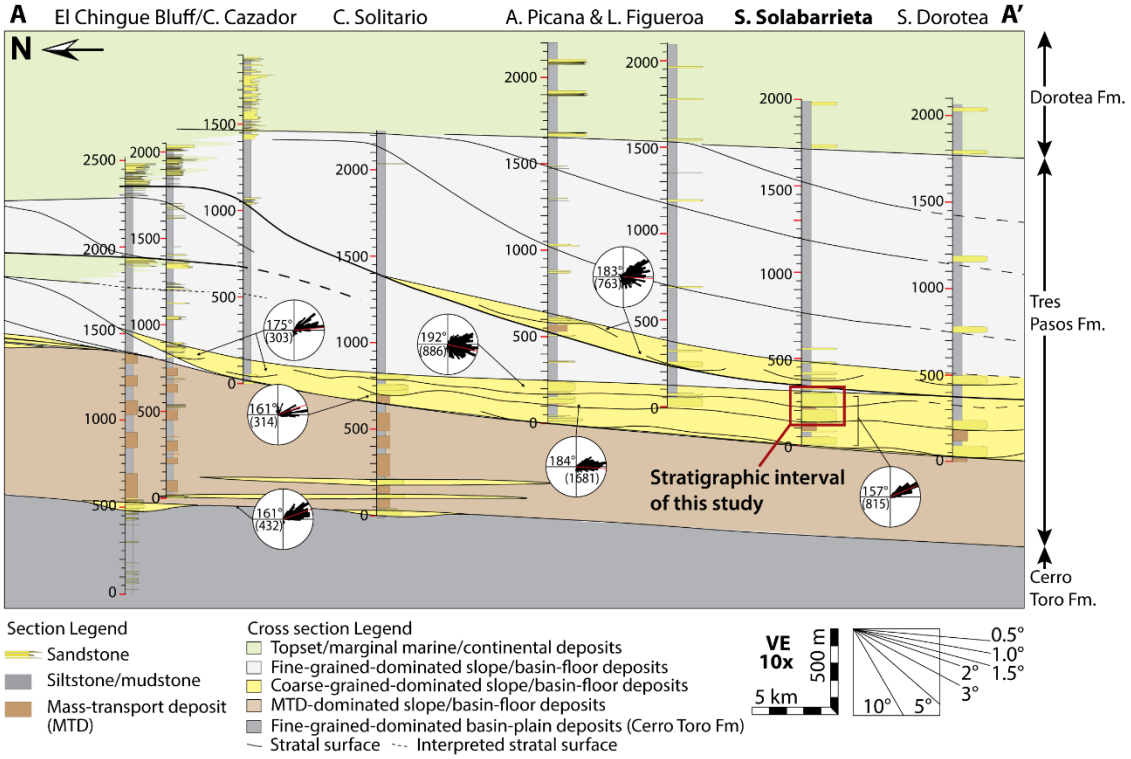

Figure 2.3: Location of this study in the context of the Tres Pasos slope system. Interpretative dip-oriented cross section is based on outcrop observations by previous authors (modified from Bauer *et al.*, 2020). Rose diagrams have been rotated 90° counterclockwise to match the orientation of the outcrop (left = north).

2.3 | STUDY AREA AND METHODS

In this study we investigate slope channel deposits of the Tres Pasos Formation exposed in the Tomas Rogers Ridge located in the Última Esperanza District (Southern Chile). The studied area is part of a 6.8 km long, north-south oriented, previously undocumented outcrop belt, that runs parallel to the highway, approximately 27 km north of the town of Puerto Natales (here we use the name Sierra Solabarrieta, after

the landowner, Mr. Ciro Solabarrieta, to refer to this specific part of the Tomas Rogers Ridge). The deposits of this study are located ~10 km south of the exposures previously mapped by Macauley and Hubbard (2013) and Hubbard *et al.* (2014), and ~14 km south from those of Pemberton *et al.* (2016), along the same general sediment pathway (*i.e.* within the same mapped clinoform system), however precise correlation between outcrop belts is hindered by a 1.5 km wide EW oriented glacial valley of the Chorrillo Tres Pasos. At Solabarrieta Ridge, the east-dipping Tres Pasos Formation is exposed in north-south scarps dissected by east-west oriented gullies, providing exceptional 3D perspectives of sandstone-rich slope channel deposits. This study is focused on a 750 m long by 300 m thick exposure along the most pronounced gully, in the center of the outcrop belt (**Figure 2.4A**).

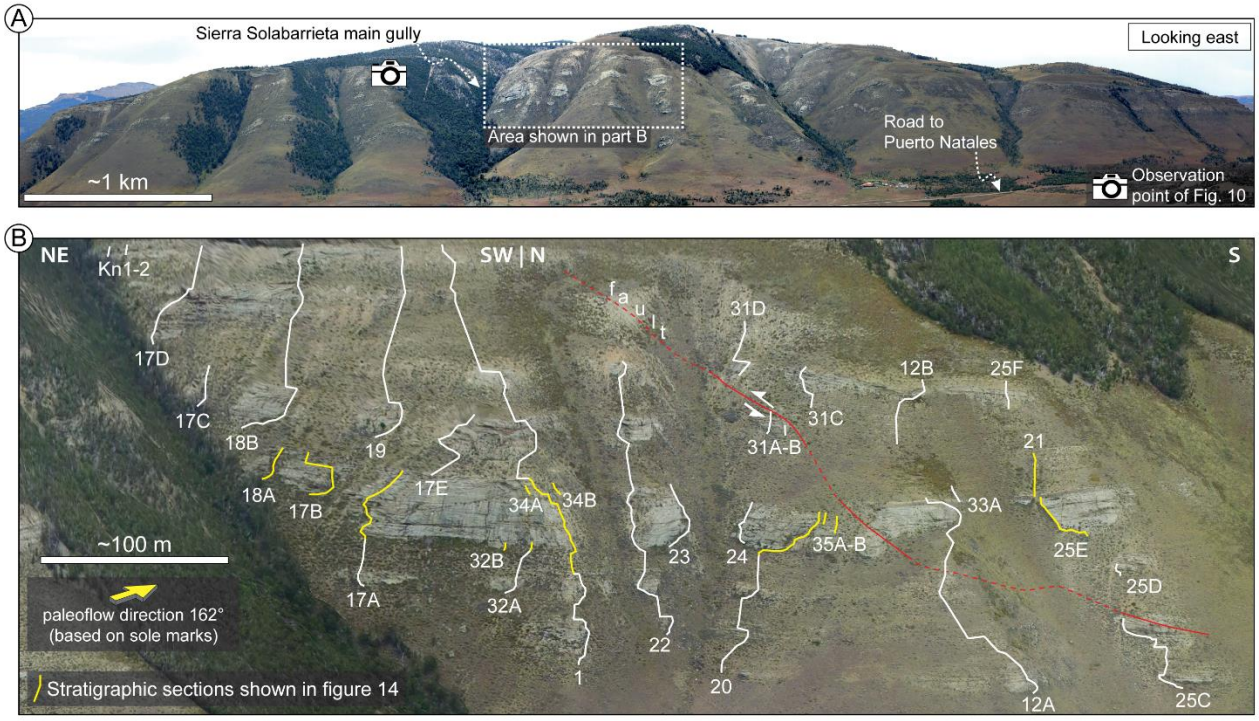

Figure 2.4: Overview of the studied outcrop. **(A)** View towards the east showing the location of the study area in the context of Sierra Solabarrieta. Overall paleoflow is to the SSE. **(B)** Photomosaic extracted from drone-based photogrammetry showing the stratigraphic interval and measured sections considered in this study. White and yellow lines represent the measured stratigraphic sections.

The outcrop was characterized using a combination of field mapping and observations enhanced with aerial imagery and the use of a differential global positioning system (dGPS) for surface correlation. The framework is provided by ~1,800 m of measured stratigraphy at 1:40 scale distributed in 32 sections that document bed thickness, vertical grain-size variations, sedimentary structures, and bed contacts (**Figure 2.4B**). Correlation between sections, facies interpretation, and depositional architecture

characterization were made through observation supported by photomosaic analysis, thousands of data points collected across prominent stratigraphic surfaces using a dGPS and improved with structure-from-motion (SFM) 3D photogrammetry based on ground and unmanned aerial vehicle (UAV) imagery using Agisoft Photoscan®. Paleocurrent measurements (n = 499) from sole marks (*e.g.*, flutes, tools and grooves; 60%), sedimentary structures (*e.g.*, ripples surfaces and imbricated clasts; 13% and 23%, respectively) and erosive surfaces (*e.g.*, scour edges; 4%) show an overall paleoflow azimuth of 175° (162° for sole marks). Thus, slope channels at this location can be assumed to intersect the most pronounced gully perpendicularly and run subparallel to Solabarrieta Ridge towards the south, allowing us to characterize these deposits along their depositional strike and dip (**Figure 2.5**).

2.4 | RESULTS

2.4.1 | Sedimentary lithofacies

Previous studies have provided a sedimentological framework to describe the deposits of the Tres Pasos Formation. Macauley and Hubbard (2013) utilized the term sedimentation unit as an equivalent to facies to define the depositional products of individual sediment gravity flows, however, similarly to Pemberton *et al.* (2016), their smallest descriptive order corresponds to sedimentation unit associations (*i.e.*, facies associations). Hubbard *et al.* (2014) divided the fill of slope channels into thick-bedded sandstone, thinly interbedded sandstone and mudstone and mudstone-prone facies, which can be correlated to Macauley and Hubbard (2013) sedimentation unit associations.

In this study we describe nine lithofacies (LF), distinguished by bed thickness (as defined by Pickering and Hiscott, 2015), dominant grain size (visible in the field), sedimentary structures, and turbidite divisions. Each one the result of individual subaqueous sediment gravity flows and its interaction (*e.g.*, high- and low-density turbidity current or cohesive density flow) (cf., Bouma, 1962; Lowe, 1982; Talling *et al.*, 2012). The lithofacies include: (i) a spectrum ranging from amalgamated thick-bedded sandstone with mudstone intraclasts (mudclasts) of LF-1 to siltstone with sparse sandstone laminae of LF-6; with decreasing levels of sandstone bed thickness, dominant grain size and variable sedimentary structures in between LF-1 and LF-6; (ii) structureless siltstone of LF-7; and (iii) disorganized gravelly matrix-supported mudstone and contorted beds of LF-9 and LF-9. A detailed description of their physical attributes and interpretation of their depositional processes is provided in **figure 2.6** and **table 2.1**.

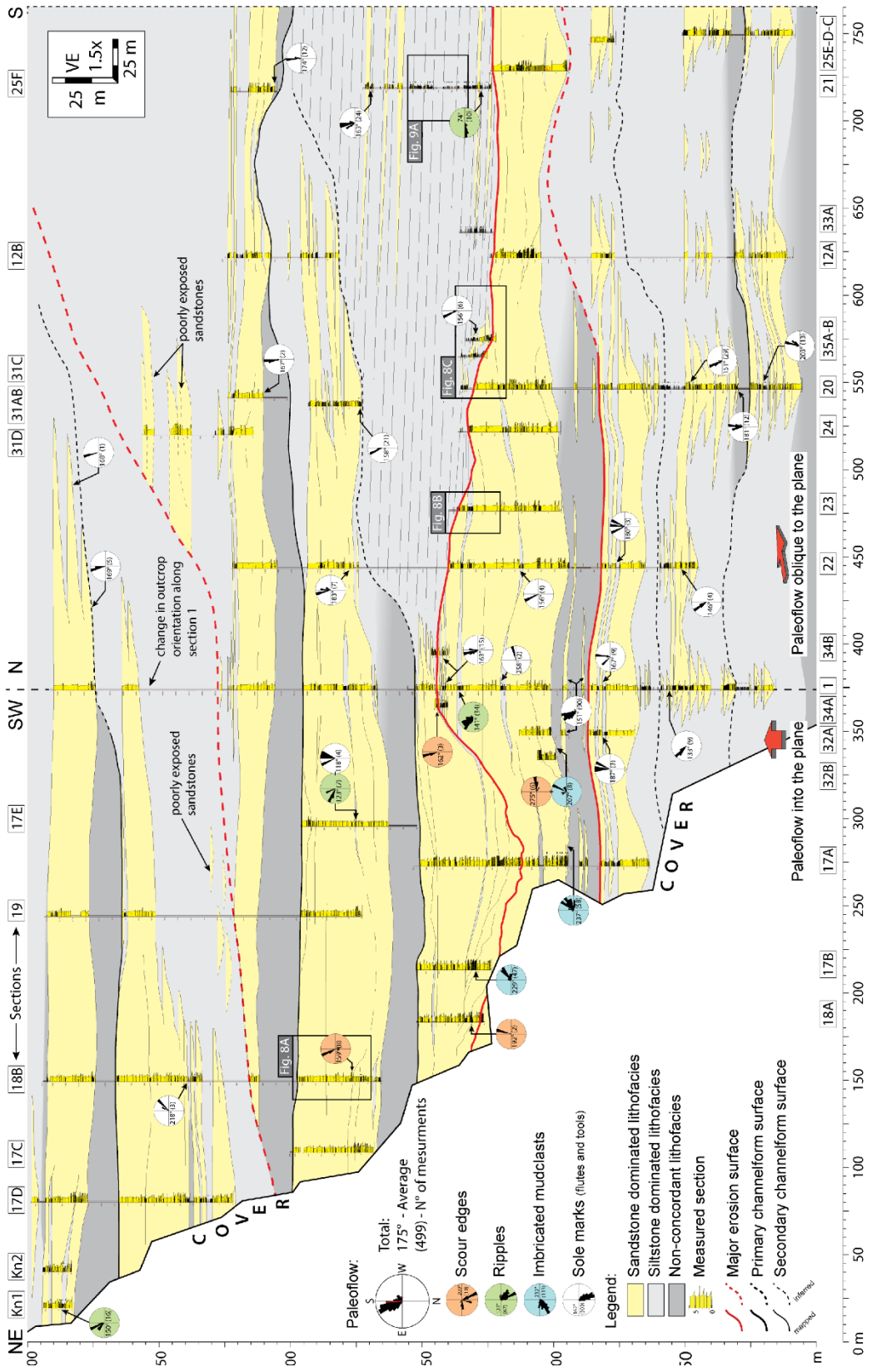

Figure 2.5: Stratigraphic cross-section highlighting the correlations of channelform strata and channelized surfaces in the studied outcrop. The cross-section was projected from two planes, the northeast-southwest plane (left half) provides a perspective oriented along the depositional strike, whereas the north-south plane (right half) a perspective along the depositional dip.

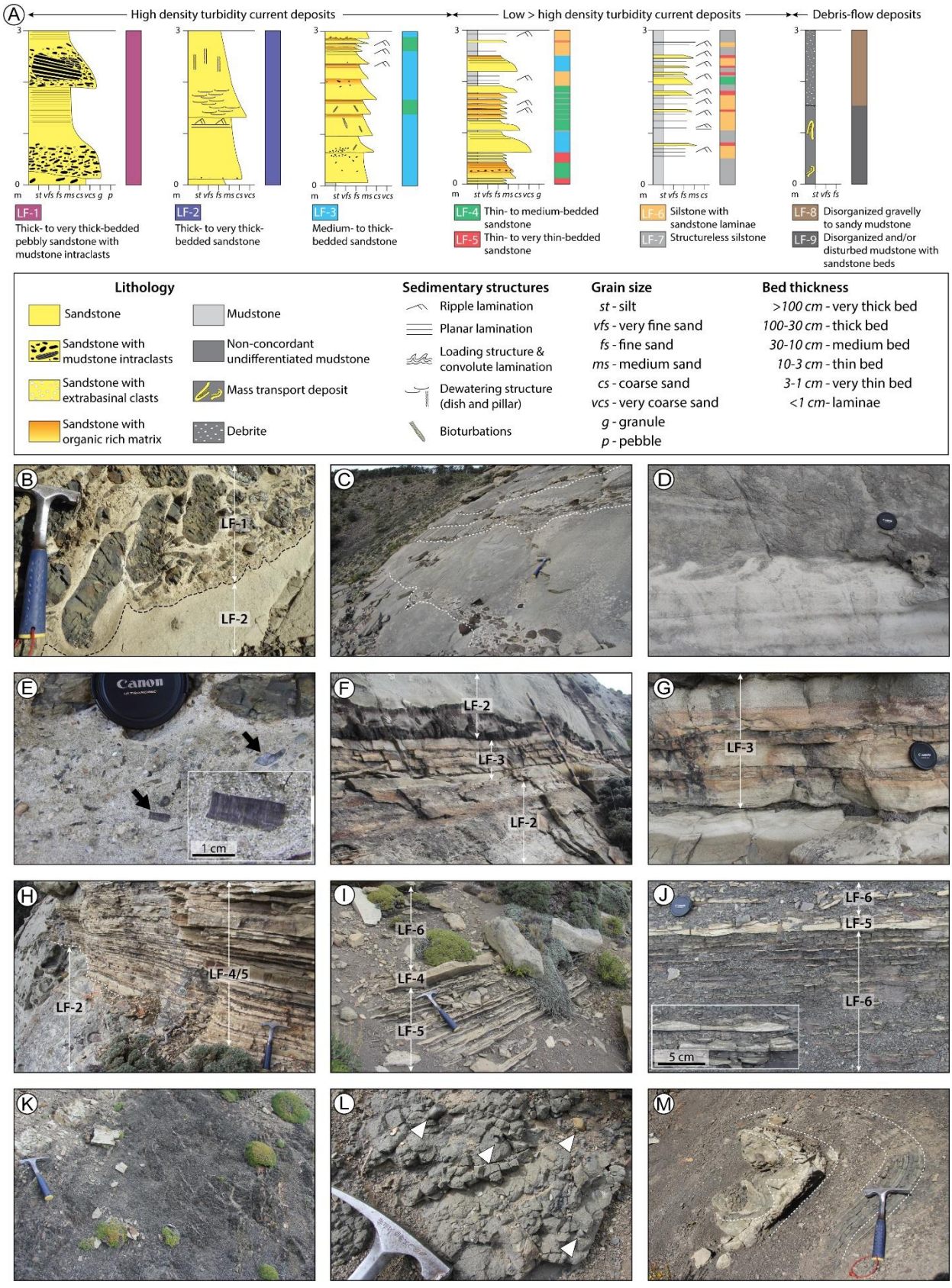
A
High density turbidity current deposits
Low > high density turbidity current deposits
Debris-flow deposits
LF-1
Thick- to very thick-bedded pebbly sandstone with mudstone intraclasts
LF-2
Thick- to very thick-bedded sandstone
LF-3
Medium- to thick-bedded sandstone
LF-4
Thin- to medium-bedded sandstone
LF-5
Thin- to very thin-bedded sandstone
LF-6
Silstone with sandstone laminae
LF-7
Structureless silstone
LF-8
Disorganized gravelly to sandy mudstone
LF-9
Disorganized and/or disturbed mudstone with sandstone beds
Lithology
Sandstone
Mudstone
Sandstone with mudstone intraclasts
Non-concordant undifferentiated mudstone
Sandstone with extrabasinal clasts
Mass transport deposit
Sandstone with organic rich matrix
Debrite
Sedimentary structures
Ripple lamination
Planar lamination
Loading structure & convolute lamination
Dewatering structure (dish and pillar)
Bioturbations
Grain size
st - silt
vfs - very fine sand
fs - fine sand
ms - medium sand
cs - coarse sand
vcs - very coarse sand
g - granule
p - pebble
Bed thickness
>100 cm - very thick bed
100-30 cm - thick bed
30-10 cm - medium bed
10-3 cm - thin bed
3-1 cm - very thin bed
<1 cm - laminae
B
LF-1
LF-2
C
D
E
1 cm
F
LF-2
LF-3
LF-2
G
LF-3
H
LF-4/5
LF-2
I
LF-6
LF-4
LF-5
J
LF-6
LF-5
LF-6
5 cm
K
L
M

Figure 2.6: Stratigraphic and outcrop expressions of lithofacies at Solabarrieta Ridge (rock hammer is 28 cm long and 16 cm wide; lens cap is 7 cm in diameter; Jacob's staff divisions every 10 cm). **(A)** Representative lithofacies section profiles. **(B)** Imbricated mudstone intraclasts in thick- to very-thick bedded sandstone of LF-1 overlying thick- to very-thick bedded massive sandstone of LF-2. **(C)** Amalgamated sandstones of LF-1 and LF-2 with erosive surfaces defined by mudclast lags. **(D)** Detailed example of an amalgamation surface marked by flame structures above spaced laminated sandstones of LF-2. (E) Extrabasinal clasts and shell fragments occasionally observed at the base of LF-1 and LF-2. Inset showing the inner structure of an inoceramid shell. **(F)** Vertical transition from thick- to very-thick sandstones of LF-2 to medium- to thick bedded sandstones of LF-3, overlain by massive sandstone of LF-2. **(G)** Planar lamination and diffuse ripple lamination (Bouma T_b and T_c) with organic-rich matrix observed at the top of LF-3. **(H)** Thin- to medium-bedded sandstones of LF-4 and LF-5 with organic-rich matrix interbedded with very-thin siltstone beds. **(I)** Very thin-bedded sandstone of LF-5 with ripple lamination. **(J)** Siltstone with starved rippled sandstone laminations of LF-6. Inset showing a magnified starved ripple. **(K)** Structureless siltstone of LF-7, commonly covered by the local vegetation. **(L)** Sandy mudstone of LF-8 with extrabasinal gravel sized clasts. **(M)** Contorted beds in otherwise massive siltstone indicative of LF-9.

Table 2.1: *Continues on next page*. Description and interpretation of the lithofacies recognized in the studied interval. Turbidity division and interpretations based on Bouma (1962); *Lowe (1982), **Talling *et al.* (2012) and Pickering and Hiscott (2015). Bed thickness as classified by Pickering and Hiscott (2016) (very thick beds: >100 cm; thick beds: 30-100 cm; medium beds: 10-30 cm; thin beds: 3-10 cm; Very thin beds: 1-3 cm; laminae: <1cm).

Lithofacies	Lithology Description	Grading	Bed and facies thickness	Basal Bounding Surface	Physical and Sedimentary Structures	Lithological Accessories	Overall Bioturbation	Turbidite Division	Interpreted Transport and Depositional Process(es)
LF-1: Thick- to very thick-bedded pebbly sandstone with abundant mudstone intraclasts	Clast- and matrix-supported mudstone intraclasts conglomerate. Very-coarse to medium-grained pebbly sandstone matrix	Normally graded. Commonly very coarse sandstone with granule and pebble floaters at the base.	Beds: 0.3 to ~4.3 m Facies: ~10 m	Sharp to undulating, commonly amalgamated, erosive	Commonly structureless. In some cases dewatering structures and planar or low angle cross lamination. Sole marks	Abundant intrabasinal mudstone clasts (5-60 cm) concentrated in the lower half of beds. Extrabasinal granules and pebbles. Bioclasts may be present	None, rare	Ta/S_3*, Tb	High density turbidity current with bedload (or concentrated density flow); traction and rapid deposition from suspension. Bypass recorded by mudstone clasts and extrabasinal lag deposits
LF-2: Thick- to very thick-bedded sandstone	Coarse- to fine-grained sandstone. In some cases very coarse-grained at the base with granule and pebble floaters	Normally graded	Beds: 0.3-6.5 m Facies: ~14.5 m	Sharp to undulating, commonly amalgamated. In some cases erosive	Commonly structureless, planar lamination, dewatering structures can be present. Rarely spaced planar laminations at the base (Tb-3**). In some cases flame structures and sole marks	Occasional to abundant intrabasinal mudstone intraclasts (1-40 cm) at the base or top or suspended randomly in the bed. Rarely organic rich matrix at the top. Bioclasts may be present	None to very low	Mostly Ta/S_3*. Also Tab, Tb	High-density turbidity current; mostly deposited by traction and rapid fall out of suspension. Bypass recorded by mudstone clasts and extrabasinal lag deposits
LF-3: Medium- to thick bedded sandstone	Medium- to fine-grained sandstone	Normally graded	Beds: 0.2-1 m Facies: ~10 m	Sharp to undulating. Commonly amalgamated	Planar and ripple laminations. Bioturbations may be abundant. Sole marks	In some cases intrabasinal mudstone clasts (Dominantly <5 cm) and organic rich matrix	None to low	Ta/S_3*, Tab, Tabc, Tabcd, Tbcd	Transition from high- to low-density turbidity currents with depletive steady and unsteady flows
LF-4: Thin- to medium-bedded sandstone	Medium- to fine-grained sandstone	Normally graded	Beds: 5-30 cm Facies: ~1 m	Sharp, undulating. Rarely amalgamated	In some cases structureless. Planar and wavy laminations, ripples, rare low angle cross stratification. Rarely sole marks	Occasional rounded intrabasinal mudstone clasts (Dominantly <5 cm), in some cases organic rich matrix and organic detritus.	None to high in organic detritus rich intervals	Tab, Tb, Tbc, Tc	High- to low-density turbidity current with progressively lower concentration and velocity
LF-5: Thin- to very thin-bedded sandstone	Fine- to very fine-grained sandstone, occasionally interbedded with siltstone	Normally graded	Beds: 1-15 cm sandstone; <3 cm siltstone. Facies: <2 m	Sharp to undulating. Not amalgamated	Planar and ripple laminations	Commonly organic rich matrix	Medium to high	Ta (rare), Tb, Tbc, Tc, Te	Predominantly low-density turbidity current; sedimentation mostly from traction and suspension deposition
LF-6: Siltstone with sandstone laminae	Predominately siltstone with limited fine- to very fine-grained sandstone	Normally graded sandstone	Beds: <1 to 5 cm sandstone; <10 cm siltstone. Facies: <5 m	Sharp	Ripple, planar and wavy continuous and discontinuous laminations	In some cases organic rich matrix	None to very low	Tbc, Tc, Tcd, Te	Low-density turbidity current; mostly suspension deposition during waning flow conditions.

Table 2.2: *Continued from previous page*. Description and interpretation of the lithofacies recognized in the studied interval. Turbidity division and interpretations based on Bouma (1962); *Lowe (1982), **Talling *et al.* (2012) and Pickering and Hiscott (2015). Bed thickness as classified by Pickering and Hiscott (2016) (very thick beds: >100 cm; thick beds: 30-100 cm; medium beds: 10-30 cm; thin beds: 3-10 cm; Very thin beds: 1-3 cm; laminae: <1cm).

Lithofacies	Lithology Description	Grading	Bed and facies thickness	Basal Bounding Surface	Physical and Sedimentary Structures	Lithological Accessories	Overall Bioturbation	Turbidite Division	Interpreted Transport and Depositional Process(es)
LF-7: Structureless siltstone	Siltstone with very rare very fine-grained sandstone laminae	Absent	>10 cm and up to 35 m	Sharp	None observed	None observed	None	Te	Hemipelagic and dilute low-density turbidity current; fall out from suspension deposition
LF-8: Disorganized gravelly to sandy mudstone	Sand, granules and/or pebbles (in some cases cobbles) immersed in a muddy matrix	Absent	Up to 15 m	Sharp	Floating extrabasinal granules and pebbles. Occasional contorted beds.	None observed	None	None	Cohesive mud flows (D_{M-2}**) or debris flows; deposition by 'freezing' as shear stress at the base of the flow become less than cohesive strength
LF-9: Disorganized and/or disturbed mudstone with sandstone beds	Mudstone, siltstone, fine-grained sandstone	Normally graded in contorted sandstones.	Up to 5,5 m	Sharp	Contorted, overturned sandstone beds in mudstone fabric	Rare floating extrabasinal granules and pebbles	Sometimes preserved	None	Mass wasting or slumping due to depositional overloading or gravity induced sliding; cessation of movement caused by basal and internal friction

2.4.2 | Lithofacies associations

The next order of classification groups mappable, systematic combinations of lithofacies into lithofacies associations (LFA). We distinguish six LFAs grouped into three categories based on their interpreted location and processes associated with the different subenvironments found in slope channel-levee depositional systems. A summary of the characteristics for each LFA is provided in **table 2.2** and **figure 2.7**.

Table 2.2: Summary of lithofacies associations of the Tres Pasos Formation in the study area.

Environment	Category	Lithofacies Association	Recognized lithofacies in order of abundance	Subenvironment
DEEP-MARINE CHANNEL and LEVEE	Channel-fill	**LFA-1**: Very thick- to medium-bedded amalgamated sandstone	Primary: LF-2, LF-1 Secondary: LF-3	Channel axis
		LFA-2: Medium- to thick-bedded semi-amalgamated to non-amalgamated sandstone	Primary: LF-3, LF-4 Secondary: LF-5, LF-2	Channel off-axis
		LFA-3: Thin-bedded non-amalgamated sandstone	Primary: LF-5, LF-4 Secondary: LF-6	Channel margin
		LFA-4: Lenticular thin- to medium-bedded semi- to non-amalgamated sandstone	Primary: LF-6, LF-3, LF-4, LF-1 Secondary: LF-5	Early channel fill
	Out-of-channel	**LFA-5**: Very thin- to thin-bedded non-amalgamated sandstone	Primary: LF-6, LF-7, LF-5 Secondary: LF-4, LF-3	Overbank (Internal levee)
	Non-stratified and chaotic	**LFA-6**: Disorganized mudstone with contorted sandstone beds and gravelly mudstone	Primary: LF-8, LF-9 Secondary: LF-7	Mass wasting and debris flow deposit

Intra-channel lithofacies associations

Intra-channel (or channel-fill) LFAs are the result of deposition within long-lived sedimentary pathways across the slope. However, despite being volumetrically restricted to a channel at any given time when active, the continuous migration, aggradation and coarser grainsize of its deposits summed to the unpredictability of the erosion when exhumed, result in prominent and well-exposed successions that rarely preserve a channelized geometry. In the studied interval, intra-channel lithofaciaes associations reach up to 55 m in thickness when stacked. Lithofacies associations described in this section complement the observations made in equivalent deposits by Macauley and Hubbard (2013) and Hubbard *et al.* (2014) for channel-fill deposits (LFA-1, LFA-2 and LFA-3) and adds a new classification (LFA-4) that is relevant to the interpreted channel evolution in this area.

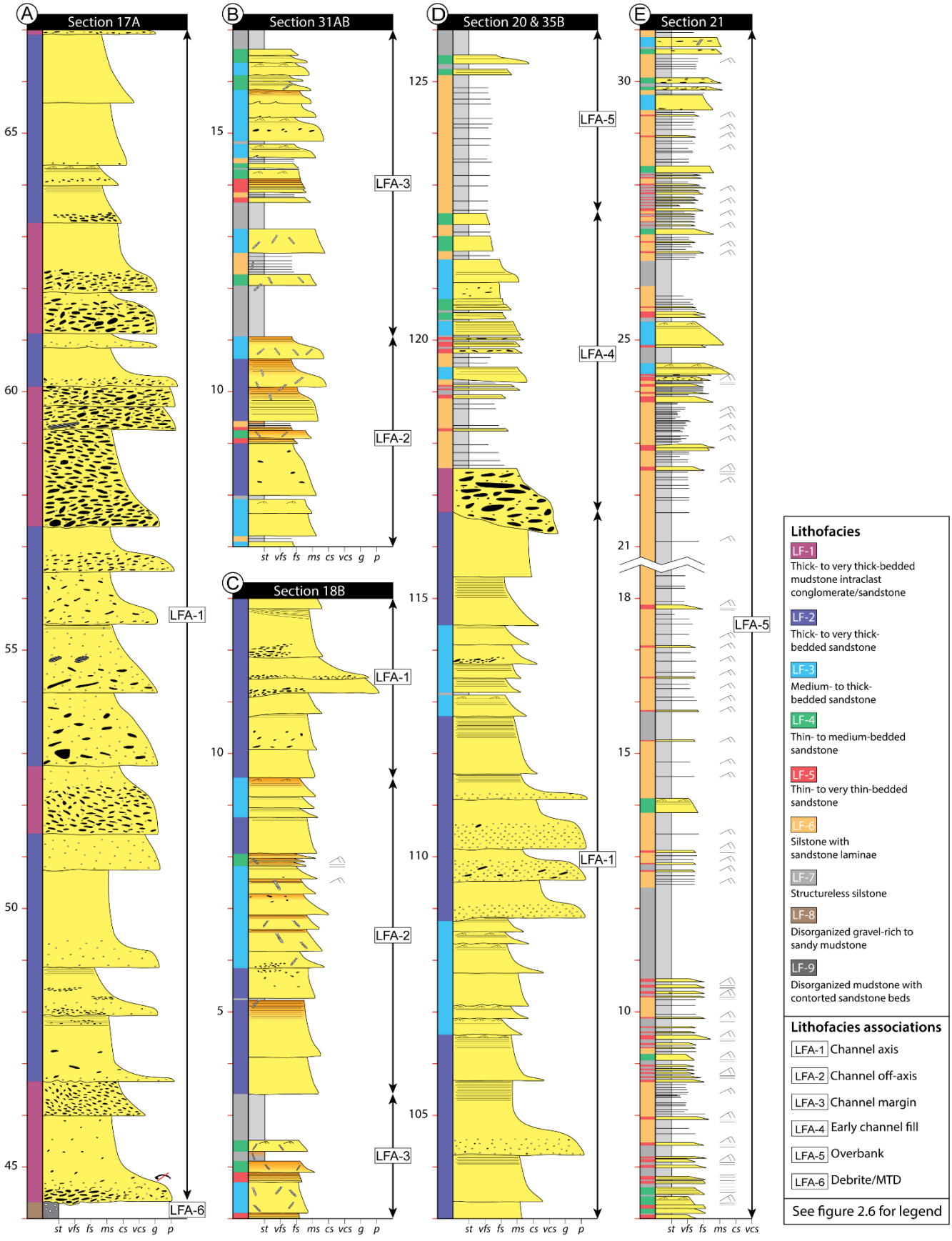
A
Section 17A
B
Section 31AB
C
Section 18B
D
Section 20 & 35B
E
Section 21
LFA-1
LFA-2
LFA-3
LFA-4
LFA-5
LFA-6
st vfs fs ms cs vcs g p
Lithofacies
LF-1
Thick- to very thick-bedded mudstone intraclast conglomerate/sandstone
LF-2
Thick- to very thick-bedded sandstone
LF-3
Medium- to thick-bedded sandstone
LF-4
Thin- to medium-bedded sandstone
LF-5
Thin- to very thin-bedded sandstone
LF-6
Silstone with sandstone laminae
LF-7
Structureless silstone
LF-8
Disorganized gravel-rich to sandy mudstone
LF-9
Disorganized mudstone with contorted sandstone beds
Lithofacies associations
LFA-1 Channel axis
LFA-2 Channel off-axis
LFA-3 Channel margin
LFA-4 Early channel fill
LFA-5 Overbank
LFA-6 Debrite/MTD
See figure 2.6 for legend

Figure 2.7: Stratigraphic expressions of lithofacies associations (see figure 2.5 for column location and figure 2.6 for legend). **(A)** Thick bedded lithofacies association attributed to channel axis (LFA-1). **(B)** Medium- to thin-bedded non-amalgamated sandstones attributed to channel off-axis and margin (LFA-2 and LFA-3). **(C)** Thickening upward transition from non-amalgamated to amalgamated sandstones representative of channel margin to off-axis to axis lithofacies association (LFA-3 to LFA-2 to LFA-1). **(D)** Channel axis lithofacies association overlain by an interbedded fining and thinning upward succession attributed to early channel-fill deposits (LFA-1 and LFA-4). **(E)** Thin-bedded, mudstone dominated deposits interpreted as an internal levee (LFA-5).

LFA-1: Very thick- to medium-bedded amalgamated sandstone

Description

LFA-1 makes up most of the described stratigraphic sections in the studied area. It is characterized by a combination of amalgamated thick- to very thick-bedded, coarse-grained mudclast-rich sandstone (LF-1) and medium- to very thick-bedded structureless sandstones (LF-2 and LF-3) in successions up to ~35 m thick, with individual beds between 0.25 to 6.5 m thick (**Figures 2.6B, 2.6C, 7A and 2.7D**). Contacts between amalgamated beds are commonly sharp but can be difficult to observe when the contrast between the top and basal grainsize is low. The basal surface of this LFA is sharp, flat to undulous, composite in nature and may erode into other LFAs producing channelized geometries with >1 m of relief (**Figures 2.8A and 2.8B**), commonly preserving sole marks when in contact with fine-grained deposits, whereas the top is commonly sharp and flat without signs of erosion.

Internally, beds are normally graded, from coarse- to fine-grained structureless sandstone (T_a division) with occasional dewatering structures, although in some cases spaced planar lamination may be present at the base (S_3 division) and planar and ripple lamination at the top (T_b and T_c divisions). Granule- and pebble-size grains are commonly present at the base of the thickest beds, occasionally accompanied by oyster and/or inoceramid bioclast fragments (**Figure 2.6E**) and mudclasts. Mudstone intraclasts are rounded to subrounded with a prismatic to discoidal shape that range from a few millimeters up to >60 cm in diameter, occasionally imbricated, forming basal clast-supported conglomerates or restricted lenses within LFA-1.

Interpretation

LFA-1 is interpreted as the result of focused high-density turbidity currents. Concave-upward amalgamation surfaces in sandstone-sandstone contacts and the presence of sole marks in sandstone-siltstone contacts suggest erosion by turbulent flows, where the fine-grained portion of the deposit is removed and/or incorporated into subsequent flows. High energy bedload transport and erosion are also recorded by imbricated rounded mudclasts, some of which still preserve internal laminations suggesting

"rip-up" processes that incorporate the muddy substrate, whether hemipelagic or debritic (*e.g.*, Lowe, 1982; Butler and Tavarnelli, 2006). The presence of mudclasts and extrabasinal gravel-sized grains at the base of thick-bedded sandstones has also been interpreted by Stevenson *et al.* (2015) as the result of bypassing flows in axial channel fills (*i.e.*, only the coarsest sediment is left behind). Rapid deceleration or collapse of high-density flows is manifested by dish and pillar dewatering structures in otherwise structureless sandstone, although tractional processes are also present.

LFA-1 groups the thickest sandstone beds in the outcrop, with evidence for erosion, bypass, and deposition suggesting sediment accumulation along the channel thalweg; thus, representing the channel-axis (*e.g.*, Mutti and Normark, 1987; Beaubouef, 2004; McHargue *et al.*, 2011; Macauley and Hubbard, 2013).

LFA-2: Medium- to thick-bedded amalgamated to semi-amalgamated sandstone

Description

LFA-2 is composed of amalgamated to semi-amalgamated medium- to thick-bedded sandstone beds of LF-3 and LF-4 in successions that reach up to ~10 m in thickness (**Figures 2.6F, 2.7B and 2.7C**). Individual sandstone beds range from 0.2 to 1.0 m thick and tend to exhibit most Bouma divisions, from medium-grained (rarely coarse-grained) structureless sandstone (T_a division) that makes up most of the bed to fine-grained planar and ripple cross-laminated sandstone (T_b and T_c divisions), which is occasionally capped by very fine-grained sandstone-siltstone laminations and/or siltstone that rarely exceed 5 cm thick (T_d and T_e divisions). In some beds, an organic-rich matrix, commonly accompanied by an increase in bioturbation, can be distinguished by an oxidized red to orange color in fine- to very fine-grained sandstones (**Figure 2.6G**). Mudstone intraclasts, when present, are mostly observed as isolated clasts <5 cm in diameter dispersed randomly throughout the bed. The base of LFA-2 is commonly a sharp contact with LFA-1 or LFA-3 (**Figures 2.8A and 2.8B**), although it has also been observed to transition laterally to these LFAs.

Interpretation

The presence of most, if not all, Bouma divisions within LFA-2 suggest that sediment deposition results mainly from high- to low-density sediment gravity flows. Structureless sandstones are indicative of rapid fallout without the time to develop tractional structures, as the flow energy decrease planar and ripple laminations begin to form until mud start falling out of suspension (Lowe, 1982). The spatial

distribution and thinner and finer-grained nature of sandstones beds of LFA-2, which are lateral to and on occasion truncated by LFA-1, suggest a location that is adjacent to the channel-axis (*i.e.* channel off-axis; Macauley and Hubbard 2013; Hubbard *et al.*, 2014) where deposition prevails over erosion, resulting in a higher number of comparatively thinner beds and the preservation of upper Bouma divisions.

LFA-3: Thin-bedded non-amalgamated sandstone

Description

LFA-3 is dominated by interbedded fine to very fine-grained sandstone and siltstone of LF-5, non-amalgamated thin- to medium-bedded sandstone of LF-4 and occasional siltstone with sparse sandstone laminae of LF-6 and structureless siltstone of LF-7 (**Figures 2.6H, 2.7B and 2.7C**). Thicker sandstone beds of LF-3 are rarely present in between thinner beds. Individual sandstone beds are normally graded and less than 15 cm thick. They are rarely structureless, sometimes exhibit planar lamination (T_b), but more commonly ripple lamination (T_b) and are capped by thinner siltstone-sandstone laminations (T_d) and/or siltstone beds of less than 3 cm thick (except where LF-6 is present). Thin-bedded sandstones of LF-5 and sometimes LF-4 are often highly bioturbated and contain oxidized organic material in the matrix, giving them a red to orange color. Undulating bases due to ripples of underlying beds are common. The base and top surfaces of LFA-3 are sharp and commonly flat, although LFA-3 have been observed to fill erosive surfaces as well, with thin-bedded sandstones onlapping on thick-bedded sandstones of LFA-1 (**Figure 2.8A and 2.8B**).

Interpretation

We interpret LFA-3 as the product of low-density sediment gravity flows, whether by themselves or as the lateral or tail portion of bypassing high-density turbidity currents, resulting in thin-bedded planar and ripple laminated sandstones and sandstone-siltstone laminations deposited by traction of sand grains and silt falling out of suspension simultaneously from a waning flow. The depositional product will be oftentimes eroded by subsequent flows, causing abrupt lateral facies changes from thick-bedded sandstones of LFA-1 to the thin-bedded sandstones of LFA-3, although on occasion a gradual lateral transition from LFA-2 is observed. Based on these observations, it is interpreted that these deposits represent the laterally furthest region of the channel-fill (*i.e.*, the channel-margin; Macauley and Hubbard 2013; Hubbard *et al.*, 2014).

Figure 2.8: Intra-channel lithofacies association as seen in the field (see figure 5 for picture location). **(A)** Vertical transition from non-amalgamated to semi- and amalgamated sandstones beds interpreted as a margin, to off-axis to axis succession. Note the erosive surface that defines the base of axial deposits. **(B)** Amalgamated thick-bedded axial sandstone deposits overlain by margin and off-axis non- to semi-amalgamated sandstones. Note the composite erosional surface within LFA-3 and below mudstone dominated deposits of LFA-5 **(C)** Amalgamated thick-bedded sandstones of LFA-1 truncated by a composite incisional surface filled with lenticular thin- to medium-bedded

semi- to non-amalgamated sandstones of LFA-4. **(D)** Lenticular sandstone beds onlapping towards the incisional surface. **(E)** Detail of onlapping beds.

LFA-4: Interbedded mudstone with lenticular thin- to medium-bedded semi- to non-amalgamated sandstone

Description

LFA-4 is observed overlying a sharp incisional surface with ~25 m of relief over thick-bedded structureless sandstones of LFA-1 between sections 12 and 20 (**Figures 2.5 and 2.8C**). Unlike other LFAs, its spatial distribution is limited to just this location. The deposits of LFA-4 are characterized by an overall upward fining and thinning succession that ranges from non-amalgamated, thick-bedded, very coarse- to coarse-grained, mudclast-rich structureless sandstone of LF-1 to siltstone with sparse sandstone laminae of LF-6 (**Figure 2.7D**). The basal portion of this LFA, directly overlying the lowest areas of the incisional surface, is dominated by very coarse-grained sandstones with occasional granule- and pebble-sized extrabasinal clasts and mudclast rich LF-1, whereas upwards sandstone beds are considerably decreased in thickness, grainsize and mudclast content. The middle portion is characterized by an intercalation of amalgamated and non-amalgamated structureless and planar laminated (T_a and T_b divisions) sandstone beds of LF-2, mostly non-amalgamated thin- to medium-bedded, planar laminated (T_b divisions) sandstones of LF-3 and LF-4, and intervals of siltstone with sparse sandstone laminae of LF-6. Finally, up section, very fine-grained thin-bedded sandstone of LF-5 and laminae in LF-6 are minor in comparison to mudstone. Sandstone beds within this LFA were observed to systematically pinch and onlap on siltstone-dominated deposits of LF-6 and LF-7 towards the incisional surface and truncated on the other end (**Figures 2.8D and 2.8E**).

Interpretation

Lithofacies in LFA-4 record a combination of bypassing high- and low-density sediment gravity flows (Stevenson *et al.*, 2015). Basal mudclast lags in thick-bedded sandstones of LF-1 at the base of LFA-4 are interpreted to be the product of bypass and erosion from successive high-density turbidity currents that resulted in the stepped composite incisional surface over which this LFA is found, whereas thin-bedded sandstones and siltstone-dominated deposits of LF-5 and LF-6 represent deposition from low-density turbidity currents that drape underlying beds. The progressive transition into thin-bedded sandstone and siltstone-dominated deposits suggest a gradual waning from bypassing flows (Bouma, 1962; Talling et al., 2012; Mutti and Normark, 1987).

Based on the location of this LFA, at the base of a ~25 m deep composite incisional surface, paleoflow measurements (156°) generally consistent with the overall paleoflow trend of the studied interval (175°) and onlapping sandstones towards the erosive surface, we interpret that LFA-4 represents the fill of a sedimentary conduit. Repeated cut and fill events record a history of high energy sediment transport, erosion, bypass and ultimately sediment deposition within an active channel. Therefore, this particular combination of lithofacies represents early deposition within a channel (*i.e.*, early stage channel-fill deposits) that was not subsequently filled by thick- to thin-bedded sandstone (*e.g.*, LFAs 1, 2 and 3).

Out-of-channel facies association

Undifferentiated out-of-channel successions comprise a significant portion of the studied outcrop belt, however, due to their inherent nature, fine-grained deposits tend to be heavily weathered and/or covered by a layer of soil and vegetation that makes them difficult to characterize (Macauley and Hubbard, 2013; Thomas and Bodin, 2013; Nesbit *et al.*, 2021).

LFA-5: Thin-bedded mudstone dominated deposits

Description

LFA-5 is the dominant association in stratigraphic sections 21 and 33A (**Figures 2.5 and 2.7E**). Its deposits range from structureless siltstone with or without sandstone laminae of LF-6 and LF-7 to interbedded thin-bedded sandstone and siltstone of LF-5 (**Figures 2.6I and 2.6K**). Sandstone beds are fine to very-fine grained and are commonly ripple laminated (T_c division), although planar laminations (T_d division) are also present (**Figure 2.6J**). Medium- to thick-bedded sandstone facies (LF-3 and LF-2) are found as isolated, non-amalgamated, tabular beds. Internally they range from coarse to fine-grained, arecommonly structureless (T_a division) with a moderate to low content of mudclasts at the base, with planar and ripple laminations towards the top (T_b and T_c divisions).

Interpretation

Siltstone deposits make up the bulk of LFA-5, with minor sandstone beds and laminae in LF-5 and LF-6, suggesting the prevalence of low-density sediment gravity flows where fall out from suspension dominates over bedload transport and tractional processes (**Figure 2.9A**). Based on the specific location of LFA-6, above and lateral to intra-channel lithofacies associations (located 10s of meters eastward), its fine-grained nature, and the absence of erosive surfaces we interpret this succession as an overbank. Under

this assumption, the high-density portion of the sediment gravity flows remained confined in the sedimentary pathway (*i.e.*, intra-channel deposits), whereas the low-density portion would overspilled from the main current and lead to further confining of the channel (Kane *et al.*, 2007; Kane and Hodgson, 2011; Hansen *et al.*, 2015).

Thicker and coarse-grained sandstone beds with tabular geometries and no amalgamation suggest sporadic overspill of high-density currents resulting in splay deposits in the overbank (**Figure 2.9B**). Paleoflow measurements on ripples within this LFA show an overall direction of 74°, which is oriented towards the channel deposits. Such paleoflow deviation in thin-bedded turbidites in channel-levee systems have been attributed to flow reflection and deflection caused by larger-scale external confinement (*i.e.*, an external levee). Thus, based on the characteristics described above, we interpret deposits of LFA-5 as being deposited in an internal levee (Kane and Hodgson, 2011; Hansen *et al.*, 2015; 2017a).

Non-stratified and chaotic lithofacies associations

In the studied interval, non-stratified and chaotic lithofacies associations are commonly found underlying coarse-grained thick-bedded intra-channel sandstones, range between 5 and 15 m in thickness, and contain isolated lenticular or contorted bodies of stratified sandstone beds.

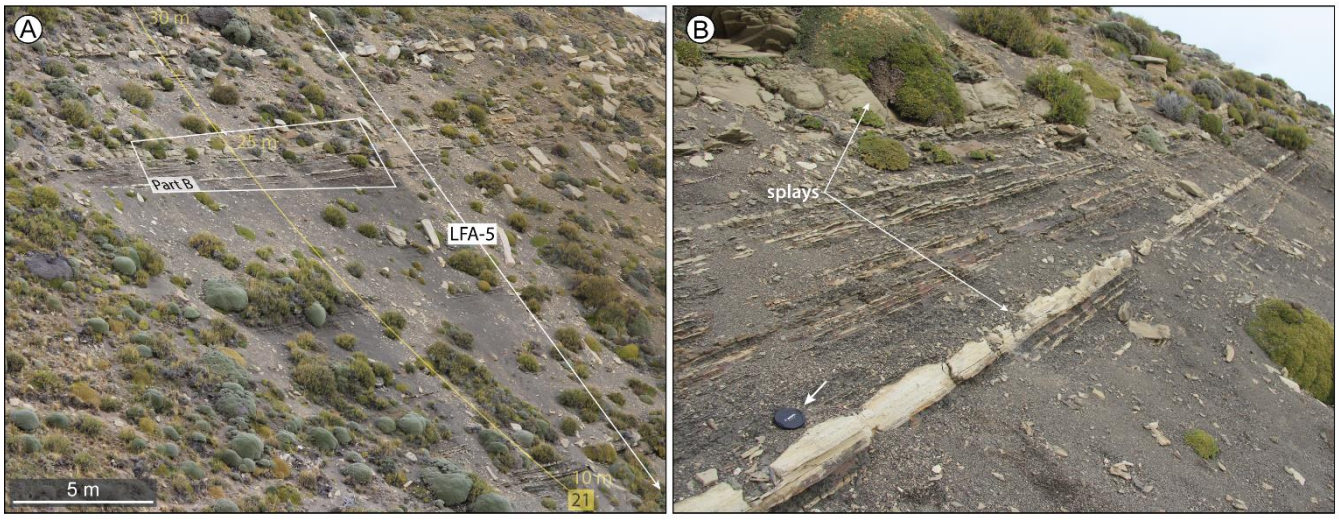

Figure 2.9: Out-of-channel lithofacies association as seen in the field (see figure 2.5 for picture location). **(A)** Thin-bedded mudstone dominated deposits interpreted as an internal levee. **(B)** Detail of local medium-bedded sandstones interpreted as splay deposits on the internal levee.

LFA-6: Massive and chaotic mudstone-rich deposits

Description

LFA-6 groups two types of disorganized lithofacies where structureless mudstone makes up the bulk of the succession (LF-8 and LF-9). LF-8 consists of structureless gravel-rich to sandy mudstones. Gravels within this LF are poorly sorted, well rounded and made up largely by extrabasinal granules and pebbles, although mudclasts may also be present. Sand is medium- to coarse-grained, with both grain sizes randomly distributed randomly throughout the lithofacies. The basal contact is commonly characterized by an erosive surface on intra-channel sandstones.

Deposits of LF-9 correspond to disorganized mudstone with blocks of contorted sandstone beds. They present a patchy texture defined by discrete changes in color and may contain poorly sorted gravels. The contorted sandstone beds enclosed in this lithofacies are discontinuous, chaotically folded, non-amalgamated and range from thin-bedded fine-grained to medium-bedded medium-grained, with dimensions of 10s cm to meters long and up to 10s cm thick. The upper contact of LFA-6 is sharp and erosive, overlain by intra-channel sandstones or concordant siltstone of LF-7.

Interpretation

Both lithofacies included in LFA-6 are the product of *en masse* deposition (*i.e.*, by 'cohesive freezing' of the sediments) due to a decrease of the shear stress below the cohesive strength leading to an almost instantaneous cessation of movement (Lowe, 1982; Talling *et al.*, 2012). Deposits of LF-8 are attributed to debris flows. Studies on these types of deposits have shown that debris flows can travel as far as 10s to 100s kms downslope from their source and can make up an important portion of submarine channel fills (Georgiopoulou *et al.*, 2009; Bernhardt *et al.*, 2012). The presence of extrabasinal gravels, larger than the coarsest grains within sandstones of LF-1 and LF-2, suggest that some debris-flow deposits could potentially be derived from the collapse of coeval shelf to shelf-margin regions located >40 km north (**Figure 2.3**) (Bauer *et al.*, 2020). Because of the irregular topography of debris-flow deposits, sandstone deposition would initially occur as lenticular bodies forming scour fills in the form of concordant amalgamated and non-amalgamated isolated turbiditic successions.

On the other hand, mudstone-rich deposits of LF-9 are attributed to mass-wasting processes such as slumping, sliding, and rafting of previously deposited successions. The partially preserved but deformed strata of thin- to medium-bedded sandstones contained in this lithofacies is similar to lithofacies found in LFA-3 (channel margin) and LFA-2 (channel off-axis). Thus, we suggest that they result from the

destabilization of mudstone-rich inner overbank deposits, and channel off-axis and margin deposits accumulated by previous flows inside the channel conduit.

2.4.3 | Stratigraphic hierarchy and architecture

The use of a hierarchical approach to describe stratigraphic patterns in submarine channel systems provides a common framework to link channelized deposits at different scales and to compare them with equivalent deposits in other locations and/or derived from different data sets (Mutti and Normark, 1987; Sprague *et al.*, 2005; Di Celma *et al.*, 2011; Macauley and Hubbard, 2013; Bell et a., 2021). The objective of a hierarchical description in our study is to subdivide stratigraphic architecture that includes larger composite features with smaller-scale and geometrically similar component bodies. Our approach largely resembles the scheme proposed by Sprague *et al.* (2005), McHargue *et al.* (2011) and other subsequent studies (see Cullis *et al.*, 2018 for a review on hierarchical classifications). Under this classification, spatially related intra-channel lithofacies associations form the fundamental building blocks, termed *channel elements* (Macauley and Hubbard, 2013; Hubbard *et al.*, 2014; Hansen *et al.*, 2015). The transition between one channel element and another is, in most cases, marked by an abrupt vertical change in lithofacies association. However, closely stacked channel elements may be separated only by discrete erosion surfaces without changes in lithofacies associations making the distinction uncertain. Genetically related channel elements (*i.e.,* similar architectural and stacking patterns) compose larger-scale units referred to as a *channel complex*, separated by a composite erosional surface and thick successions of chaotic mudstone-rich deposits. In conventional seismic-reflection data, channel complexes are commonly the finest resolvable unit. Finally, genetically related channel complexes (*i.e.*, deposited in the same channel belt) can then be grouped into a *channel complex set* (Campion *et al.*, 2000; Beaubouef, 2004; Sprague *et al.*, 2002; McHargue *et al.*, 2011).

The studied interval consists of approximately 300 m of stratigraphy in which the distribution of lithofacies associations and architectural patterns allowed us to define four channel complexes (designated in relative stratigraphic order as CC-I, CC-II, CC-III and CC-IV) consisting of multiple channel elements (designated in relative stratigraphic order as A, B, C and D) (**Figures 2.10, 2.11 and 2.12**).

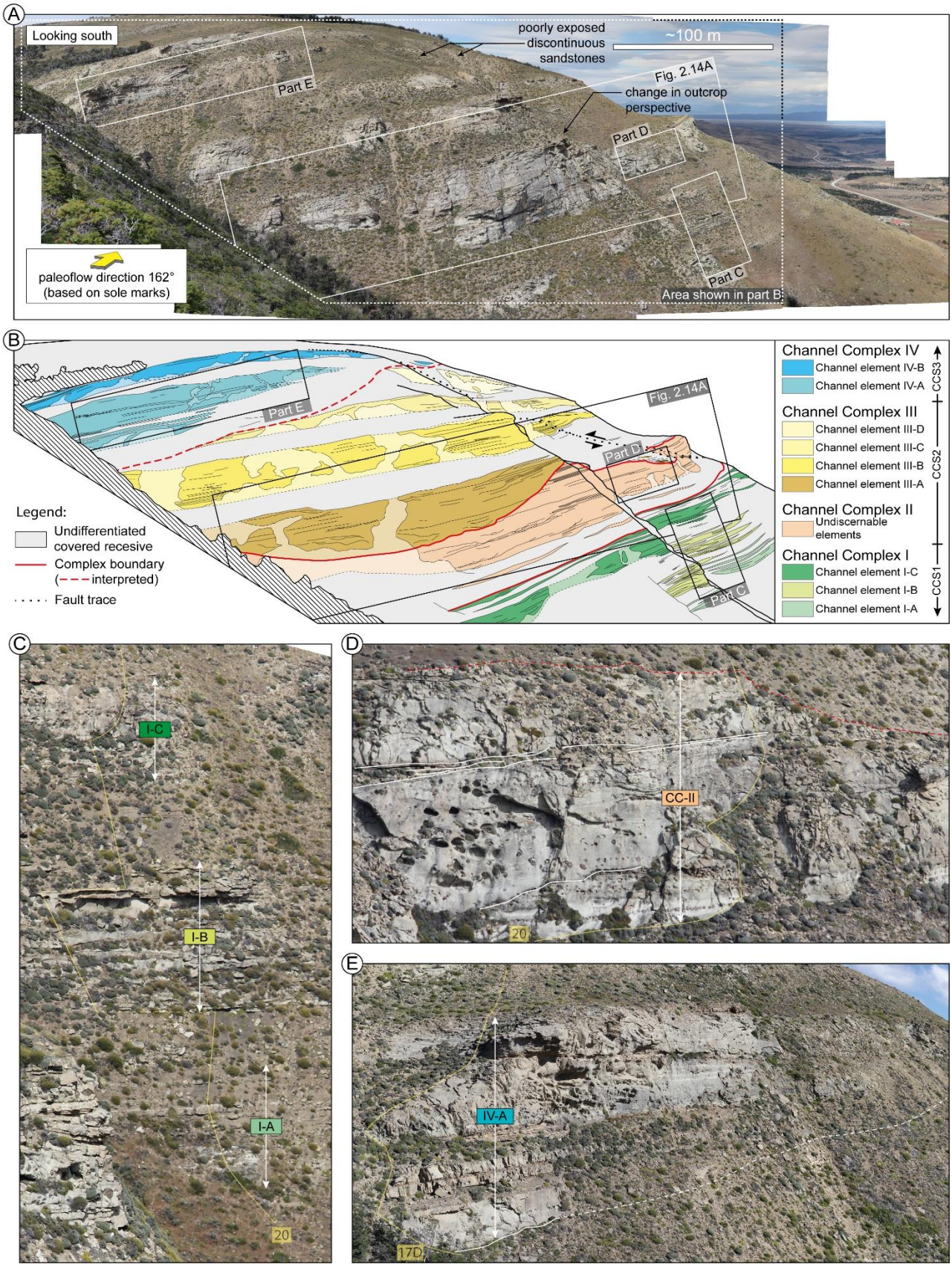
A
Looking south
poorly exposed
discontinuous
sandstones
~100 m
Fig. 2.14A
change in outcrop
perspective
Part E
Part D
Part C
Area shown in part B
paleoflow direction 162°
(based on sole marks)
B
Part E
Fig. 2.14A
Part D
Part C
Legend:
Undifferentiated
covered recesive
Complex boundary
(interpreted)
Fault trace
Channel Complex IV
Channel element IV-B
Channel element IV-A
Channel Complex III
Channel element III-D
Channel element III-C
Channel element III-B
Channel element III-A
Channel Complex II
Undiscernable
elements
Channel Complex I
Channel element I-C
Channel element I-B
Channel element I-A
CCS3
CCS2
CCS1
C
I-C
I-B
I-A
20
D
CC-II
20
E
IV-A
17D

Figure 2.10: Stratigraphic Hierarchy. **(A)** Depositional strike-oriented photomosaic of the studied channelized deposits. **(B)** Interpreted line drawing of the photomosaic shown in A highlighting the hierarchy and architecture of submarine channels. **(C)** Outcrop expression of channel elements I-A, I-B, and I-C vertically transitioning from margin to off-axis to axial deposits suggesting a dominantly aggradational, with minor lateral offset, stacking pattern. **(D)** Outcrop expression of highly amalgamated, laterally offset channelized deposits in channel complex II. The dashed red line denotes the composite incisional surface shown in figure 8C. **(E)** Outcrop expression of channel element IV-A. Note the rapid decrease in thickness.

Channel complex I (CC-I)

CC-I crops out along the N-S oriented face of the outcrop, and it is best represented by sections 1 and 20 (**Figure 2.5**). It consists of 75 to 85 m of discontinuous exposures of non-amalgamated to amalgamated medium- to thick-bedded sandstones of LFA-2 and LFA-1 interrupted by fine-grained thin-bedded sandstones and mudstone dominated deposits of LFA-3 with an overall increase in sandstone beds thickness and amalgamation upwards (**Figure 2.10C**). We identified three vertically stacked channel elements withing this complex:

Channel element I-A

Element I-A is partially exposed in the basal 20 m of this complex, with its thickest exposures in sections 12A and 20 (**Figure 2.5**). From its base to the top it comprises: (i) chaotic mudstone-rich deposits of LF-9 (mass-wasting deposits) in sections 12A and 20; truncated by a sharp surface overlain by (ii) 5 to 10 m thick- to medium-bedded amalgamated coarse-grained sandstone of LF-2 and LF-3; and (iii) 5 to 15 m of mostly non-amalgamated medium-bedded coarse- to medium-grained sandstone of LF-3 and LF-4 intercalated with thin-bedded sandstones of LF-5 and siltstone-dominated lithofacies of LF-6, LF-7 and LF-8. Overall, the vertical trend of lithofacies associations in element I-A suggests a transition from channel-axis (LFA-1) to channel off-axis (LFA-2) and channel margin (LFA-3) (**Figure 2.10C**).

Channel element I-B

The base of element I-B is marked by an erosional surface on element I-A, above which the stratigraphy is as follows: in sections 12A, 20 and 25C the basal surface is overlain by (i) ~5 m of chaotic mudstone-rich deposits (debris flow deposits) of LF-8, whereas in section 1 the erosive surface truncates mudstone dominated deposits of LF-6 of the underlying element with a sharp contact with medium- to thick bedded sandstones of LF-1 and LF-2; (ii) ~10 m of thick- to medium-bedded semi-amalgamated coarse-grained sandstone of lithofacies LF-2 and LF-3 with occasional mudclasts, intercalated with thin- to medium-bedded sandstones of LF-4 and LF-5 and siltstone-dominated lithofacies of LF-7 with abundant bioturbation and organic rich matrix, indicative of channel off-axis (LFA-2) and channel-margin

(LFA-3). This succession is overlain by (iii) 5 to 10 m of thick-bedded, amalgamated and coarse- to very coarse-grained sandstones with abundant mudclasts locally and thick intervals with planar lamination of lithofacies LF-2 and LF-1; and (iv) ~5 m of medium- to thin-bedded, non-amalgamated fine- to coarse-grained sandstones of LF-5 and LF-6 and siltstone-dominated LF-7 and LF-8. The distribution of these lithofacies is interpreted as a vertical transition from channel-off-axis (LFA-2) to channel-axis (LFA-1) and channel-margin (LFA-3) (**Figure 2.10C**).

Channel element I-C

The transition into the upper and last element of CC-I in the studied interval is characterized by 5 to 10 m of concordant siltstone dominated deposits of lithofacies LF-6, LF-7 and locally thin-bedded sandstones of LF-5; thus the boundary with the underlying element cannot be established with certainty. Above this transition, element I-C is characterized by (i) 5 m of discontinuous medium- to thin-bedded, non-amalgamated, medium- to fine-grained sandstones of LF-4, LF-3 and LF-5, and siltstone dominated deposits of LF-6 exposed in sections 1 and 20; (ii) 10 to 12 m of continuous thick-bedded, amalgamated, coarse-grained sandstones of LF-2 and LF-3 with local mudclasts; and (iii) 5 to 7 m of a combination of thick- to medium-bedded, mostly non-amalgamated sandstone of lithofacies LF-2 and LF-3, and thin-bedded lithofacies LF-4 and LF-5, with intercalations of siltstone dominated deposits of LF-6. This overall trend is attributed to channel-margin deposits (LFA-3) overlain by channel-axis (LFA-1) and again channel-margin deposits (LFA-3) (**Figure 2.10C**).

Based on the exposure, lithofacies associations, and erosion surfaces, we estimate channel-element thicknesses of 30 to 40 m, with the bulk of the complex channel fills outside the plane of the outcrop. The S to SE paleoflow measured in these elements (*i.e.*, subparallel to the outcrop), the recessive successions separating channel elements, and the general increase in sandstone amalgamation suggest an aggradational stacking pattern with a moderate eastward lateral component as the complex evolves.

Channel complex II (CC-II)

CC-II is defined by a sharp erosive surface overlain by: (i) 10 to 15 m of chaotic mudstone-rich deposits of LF-8 and LF-9 (*i.e.*, LFA-6: debris flow and mass transport deposits respectively) with isolated, <2 m thick, sandstone filled scour in the form of lenticular bodies; and (ii) sandstone-dominated channel-fill deposits of variable thickness between 15 and 45 m. Channel-fill deposits are largely comprised of very thick to thick-bedded, amalgamated, conglomeratic to coarse-grained sandstones of

lithofacies LF-1 and LF-2 with strong evidence for bypass and erosion, expressed by abundant amalgamation surfaces between sandstones, some of which can reach up to ~10 m of relief (**Figure 2.10D**), and mudclasts lags. Mudstone intraclasts in LF-1 are as large as >1 m long and are commonly concentrated towards the base of massive very thick-bedded sandstones containing gravel size extrabasinal clasts and bioclasts derived from inoceramid and oyster shells. There are at least two major internal surfaces, that can be traced along the outcrop, characterized by <2 m thick, thin-bedded sandstones of LF-4 and LF-5 with siltstone dominated deposits of LF-6 and debris flow deposits of LF-8 in lower areas (LFA-6). These surfaces are interpreted as the boundaries between three highly amalgamated channel elements of up to 20 m thick filled with mostly channel-axis deposits (LFA-1) and poor developed channel off-axis (LFA-2) and channel-margins (LFA-3) (**Figures 2.8B and 2.8C**).

Channel complex III (CC-III)

Channel Complex III is associated with the main sedimentological and architectural features discussed in this study. The majority of this complex crops out in the middle of the studied interval, with its best exposures located in the NE-SW face of the outcrop. With a general paleoflow of 175°, this side of the outcrop provides a perspective that is almost perpendicular to the depositional dip of the channel system at Sierra Solabarrieta. The ~115 m thick channel complex is composed of three well defined vertically stacked channel elements and a potential fourth element if an overlying, ~30 m thick and poorly exposed, succession is also considered (**Figure 2.10**):

Channel element III-A

Contrary to the other channel elements in the studied interval, element III-A lacks the basal debritic succession that typifies the boundary between units (elements or complexes). Instead, its base is defined by a pronounced channelized incisional surface with relief between 35 to 40 m that truncates the top of CC-II. Intra-channel deposits are predominately thick- to very thick-bedded sandstones of LF-1, LF-2 and to a lesser degree LF-3 attributed to channel-axis deposits (LFA-1) with abundant secondary channelform surfaces nested within the main incision that forms the base of this element (sections 17-A, 17-B and 18A) (**Figure 2.5**). Right where the outcrop changes its orientation from NE-SW to NS, intra-channel deposits rapidly decrease their thickness from ~40 m thick thick-bedded sandstones of LF-1 and LF-2 in section 17A attributed to axis deposits (LFA-1) to less than 10 m of medium- to thin bedded dominated sandstones of LF-3 and LF-4 in sections 1 and 34-B in the margin (LFA-3) (**Figure 2.5**). Externally, the basal and nested incisional surfaces of channel element III-A show an asymmetric profile, with a steep relief towards

SW and gentle relief towards NE. Even though the NE margin of this channel element is not expose, its width can be estimated by projecting its basal surface, resulting in an approximate width between 350 and 400 m (**Figure 2.10**).

The basal incision that truncates CC-II can be traced along the entire extent of the studied outcrop towards the south, however, the nature of the overlying deposits changes significantly. Where sections 18A, 17B, 17A, 34A and 1 show sandstone-rich lithofacies attributed to intra-channel deposits (LFA-1 and LFA-3); sections 23, 24, 33A and 21 display mostly mudstone-rich out-of-channel lithofacies (LFA-5) (**Figure 2.9A**). However at the top of sections 20, 35A and 35B, overlying deposits show a combination of siltstone dominated, thin-bedded and fine-grained sandstone as well as thick- to thin-bedded partially amalgamated sandstones that onlap towards the incision that we interpreted as deposition related to the early stage of the channel evolution (**Figures 2.8C and 2.8D**).

Channel element III-B

The base of channel element III-B is defined by an erosional surface of up to 5 m in relief that truncates the top of channel element III-A and overlain by 10 to 15 m of structureless gravel-rich to sandy mudstones to of LF-8 (LFA-6). Sandstone-dominated intra-channel lithofacies reach its maximum thickness of 30 to 35 m in sections 17C, 17E and 18B, in which the stratigraphic succession can be described by: (i) 10 m of medium- to thick-bedded amalgamated sandstones with localized thin-bedded sandstones of channel off-axis deposits (LFA-2); (ii) up to 2 m of channel-margin related non-amalgamated and very thin-bedded sandstones (LFA-3) that can be traced between section 1 and 17E and expressed as an incision surface in section 18B (**Figure 2.8A**); and (iii) ~20 m of axial thick- to very thick-bedded amalgamated sandstones (LFA-1). South of section 1, the succession gets increasingly thinner and less amalgamated towards section 31AB until it is no longer distinguishable beyond section 12A, where isolated pockets of siltstone-dominated lithofacies (LF-5 and LF6) attributed to overbank deposits (LFA-5) are observed. The exact contact between the two distinct deposits could not be established with certainty due to cover.

Channel element III-C and III-D

Channel element III-C resembles element III-B, its base is defined by a slightly erosive surface that truncates previous intra-channel deposits followed by 10 to 15 m of structureless gravel-rich to sandy mudstones of LF-8 attributed to debris flow deposits and sandstone-dominated intra-channel deposits

(LFA-1 and LFA-2) with an estimated outcropping thickness of 15 to 20 m in sections 1 and 22 that become progressively less amalgamated to the south (LFA-3), particularly in sections 12A and 25F; whereas towards the north the same intra-channel deposits appear to be truncated in section 18B. A potential fourth channel element (III-D) was identified ~15 m above element III-C in section 31D. Like the underlying channel element, its deposits appear to also be truncated northwards, however, debris cover, and the extremely low quality of the outcrop thwarted further observations for these channel elements.

Channel complex IV (CC-IV)

Channel complex IV crops out above channel element III-C and is partially lateral to III-D, which ends abruptly by what we interpret as the basal erosional surface of a new complex set, with a composite incision of at least 40 m in relief. However, the quality of the outcrop and extensive cover makes it difficult to establish the exact geometry of this surface and nature of the fine-grained sediments that drape it. CC-IV has a total estimated thickness of 85 to 90 m, of which the upper ~75 m is exposed, revealing two vertically stacked channel elements (**Figure 2.10**).

Channel element IV-A

The thickest section of element IV-A was measured in section 17D, here the channel element is comprised of: (i) ~8 m of amalgamated to non-amalgamated thick- to medium-bedded sandstones of LF2 and LF-3 attributed to channel off-axis deposits (LFA-2); (ii) ~10 m of thin- and very thin-bedded sandstone with mudstone prone intervals of LF-5 and LF-6 and medium- to thick-bedded semi-amalgamated sandstones of LF-3 attributed to channel-margin deposits (LFA-3) and a ~1,75 m thick debris flow deposit (LFA-6); and (iii) ~25 m of amalgamated very thick- to thick-bedded, coarse- to very coarse-grained sandstones with abundant mudclasts and extrabasinal granules attributed to channel-axis (LFA-1) in sections 17D and 18B (**Figure 2.10E**). All this succession thins and pinch out towards south, with only 10 and then 6 meters of intra-channel deposits exposed in sections 19 and 1, respectively (**Figure 2.5**).

Channel element IV-B

Element IV-B is the uppermost channelform unit of the studied interval. Its base is defined by a low-relief erosive surface overlain by (i) 10 to 15 m of structureless gravel-rich to sandy mudstones of LF-8 attributed to debris flow deposits (LFA-6); (ii) 12 to 18 m of laterally variable intra-channel deposits. Sections 18B and 19 are dominated by amalgamated thick- to very-thick bedded sandstones of LF-2 and

LF-1 interpreted as channel-axis deposits (LFA-1), whereas northwards, intra-channel deposits thin and pinch out, becoming increasingly less amalgamated. Section 17D, although coarser in grain size, records 5 and 3 m of semi-amalgamated thick- and thin-bedded sandstones at its base and top respectively, attributed to channel off-axis deposits (LFA-2) and 9 m of amalgamated very thick- to thick-bedded sandstones in between (LFA-1). Further north, sections Kn1 and Kn2 record thicker intervals of channel-margin (LFA-3) thin-bedded non-amalgamated sandstones of LF-4 and LF-5 intercalated with amalgamated thick- to medium-bedded sandstones of channel off-axis deposits (LFA-2). To the south, element IV-B is mostly covered by rubble and soil, although section 1 appears to have mostly thick- to very-thick bedded sandstones (LFA-1) (**Figure 2.5**).

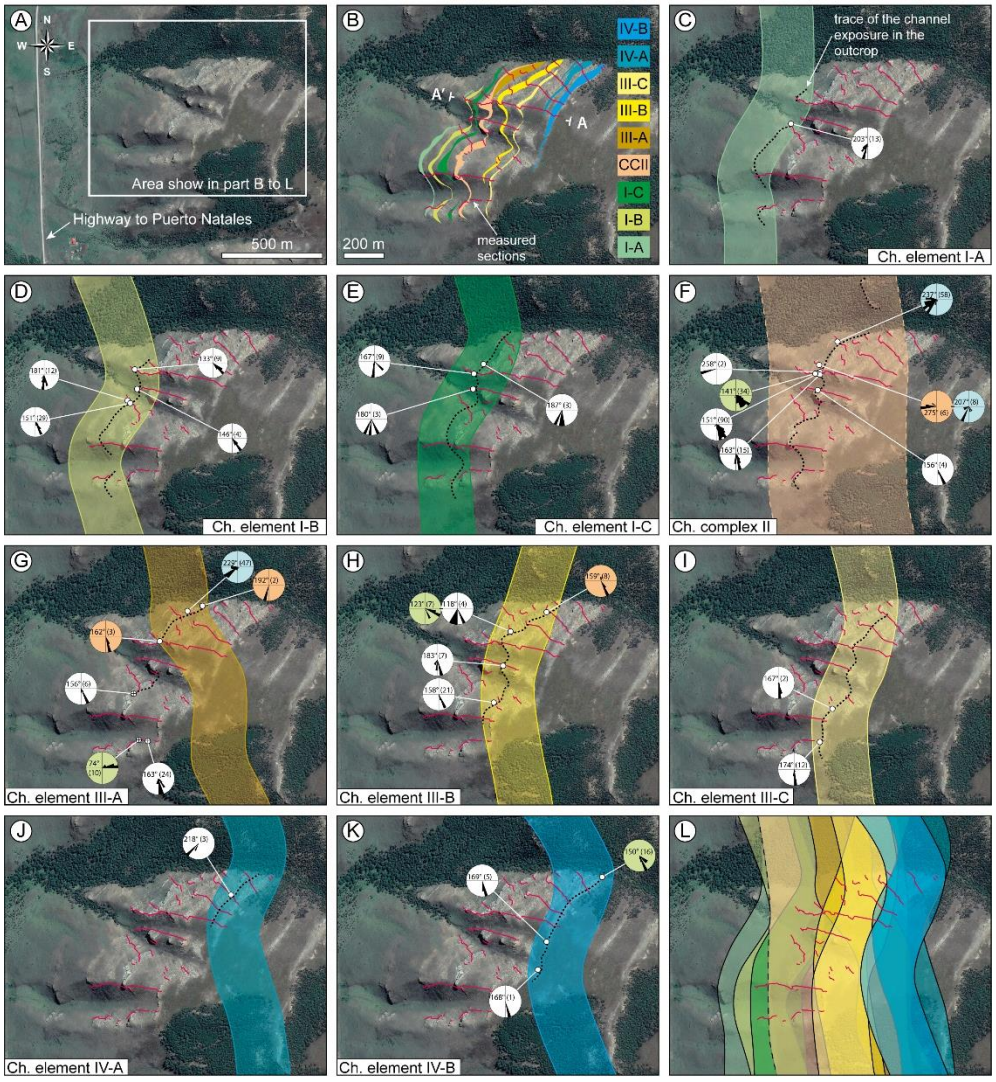

Figure 2.11: Interpreted reconstruction of the planform geometry of channelized deposits. **(A)** Location of the studied outcrop. **(B)** Distribution of outcropping channelized deposits. Cross-section is shown in figure 12 **(C-K)** Interpreted planform expression of channel elements and complex (CC-II) based on lithofacies associations

distribution and measured paleoflows. Channel-width is interpreted to be ~310-380 m based on the exposure along the depositional strike of channel element III-A. Paleoflows measured outside this element are genetically related to it in the form of early channel-fill and overbank deposits. Due to the lack of a confining surface or channel-margin deposits in CC-II, it's width cannot be estimated. **(L)** Planform distribution of all channel elements and CC-II showing an overall aggradational, slightly offset stacking pattern.

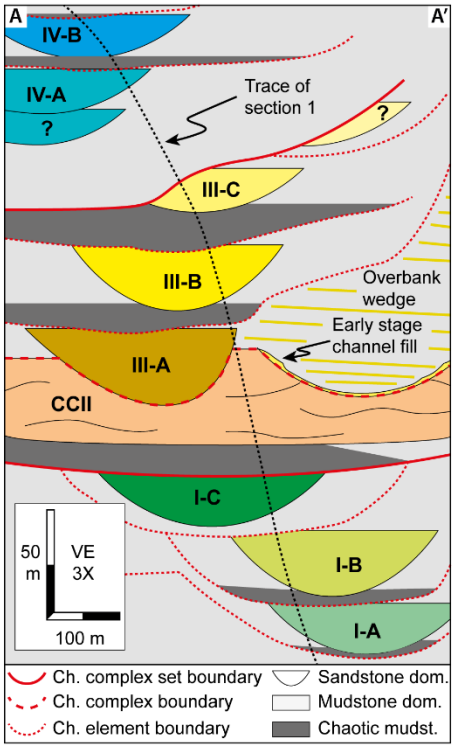

Figure 2.12: Interpreted simplified stratigraphic summary. Stacking pattern along the depositional strike of the studied succession as seen from the observation point depicted in figure 2.4A. Color code follows the one used in figures 2.10 and 2.11. The black dashed line follows the outcrop elevation profile along section 1 (see figure 2.11 for location of profile).

2.5 | DEPOSITIONAL EVOLUTION

The description and interpretation of the stratigraphic hierarchy and architecture of slope channels exposed in the studied area of Sierra Solabarrieta allow us to reconstruct their depositional evolution and evaluate conceptual models. The studied sedimentary succession includes an interval that records a protracted phase of bypass and erosion followed by a comparatively rapid phase of channel filling commonly described in similar systems (Englert *et al.*, 2020; Hubbard *et al.*, 2020). This interval also marks the transition between two styles of depositional architecture commonly observed in seismic-reflection datasets (Pirmez and Imran, 2003; Deptuck *et al.*, 2007; Sansom, 2018) but comparably rare in outcropping successions: laterally stacked/low-aggradation and vertically stacked/high-aggradation. Here,

we focus on the two channel complexes that represent this transition, CC-II and CC-III, in the context of the overall system evolution (**Figure 2.13**).

The abrupt change in depositional architecture observed between CC-I and CC-II suggest that the latter represents the onset of a new channel complex set at the base of a large-scale conduit that would have served as the main pathway for sediment gravity flows during the development of complexes CC-II to CC-IV. The establishment of this conduit is marked by 10 to 15 m thick debris flow deposits. The extensive deposition of channel-axis lithofacies associations (LFA-1) in comparison to poorly developed margin and off-axis lithofacies associations (LFA-2 and LFA-3) within channel complex II is interpreted to record deposition from high-density turbidity currents in an overall weakly confined setting, which allowed widespread lateral migration, high amalgamation, and low aggradation between channel elements of CC-II (**Figure 2.13A**).

As the system evolved, subsequent bypass and erosion by high-density turbidity currents promoted flows to focus on preferred pathways, thus, scouring into the underlying intra-channel deposits of CC-II (**Figure 2.13B**). Bypass and erosion along these scours resulted in the inception of a new channel complex (CC-III) and the establishment of a new pathway for sediment gravity flows where confinement was achieved through a ~25 m deep incision into underlying CC-II deposits. The nature of this channel as an active pathway is revealed by the composite character of the incisional surface and the truncation towards the interpreted thalweg of early channel-fill deposits (LFA-4) that onlap on the incisional surface (**Figure 2.13C**). However, the absence of thick-bedded amalgamated sandstones (LFA-1) suggests that this fairway was abandoned before being filled with late intra-channel deposits (**Figures 2.8C and 2.8D**).

We interpret that as the initial channel pathway was being abandoned, a coeval or partially coeval incision located ~60 m east became the preferred fairway, resulting in erosional relief that would later be filled with the intra-channel deposits that characterize channel element III-A. Sediment gravity flows focused in this fairway would erode as much as 35 m deep into underlying CC-II and sporadically overspill the confining relief, resulting in overbank deposition and the buildup of an internal levee (*e.g.*, Hansen *et al.*, 2017b). These overbank deposits, characterized by siltstone and thin bedded, fine-grained sandstones (LFA-5), developed on top of the abandoned channel pathway, thus preserving early channel-fill deposits (LFA-4) (**Figure 2.13D**). We also interpret that the development of the internal levee hampered lateral migration of channels and contributed to the aggradational stacking pattern that distinguishes overlying

channel elements III-C and III-D and CC-IV, therefore changing the larger-scale stacking pattern and overall depositional architectural (**Figure 2.13E-2.13G**).

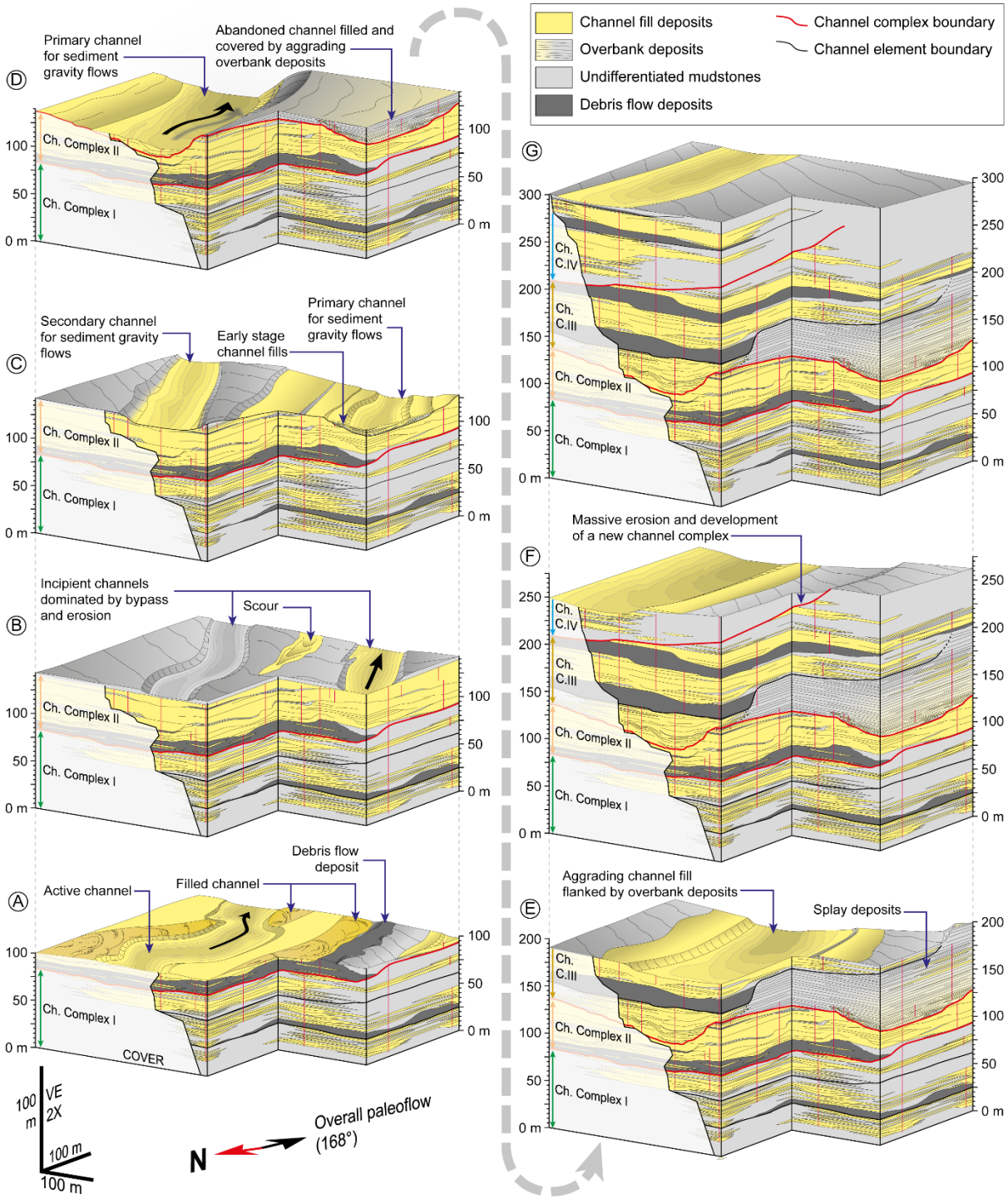

Figure 2.13: Interpreted evolution of the studied interval highlighting the stratigraphic architecture and components of a slope channel system (stratigraphic sections marked by vertical red lines; translucent area corresponds to covered/interpreted stratigraphy). **(A)** Widespread deposition of poorly confined, laterally migrating channels

hinders the vertical growth of Channel Complex II. **(B)** Repeated bypass and erosion promote flow concentration along preferred fairways that incise into the underlying channel complex. **(C)** Repeated erosion generates a composite incisional surface where early-stage channel-fill deposition occurs (Basal surface of Channel Complex III). **(D)** Abandonment of the previous primary channel and development of a new preferred fairway dominated by bypass and erosion. Overbank deposition on top of the initial incision contributes to the preservation of early-stage channel-fill deposits. **(E)** New sediment gravity flows are restricted by overbank deposits, facilitating channel aggradation. **(F-G)** Development a new channel complex (Channel Complex IV) characterized by a deep initial incision and high aggradation by confinement with a stratigraphic architecture comparable to Channel Complex III.

2.6 | DISCUSSION

2.6.1 | Importance of erosion and bypass in the architectural transition from lateral to vertical stacking patterns

The architectural transition from laterally offset channels to vertically stacked aggradational channels has been recognized in numerous channel-levee depositional systems in the stratigraphic record (Hodgson *et al.*, 2011; Englert *et al.*, 2020) as well as in seismic-reflection datasets (Pirmez and Imran, 2003; Deptuck *et al.*, 2007; Sansom, 2018). The controls behind this change in stacking patterns have been attributed to autogenic processes inherent to channel evolution, tectonics and a combination of both (Hubbard *et al.*, 2009; McHargue *et al.*, 2011; Casciano *et al.*, 2019), however, the sedimentologic and stratigraphic expression of the processes that reign this transition have been poorly discussed. The outcropping interval studied at Sierra Solabarrieta records this transition in the context of channel evolution, thus allowing us to integrate bed-scale observations into the larger channel complex-scale.

Based on their depositional architecture, we interpret CC-II and CC-III to represent a laterally stacked/low-aggradational channel complex overlain by vertically stacked aggradational complex. The boundary between both complexes is defined by a composite erosional surface with two adjacent element-scale channelized incisions along an EW profile with distinctive sedimentary infill: the western incision (~25 m deep) is characterized by a basal drape of thick-bedded, mudclast-rich coarse grained sandstones overlain by a thinning- and fining-upward succession of non-amalgamated medium- to thin-bedded sandstones with siltstone-dominated intervals (LFA-4) that transitions into thin-bedded turbidites (LFA-5); whereas the eastern incision (~35 m deep) is primarily filled with amalgamated very thick- to medium bedded sandstones in the axis (LFA-1) that rapidly transition into medium- and thin-bedded sandstones towards its margin (LFA-3) (**Figure 2.14**).

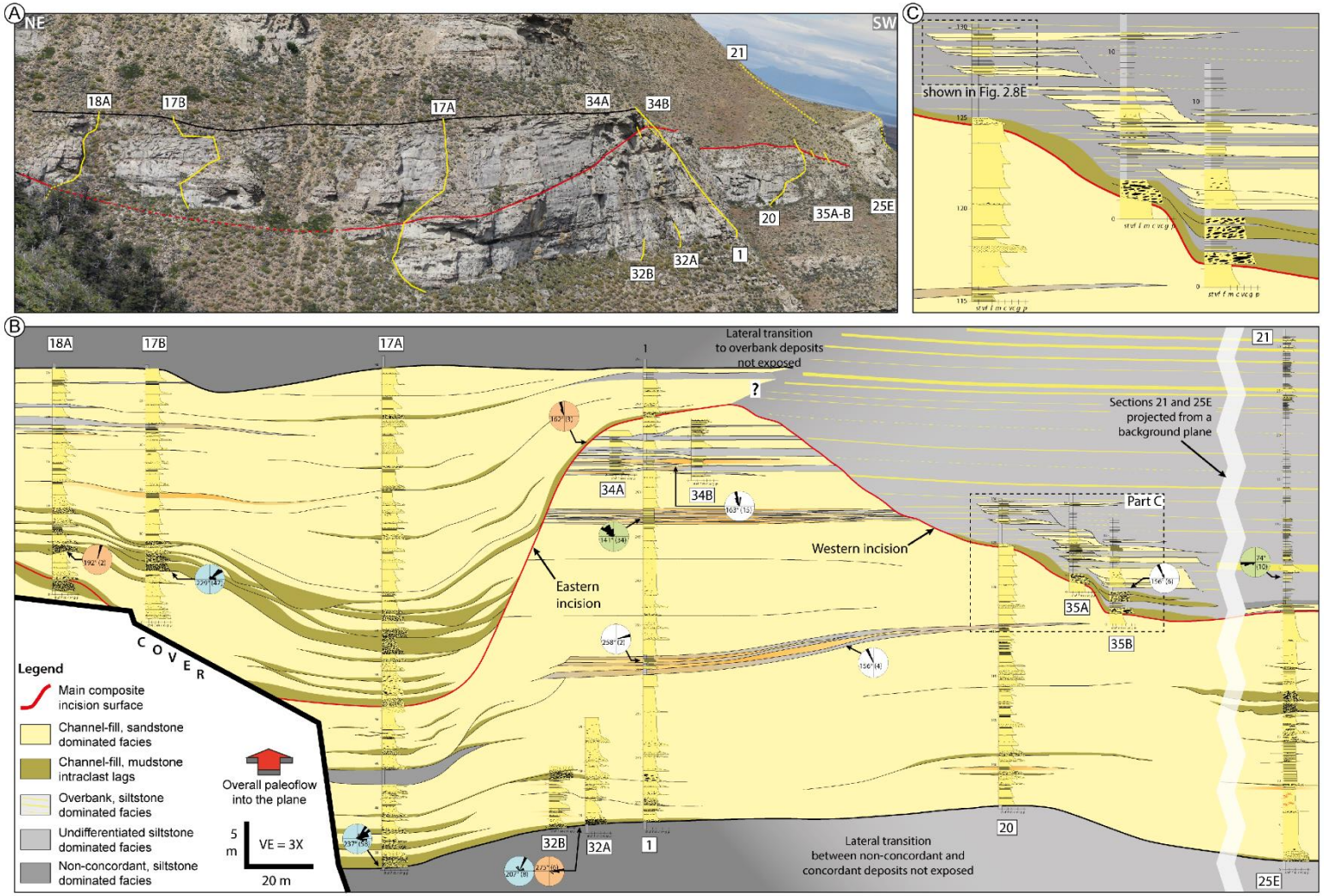

Figure 2.14: Detailed reconstruction of the transition from laterally offset channels to vertically stacked aggradational channels. (A) Horizontally aligned view that highlights the transition from CC-II to CC-III and the incisional nature of the sharp composite surface that separates them. (B) Interpretative cross-section obtained from part A. Note how the channel complexes are bounded by a composite surface with two 10s m deep channelized incisions; one filled with early-stage channel-fill deposits covered by overbank deposits and the other by fully evolved channel-fill deposits. (C) Detail of the stratigraphic expression along the depositional strike of early-stage channel-fill deposits illustrating the complexity caused by successive erosion and deposition while the channel was active.

Our interpretation suggests that following the development of laterally stacked/low-aggradational channels at the base of a channel complex set, there was a period of bypass and erosion in which subsequent sediment gravity flows would have scoured the underlying deposits, resulting in a composite incisional surface where one or more incipient channels may have been present at the same time as a sinuous channel (see figure 13 of Hansen *et al.*, 2015) or as separate subparallel conduits (**Figure 2.13C**). Further erosion of the western incision would have deepened it enough for it to become an active channel, as shown by the basal thick-bedded, mudclast-rich coarse grained sandstone that drape the surface, the overlying sandstone onlapping on it and the truncation of the latter towards the interpreted thalweg of the channel (**Figure 2.14C**). For reasons that cannot be ascertained with the available dataset, the western incision (*i.e.*, channel) was abandoned before being filled with typical intra-channel deposits (LFA-1 to LFA-3) and the eastern incision became the dominant channel. Thin-bedded turbidites (LFA-5) partially juxtaposed with channel fill deposits of the eastern incision (channel element III-A), that also fill and cover the western incision (**Figures 2.5 and 2.13D**), are interpreted to be the product of overspill from turbidity currents within the eastern incision.

The detailed characterization of this transition suggests that **(i)** in between the two depositional architecture styles (the older laterally offset and the younger aggradational) there is a significant phase of erosion and bypass at a complex-scale (or larger) and that **(ii)** the relief achieved via deep incision of one or multiple near contemporaneous active conduits is necessary to set up the conditions for flow stripping and, thus, overbank deposition within the channel master-conduit, resulting in the instauration of an aggradational stacking pattern through a combination of erosional processes and levee buildup. Furthermore, this interpretation proposes that the development of a complex-scale aggradational stacking pattern follows a similar mechanism than the one proposes for the inception of single element-scale channels (Fildani *et al.*, 2013; Janocko *et al.*, 2013; Bell *et al.*, 2021).

2.6.2 | Sedimentological and stratigraphic expressions of rarely preserved early channel-fill deposits

Linking the stratigraphic record to observations made in modern submarine channels systems has proved difficult due to their incompleteness and the different spatial and temporal scales associated with each one (Gamberi *et al.*, 2013; Vendettuoli *et al.*, 2019; Hubbard *et al.*, 2020). The inherent nature of submarine channel systems as long-lived conveyors of sediment means that the bulk of the depositional product observed in the stratigraphic record is commonly biased to the final phases of channel evolution,

and therefore a fraction of the complete history of the channel system. For example, Hubbard *et al.* (2020), using data 14 km to the north in the same general depositional system as this study, analyzed the relationship between the commonly amalgamated, thick-bedded sandstone lithofacies contained in a channel-element axis and thinly interbedded bedded channel-margin deposits. The results showed that, while volumetrically dominant (~70-80%), channel-axis deposits recorded less than a 10% of the sedimentation events preserved in the margin. Another study, carried out by Englert *et al.* (2020) in the Upper Cretaceous Nanaimo Group channel system in British Columbia (Canada), leveraged robust geochronologic control to show that ~60% of the 16.0±1.7 my lifespan of the system is recorded as bypass and incision.

Whereas the stratigraphic record represents the final depositional product, modern systems offer a glimpse of submarine channel systems at various stages in their lifespan. Accordingly, the observed morphologies and deposits have a high probability of being at least partially removed by subsequent erosion. Recent observations on the modern seafloor of channels subjected to turbidity currents validate this premise by demonstrating the development, up-slope migration, and ultimately low preservation of crescent-shaped bedforms termed cyclic steps (50-100 m long wavelengths) and erosional knickpoints (>1-5 km long wavelengths) as a result of supercritical flows (Hughes Clarke, 2016; Hage *et al.*, 2018; Vendettuoli *et al.*, 2019; Heijnen *et al.*, 2020; Englert *et al.*, 2021). Attempts to link modern channel seafloor bedforms to the stratigraphic record have resulted in the definition of diagnostic features attributed to supercritical-flow deposits, including (i) backfilling structures characterized by up-dip low-angle stratification, (ii) backstepping lenticular or scour-filling sandstones and (iii) highly discontinuous high-aspect ratio deposits (<1 m thick by 10s m long/wide) (Hage *et al.*, 2018; Cornard *et al.*, 2019; Englert *et al.*, 2021).

As discussed above, the transition between CC-II and CC-III is defined by a composite incisional surface with two deep incisions, one of which (the western incision) preserves a sedimentary succession directly overlying the main surface that cannot be attributed to typical intra-channel filled deposits. This succession (LFA-4) is characterized by basal mudclast-rich, coarse-grained sandstones that drape the incisional surface, which are overlain by amalgamated and non-amalgamated massive, and sometimes laminated, sandstones in an overall thinning- and fining-upward arrangement with mudstone-rich intervals. Sandstone beds within this LFA thin and pinch out in siltstone-dominated strata towards the incisional surface. In contrast, towards the deepest part of the incision, there is an abrupt transition to

mudstone-dominated lithofacies suggesting truncation in this more poorly exposed part of the outcrop (**Figures 2.8D, 2.8E and 2.14C**).

We hypothesize that this unusual intra-channel LFA is the expression of the earliest deposits of an active submarine channel (*i.e.*, equivalent to the bedforms and associated features observed in modern systems). Therefore, we propose that these deposits could represent the along-strike expression of bedforms such as cyclic steps based on the following: (i) the location at the base of a channel, (ii) onlap of sandstone beds towards the edge of the channel, (iii) mudstone-dominated intervals within the succession and towards the edge of the channel are the result of bypassing turbidity currents, (iv) subsequent bypassing turbidity currents eroded previous deposits towards the axis of the channel, (v) the lithofacies association closely resemble those described by Englert *et al.* (2021) in the Nanaimo Group and Squamish sediment cores, and (vi) the nested, wedge-shape architecture of these deposits. A pattern that has also been recognized in modern and interpreted ancient cyclic steps (Englert *et al.*, 2021). We explain the absence of sedimentary structures diagnostic of supercritical conditions to the fact that these deposits are aligned along their depositional strike, whereas previously described cyclic steps in the stratigraphic record are oriented along their depositional dip, which facilitates their recognition. Finally, such stratigraphically uncommon deposits were preserved in the record due to the abrupt abandonment of this channel and the development of a new adjacent one (the eastern channel), which resulted in the former being filled and covered with fine-grained overbank deposits (**Figure 2.13D**).

2.7 | CONCLUSIONS

We characterized a previously undocumented succession of outcropping submarine slope-channel deposits of the Upper Cretaceous Tres Pasos Formation in the Magallanes-Austral retroarc foreland basin of Southern Chile. The 750 m wide by 300 m thick studied stratigraphic interval is exposed along its depositional strike and dip, and feature key elements of submarine slope-channel systems that have been widely recognized in seismic-reflection datasets and in modern active submarine channel systems, but rarely observed in the stratigraphic record.

The stratigraphic succession is characterized by six lithofacies associations grouped into intra-channel associations, out-of-channel associations, and non-stratified and chaotic associations. The spatial distribution and relationship between these lithofacies associations defines a stratigraphic hierarchy comprising 4 channel complexes (CC) consisting of 9+ channel elements with laterally migrating (CC-II)

and vertically aggrading (CC-I, CC-III, CC-IV) stacking patterns. Our study is focused on the stratigraphic and sedimentological expressions of the transition from laterally stacked/low-aggradational channels of CC-II to vertically stacked aggradational channels of CC-III. The boundary between these channel complexes is defined by a composite erosional surface with two adjacent element-scale channelized incisions with contrasting sedimentary infills. We suggest that at a complex-scale level, in order to aggrade, a significant phase of erosion and bypass is required. At this stage, one or multiple conduits may be active, however, once a conduit is established as the primary pathway for subsequent turbidity currents, flow stripping and overbank deposition within the channel master-conduit will set up the conditions necessary to generate an aggradational stacking pattern through a combination of erosional processes and levee buildup.

In addition, we defined an unusual intra-channel lithofacies association within one of the incisions consisting of a distinctive thinning- and fining-upward succession with mudclast-rich sandstones at its base, which we interpret to represent the stratigraphic expression of the earliest deposits of an active submarine channel. We hypothesize the idea that these deposits could represent the along-strike expression of bedforms found in modern channels such as cyclic steps. Hence, this study provides the unusual opportunity to link seismic-scale architectural patterns and sedimentary processes of active systems to the detailed observations offered by studying the stratigraphic record.

REFERENCES

Armitage, D.A., Romans, B.W., Covault, J.A., Graham, S.A., 2009. The Influence of Mass-Transport-Deposit Surface Topography on the Evolution of Turbidite Architecture: The Sierra Contreras, Tres Pasos Formation (Cretaceous), Southern Chile. J. Sediment. Res. 79, 287–301. https://doi.org/10.2110/jsr.2009.035

Auchter, N.C., Romans, B.W., Hubbard, S.M., 2016. Influence of deposit architecture on intrastratal deformation, slope deposits of the Tres Pasos Formation, Chile. Sediment. Geol. 341, 13–26. https://doi.org/10.1016/j.sedgeo.2016.05.005

Bailey, L.P., Clare, M.A., Rosenberger, K.J., Cartigny, M.J.B., Talling, P.J., Paull, C.K., Gwiazda, R., Parsons, D.R., Simmons, S.M., Xu, J., Haigh, I.D., Maier, K.L., McGann, M., Lundsten, E., 2021. Preconditioning by sediment accumulation can produce powerful turbidity currents without major external triggers. Earth Planet. Sci. Lett. 562, 116845. https://doi.org/10.1016/j.epsl.2021.116845

Bain, H.A., Hubbard, S.M., 2016. Stratigraphic evolution of a long-lived submarine channel system in the Late Cretaceous Nanaimo Group, British Columbia, Canada. Sediment. Geol. 337, 113–132. https://doi.org/10.1016/j.sedgeo.2016.03.010

Bauer, D.B., Hubbard, S.M., Covault, J.A., Romans, B.W., 2020. Inherited depositional topography control on shelf-margin oversteepening, readjustment, and coarse-grained sediment delivery to deep water, Magallanes Basin, Chile. Front. Earth Sci. 7. https://doi.org/10.3389/feart.2019.00358

Beaubouef, R.T., 2004. Deep-water leveed-channel complexes of the Cerro Toro Formation, Upper Cretaceous, southern Chile. Am. Assoc. Pet. Geol. Bull. 88, 1471–1500. https://doi.org/10.1306/06210403130

Bell, D., Hodgson, D.M., Pontén, A.S.M., Hansen, L.A.S., Flint, S.S., Kane, I.A., 2020. Stratigraphic hierarchy and three-dimensional evolution of an exhumed submarine slope channel system. Sedimentology 67, 3259–3289. https://doi.org/10.1111/sed.12746

Bernhardt, A., Jobe, Z.R., Lowe, D.R., 2011. Stratigraphic evolution of a submarine channel–lobe complex system in a narrow fairway within the Magallanes foreland basin, Cerro Toro Formation, southern Chile. Mar. Pet. Geol. 28, 785–806. https://doi.org/10.1016/j.marpetgeo.2010.05.013

Bernhardt, A., Stright, L., Lowe, D.R., 2012. Channelized debris-flow deposits and their impact on turbidity currents: The Puchkirchen axial channel belt in the Austrian Molasse Basin. Sedimentology 59, 2042–2070. https://doi.org/10.1111/j.1365-3091.2012.01334.x

Blum, M., Rogers, K., Gleason, J., Najman, Y., Cruz, J., Fox, L., 2018. Allogenic and autogenic signals in the stratigraphic record of the deep-sea Bengal Fan. Sci. Rep. 8. https://doi.org/10.1038/s41598-018-25819-5

Bouma, A.H., 1962. Sedimentology of some flysch deposits, a graphic approach to facies interpretation. Developments in Sedimentology. Elsevier Pub. Co., Amsterdam,.

Bruhn, R.L., Stern, C.R., De Wit, M.J., 1978. Field and geochemical data bearing on the development of a mesozoic volcano-tectonic rift zone and back-arc basin in southernmost South America. Earth Planet. Sci. Lett. 41, 32–46. https://doi.org/10.1016/0012-821X(78)90039-0

Butler, R.W.H., Tavarnelli, E., 2006. The structure and kinematics of substrate entrainment into high-concentration sandy turbidites: A field example from the Gorgoglione “flysch” of southern Italy. Sedimentology 53, 655–670. https://doi.org/10.1111/j.1365-3091.2006.00789.x

Calderón, M., Fildani, A., Hervé, F., Fanning, C.M., Weislogel, A., Cordani, U., 2007. Late Jurassic bimodal magmatism in the northern sea-floor remnant of the Rocas Verdes basin, southern Patagonian Andes. J. Geol. Soc. London. 164, 1011–1022. https://doi.org/10.1144/0016-76492006-102

Campion, K.M., Sprague, A.R., Mohrig, D., Lovell, R.W., Drzewiecki, P.A., Sullivan, M.D., Ardill, J.A., Jensen, G.N., Sickafoose, D.K., 2000. Outcrop expression of confined channel complexes, in: deep-water reservoirs of the world: 20th Annual. Society Of Economic Paleontologists And Mineralogists, pp. 127–150. https://doi.org/10.5724/gcs.00.15.0127

Casciano, C.I., Patacci, M., Longhitano, S.G., Tropeano, M., McCaffrey, W.D., Di Celma, C., 2019. Multi-scale analysis of a migrating submarine channel system in a tectonically-confined basin: The Miocene Gorgoglione Flysch Formation, southern Italy. Sedimentology 66, 205–240. https://doi.org/10.1111/sed.12490

Castelltort, S., Honegger, L., Adatte, T., Clark, J.D., Puigdefàbregas, C., Spangenberg, J.E., Dykstra, M.L., Fildani, A., 2017. Detecting eustatic and tectonic signals with carbon isotopes in deep-marine strata, Eocene Ainsa Basin, Spanish Pyrenees. Geology 45, 707–710. https://doi.org/10.1130/G39068.1

Cornard, P.H., Pickering, K.T., 2019. Supercritical-flow deposits and their distribution in a submarine channel system, Middle Eocene, Ainsa Basin, Spanish Pyrenees. J. Sediment. Res. 89, 576–597. https://doi.org/10.2110/jsr.2019.34

Covault, J.A., Citation, N.E., Fans, S., Systems, C., 2016. Submarine fans and canyon-channel systems : A review of processes , products , and models A review of processes , products , and models.

Covault, J.A., Fildani, A., Romans, B.W., McHargue, T., 2011. The natural range of submarine canyon-and-channel longitudinal profiles. Geosphere 7, 313–332. https://doi.org/10.1130/GES00610.1

Covault, J.A., Romans, B.W., Graham, S.A., 2009. Outcrop Expression of a Continental-Margin-Scale Shelf-Edge Delta from the Cretaceous Magallanes Basin, Chile. J. Sediment. Res. 79, 523–539. https://doi.org/10.2110/jsr.2009.053

Cullis, S., Colombera, L., Patacci, M., McCaffrey, W.D., 2018. Hierarchical classifications of the sedimentary architecture of deep-marine depositional systems. Earth-Science Rev. 179, 38–71. https://doi.org/10.1016/j.earscirev.2018.01.016

Daniels, B.G., Auchter, N.C., Hubbard, S.M., Romans, B.W., Matthews, W.A., Stright, L., 2018. Timing of deep-water slope evolution constrained by large-n detrital and volcanic ash zircon geochronology, Cretaceous Magallanes Basin, Chile. GSA Bull. 130, 438–454. https://doi.org/10.1130/B31757.1

Daniels, B.G., Hubbard, S.M., Romans, B.W., Malkowski, M.A., Matthews, W.A., Bernhardt, A., Kaempfe-Droguett, S., Jobe, Z.R., Fosdick, J.C., Schwartz, T.M., Fildani, A., Graham, S.A., 2019. Revised chronostratigraphic framework for the Cretaceous Magallanes-Austral Basin, Última Esperanza Province, Chile. J. South Am. Earth Sci. 94. https://doi.org/10.1016/j.jsames.2019.05.025

de Leeuw, J., Eggenhuisen, J.T., Cartigny, M.J.B., 2018. Linking submarine channel–levee facies and architecture to flow structure of turbidity currents: insights from flume tank experiments. Sedimentology 65, 931–951. https://doi.org/10.1111/sed.12411

Deptuck, M.E., Steffens, G.S., Barton, M., Pirmez, C., 2003. Architecture and evolution of upper fan channel-belts on the Niger Delta slope and in the Arabian Sea. Mar. Pet. Geol. 20, 649–676. https://doi.org/10.1016/j.marpetgeo.2003.01.004

Deptuck, M.E., Sylvester, Z., Pirmez, C., O'Byrne, C., 2007. Migration-aggradation history and 3-D seismic geomorphology of submarine channels in the Pleistocene Benin-major Canyon, western Niger Delta slope. Mar. Pet. Geol. 24, 406–433. https://doi.org/10.1016/j.marpetgeo.2007.01.005

Di Celma, C.N., Brunt, R.L., Hodgson, D.M., Flint, S.S., Kavanagh, J.P., 2011. Spatial and temporal evolution of a permian submarine slope channel-levee system, Karoo Basin, South Africa. J. Sediment. Res. 81, 579–599. https://doi.org/10.2110/jsr.2011.49

Englert, R.G., Hubbard, S.M., Cartigny, M.J.B., Clare, M.A., Coutts, D.S., Hage, S., Hughes Clarke, J., Jobe, Z., Lintern, D.G., Stacey, C., Vendettuoli, D., 2021. Quantifying the three-dimensional stratigraphic expression of cyclic steps by integrating seafloor and deep-water outcrop observations. Sedimentology 68, 1465–1501. https://doi.org/10.1111/sed.12772

Englert, R.G., Hubbard, S.M., Matthews, W.A., Coutts, D.S., Covault, J.A., 2020. The evolution of submarine slope-channel systems: Timing of incision, bypass, and aggradation in late cretaceous nanaimo group channel-system strata, British Columbia, Canada. Geosphere 16, 281–296. https://doi.org/10.1130/GES02091.1

Fildani, A., Cope, T.D., Graham, S.A., Wooden, J.L., 2003. Initiation of the Magallanes foreland basin: Timing of the southernmost Patagonian Andes orogeny revised by detrital zircon provenance analysis. Geology 31, 1081–1084. https://doi.org/10.1130/G20016.1

Fildani, A., Hessler, A.M., 2005. Stratigraphic record across a retroarc basin inversion: Rocas Verdes-Magallanes Basin, Patagonian Andes, Chile. Bull. Geol. Soc. Am. 117, 1596–1614. https://doi.org/10.1130/B25708.1

Fildani, A., Hubbard, S.M., Covault, J.A., Maier, K.L., Romans, B.W., Traer, M., Rowland, J.C., 2013. Erosion at inception of deep-sea channels. Mar. Pet. Geol. 41, 48–61. https://doi.org/10.1016/j.marpetgeo.2012.03.006

Fildani, A., McKay, M.P., Stockli, D., Clark, J., Dykstra, M.L., Stockli, L., Hessler, A.M., 2016. The ancestral Mississippi drainage archived in the late Wisconsin Mississippi deep-sea fan. Geology 44, 479–482. https://doi.org/10.1130/G37657.1

Fogwill, C.J., Kubik, P.W., 2005. A glacial stage spanning the Antarctic Cold Reversal in Torres del Paine (51°S), Chile, based on preliminary cosmogenic exposure ages. Geogr. Ann. Ser. A Phys. Geogr. 87, 403–408. https://doi.org/10.1111/j.0435-3676.2005.00266.x

Fosdick, J.C., Romans, B.W., Fildani, A., Bernhardt, A., Calderón, M., Graham, S.A., 2011. Kinematic evolution of the Patagonian retroarc fold-and-thrust belt and Magallanes foreland basin, Chile and Argentina, 51°30's. Bull. Geol. Soc. Am. 123, 1679–1698. https://doi.org/10.1130/B30242.1

Gamberi, F., Rovere, M., Dykstra, M., Kane, I.A., Kneller, B.C., 2013. Integrating modern seafloor and outcrop data in the analysis of slope channel architecture and fill. Mar. Pet. Geol. 41, 83–103. https://doi.org/10.1016/j.marpetgeo.2012.04.002

García, J.L., Hall, B.L., Kaplan, M.R., Vega, R.M., Strelin, J.A., 2014. Glacial geomorphology of the Torres del Paine region (southern Patagonia): Implications for glaciation, deglaciation and paleolake history. Geomorphology 204, 599–616. https://doi.org/10.1016/j.geomorph.2013.08.036

García, J.L., Hein, A.S., Binnie, S.A., Gómez, G.A., González, M.A., Dunai, T.J., 2018. The MIS 3 maximum of the Torres del Paine and Última Esperanza ice lobes in Patagonia and the pacing of southern mountain glaciation. Quat. Sci. Rev. 185, 9–26. https://doi.org/10.1016/j.quascirev.2018.01.013

García, J.L., Strelin, J.A., Vega, R.M., Hall, B.L., Stern, C.R., 2015. Deglacial ice-marginal glaciolacustrine environments and structural moraine building in torres del paine, chilean southern patagonia. Andean Geol. 42, 190–212. https://doi.org/10.5027/andgeoV42n2-a03

George, S.W.M., Davis, S.N., Fernández, R.A., Manríquez, L.M.E., Leppe, M.A., Horton, B.K., Clarke, J.A., 2020. Chronology of deposition and unconformity development across the Cretaceous–Paleogene boundary, Magallanes-Austral Basin, Patagonian Andes. J. South Am. Earth Sci. 97, 102237. https://doi.org/10.1016/j.jsames.2019.102237

Georgiopoulou, A., Wynn, R.B., Masson, D.G., Frenz, M., 2009. Linked turbidite-debrite resulting from recent Sahara Slide headwall reactivation. Mar. Pet. Geol. 26, 2021–2031. https://doi.org/10.1016/j.marpetgeo.2009.02.013

Hage, S., Cartigny, M.J.B., Clare, M.A., Sumner, E.J., Vendettuoli, D., Clarke, J.E.H., Hubbard, S.M., Talling, P.J., Gwyn Lintern, D., Stacey, C.D., Englert, R.G., Vardy, M.E., Hunt, J.E., Yokokawa, M., Parsons, D.R., Hizzett, J.L., Azpiroz-Zabala, M., Vellinga, A.J., 2018. How to recognize crescentic bedforms formed by supercritical turbidity currents in the geologic record: Insights from active submarine channels. Geology 46, 563–566. https://doi.org/10.1130/G40095.1

Hansen, L., Callow, R., Kane, I., Kneller, B., 2017a. Differentiating submarine channel-related thin-bedded turbidite facies: Outcrop examples from the Rosario Formation, Mexico. Sediment. Geol. 358, 19–34. https://doi.org/10.1016/j.sedgeo.2017.06.009

Hansen, L., Janocko, M., Kane, I., Kneller, B., 2017b. Submarine channel evolution, terrace development, and preservation of intra-channel thin-bedded turbidites: Mahin and Avon channels, offshore Nigeria. Mar. Geol. 383, 146–167. https://doi.org/10.1016/j.margeo.2016.11.011

Hansen, L.A.S., Callow, R.H.T., Kane, I.A., Gamberi, F., Rovere, M., Cronin, B.T., Kneller, B.C., 2015. Genesis and character of thin-bedded turbidites associated with submarine channels. Mar. Pet. Geol. 67, 852–879. https://doi.org/10.1016/j.marpetgeo.2015.06.007

Heijnen, M.S., Clare, M.A., Cartigny, M.J.B., Talling, P.J., Hage, S., Lintern, D.G., Stacey, C., Parsons, D.R., Simmons, S.M., Chen, Y., Sumner, E.J., Dix, J.K., Hughes Clarke, J.E., 2020. Rapidly-migrating and internally-generated knickpoints can control submarine channel evolution. Nat. Commun. 11, 1–15. https://doi.org/10.1038/s41467-020-16861-x

Hodgson, D.M., Di Celma, C.N., Brunt, R.L., Flint, S.S., 2011. Submarine slope degradation and aggradation and the stratigraphic evolution of channel-levee systems. J. Geol. Soc. London. 168, 625–628. https://doi.org/10.1144/0016-76492010-177

Hubbard, S.M., Covault, J.A., Fildani, A., Romans, B.W., 2014. Sediment transfer and deposition in slope channels: Deciphering the record of enigmatic deep-sea processes from outcrop. Bull. Geol. Soc. Am. 126, 857–871. https://doi.org/10.1130/B30996.1

Hubbard, S.M., de Ruig, M.J., Graham, S.A., 2009. Confined channel-levee complex development in an elongate depo-center: Deep-water Tertiary strata of the Austrian Molasse basin. Mar. Pet. Geol. 26, 85–112. https://doi.org/10.1016/j.marpetgeo.2007.11.006

Hubbard, S.M., Fildani, A., Romans, B.W., Covault, J.A., McHargue, T.R., 2010. High-relief slope clinoform development: Insights from outcrop, magallanes Basin, Chile. J. Sediment. Res. 80, 357–375. https://doi.org/10.2110/jsr.2010.042

Hubbard, S.M., Jobe, Z.R., Romans, B.W., Covault, J.A., Sylvester, Z., Fildani, A., 2020. The stratigraphic evolution of a submarine channel: Linking seafloor dynamics to depositional products. J. Sediment. Res. 90, 673–686. https://doi.org/10.2110/jsr.2020.36

Hughes Clarke, J.E., 2016. First wide-angle view of channelized turbidity currents links migrating cyclic steps to flow characteristics. Nat. Commun. 7, 1–13. https://doi.org/10.1038/ncomms11896

Janocko, M., Nemec, W., Henriksen, S., Warchoł, M., 2013. The diversity of deep-water sinuous channel belts and slope valley-fill complexes. Mar. Pet. Geol. 41, 7–34. https://doi.org/10.1016/j.marpetgeo.2012.06.012

Kane, I.A., Hodgson, D.M., 2011. Sedimentological criteria to differentiate submarine channel levee subenvironments: Exhumed examples from the Rosario Fm. (Upper Cretaceous) of Baja California, Mexico, and the Fort Brown Fm. (Permian), Karoo Basin, S. Africa. Mar. Pet. Geol. 28, 807–823. https://doi.org/10.1016/j.marpetgeo.2010.05.009

Kane, I.A., Kneller, B.C., Dykstra, M., Kassem, A., McCaffrey, W.D., 2007. Anatomy of a submarine channel-levee: An example from Upper Cretaceous slope sediments, Rosario Formation, Baja California, Mexico. Mar. Pet. Geol. 24, 540–563. https://doi.org/10.1016/j.marpetgeo.2007.01.003

Katz, H., 1963. Revision of Cretaceous Stratigraphy in Patagonian Cordillera of Ultima Esperanza, Magallanes Province, Chile. Am. Assoc. Pet. Geol. Bull. 47. https://doi.org/10.1306/bc743a5d-16be-11d7-8645000102c1865d

Khripounoff, A., Vangriesheim, A., Babonneau, N., Crassous, P., Dennielou, B., Savoye, B., 2003. Direct observation of intense turbidity current activity in the Zaire submarine valley at 4000 m water depth. Mar. Geol. 194, 151–158. https://doi.org/10.1016/S0025-3227(02)00677-1

Labourdette, R., 2007. Integrated three-dimensional modeling approach of stacked turbidite channels. Am. Assoc. Pet. Geol. Bull. 91, 1603–1618. https://doi.org/10.1306/06210706143

Li, P., Kneller, B., Thompson, P., Bozetti, G., dos Santos, T., 2018. Architectural and facies organisation of slope channel fills: Upper Cretaceous Rosario Formation, Baja California, Mexico. Mar. Pet. Geol. 92, 632–649. https://doi.org/10.1016/j.marpetgeo.2017.11.026

Lowe, D.R., 1982. Sediment gravity flows: II. Depositional models with special reference to the deposits of high-density turbidity currents. J. Sediment. Petrol. 52, 279–297. https://doi.org/10.1306/212f7f31-2b24-11d7-8648000102c1865d

Macauley, R. V., Hubbard, S.M., 2013. Slope channel sedimentary processes and stratigraphic stacking, Cretaceous Tres Pasos Formation slope system, Chilean Patagonia. Mar. Pet. Geol. 41, 146–162. https://doi.org/10.1016/j.marpetgeo.2012.02.004

Macellari, C.E., Barrio, C.A., Manassero, M.J., 1989. Upper cretaceous to paleocene depositional sequences and sandstone petrography of southwestern Patagonia (Argentina and Chile). J. South Am. Earth Sci. 2, 223–239. https://doi.org/10.1016/0895-9811(89)90031-X

Maier, K.L., Gales, J.A., Paull, C.K., Rosenberger, K., Talling, P.J., Simmons, S.M., Gwiazda, R., McGann, M., Cartigny, M.J.B., Lundsten, E., Anderson, K., Clare, M.A., Xu, J., Parsons, D., Barry, J.P., Wolfson-Schwehr, M., Nieminski, N.M., Sumner, E.J., 2019. Linking direct measurements of turbidity currents to submarine canyon-floor deposits. Front. Earth Sci. 7, 1–18. https://doi.org/10.3389/feart.2019.00144

Malkowski, M.A., Jobe, Z.R., Sharman, G.R., Graham, S.A., 2018. Down-slope facies variability within deep-water channel systems: Insights from the Upper Cretaceous Cerro Toro Formation, southern Patagonia. Sedimentology 65, 1918–1946. https://doi.org/10.1111/sed.12452

Mayall, M., Jones, E., Casey, M., 2006. Turbidite channel reservoirs-Key elements in facies prediction and effective development. Mar. Pet. Geol. 23, 821–841. https://doi.org/10.1016/j.marpetgeo.2006.08.001

McHargue, T., Pyrcz, M.J., Sullivan, M.D., Clark, J.D., Fildani, A., Romans, B.W., Covault, J.A., Levy, M., Posamentier, H.W., Drinkwater, N.J., 2011. Architecture of turbidite channel systems on the continental slope: Patterns and predictions. Mar. Pet. Geol. 28, 728–743. https://doi.org/10.1016/j.marpetgeo.2010.07.008

Mutti, E., 1977. Distinctive thin-bedded turbidite facies and related depositional environments in the Eocene Hecho Group (South-central Pyrenees, Spain). Sedimentology 24, 107–131. https://doi.org/10.1111/j.1365-3091.1977.tb00122.x

Mutti, E., Normark, W.R., 1987. Comparing Examples of Modern and Ancient Turbidite Systems: Problems and Concepts. Mar. Clastic Sedimentol. 1–38. https://doi.org/10.1007/978-94-009-3241-8_1

Natland, M.L., Eduardo, G.P., Cañon, A., 1974. Introduction. Mem. Geol. Soc. Am. 139, 1–117. https://doi.org/10.1130/MEM139-p1

Nesbit, P., Hubbard, S., Daniels, B., Bell, D., Englert, R., Hugenholtz, C., 2021. Digital re-evaluation of down-dip channel-fill architecture in deep-water slope deposits: Multi-scale perspectives from UAV-SfM. The Depositional Record 7: 480-499. https://doi.org/10.1002/dep2.137

Normark, W.R., Posamentier, H., Mutti, E., 1993. Turbidite systems: State of the art and future directions. Rev. Geophys. 31, 91–116. https://doi.org/10.1029/93RG02832

Pankhurst, R.J., Riley, T.R., Fanning, C.M., Kelley, S.P., 2000. Episodic silicic volcanism in Patagonia and the Antarctic Peninsula: Chronology of magmatism associated with the break-up of Gondwana. J. Petrol. 41, 605–625. https://doi.org/10.1093/petrology/41.5.605

Paull, C.K., Talling, P.J., Maier, K.L., Parsons, D., Xu, J., Caress, D.W., Gwiazda, R., Lundsten, E.M., Anderson, K., Barry, J.P., Chaffey, M., O'Reilly, T., Rosenberger, K.J., Gales, J.A., Kieft, B., McGann, M., Simmons, S.M., McCann, M., Sumner, E.J., Clare, M.A., Cartigny, M.J., 2018. Powerful turbidity currents driven by dense basal layers. Nat. Commun. 9, 1–9. https://doi.org/10.1038/s41467-018-06254-6

Pemberton, E.A.L., Hubbard, S.M., Fildani, A., Romans, B., Stright, L., 2016. The stratigraphic expression of decreasing confinement along a deep-water sediment routing system: Outcrop example from southern Chile. Geosphere 12, 114–134. https://doi.org/10.1130/GES01233.1

Pickering, K.T. (Kevin T.., Hiscott, R.N., 2015. Deep-marine systems : processes, deposits, environments, tectonics and sedimentation. John Wiley and Sons Inc., Chichester, West Sussex ;

Pirmez, C., Imran, J., 2003. Reconstruction of turbidity currents in Amazon Channel. Mar. Pet. Geol. 20, 823–849. https://doi.org/10.1016/j.marpetgeo.2003.03.005

Posamentier, H.W., Kolla, V., 2003. Seismic geomorphology and stratigraphy of depositional elements in deep-water settings. J. Sediment. Res. 73, 367–388. https://doi.org/10.1306/111302730367

Qin, Y., Alves, T.M., Constantine, J., Gamboa, D., 2016. Quantitative seismic geomorphology of a submarine channel system in SE Brazil (Espírito Santo Basin): Scale comparison with other submarine channel systems. Mar. Pet. Geol. 78, 455–473. https://doi.org/10.1016/j.marpetgeo.2016.09.024

Romans, B.W., Castelltort, S., Covault, J.A., Fildani, A., Walsh, J.P., 2016. Environmental signal propagation in sedimentary systems across timescales. Earth-Science Rev. 153, 7–29. https://doi.org/10.1016/j.earscirev.2015.07.012

Romans, B.W., Fildani, A., Graham, S.A., Hubbard, S.M., Covault, J.A., 2010. Importance of predecessor basin history on sedimentary fill of a retroarc foreland basin: provenance analysis of the Cretaceous Magallanes basin, Chile (50-52°S). Basin Res. 22, 640–658. https://doi.org/10.1111/j.1365-2117.2009.00443.x

Romans, B.W., Fildani, A., Hubbard, S.M., Covault, J.A., Fosdick, J.C., Graham, S.A., 2011. Evolution of deep-water stratigraphic architecture, Magallanes Basin, Chile. Mar. Pet. Geol. 28, 612–628. https://doi.org/10.1016/j.marpetgeo.2010.05.002

Romans, B.W., Hubbard, S.M., Graham, S.A., 2009. Stratigraphic evolution of an outcropping continental slope system, Tres Pasos Formation at Cerro Divisadero, Chile. Sedimentology 56, 737–764. https://doi.org/10.1111/j.1365-3091.2008.00995.x

Sansom, P., 2018. Hybrid turbidite-contourite systems of the Tanzanian margin. Pet. Geosci. 24, 258–276. https://doi.org/10.1144/petgeo2018-044

Schwartz, T.M., Fosdick, J.C., Graham, S.A., 2017. Using detrital zircon U-Pb ages to calculate Late Cretaceous sedimentation rates in the Magallanes-Austral basin, Patagonia. Basin Res. 29, 725–746. https://doi.org/10.1111/bre.12198

Schwarz, E., Arnott, R.W.C., 2007. Anatomy and evolution of a slope channel-complex set (Neoproterozoic Isaac Formation, Windermere Supergroup, southern Canadian cordillera): Implications for reservoir characterization. J. Sediment. Res. 77, 89–109. https://doi.org/10.2110/jsr.2007.015

Shultz, M.R., Fildani, A., Cope, T.D., Graham, S.A., 2005. Deposition and stratigraphic architecture of an outcropping ancient slope system: Tres Pasos Formation, Magallanes Basin, southern Chile. Geol. Soc. London, Spec. Publ. 244, 27–50. https://doi.org/10.1144/GSL.SP.2005.244.01.03

Shultz, M.R., Hubbard, S.M., 2005. Sedimentology, stratigraphic architecture, and ichnology of gravity-flow deposits partially ponded in a growth-fault-controlled slope minibasin, Tres Pasos Formation (Cretaceous), southern Chile. J. Sediment. Res. 75, 440–453. https://doi.org/10.2110/jsr.2005.034

Sprague, A., Garfield, T., 2005. Integrated slope channel depositional models: the key to successful prediction of reservoir presence and quality in offshore West Africa. CIPM, cuarto E- … 17, 1–13.

Sprague, A.R., Patterson, P.E., 2002. The Physical Stratigraphy of Fluvial Strata: A Hierarchical Approach to the Analysis of Genetically Related Stratigraphic Elements for Improved Reservoir Prediction. Am. Assoc. Pet. Geol. Bull. 86. https://doi.org/10.1306/3fef4cc1-1741-11d7-8645000102c1865d

Smith, C., 1977. Sedimentology of the Late Cretaceous (Santonian–Maastrichtian) Tres Pasos Formation, Ultima Esperanza District, southern Chile. M.Sc Thesis, University of Wisconsin, Madison, WI, 129 p.

Stacey, C.D., Hill, P.R., Talling, P.J., Enkin, R.J., Hughes Clarke, J., Lintern, D.G., 2019. How turbidity current frequency and character varies down a fjord-delta system: Combining direct monitoring, deposits and seismic data. Sedimentology 66, 1–31. https://doi.org/10.1111/sed.12488

Stevenson, C.J., Jackson, C.A.L., Hodgson, D.M., Hubbard, S.M., Eggenhuisen, J.T., 2015. Deep-Water Sediment Bypass. J. Sediment. Res. 85, 1058–1081. https://doi.org/10.2110/jsr.2015.63

Straub, K.M., Mohrig, D., McElroy, B., Buttles, J., Pirmez, C., 2008. Interactions between turbidity currents and topography in aggrading sinuous submarine channels: A laboratory study. Bull. Geol. Soc. Am. 120, 368–385. https://doi.org/10.1130/B25983.1

Sylvester, Z., Pirmez, C., Cantelli, A., 2011. A model of submarine channel-levee evolution based on channel trajectories: Implications for stratigraphic architecture. Mar. Pet. Geol. 28, 716–727. https://doi.org/10.1016/j.marpetgeo.2010.05.012

Talling, P.J., Masson, D.G., Sumner, E.J., Malgesini, G., 2012. Subaqueous sediment density flows: Depositional processes and deposit types. Sedimentology 59, 1937–2003. https://doi.org/10.1111/j.1365-3091.2012.01353.x

Thomas, M.F.H., Bodin, S., 2013. Architecture and evolution of the Finale channel system, the Numidian Flysch Formation of Sicily; insights from a hierarchical approach. Mar. Pet. Geol. 41, 163–185. https://doi.org/10.1016/j.marpetgeo.2012.02.002

Vangriesheim, A., Khripounoff, A., Crassous, P., 2009. Turbidity events observed in situ along the Congo submarine channel. Deep. Res. Part II Top. Stud. Oceanogr. 56, 2208–2222. https://doi.org/10.1016/j.dsr2.2009.04.004

Vendettuoli, D., Clare, M.A., Hughes Clarke, J.E., Vellinga, A., Hizzet, J., Hage, S., Cartigny, M.J.B., Talling, P.J., Waltham, D., Hubbard, S.M., Stacey, C., Lintern, D.G., 2019. Daily bathymetric surveys document how stratigraphy is built and its extreme incompleteness in submarine channels. Earth Planet. Sci. Lett. 515, 231–247. https://doi.org/10.1016/j.epsl.2019.03.033

Winn, R.D., Dott, R.H., 1979. Deep-water fan-channel conglomerates of Late Cretaceous age, southern Chile. Sedimentology 26, 203–228. https://doi.org/10.1111/j.1365-3091.1979.tb00351.x

3 | STRATIGRAPHY AND SYN-DEPOSITIONAL FAULTING OF AN OVERBANK SUCCESSION IN A LARGE SUBMARINE CHANNEL-LEVEE SYSTEM, UPPER CRETACEOUS CERRO TORO FORMATION AT EL CHINGUE BLUFF, SOUTHERN CHILE

Sebastian A. Kaempfe[1], Brian W. Romans[1], Stephen M. Hubbard[2], Rebecca G. Englert[2], Benjamin G. Daniels[3] and Lisa Stright[4]

[1] Department of Geosciences, Virginia Tech, 926 West Campus Drive, Blacksburg, VA, 24061, USA

[2] Department of Geoscience, University of Calgary, 2500 University Drive NW, Calgary, AB, T2N1N4, Canada

[3] Department of Earth and Environmental Sciences, Mount Royal University, 4825 Mount Royal Gate SW, Calgary, AB, T3E 6K6, Canada.

[4] Department of Geosciences, Colorado State University, 1482 Campus Delivery, Fort Collins, Colorado 80523-1482, USA.

ABSTRACT

The construction of large overbank deposits is an inherent process of many submarine channel systems. It allows channels to extend significant distances while recording the transport of sediment into the deep-marine environment, resulting in some of the largest sediment accumulations on Earth. Thus, the sedimentology and stratigraphy of overbank successions hold clues to how submarine channel systems evolve over time. However, the challenges associated with the study of these systems in the deep-marine environment resulted in the study of outcropping analogs to characterize the details of their stratigraphic framework. Outcrops show that the bulk of these successions are thin-bedded, siltstone-dominated turbidites with a lower proportion of mass wasting deposits and rare thick-bedded sandstones, commonly interpreted as splay deposits. Minor differences in depositional architecture, paleoflow variations, and sandstone content have been used to differentiate subenvironments within these depositional features. However, the influence of deformational structures that can develop on levee slopes during deposition and how these structures influence the evolution of these systems has been largely overlooked.

In this study, we use high-resolution measurements (cm scale) to characterize an extensive fine-grained dominated sedimentary succession (~500 m thick and 2 km across) and the structures that affect it in the Upper Cretaceous Cerro Toro Formation exposed at El Chingue Bluff in the Magallanes-Austral foreland basin of southern Chile. Detailed qualitative and quantitative analysis revealed the presence of five sandstone-prone intervals defined by an increased sandstone content in comparison to underlying and overlying strata. The entire succession is cut by large synsedimentary normal faults that systematically change their orientation and dip-direction from north to south and crosscut by a broad network of injectites

not affected by faulting, thus post-dating the timing of normal faulting. Based on previous geologic mapping, geochronologic constraints, depositional architecture, and paleoflow relationships we interpret this entire succession to record deposition within an external levee associated with the axial channel-belt of the Cerro Toro Formation. Furthermore, our results suggest that large levee slopes associated with submarine channel systems might share characteristics with other depositional slopes, where synsedimentary structures control paleoflow direction and influence over the depositional architecture of coarser sediment. Finally, our interpretation indicates that the uppermost interval of this succession directly underlying extensive debris flow deposits and previously linked to a prograding slope by Shultz and Hubbard (2005), is in fact part of the Cerro Toro Axial channel-belt external levee.

Keywords: overbank stratigraphy, growth faults, levee deposits, Cerro Toro Formation

3.1 | INTRODUCTION

Submarine channel-levee systems are composite geomorphologic features comprised of an elongate concave sedimentary pathway flanked by parallel depositional highs, commonly on both sides (Mutti and Normark, 1987; Clark and Pieckering, 1996). They are present in a wide variety of deep-marine environments and represent one of the most important features of sediment transfer on Earth (McArthur *et al.*, 2020; Normark *et al.*, 1993; Normark and Carlson, 2003). Whereas deposition within channels is commonly subjected to erosion until the later stages of its evolution (Bain and Hubbard, 2016; Deptuck *et al.*, 2003; Englert *et al.*, 2020; Li *et al.*, 2018; Macauley and Hubbard, 2013; McHargue *et al.*, 2011; Stevenson *et al.*, 2015), overbank sedimentation can occur during the entire lifespan of the channel system due to different mechanisms of overspill (Hansen *et al.*, 2017, 2015; Kane *et al.*, 2007; Kane and Hodgson, 2011; McArthur *et al.*, 2020). The result is a stratigraphic succession seldomly affected by erosion, and therefore, a relatively uninterrupted record of the sedimentation history that can be used to reconstruct tectonic and/or climatic processes (Kohl *et al.*, n.d.; Lin *et al.*, 2014). For example, levees of the Bengal submarine fan were targets of recent scientific ocean drilling because of their presumed high-quality record of onshore tectonics and climatic fluctuations (Blum *et al.*, 2018; France-Lanord *et al.*, 2016). Nevertheless, the role of processes inherent to levee construction that might impact interpretations of external forcings remain poorly understood.

Channel-levee successions have been recognized in deep-marine environments since the early studies of Normark (1978; 1970) and Walker (1975). Subsequent studies based on seismic reflection and

bathymetric data identified, the now widely assumed, 'gull wing' geometry that characterize the depositional architecture of these systems and provided insight into their stratigraphic evolution (Popescu *et al.*, 2001; Babonneau *et al.*, 2002; Deptuck *et al.*, 2003). However, historically, the characterization of these systems has largely been focused on the processes and products within the channel (*i.e.*, sedimentary pathway), in part due to the lower sandstone content that limits its value as hydrocarbon reservoirs in comparison to channel-fill deposits (Posamentier, 2003; Shew *et al.*, 1995; Slatt *et al.*, 1998), resulting in a comparatively lower number of studies focused on the fine-grained levee deposits.

In outcropping successions, fine-grained deposits (as the ones that characterize levee successions) tend to be covered or eroded away more easily than coarse-grained channel-fill deposits and to exhibit a lower preservation potential against tectonism and/or plastic deformation (Macauley and Hubbard, 2013). Such limitations regarding outcrop preservation and quality are particularly important in the case of overbank successions associated with large channel-levee systems (*e.g.*, levees that extend for 10s of km away from the associated channel). Recent studies on outcropping successions like the ones in the Neoproterozoic Windermere Supergroup in Canada (Meyer and Ross, 2007; Khan and Arnott, 2011), the Upper Cretaceous Rosario Formation in Mexico (Kane *et al.*, 2007, 2010; Hansen *et al.*, 2015, 2017), and the Permian Laingsburg and Fort Brown Formation in South Africa (Di Celma *et al.*, 2011; Kane and Hodgson, 2011; Brunt *et al.*, 2012), among others, have provided the stratigraphic and sedimentologic framework upon which these systems are characterized. However, the influence of deformational structures that can develop on levee slopes (*e.g.*, normal faults) on the sedimentary succession and depositional evolution has been largely overlooked.

In this study we examine a ~2 km long by 500 m thick superbly exposed stratigraphic succession composed of thin-bedded turbidites of the Upper Cretaceous Cerro Toro Formation in the Magallanes-Austral Basin of Southern Chile in an understudied outcrop. The scale of this outcrop allows us to integrate high-resolution sedimentologic parameters into a spatial scale comparable to seismic-reflection data and levees found associated with submarine channels on continental margins. Objectives of this study are to: (i) Characterize sedimentary parameters of a mostly thin-bedded turbiditic succession coeval to axial channel-belt deposits of the Cerro Toro Formation at a location where erosion by sediment gravity flows is interpreted to be minimal; (ii) Integrate stratigraphic and sedimentologic features and trends into an outcrop with dimensions comparable to seismic-reflection data; and (iii) Resolve the relationship between sedimentary packages and structural features that are commonly overlooked or beyond the resolution of

datasets derived from other sources. Finally, the relationship between sediments and extensional features in the context of levee-slope dynamics and foreland basin evolution is discussed.

3.2 | GEOLOGIC SETTING

3.2.1 | The Magallanes-Austral retroarc foreland basin

The Magallanes-Austral Basin (MAB) is a retroarc foreland basin located east of the Andean magmatic arc and fold-thrust belt in southern Patagonia. Unlike most retroarc foreland basins, which are dominated by shallow-marine and nonmarine strata, the MAB accumulated more than ~4,000 m of deep-marine strata during a period of ~20-25 Myr of its depositional evolution. This long-lived deep-marine foredeep was the result of a predecessor extensional phase associated with the break-up of Gondwana during mid-late Jurassic and Early Cretaceous that culminated in the opening and closure of the Rocas Verdes back-arc basin (RVB) and the subsequent inception of the MAB during the Late Cretaceous (Dalziel, 1981; Biddle *et al.*, 1986; Wilson, 1991; Pankhurst *et al.*, 2000; Stern and De Witt, 2003; Fildani and Hessler, 2005).

Closure of the RVB and following transition to a compressional foreland basin has been attributed to an increase in the spreading rate of the proto–Atlantic Ocean and subduction initiation along the Pacific margin, resulting in the inception of the Andean orogeny and the development of the Magallanes fold-thrust belt during the Turonian (Wilson, 1991; Ramos, 1994; Fildani *et al.*, 2003; Romans *et al.*, 2010; Calderón *et al.*, 2012; Fosdick *et al.*, 2014). Continuing crustal loading and shortening coupled with the inherited attenuated lithosphere derived from the extensional phase led to enhanced subsidence parallel to the orogen and the development of a narrow N-S elongated retroarc foredeep that subsided to bathyal water depths (Natland *et al.*, 1974; Hubbard *et al.*, 2010; Fosdick *et al.*, 2011; Romans *et al.*, 2011). The onset of deep-water sedimentation in the MAB is defined by laterally extensive tabular sandstone-rich turbidites of the Punta Barrosa Formation (~100-90 Ma; <1000 m), deposited in unconfined to weakly confined submarine fan systems (Daniels *et al.*, 2019; Fildani *et al.*, 2006; Romans *et al.*, 2011). As convergence and subsidence reached its peak, sandstone-rich turbidites were transitionally replaced by fine-grained deposits with conglomeratic-rich intervals of the Cerro Toro Formation (~90-80 Ma; ~2000 m), interpreted to be deposited in an axial channel-belt system at depths between a 1,000 and 2,000 m (Katz, 1963; Scott, 1966; Natland *et al.*, 1974; Winn and Dott, 1979; Hubbard *et al.*, 2008; Romans *et al.*, 2011; Bernhardt *et al.*, 2012; Malkowski *et al.*, 2018). As basin subsidence diminished, accommodation

generation was eventually outpaced by sediment deposition, beginning the filling stage of the MAB, recorded by the Tres Pasos (~81-72 Ma; 1200 – 1500 m) and Dorotea Formations (~73-65 Ma; ~1250 m thick) (Katz, 1963; Natland *et al.*, 1974; Smith, 1977; Romans *et al.*, 2010, 2011; Hubbard *et al.*, 2010; Daniels *et al.*, 2017, 2019) (**Figures 3.1 and 3.2)**.

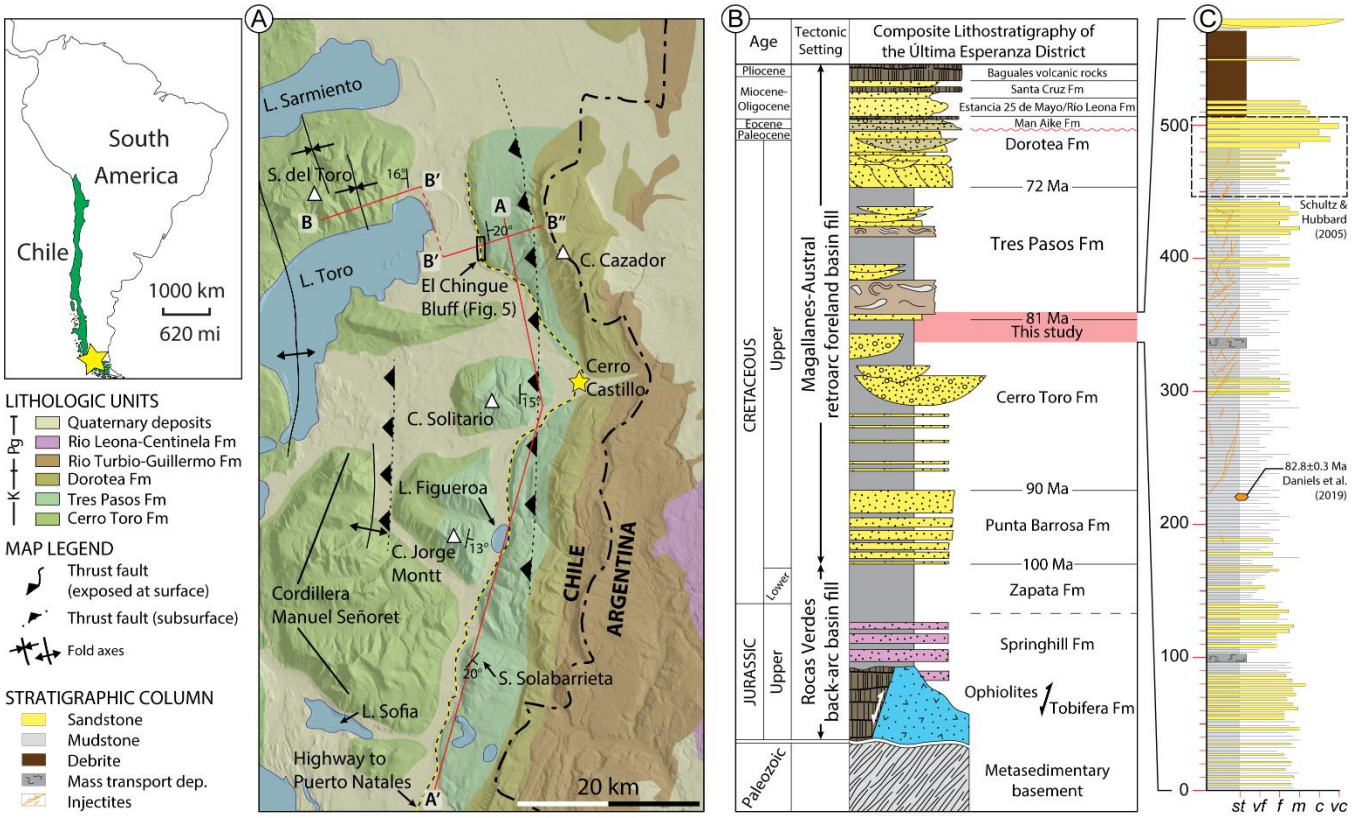

Figure 3.1: Geologic and stratigraphic context. **(A)** Geologic map with the location of the studied area (modified from Fosdick *et al.*, 2011). **(B)** Generalized lithostratigraphic section of the Magallanes Basin in the Última Esperanza Province (modified from Wilson, 1991; Fildani and Hessler, 2005; Fosdick *et al.*, 2011; Schwartz *et al.*, 2017; and George *et al.*, 2020) (age constraints from Daniels *et al.*, 2019). **(C)** Simplified composite stratigraphic section at El Chingue Bluff focused on in this study. Horizontal axis refers to observed grain size (st = siltstone; vf = very fine sandstone; f = fine sandstones; m = medium sandstone; c = coarse sandstone; vc = very coarse sandstone).

3.2.2 | Stratigraphic overview of the Cerro Toro and Tres Pasos formations

In the Última Esperanza Province, the Cerro Toro Formation comprises a >2,000 m thick succession of rhythmic alternation of mudstone and very fine-grained, thin-bedded sandstone that includes 100s of meters of thick conglomeratic-rich intervals in its upper section (Cecioni, 1957; Katz, 1963; Scott, 1966;

Winn and Dott, 1979). The well documented conglomeratic strata, mapped for more than 100 km along a north-south belt from Laguna Tres de Abril (Argentina), Laguna Azul, Sierra del Toro and Cordillera Manuel Señoret to the south, have been attributed to a 400 to 1,000 m thick, 4 to 8 km wide, low-sinuosity, axial channel-belt fed from the north and composed of at least three channel complexes in Sierra del Toro that occupied the foredeep of the Late Cretaceous MAB (Barton *et al.*, 2007; Hubbard *et al.*, 2008; Jobe *et al.*, 2010; Romans *et al.*, 2011; Malkowski *et al.*, 2018). Westward exposures of conglomeratic facies at La Silla Syncline in the Torres del Paine National Park and Cerro Ballena have been interpreted to represent tributary channel complexes systems in part coeval to the main channel-belt (Coleman, 2000; Sohn *et al.*, 2002; Crane and Lowe, 2008; Campion *et al.*, 2011; Bernhardt *et al.*, 2011, 2012), whereas the relation to southern outcrops with equivalent lithofacies at Monte Rotunda (Southern Ultima Esperanza) and as far south as Isla Riesco and Tierra del Fuego under the names of Escarpada and Cerro Matrero Formation remain poorly understood (Katz, 1963; Dott *et al.*, 1982; McAtamney *et al.*, 2011).

The lithostratigraphic transition to the Tres Pasos Formation is defined by the first significant sandstone succession overlying fine-grained deposits of the Cerro Toro Formation (Katz, 1963; Smith, 1977; Macellari *et al.*, 1989; Schultz *et al.*, 2005; Covault *et al.*, 2009; Romans *et al.*, 2009). Similarly, the Tres Pasos Formation is exposed for >100 km along a north-south, east-dipping monocline that crops out intermittently from the town of El Calafate (Argentina) to the North, to the town of Puerto Natales (Chile) to the South. A series of resistant ridges of turbiditic sandstones or conglomeratic sandstone interpreted as submarine channels record the axial filling of the Magallanes-Austral Basin through southward prograding clinoforms with paleo-bathymetric reliefs as much as >1,100 m in paleo-water depths that reach >1500 m during the early fill of the basin (Natland, *et al.*, 1974; Covault *et al.*, 2009; Romans *et al.*, 2009; Hubbard *et al.*, 2010; Macauley and Hubbard, 2013; Bauer *et al.*, 2020). The onset of the slope system is characterized by massive (up to 800 m thick) chaotically bedded siltstone-prone deposits containing onlapping sandstone-prone deposits interpreted as amalgamated mass-transport deposits (Armitage *et al.*, 2009; Auchter *et al.*, 2016; Daniels *et al.*, 2018; Romans *et al.*, 2009; Shultz *et al.*, 2005; Shultz and Hubbard, 2005) (**Figure 3.2**).

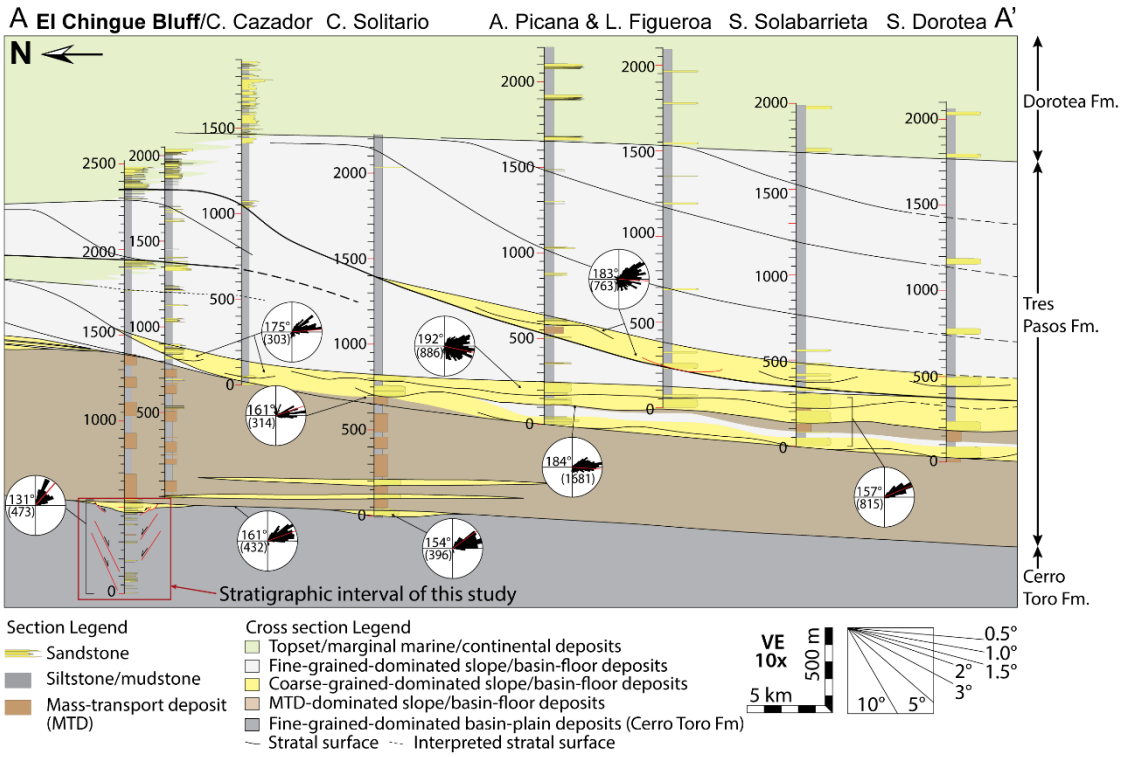

Figure 3.2: Interpreted dip-oriented regional cross section with the location of the studied area in the context of the overlying Tres Pasos Formation slope system. Modified from Daniels *et al*. (2017).

3.3 | STUDY AREA

We examine the stratigraphic succession of the uppermost Cerro Toro Formation, directly underlying mass transport complex deposits of the lower part of the Tres Pasos Formation at Estancia El Chingue, located ~15.5 km north of the Village of Cerro Castillo, along the road Y-185, in the Última Esperanza Province (Southern Chile) (**Figure 3.1**). The studied area is part of a ~6 km long north-south ridge that constitutes the east flank of a ~7 km wide, N-S oriented glacial valley associated with Pleistocene glaciations (Fogwill and Kubik, 2005; García *et al*., 2018, 2015, 2014), which has been interpreted to coincide with the axis of a large fault-propagation anticline attributed to inverted Late Jurassic hemi-grabens (Harambour, 2002). The west side of the valley is defined by the east face of Sierra del Toro, where similar fine-grained deposits crop out adjacent to and underlying massive conglomeratic successions with an age between 86.03±1.3 and 83.1±2.0 Ma (Bernhardt *et al*., 2012). A thorough description of the channel-fill facies at this location is provided in Jobe *et al.* (2010) (**Figure 3.3**).

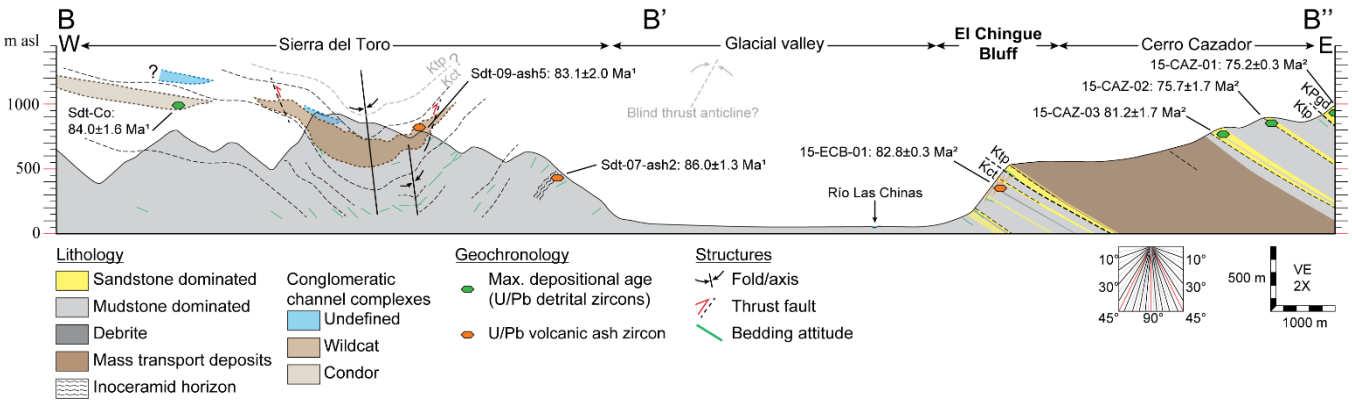

Figure 3.3: Structural cross-section depicting the stratigraphic relationships between the outcrops at Sierra del Toro and El Chingue Bluff (ECB) (see figure 1A for location). Structural cross-section at Sierra del Toro adapted from Stright *et al*. (2017) with data from Jobe *et al*. (2010). Age control from [1]Bernhardt *et al*. (2012) and [2]Daniels *et al*. (2017). Further insight into the subsurface structures that control outcropping folding within the area can be found in Ghiglione *et al*. (2009) and Fosdick *et al*. (2011).

Our study focuses on the east side of the glacial valley, where three modern erosional gullies define a ~2 km long transect informally called El Chingue Bluff (UTM: 676.500 E, 4.330.500), exposing up to ~500 m of stratigraphy. The three gullies are designated as El Chingue Bluff North, Central, and South (ECB-N, ECB-C and ECB-S). The only previous study of this outcrop was carried out by Shultz and Hubbard (2005) in the uppermost part of the succession exposed in ECB-C, where they documented the sedimentology, stratigraphic architecture, and trace-fossils assemblages of the uppermost sandstone-prone interval. Daniels *et al*. (2017) reported ash layers ages of 82.8±0.3 Ma within underlying deposits at ECB-S and 80.5±0.3 Ma for equivalent deposits located ~13.5 km south at Cerro Solitario (**Figures 3.1A and 3.2**). The new data presented here substantially extends the geologic data of El Chingue Bluff to include the entire (>500 m thick) succession and over a larger area.

3.4 | DATA AND METHODS

The framework of this study is provided by 10 sections totaling ~1,500 m of measured stratigraphy. Individual and composite sections were measured throughout the entire exposed and accessible stratigraphy of each gully (composite section 3B/D/E in ECB-N, section 1 in ECB-C and section 2/2alt/8 in ECB-S). These sections range from 370 to 467 m thick and collectively encompass more than 500 m of eastward-dipping mudstone-dominated deposits (**Figure 3.4**). We documented sedimentary features including vertical grain size variations, sedimentary structures, and bed contacts using a Jacob staff at a measuring scale of 1:40, which allowed us to include beds as thin as 1 cm thick. Four high-resolution, 6 m thick sections were also measured at a scale of 1:20 to record additional details. Paleoflow

measurements (N = 473) were obtained from lineal sole marks such as flute casts and tool marks, using the former to resolve the bidirectional nature of the latter.

To reveal sedimentary trends obscured by the overall uniform stratigraphy, more than 3,800 sandstone beds were tabulated by grain size, thickness, and sandstone percentage (*i.e.*, sandstone thickness/total thickness) and analyzed with moving-window curves. Grain size and bed thickness are shown with moving-window curves based on number of observations. Sandstone percentage uses a boxcar smoothing method, which averages over designated thicknesses (5 and 15 m) at 20 cm increments throughout the succession.

Structurally, ECB is affected by a series of S and N dipping faults that cut through the entire succession with less than 50 m of vertical displacements and numerous subordinate minor faults with vertical displacements of less than 5 meters, and thus, easily resolved in the field. In addition, a network of clastic intrusions (*i.e.*, injectites) crops out in the upper half of the succession. Both features, faults and injectites, were measured in terms of strike, dip, and thickness (for the latter). The collected structural data was analyzed to establish preferred orientation and restored using stereonet projections for visualization (Allmendinger *et al.*, 2011). The analysis of these features and correlation of sedimentary packages was accompanied with unmanned aerial vehicle (UAV) imagery using Agisoft Photoscan® to create an outcrop model made up from 2,236 individual photos (**Figure 3.5**).

3.5 | RESULTS

3.5.1 | Stratigraphy

The succession exposed at ECB collectively makes up >500 m of stratigraphy composed of the following sedimentary elements: (1) thinly interbedded siltstone and very fine- to fine-grained, thin- to very thin-bedded (<10 cm thick) sandstone that makes the bulk of the outcrop; (2) five sandstone-prone intervals dominated by interbedded medium-grained, thin- to medium-bedded (commonly <30 cm thick) sandstone and siltstone; (3) four mudstone deposits with contorted beds of up to ~8 m; and (4) a massive pebbly mudstone deposit that caps previous elements (**Figure 3.5C**). The average sandstone percentage of the entire succession below the capping pebbly mudstone deposit ranges from 22% at ECB-N to 8% at ECB-S.

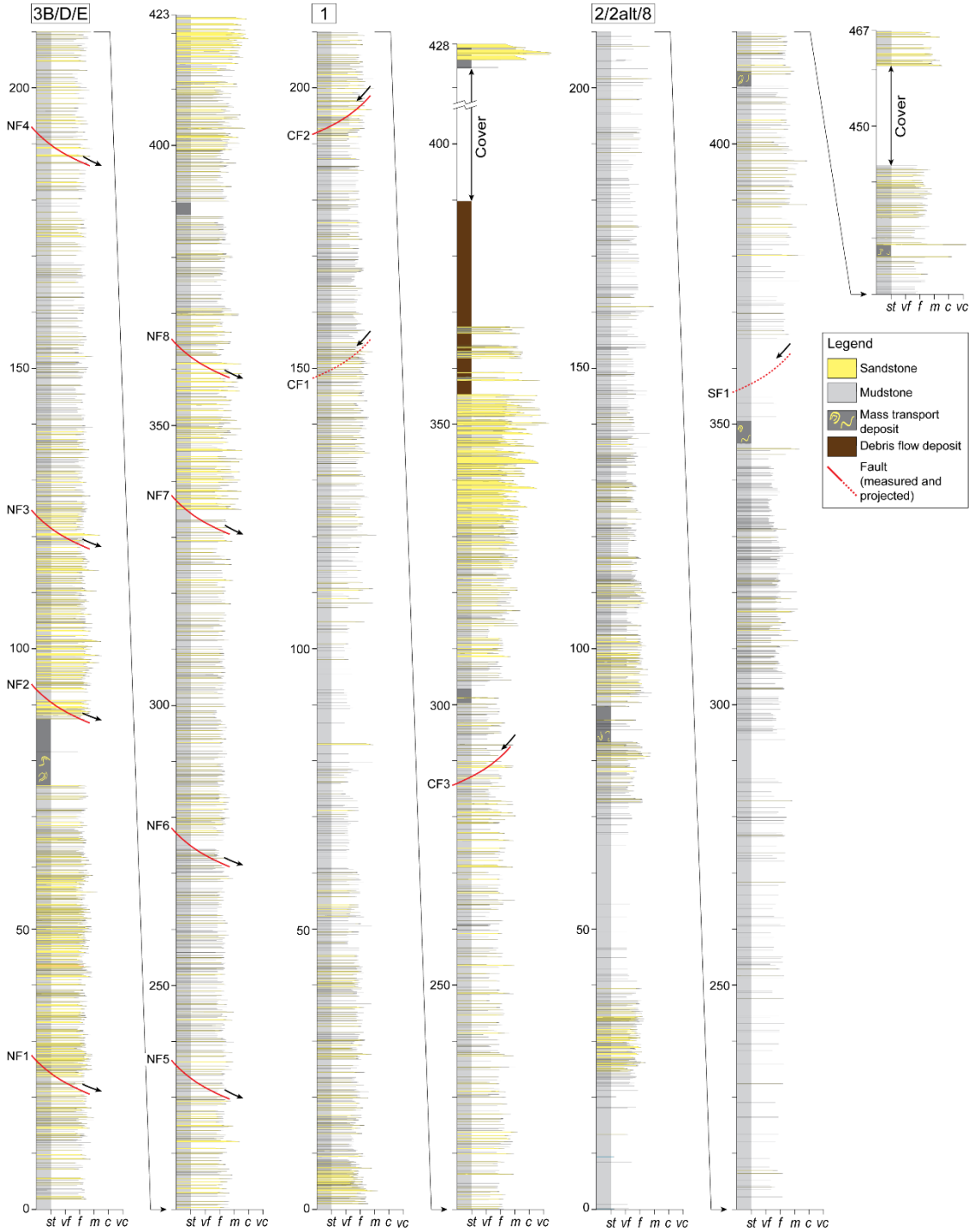

Figure 3.4: Main stratigraphic sections measured at ECB. The red lines mark the stratigraphic location of normal faults and their apparent dip direction where stratigraphic correlation was not possible due to stratal omission (see figure 3.5 for section location and fault distribution). Note that sedimentary structures were not included at the scale of this figure. See figure 3.1 caption for grain-size abbreviation key.

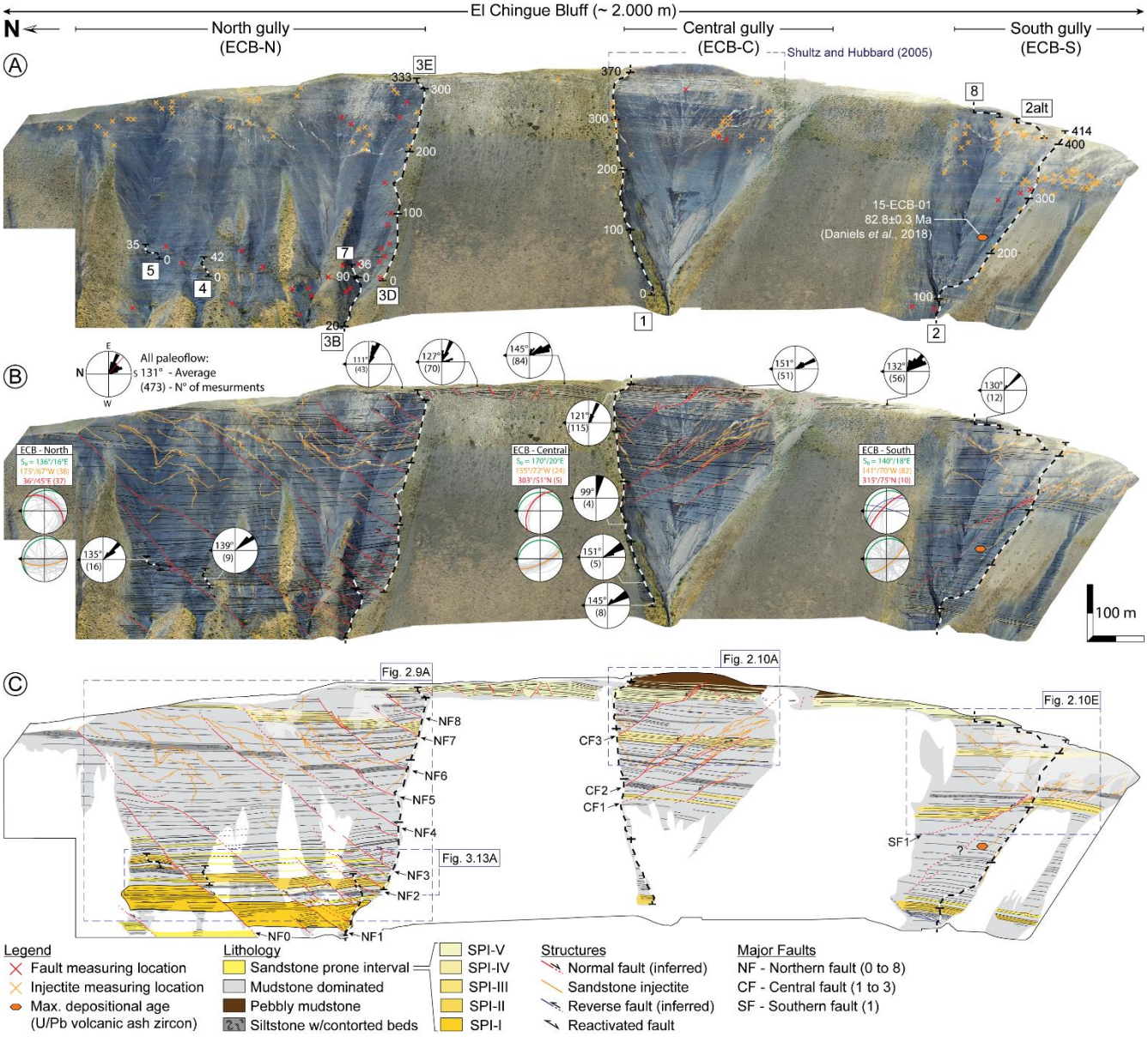

Figure 3.5: Summary of full data set at ECB. **(A)** Distribution of the measured sections and locations where faults and injectites data were collected (orange: injectites; red: normal faults). **(B)** Structural trends in stereonet and paleoflow rose diagrams (red planes correspond to faults, orange to injectites, and green to average strike and tip of each gully). Stereonet and rose diagrams have been rotated 90° counterclockwise to match the orientation of the outcrop (left = north). **(C)** Correlation diagram at ECB depicting the relationship between the main features of the outcrop, as well as identified mass transport deposits. Scale is approximate due to 3D nature of the outcrop.

Lithofacies at El Chingue Bluff

Based on bed-scale characteristics we identified six lithofacies associated with sediment-gravity flow processes in deep-marine environments. The bulk of the succession is composed of interbedded siltstone and thin- to very thin-bedded sandstone (LF1) in packages of up to 200 m. This facies is

interpreted as the deposits of low-density turbidity currents where slow deposition from suspension dominated over tractional processes. Thicker-bedded and coarser-grained tabular sandstones interbedded with siltstone are found in sandstone-prone intervals and are characterized by mud-rich banding (LF2a) and convolute laminations (LF2b) (occasionally combined in one bed), which is attributed to low-density turbidity currents in muddy settings and flow reflection, and/or thick-bedded sandstones (>30 cm; LF3) with traditional Bouma divisions deposited by high-density turbidity currents where tractional processes dominate over suspension fall-out. Laterally continuous, siltstone deposits up to ~8 m thick with deformed and discontinuous sandstone beds (LF4) are interpreted as the result of mass wasting or slumping that locally interrupts the stratigraphy. In some cases, these distinct intervals extend across most or all of the outcrop, making them valuable stratigraphic markers. Finally, a >30 m thick pebbly mudstone deposit (LF5) at the very top of the outcrop is interpreted to be the result of cohesive mud-rich flows (**Figure 3.6** and **Table 3.1**).

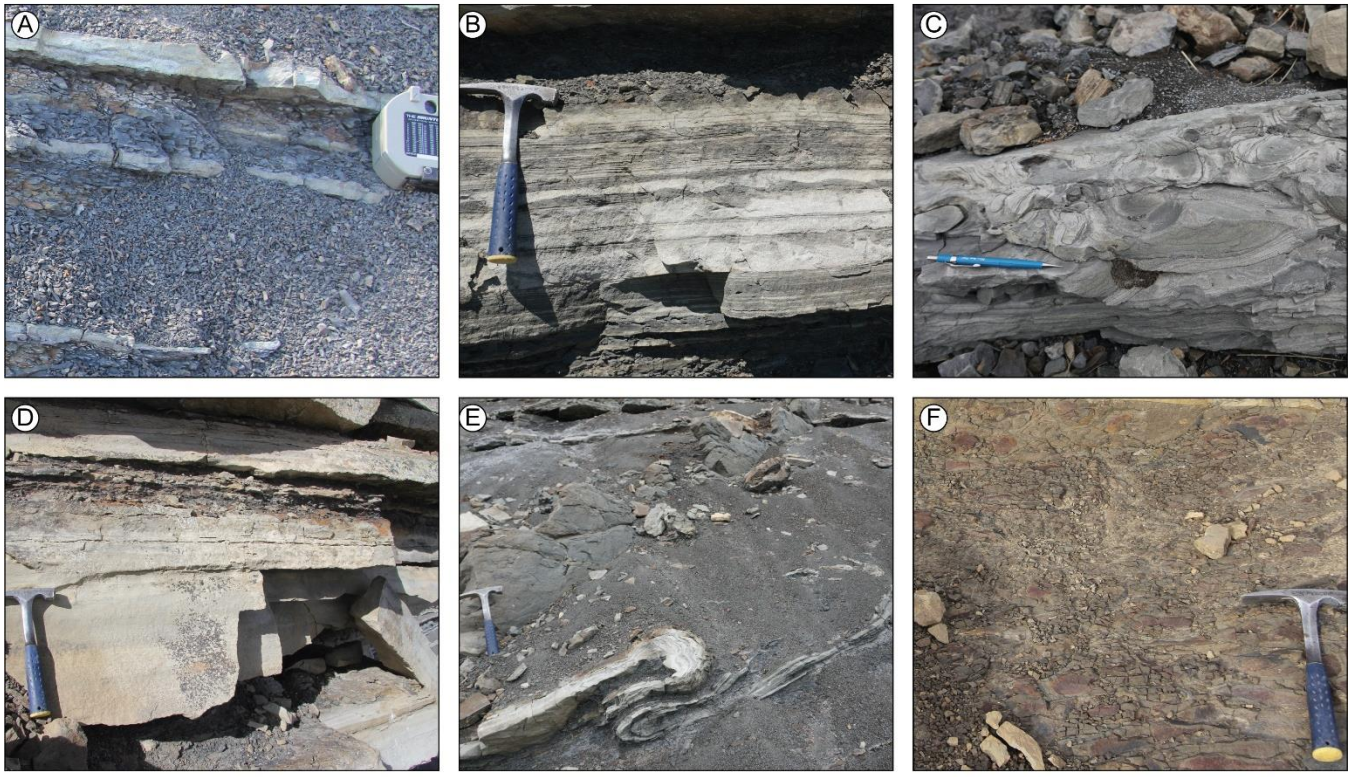

Figure 3.6: Representative lithofacies at ECB (rock hammer is 28 cm long and 16 cm wide; compass is 8 cm in diameter; pencil is 15 cm long). **(A)** Interbedded siltstone and thin- to very thin-bedded sandstone of LF1. **(B)** Interbedded sandstone with mud-rich banding and siltstone of LF2a. **(C)** Interbedded sandstone with convolute laminations and siltstone of LF2b. **(D)** Interbedded medium to thick sandstone and siltstone of LF3. **(E)** Siltstone with deformed and/or discontinuous sandstone beds of LF4. **(F)** Pebbly mudstone of LF5.

Table 3.1: Main characteristics of lithofacies at El Chingue Bluff outcrop.

Lithofacies association	Sandstone grain size	Sandstone bed thickness and geometry	Physical structures and accessories	Process based interpretation
LF1: Interbedded siltstone and thin- to very thin-bedded sandstone	Very fine- to fine-grained	<10 cm, tabular	*Siltstone*: massive *Sandstone*: planar, ripple and/or wavy lamination, siltstone lamination	Low-density turbidity currents. Slow deposition from suspension dominates over tractional processes
LF2a: Interbedded sandstone with mud-rich banding and siltstone	Fine- to very fine-grained, medium-grained (very rare)	>10 cm, up to ~40 cm, tabular	*Siltstone*: massive *Sandstone*: Structureless (rare), planar lamination and sub-parallel to low angle-banding formed by mud-rich layers of varying thickness, ripple and convolute lamination (occasional), climbing ripples (rare)	Slow deceleration of clay-rich transitional flows or turbidity currents in muddy settings (as part of the flow and/or the substrate). Deposition by traction over muddy substrates (Baas *et al*., 2011, 2016; Stevenson *et al*., 2020)
LF2b: Interbedded sandstone with convolute laminations and siltstone	Fine- to very fine-grained, medium-grained (very rare)	>10 cm, up to ~40 cm, tabular	*Siltstone*: massive *Sandstone*: Structureless (rare), planar and ripple lamination, convolute lamination and soft sediment deformation, mud-rich banding (occasional), water-escape structures (rare)	Deceleration and reflection of clay-rich transitional flows or turbidity currents in muddy settings (as part of the flow and/or the substrate). Deposition by traction and fallout of suspension affected by reflected waves or bores (Stevenson *et al*., 2020; Tinterri *et al*., 2016)
LF3: Interbedded medium to thick sandstone and siltstone	Medium- to coarse-grained, locally very coarse-grained	>30 cm, up to ~1 m, mostly tabular, locally lenticular	*Siltstone*: massive *Sandstone*: Structureless, planar and ripple lamination, cross-bedding (rare)	High-density turbidity currents. Mostly deposition by traction and rapid fall out of suspension
LF4: Siltstone with deformed and/or discontinuous sandstone beds	Fine- to very fine-grained	<15 cm, tabular discontinuous beds	Contorted sandstone beds	Mass wasting or slumping due to gravity induced sliding. Rapid cessation of movement caused by basal and internal friction. Mass transport deposit
LF5: Pebbly mudstone	-	-	Sparse pebble in a muddy matrix	Cohesive mud-rich flows or debris flows. Deposition by 'freezing' (Talling *et al*., 2012)

Sandstone prone intervals and sedimentary trends

A combination of field observations and qualitative analysis of grain size, bed thickness, and sandstone percentage of the stratigraphic succession exposed at ECB allowed us to recognize five distinct sandstone-prone intervals (SPI). A sandstone-prone interval represents a stratigraphic package with an increased sandstone content in comparison to underlying and overlying strata, as expressed in bed thickness and sandstone percentage, which is also typically accompanied by a coarser grain-size (**Figure 3.7**). However, due to vertical and lateral variations in lithofacies between and across sandstone packages and stratal omission caused by non-resolvable normal faults, it was not possible to determine a single

cutoff value of the quantitative parameters for the entire outcrop. Thus, the definition and correlation of SPIs is meant to provide a stratigraphic reference rather than an exact correlation between beds.

Sandstone-prone interval I (SPI-I) crops out at the base of the stratigraphic succession at ECB-N and ECB-S, where active alluvial channels cut through alluvium exposing the rock substrate, whereas at ECB-C its covered by those modern deposits. At ECB-N, SPI-I is expressed as a ~36 m thick package with 44% of mostly thin and medium-bedded, fine and very fine-grained sandstones of LF2a and LF2b and a lower proportion of very thin-bedded, very fine-grained sandstone of LF1 in a thickening and thinning upward trend. At ECB-S, SPI-I is significantly thinner (~15 m), with the same facies in a similar vertical arrangement and sandstone percentage of 36%.

The lower boundary of *Sandstone-prone interval II* (SPI-II) is defined by a 15 to 7 m thick MTD horizon of LF4, identified at ECB-N and ECB-S, whereas at ECB-C only the upper part of the interval crops out. SPI-II thickness decreases from ~20 m at ECB-N to ~13 m at ECB-S, whereas at ECB-C it's estimated in at least ~11 m. Overall sandstone percentage in this interval ranges between 30% and 40%, and it's composed mainly of LF2a and LF2b with rare beds of LF3 in a general finning upwards arrangement.

Sandstone-prone interval III (SPI-III) was fully characterized only at ECB-S, although based on the presence of an overlying MTD horizon used as a marker, it is inferred that it should also be present at ECB-N and ECB-C, just not in the path of the measured sections at ECB-N and only the very top of it at ECB-C, in both cases due to stratal omission caused by normal faulting. At ECB-S, SPI-III is barely distinguishable from underlying and overlying strata; however, a small increase in bed thickness (**Figure 3.7**) is accompanied by a slightly coarser grain size and a sandstone percentage of ~17%. In contrast to underlying and overlying SPI, SPI-III's main lithofacies corresponds to very thin to thin-bedded and very fine-grained sandstones of LF1.

Sandstone-prone interval IV (SPI-IV) was recorded in the three gullies exposed at ECB, with a thickness that range from ~17 m at ECB-N, ~25 m at ECB-C, and ~16 m at ECB-S, although at ECB-N and ECB-S the respective base and top of the interval is not present due to normal faulting. Overall sandstone percentage decreases southwards from 35% to 13% with mostly thin- to medium-bedded, fine-grained sandstone of LF2a and LF2b in a coarsening-fining and thickening-thinning upward arrangement.

Sandstone-prone interval V (SPI-V) is exposed at the very top of the outcrop with a thickness that ranges from ~24 to ~30 m and a sandstone percentage as high as 61% at ECB-C and 37% to ~29% at ECB-N and ECB-S, respectively. Sandstone beds within this interval are the thickest and coarsest of the outcrop, with mostly medium-grained and in some cases thick-bedded, fine and up to very coarse-grained sandstones of LF3. In contrast to underlying SPIs, sandstone beds in SPI-V show not only tabular geometries, but also lenticular and are affected by a synsedimentary fault with signs of growth. As mentioned above, this sandstone-prone interval was the focus of Shultz and Hubbard (2005).

Even though not all SPIs were recorded in their entirety in the measured sections, we plotted and compared the properties of each SPI to help visualize potential stratigraphic trends in space (from north to south) and time (from SPI-I to SPI-V) (**Figure 3.8**). The results show that SPI-I to SPI-IV tend to decrease their grain size, bed thickness, and sandstone percentage southwards (with the exception of SPI-IV's grain size, which increases from ECB-C to ECB-S). In contrast, SPI-V shows a clear peak in grain size, bed thickness and sandstone percentage at ECB-C.

Paleoflow at El Chingue Bluff

A total of 473 individual paleocurrent measurements were collected at ECB. Paleoflow indicators consist of sole marks, both flute casts and tool marks, mostly within sandstone-prone intervals. Individual paleoflow measurements fluctuate between 82° and 190°, whereas the average values by location vary between 99° and 151°, with a total average direction to the southeast (131°).

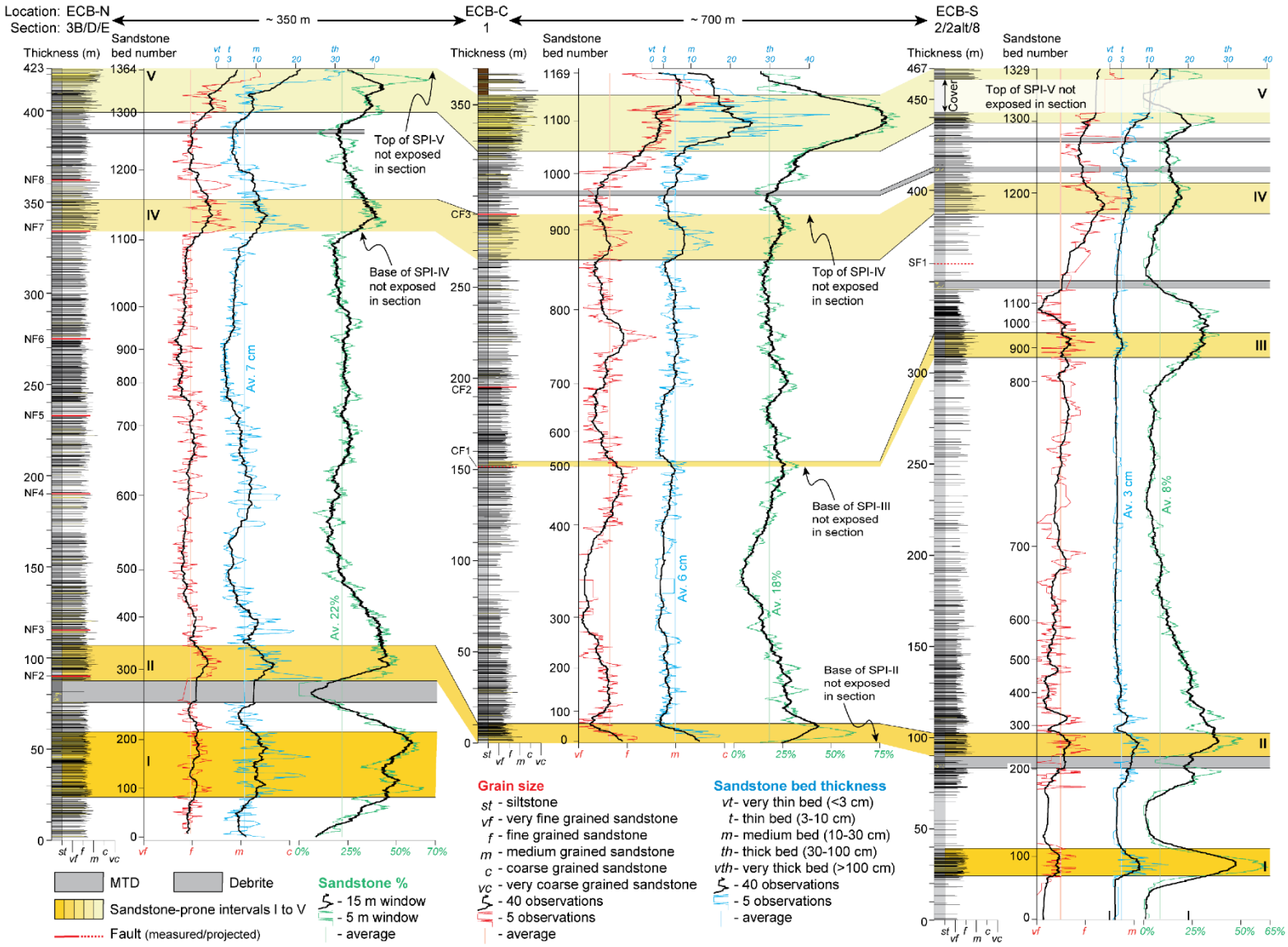

Figure 3.7: Sandstone-prone intervals based on sedimentary data displayed from 3,862 sandstone beds measured at ECB. Note that some SPI and MTD horizons were partially or not intersected by the measured sections (see figure 5 for sections and faults location and stratigraphic packages distribution). Refer to the text for explanation of moving-window curves.

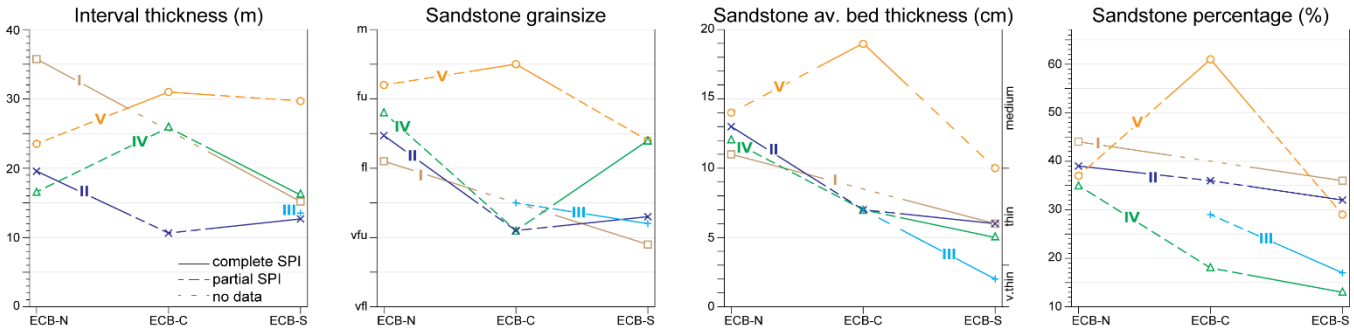

Figure 3.8: Lateral and vertical trends of quantitative sedimentary parameters determined for each sandstone-prone interval as shown in figure 3.7.

3.5.2 | Faults

The stratigraphic succession at ECB is affected by numerous faults of varying scale and nature: (1) Primary normal faults are the main structural feature of the outcrop belt. These faults cut >100 meters of stratigraphic thickness and displace entire segments of the outcrop, making correlation possible only at the scale of sedimentary packages; (2) in opposition to the former, secondary normal faults are easily resolvable at a bed-by-bed scale as offsets rarely exceed more than a meter and, in some cases, have systematically decreasing offset towards the top of the fault. Secondary normal faults are common throughout the succession and cross <10 to 10s of meters of stratigraphy; (3) subsidiary to primary and secondary normal faults in the form of antithetic and synthetic normal, and on some occasions reverse faults, make up the third group; and finally, (4) a small number of local reverse faults unrelated to primary and secondary faults, in both location and orientation, are also present.

Primary and secondary normal faults were observed throughout the entire outcrop belt; however, their attitude consistently changes from one part of the outcrop to another. Stereonet analysis shows two main orientations of faulting; at ECB-N, normal faults were observed to dip towards the southeast with an average plane of N36°E/45°S with some of them cutting the entire succession (*i.e.*, >400 m of stratigraphy) with as much as ~40 m of offset (*i.e.*, between section 5 and section 4). These major faults displace sandstone prone intervals and MTD horizons, causing stratigraphic omission in composite section 3B/D/E (**Figure 3.9**). On the contrary, at ECB-C and ECB-S, primary and secondary normal faults were observed to dip towards the north and northeast with average planes of N73°W/39°N and N46°W/57°N, respectively and estimated offsets ranging from 5 to 30 m (**Figure 3.10**).

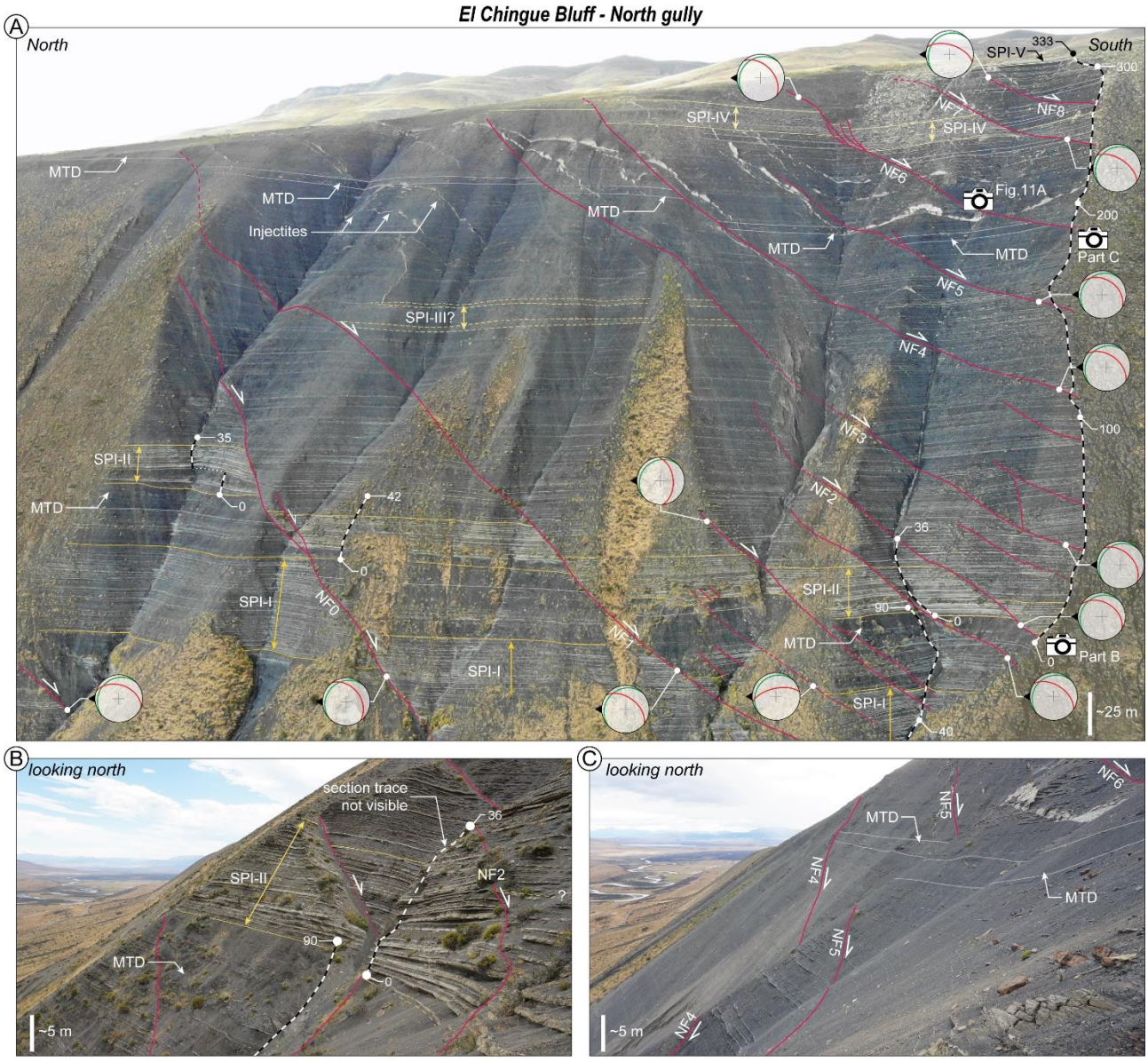

Figure 3.9: Main stratigraphic and structural features at ECB-N. **(A)** Outcrop expression of SPI, MTD and primary normal faults. Note the constant orientation of fault planes across the north gully and the different levels of offset (picture location on figure 3.5). **(B)** View of primary normal faults intersecting SPI- II. **(C)** View of primary normal faults cross cutting siltstone-dominated deposits. Scale is approximate due perspective in the photographs. Stereonet and rose diagrams have been rotated 90° counterclockwise to match the orientation of the outcrop (left = north; green plane = S_0); scale is variable due to 3D nature of the outcrop.

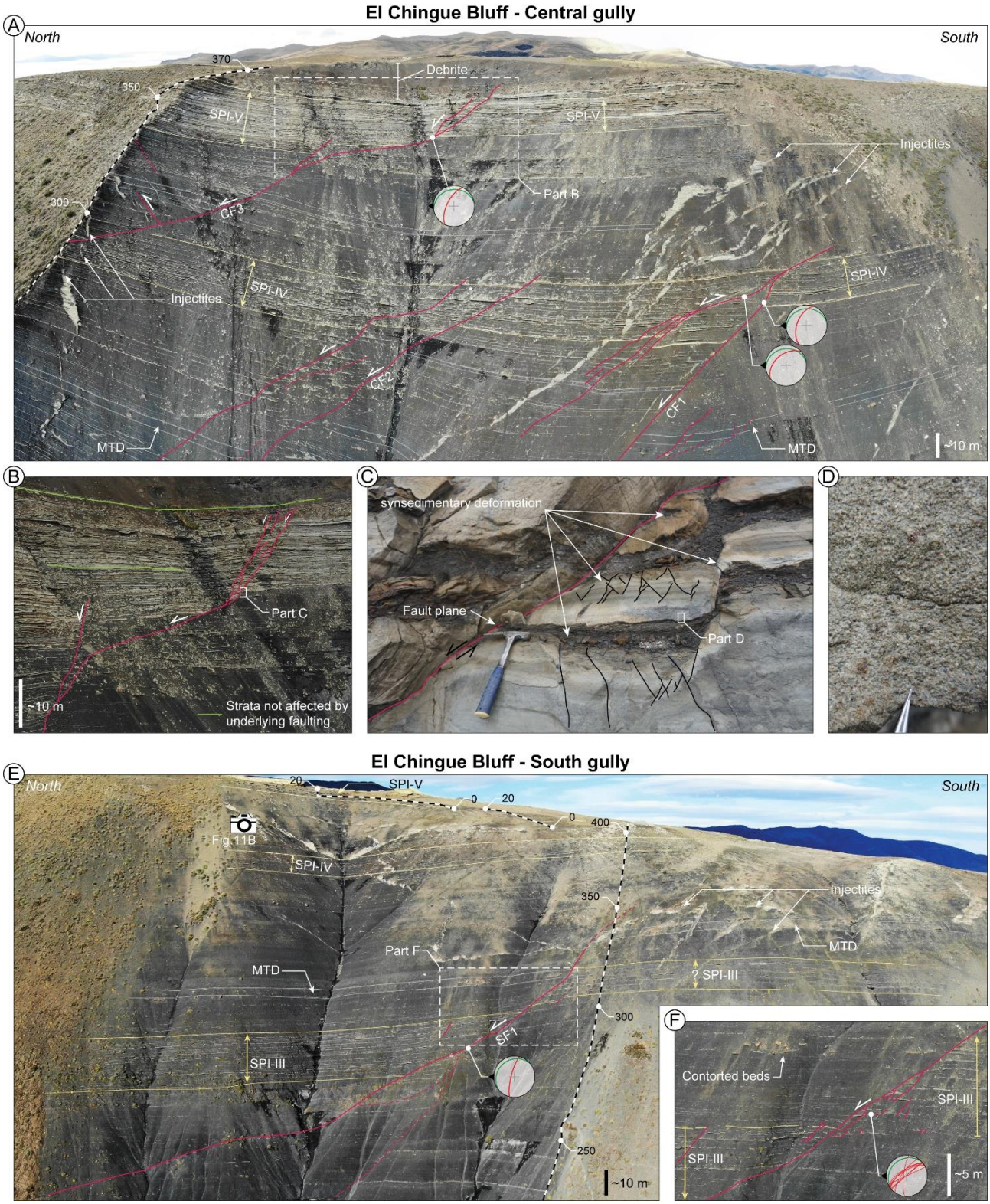

Figure 3.10: Main stratigraphic and structural features at ECB-C and ECB-S. **(A)** Outcrop expression of sandstone-prone intervals, mass-transport deposits and primary normal faults at ECB-C. Note how the uppermost fault (CF3) is healed within the overlying debrite. **(B)** Detailed view of CF3 showing synthetic subsidiary faults in SPI-V. **(C)** Bed scale view at the fault plane. Note soft deformation and intra-stratal faulting caused during faulting. **(D)** Detail

of very coarse-grained sandstone at the base of LF3 in SPI-V at ECB-C. **(E)** Outcrop distribution of sandstone-prone intervals, mass-transport deposits and primary normal faults at ECB-S. **(F)** Detailed view of SF1 showing synthetic subsidiary faults in SPI-III. Scale is approximate due to perspective in the photographs. Stereonets have been rotated 90° counterclockwise to align with the orientation of the outcrop (left = north; green plane = S_0); scale is variable due to 3D nature of the outcrop.

3.5.3 | Clastic Intrusions

Clastic intrusions (injectites) are a common feature at ECB, especially within the upper half of the outcrop, where they can be traced for hundreds of meters. They consist of well sorted fine- to medium-grained sandstone sheets discordant to the stratigraphy, in the form of semicontinuous, vertical to subvertical and thin to medium dikes (**Figure 3.11**).

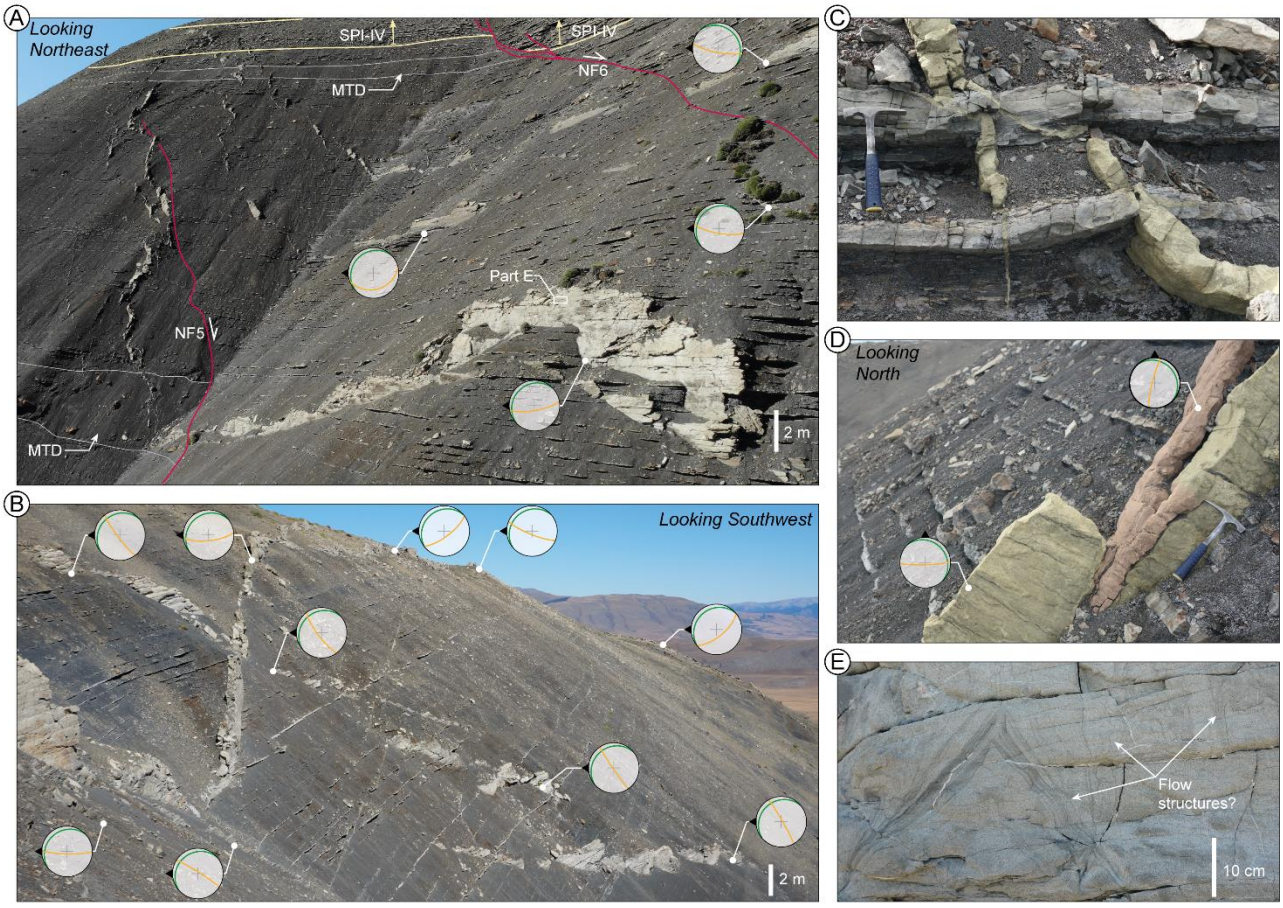

Figure 3.11: Injectites at ECB. **(A)** Injectites cross-cutting thin-bedded strata underlying SPI-IV at ECB-N. (B) Injectites cross-cutting thin-bedded strata and sandstone-prone interval IV at ECB-S. **(C)** Upward deformation of sandstone bed intruded by injectite. **(D)** NS oriented injectite intersecting and mixing with an EW injectite. **(E)** Laminations and vertical tubular structures are common withing thicker injectites. Injectites have been colored to highlight their geometry and distribution in part C and D. Scale is approximate due perspective in the photographs. Stereonet in A and B have been rotated 90° counterclockwise to align with the orientation of the outcrop (green plane = S_0); scale is variable due to 3D nature of the outcrop.

Dikes are oriented with variable strikes; however, the preferred strike orientation was found to be SE-NW dipping slightly to the SW, with over 80% dipping more than 75° when restored and an 85% measuring less than 25 cm thick (**Figure 3.12C-D**). Numerous injectites are distributed in an *en echelon* pattern (*i.e.*, in semicontinuous steps) locally thinning each time they cross a sandstone bed and with the appearance of pinching out upwards and downwards. Internally, some injectites were observed to contain faint planar laminations parallel and oblique to the edges in cross section and angular mudstone intraclasts. Mud-rich lamination and vertical tubular structures were also observed on the lateral faces of injectites, especially in thicker ones (>30 cm wide), suggesting internal flow and sediment remobilization within these structures (**Figure 3.11E**).

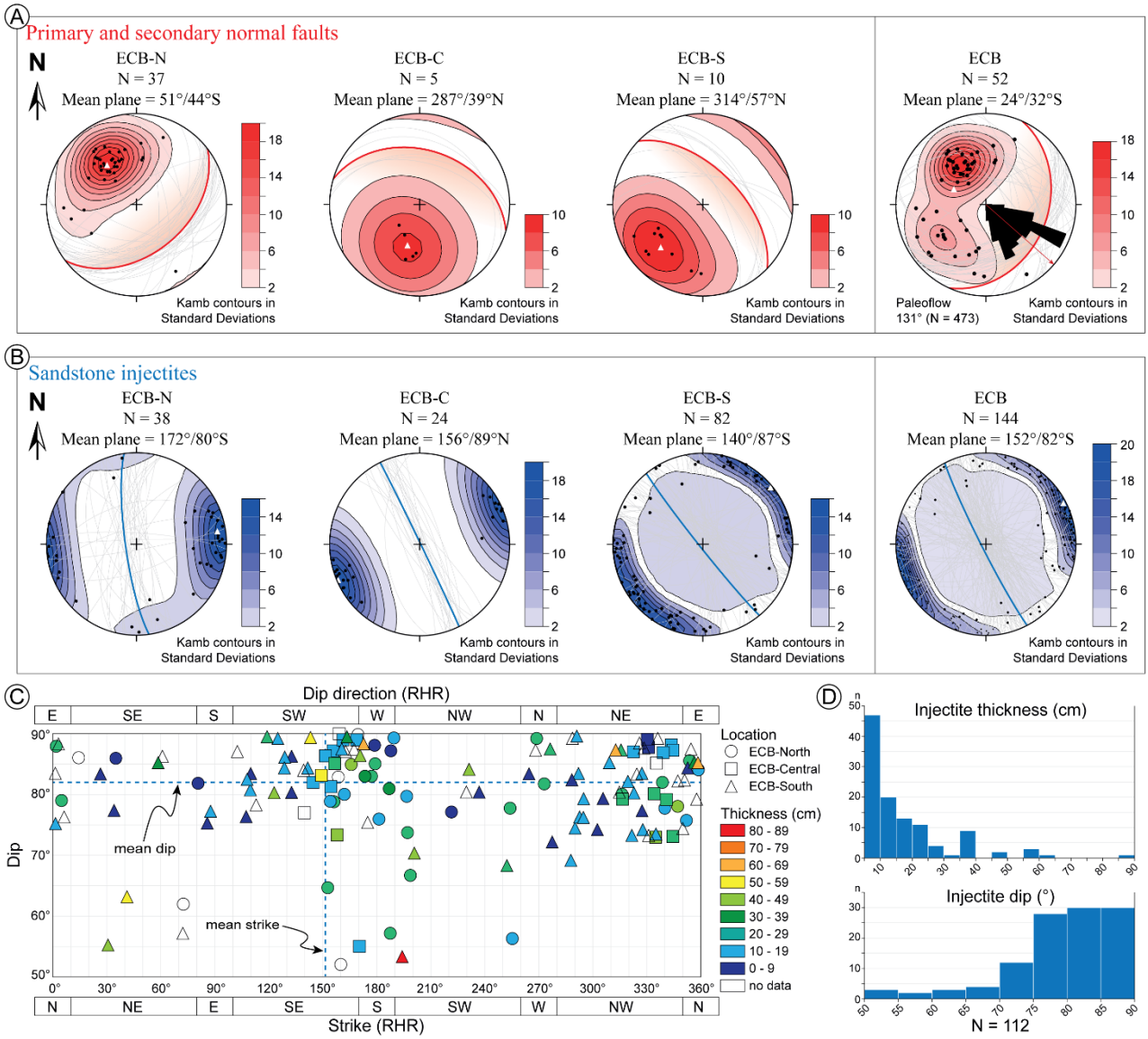

Figure 3.12: Summary of structural data at ECB. Note that plane orientation has been restored using mean S_0 for each gully (pre-folding). **(A)** Lower hemisphere stereoplots of pole-to-plane contours for primary normal faults. **(B)** Lower hemisphere stereoplots of pole-to-plane contours for injectites. **(C)** Scatter diagram of injectites strike and dip integrated with thickness and location (strike and dip direction following right hand rule). **(D)** Bar plots for injectite thickness and dip.

3.6 | RELATIVE TIMING OF EVENTS

To better understand the temporal relationship between the sedimentary succession and the structures present at El Chingue Bluff, and interpret its depositional setting, we systematically analyzed the nature, distribution, and orientation of primary faults, injectites, and paleoflow measurements of the entire outcrop belt using a qualitative and quantitative approach.

3.6.1 | Synchronous relationship between normal faulting and the sedimentary succession

There are numerous observations that collectively suggest a syndepositional nature for primary and secondary normal faults at ECB:

(1) Changes in bed thickness between strata across faults; causing precise bed-by-bed correlation challenging or impossible, even over short distances (**Figure 3.9B**).

(2) Stratal healing above some of the primary faults and over secondary faults was observed at many locations. At ECB-N, the uppermost MTD horizon is unaffected by the normal faults located between primary faults NF1 and NF3; at ECB-C, primary fault CF3 crosses SPI-V but does not affect the overlying debritic deposit (**Figures 3.9A and 3.10A**).

(3) Some sandstone beds were observed to be stretched along the fault plane without mechanical reduction of grain size at plain sight, suggesting low cohesion and fluidization of the sediment at the time of faulting (**Figure 3.10C**). A similar situation has been described in other systems affected by synsedimentary faulting (Elliot, 1965; Petit and Beauchamp, 1986; Prestholm and Walderhaug, 2000)

(4) Lack of structural brittle deformation such as fault breccia or gouge commonly associated to the deformation that led to the uplift of the outcrop belt.

(5) Lack of structural plastic deformation such as drag folds towards fault planes.

To evaluate the syndepositional relationship of normal faulting and the sedimentary succession, we measured three stratigraphic sections in SPI-II at 1 cm resolution that are displaced by primary normal faults at ECB-N along a ~350 m long transect. Bed correlation was established based on the presence of

a distinct MTD horizon, which is used as a stratigraphic datum at the base (**see figure 3.5 for location**). Then, for each subinterval (as defined by bed correlations with varying levels of confidence) we analyzed their thickness and trends in sandstone grain size, sandstone bed thickness, and sandstone percentage (**Figure 3.13**).

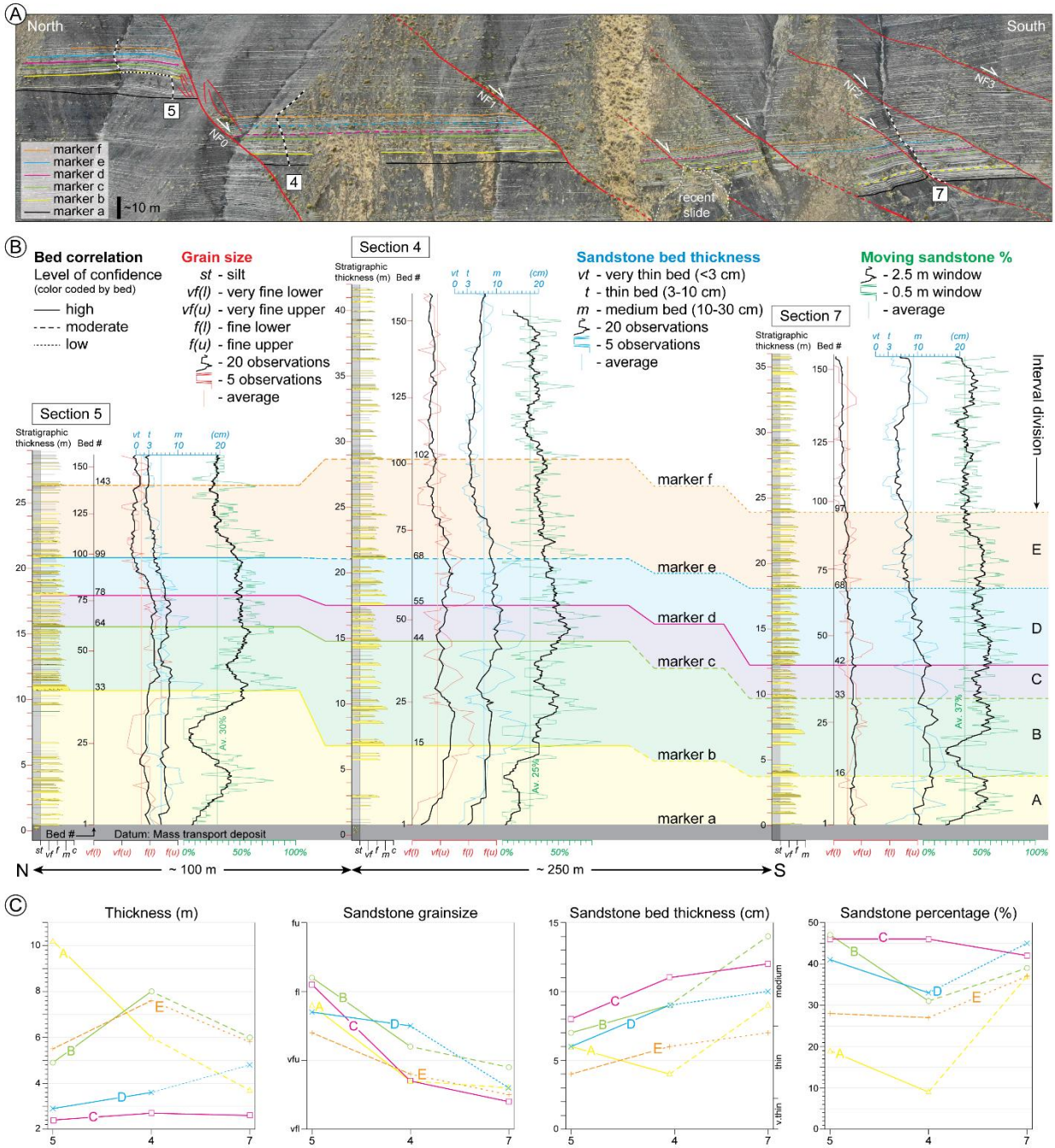

Figure 3.13: Relationship between primary faults and stratigraphy in SPI-II at ECB-N. **(A)** Location of stratigraphic sections, primary faults, and bed correlation. **(B)** Diagram of SPI-II divisions and measured parameters. **(C)** Lateral and vertical trends of sedimentary parameters measured for each division in SPI-II.

Our analysis reveals differences in overall thickness, sandstone grain size, sandstone bed thickness, sandstone percentage, and bed number within the same divisions in SPI-II (**Figure 3.13C**). Variations in thickness for division A in sections 4, 5 and 7 are interpreted to be the result of an irregular seafloor paleorelief caused by the deposition of the basal MTD horizon (marker 'a') over the already faulted substrate. As time passed, ongoing sedimentation would have 'healed' the seafloor relief caused by synsedimentary fault displacement, as shown by the presence of recognizable marker beds on both sides of the faults. However, continuing differential slip timing and rate of displacement resulted in the accumulation of thicker sandstone beds on the southward downthrown blocks at ECB-N (**Figure 3.13C**), the deposition of the convoluted and banded sandstones (LF2a and LF2b), and differences in sandstone grain size and percentage that we observed and measured as a consequence of the irregular (faulted) substrate. These observations suggest a polycyclic kinematic behavior of normal faulting, synchronous at the scale of SPIs for primary and secondary faults, but asynchronous at the scale of bed-by-bed deposition (*i.e.*, faults active differentially in time). These findings are comparable to what has been observed in other depositional systems affected by growth faults (Bourollec *et al.*, 2004; Cartwright *et al.*, 1998; Rouby *et al.*, 2002).

We are able to confirm the synsedimentary nature of faults interpreted by Shultz and Hubbard (2005), which they based on qualitative observations of SPI-V in ECB-C. Our measurements and analysis show that synsedimentary faulting occurred throughout the history of the entire ~500 m thick succession, and not just during the deposition of the uppermost (SPI-V) sandstone interval. The volcanic ash age constraints from Daniels *et al.* (2018) at ECB (**Figure 3.5**) and nearby correlative outcrops indicate that SPI-I and SPI-II are older than 82.8 ± 0.3 Ma and that SPI-V is 80.5 ± 0.3 Ma, defining a total duration of the 500 m thick succession of at least ~2-3 Myr. Additionally, our measurements and observations suggest a different spatial relationship between primary normal faults in different locations. Rather than a synthetic and antithetic fault arrangement as proposed by Shultz and Hubbard (2005), we note the possibility that primary faults located at ECB-C and ECB-S may be an extension of primary faults at ECB-N (*i.e.*, the same faults) based on their intersecting trajectory (**Figures 3.5C and 3.12A**). Furthermore, a comparison between paleoflow direction and synsedimentary faulting show a potential influence of the latter over the former, as shown by the mean flow direction ($\bar{x}$ = 131°; N = 473), almost perpendicular to the orientation of the mean plane of all primary and secondary normal faults ($\bar{x}$ = 24°; N = 52) (**Figure 3.12A**).

3.6.2 | Postdepositional injection of sandstones

The development of clastic intrusions occurs when buried unconsolidated sediment, such as sand or gravel, is forcefully remobilized into less permeable strata due pore fluid overpressure caused by compaction and/or the addition of migrating fluids (Hurst *et al.*, 2003; Kane, 2010; Cobain *et al.*, 2015). At El Chingue Bluff, even though a parental body is not evident, upward bending of sandstone beds intersected by injectite structures indicates that their emplacement occurred from an underlying source, potentially out of the plane of this outcrop, and through successive pulses as revealed by cross-cutting relationship between injectites (**Figures 3.11C and 3.11D**).

Field observations at ECB show that injectites are not displaced by normal faulting and, thus, post-date the timing of normal faulting. This relationship adds further evidence to the syndepositional interpretation of the normal faults discussed above. We also note that there's a potential geometric relationship between the faults and the injectites (*e.g.*, long-lived regional stress field that influences orientations); however, the detailed mechanisms of clastic intrusion and relationship to a common stress field are beyond the scope of this study.

3.7 | DISCUSSION

3.7.1 | Submarine levees as depositional slope systems

We interpret the stratigraphic succession at El Chingue Bluff (ECB) to record overbank sedimentation in association with the Cerro Toro Formation axial submarine channel system. In addition to the observations and measurements from ECB presented in this study, interpretation that these strata represent the external levee of the Cerro Toro channel system is supported by contextual information from previous studies. First, geologic mapping in the region indicates that this interval generally correlates to the well-documented channelized strata of the Cerro Toro Formation exposed on Sierra del Toro to the northwest (Jobe *et al.*, 2010; Bernhardt *et al.*, 2012). Additionally, the top of the ECB succession studied here marks the lithostratigraphic base of the overlying Tres Pasos Formation (Shultz *et al.*, 2005; Bauer *et al.*, 2020). Second, ages from volcanic ashes reported by Daniels *et al.* (2018) at ECB and by Bernhardt *et al*. (2012) at Sierra del Toro overlap within their uncertainty (**Figure 3.3**). Finally, the overall paleoflow at ECB (131°), oblique to channel-fill paleoflow measured by Jobe *et al.* (2010) at Sierra del Toro (153°) reinforces the potential genetic relationship between the two outcrops, suggesting that thin-bedded turbidites at ECB are the result of overspill flows (*e.g.*, Hansen *et al.*, 2015) that diverged from the axial submarine channel system. A similar interpretation was proposed by Hubbard *et al.* (2008) in equivalent

deposits at Laguna Sofia, ~45 kms south. The sedimentologic aspects that support our interpretation are thoroughly discussed below.

Our interpretation of the ECB succession as recording levee evolution provides an opportunity to consider levee slopes associated with submarine channel systems as a type of depositional slope system by themselves. Initial research on submarine levees documented the classic 'gull wing' geometry observed in bathymetry and seismic-reflection profiles and discussed their development as a consequence of flows overtopping the levee crest, leading to diminished deposition away from the channel and the construction of a depositional slope (Hiscott *et al.*, 1997). In contrast to delta-fed depositional slopes common along basin margins, levee slopes are oriented orthogonal or oblique to the overall sediment dispersal direction controlled by the channel itself. The spatial scale of levee slopes depends on the scale of the overall system, among other factors, and is typically 10s of km or more distance away from the channel (Deptuck and Sylvester, 2018). An analysis of modern submarine channel-levee systems (n=48) reveals a range of maximum slopes of levee flanks from <1˚ to 6˚, with a mean of 1.8˚ (Nakajima and Kneller, 2012). Thus, the scale and gradient of levee slopes set up a depositional system that broadly shares characteristics with other depositional slopes. With the notion of levee slopes as distinct depositional slope systems we discuss both the depositional and faulting features on display at ECB below.

3.7.2 | Deposition of sandstone-prone deposits in an external levee outer-slope

Deep-water external levee deposits are commonly described as uniform successions of siltstone-dominated, mostly thin-bedded turbidites with a wedge geometry that thins away from a genetically related channel in cross-section (Clark and Pickering, 1996; Cronin *et al.*, 2000; Kane *et al.*, 2010; Brunt *et al.*, 2013; Hansen *et al.*, 2015). Internally, these morphologic features tend to show laterally extensive beds, rare erosive surfaces and consistent paleoflows that deviate from the average flow direction of the channel (Kane and Hodgson, 2011). Overbank growth (including external levee) occurs when the height of the sediment gravity flow is greater than the relief of the confining surface, as the flow overspills above the overbank, the loss of confinement results in flow deceleration and deposition, thus increasing building up the overbank (Hansen *et al.*, 2015; Piper and Normark, 1983; Hiscott *et al.*, 1997).

The overall uniform thin-bedded succession at ECB is interrupted by five stratigraphic packages with increased sandstone grain size, bed thickness and sandstone percentage of variable thickness, referred in this study as sandstone-prone intervals I to V (SPI-I to SPI-V) (**Figure 3.7**). SPI-I to SPI-IV are

characterized by fine-grained, convoluted and/or banded medium-, and occasionally thick-bedded sandstones, with comparatively rare climbing ripples (especially within SPI-I), whereas in SPI-V, classic Bouma divisions are common, including coarse-grained and even gravel-rich structureless thick-bedded sandstones (**Figure 3.6**). Convolute deformation results from the perturbation of primary lamination in liquefied sediment during deposition. In turbiditic sandstones, convolute lamination can be developed by several processes, including load structures, water escape, flow deceleration by hydraulic jumps, bores and internal waves by reflecting flows (Tinterri *et al.*, 2016; Edwards *et al.*, 1994; Owen *et al.*, 2011). On the other hand, mud-rich banding in turbiditic sandstones, has been found to form within sustained mud-rich transitional flows in the same regime as Bouma T_b division in a variety of deep-marine environments including, but not limited to: intraslope lobes, down dip channel mouth scours and channel splays (Baas *et al.*, 2009; 2016; Stevenson *et al.*, 2020 and references therein).

Our interpretation is that sandstone-prone intervals at ECB represent splay deposits in the external levee's outer-slope formed by overspilling turbidity currents flowing through the channel belt at Sierra del Toro. The resulting divergent flows traversed a slope affected by changes in gradient, such as scarps, as a consequence of synsedimentary faulting in the levee surface, causing flow deceleration by hydraulic jumps that resulted in the convolute laminations observed within turbiditic sandstones in SPIs. The inherently mud-rich setting of levees would have also favored the formation of banded sandstones. We also consider that synsedimentary faulting would have resulted in ponded minibasins within the levee slope, influencing the paleoflow direction, distribution and depositional architecture of coarser sediment. Other cases where syndepositional structures have resulted in enhanced sediment deposition and/or modified paleoflow has been described in Morroco's Upper Triassic shallow marine sandstones of High Atlas (Petit and Beauchamp, 1986), in the delta-feed deep-water turbidites of the Grès d'Annot Formation in France (Bouroullec *et al.*, 2004) and the continental slope of the Niger Delta (Adeogba *et al.*, 2005).

Finally, in contrast to underlying SPIs, SPI-V, which lies directly underlying debritic deposits attributed to the Tres Pasos Formation, is deprived of convoluted sandstone beds, banded sandstones are rare, and sandstone content (*i.e.*, grain size, bed thickness and percentage) reach its maximum (**Figure 3.8**), thus, we do not discard the possibility that the vertical changes observed between lower SPI and SPI-V reflect the fill of the channel belt at Sierra del Toro prior to the abrupt change in depositional architecture observed between the Cerro Toro Formation and the overlying Tres Pasos Formation.

3.7.3 | Potential controls of levee-slope synsedimentary normal faulting at El Chingue Bluff

A characteristic of many depositional slope systems is the interaction and interdependence of sedimentation and deformation, the latter of which can include faulting and/or various forms of diapirism (Bourollect *et al.*, 2004). Studies on continental and other basin margins show that syndepositional normal faulting is a fundamental component of many slope systems. For example, research on sediment-nourished margins (*e.g.*, passive-margin delta systems), based primarily on regional 2-D seismic-reflection data, show that growth faults (*i.e.*, down-to-the-basin normal faults with listric geometry and significant stratigraphic growth in the hangingwall) are a common feature and can have offsets of hundreds of meters (*e.g.*, Galloway, 1986; Khani and Back, 2012). Smaller-scale growth faults (meters to 10s of meters of offset) have been documented in outcropping delta-slope systems as well (*e.g.*, Rider, 1978; Bhattacharya and Davies, 2001). Broadly similar synsedimentary normal faulting has also been documented in intra-slope settings dominated by turbiditic deposition (Adeogba *et al.*, 2005). Finally, Cartwright *et al.* (2003) discussed the prevalence and origin of normal faults that develop in dominantly fine-grained marine sediments in settings more distal to terrigenous sediment input, many examples of which include stratigraphic growth and, thus, are synsedimentary in nature. Even though submarine levees are inherently unstable, whether a generally similar style of synsedimentary normal faulting occurs in these deposits has not been established.

The only previous study of ECB, carried out by Schultz and Hubbard (2005), was limited to the uppermost section at ECB-C and the fault that cuts it (what is here defined as sandstone-prone interval V and primary normal fault CF3; **Figure 3.5**). Based on a qualitative analysis they interpreted this and underlying faults as growth faults, with CF3 as an antithetic growth fault associated with a master synthetic growth fault in ECB-N. However, Shultz and Hubbard (2005) viewed SPI-V as part of the southward prograding slope system typically associated with the Tres Pasos Formation whereas we emphasize that synsedimentary normal faulting occurred during the early phase of the ECB succession (SPI-II; **Figure 3.13**) as well as during SPI-V, from ~83-80 Ma, a time period that mostly predates the onset of the genetic Tres Pasos Formation as established by Daniels *et al.* (2018). Furthermore, our quantitative measurements of the orientation of the normal faults reveal a more complex fault geometry than previously appreciated. Whereas primary normal faults at ECB-N consistently dip to the SE, primary normal faults at ECB-C and ECB-S dip to the NE (**Figure 3.12A**). We suggest that both sets of faults are in fact part of an arcuate syndepositional fault system that displaced entire sections of the levee to the east (*i.e.*, orthogonal to

oblique to the axial submarine channel system). The accommodation generated by these syndepositional faults would in turn redirect paleoflow direction of overspilled turbidity currents and control the deposition of sandstone (*i.e.*, sandstone-prone intervals at ECB) (**Figure 3.14**).

We consider two general types of controls on the long-lived synsedimentary normal faulting at ECB. First, as has been shown in other types of slope systems, the construction of a slope of ~1-5˚ via sediment transport and deposition, regardless of tectonic setting can lead to gravitational processes working to reduce the slope in the form of mass wasting and normal faults (with the hangingwall in the downslope position) (Damuth, 1994). The relief of the fault scarp, however subtle, combined with gradient changes from footwall to hangingwall can initiate a feedback where relatively more sediment deposition on the hangingwall generates additional slip, which creates more accommodation, and so on. We also note the presence of MTDs, although rare in the ~500 m thick ECB succession, which suggests that the updip levee slope was sufficiently steep at times to lead to slope failure and mass wasting. Thus, in this case, the synsedimentary faulting is controlled by the evolution of the levee slope system itself. The fault orientations and interpreted fault geometries, and their relationship to the paleoflow (**Figure 3.14**), lend further support to this hypothesis.

The second category of controls on synsedimentary normal faulting at ECB emphasizes tectonic processes. The Magallanes-Austral Basin is a retroarc foreland basin and, thus, dynamically linked to a propagating fold-thrust belt. Seismic-reflection profiles acquired by Empresa Nacional del Petroleo (ENAP) in the mid-eighties across Sierra del Toro and Cerro Cazador (**Figure 3.1**) revealed a thick-skinned tectonic system responsible for enhancing uplift of thin-skinned blind thrusts and associated propagation folds in the frontal region of the Magallanes fold-thrust belt (Harambour, 2002; Ghiglione *et al.*, 2009). Furthermore, Fosdick *et al.* (2011), using new geological mapping, seismic-reflection data and zircon geochronology, reconstructed the kinematic evolution of the fold-thrust belt, suggesting that at least half of the crustal shortening was synchronous with Late Cretaceous foreland sedimentation. More recently, VanderLeest *et al.* (in press) used a subsidence analysis approach to show that uplift occurred in the foredeep itself in this region during the time period of ~85-78 Ma. Broad uplift of the depositional basin could have led to a regionally localized extensional stress regime expressed as normal faulting. Finally, we note the possibility of a combination of these controlling factors. For example, the magnitude and/or timing of synsedimentary faulting at ECB could have been influenced by minor tilting of the entire

eastern flank of the Cerro Toro channel-levee system via foredeep uplift such that the inherent, levee-slope conditions that promote faulting were amplified.

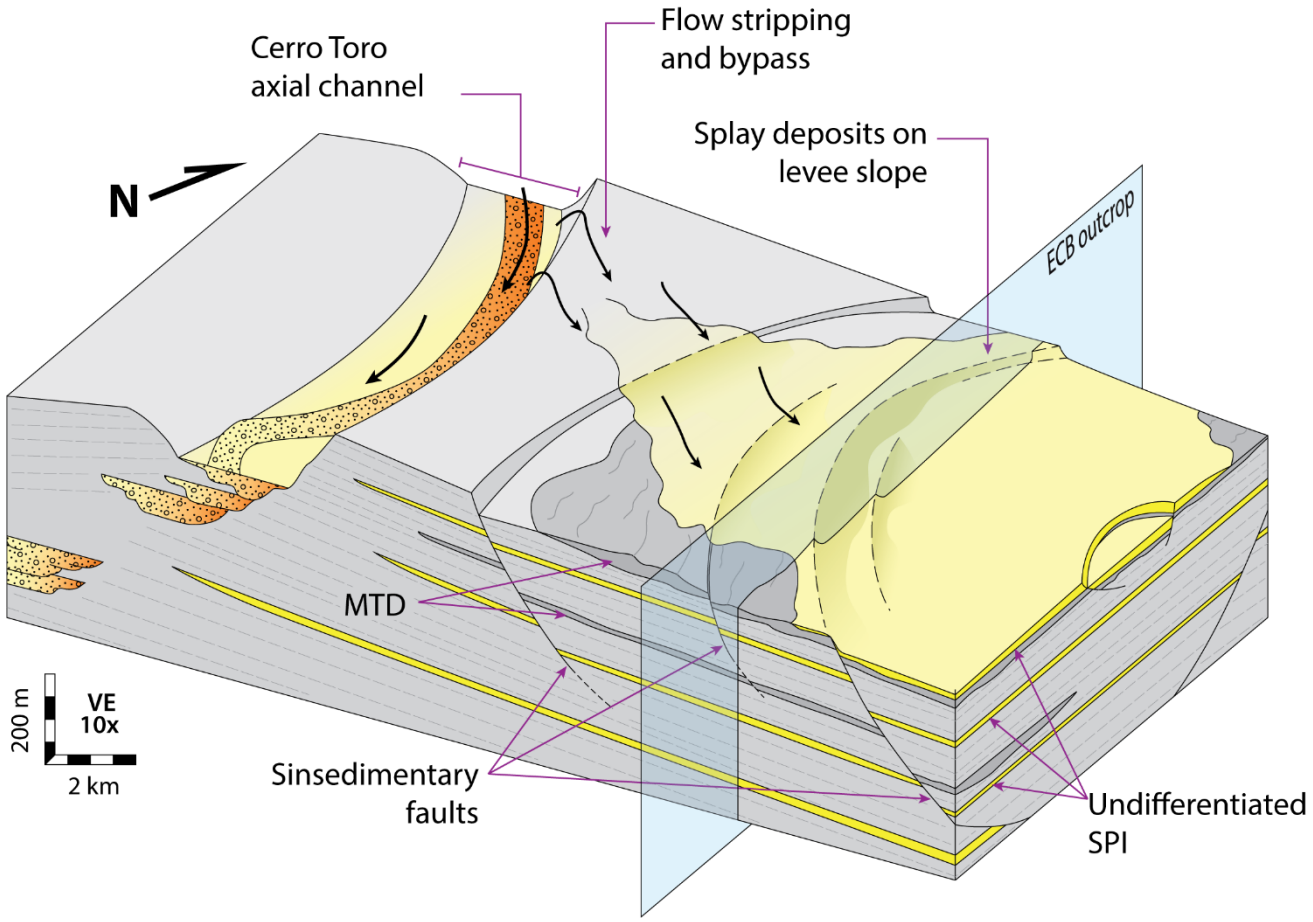

Figure 3.14: Schematic block diagram showing interpreted depositional and structural setting of ECB outcrop in context of generally age-equivalent Cerro Toro Formation channel belt deposits ~8.7 km to the west.

3.8 | CONCLUSIONS

The deep-water sedimentary succession exposed at El Chingue Bluff (ECB) features more than 500 m of stratigraphy deposited in an external levee associated with the Upper Cretaceous axial channel-belt of the Cerro Toro Formation in the Magallanes-Austral foreland basin. Detailed qualitative and quantitative analysis of the apparently uniform, fine-grained and thin-bedded succession shows the occurrence of at least three thin (~5 m) MTD horizons and five sandstone-prone intervals (10-36 m thick) defined by an increase in sandstone content in comparison to underlying and overlying strata. The entire succession is crosscut by a series of large normal faults that systematically change their dip direction from north to south and displace entire segments of the outcrop, making correlation challenging at a bed-by-bed scale. Based on field observations including fault orientation, changes in bed thickness across faults,

decreasing offset upwards and sometimes healing, and a potential relationship to paleoflow orientation, we interpret these faults to have occurred during deposition on the levee. A broad network of fine- to medium-grained, vertical to subvertical clastic intrusions, unaffected by faulting, is present within the upper half of the outcrop and is suggested to share a potential geometric relationship with faults and to further support their syndepositional nature.

The only previous study at ECB, carried out by Schultz and Hubbard (2005) also interpreted the major faults as growth faults, however, they viewed the uppermost sandstone package (SPI-V) as part of the southward prograding slope system typically associated with the Tres Pasos Formation whereas we emphasize that synsedimentary normal faulting occurred during the early phase of the ECB succession as well as during SPI-V within a deep-water levee-slope setting. Potential mechanisms for the development of normal faulting include autogenic instability during the buildup of the levee slope, tectonic forcing through the propagation of the Magallanes fold-thrust belt, or a combination of both. Our interpretation of the ECB succession as recording levee evolution provides an opportunity to consider levee slopes associated with submarine channel systems as a type of depositional slope system by themselves, that might share deformational mechanisms with other depositional slopes, to reassess the complex interaction and interdependence between sedimentation and deformation, and the influence that the latter can have on interpretations based on data collected through sampling in equivalent sedimentary successions.

REFERENCES

Adeogba, A.A., McHargue, T.R., Graham, S.A., 2005. Transient fan architecture and depositional controls from near-surface 3-D seismic data, Niger Delta continental slope. Am. Assoc. Pet. Geol. Bull. 89, 627–643. https://doi.org/10.1306/11200404025

Allmendinger, R.W., Cardozo, N., Fisher, D.M., 2011. Structural Geology Algorithms : Vectors and Tensors Fundamentals of Numerical Weather Prediction Environmental Hazards and Disasters : Contexts , Perspectives and Management, Cambridge University Press.

Armitage, D.A., Romans, B.W., Covault, J.A., Graham, S.A., 2009. The Influence of Mass-Transport-Deposit Surface Topography on the Evolution of Turbidite Architecture: The Sierra Contreras, Tres Pasos Formation (Cretaceous), Southern Chile. J. Sediment. Res. 79, 287–301. https://doi.org/10.2110/jsr.2009.035

Auchter, N.C., Romans, B.W., Hubbard, S.M., 2016. Influence of deposit architecture on intrastratal deformation, slope deposits of the Tres Pasos Formation, Chile. Sediment. Geol. 341, 13–26. https://doi.org/10.1016/j.sedgeo.2016.05.005

Baas, J.H., Best, J.L., Peakall, J., 2016. Predicting bedforms and primary current stratification in cohesive mixtures of mud and sand. J. Geol. Soc. London. https://doi.org/10.1144/jgs2015-024

Baas, J.H., Best, J.L., Peakall, J., 2011. Depositional processes, bedform development and hybrid bed formation in rapidly decelerated cohesive (mud-sand) sediment flows. Sedimentology 58, 1953–1987. https://doi.org/10.1111/j.1365-3091.2011.01247.x

Baas, J.H., Best, J.L., Peakall, J., Wang, M., 2009. A phase diagram for turbulent, transitional, and laminar clay suspension flows. J. Sediment. Res. 79, 162–183. https://doi.org/10.2110/jsr.2009.025

Babonneau, N., Savoye, B., Cremer, M., Klein, B., 2002. Morphology and architecture of the present canyon and channel system of the Zaire deep-sea fan. Mar. Pet. Geol. 19, 445–467. https://doi.org/10.1016/S0264-8172(02)00009-0

Bain, H.A., Hubbard, S.M., 2016. Stratigraphic evolution of a long-lived submarine channel system in the Late Cretaceous Nanaimo Group, British Columbia, Canada. Sediment. Geol. 337, 113–132. https://doi.org/10.1016/j.sedgeo.2016.03.010

Barton, M.D., Steffens, G.S., And O'byrne, C.J., 2007, Facies architecture of a submarine-slope channel complex, Condor West channel, Cerro Toro Formation, Chile, in Nilsen, T., Shew, R., Steffens, G., and Studlick, J., eds., Atlas of Deep-Water Outcrops, American Association of Petroleum Geologists, Studies in Geology 56, p. 149–153.

Bauer, D.B., Hubbard, S.M., Covault, J.A., Romans, B.W., 2020. Inherited Depositional Topography Control on Shelf-Margin Oversteepening, Readjustment, and Coarse-Grained Sediment Delivery to Deep Water, Magallanes Basin, Chile. Front. Earth Sci. 7. https://doi.org/10.3389/feart.2019.00358

Bernhardt, A., Jobe, Z.R., Grove, M., Lowe, D.R., 2012. Palaeogeography and diachronous infill of an ancient deep-marine foreland basin, Upper Cretaceous Cerro Toro Formation, Magallanes Basin. Basin Res. 24, 269–294. https://doi.org/10.1111/j.1365-2117.2011.00528.x

Bernhardt, A., Jobe, Z.R., Lowe, D.R., 2011. Stratigraphic evolution of a submarine channel–lobe complex system in a narrow fairway within the Magallanes foreland basin, Cerro Toro Formation, southern Chile. Mar. Pet.

Geol. 28, 785–806. https://doi.org/10.1016/j.marpetgeo.2010.05.013

Bhattacharya, J.P., Davies, R.K., 2001. Growth faults at the prodelta to delta-front transition, Cretaceous Ferron sandstone, Utah. Mar. Pet. Geol. 18, 525–534. https://doi.org/10.1016/S0264-8172(01)00015-0

Biddle, K.T., Uliana, M.A., Mitchum, R.M., Fitzgerald, M.G., Wright, R.C., 1986. The stratigraphic and structural evolution of the central and eastern Magallanes Basin, southern South America. Forel. basins 41–61. https://doi.org/10.1002/9781444303810.ch2

Blum, M., Rogers, K., Gleason, J., Najman, Y., Cruz, J., Fox, L., 2018. Allogenic and Autogenic Signals in the Stratigraphic Record of the Deep-Sea Bengal Fan. Sci. Rep. 8. https://doi.org/10.1038/s41598-018-25819-5

Bouroullec, R., Cartwright, J.A., Johnson, H.D., Lansigu, C., Quémener, J.M., Savanier, D., 2004. Syndepositional faulting in the Grès d'Annot Formation, SE France: High-resolution kinematic analysis and stratigraphic response to growth faulting. Geol. Soc. Spec. Publ. 221, 241–265. https://doi.org/10.1144/GSL.SP.2004.221.01.13

Brunt, R.L., Di Celma, C.N., Hodgson, D.M., Flint, S.S., Kavanagh, J.P., van der Merwe, W.C., 2013. Driving a channel through a levee when the levee is high: An outcrop example of submarine down-dip entrenchment. Mar. Pet. Geol. 41, 134–145. https://doi.org/10.1016/j.marpetgeo.2012.02.016

Calderón, M., Fosdick, J.C., Warren, C., Massonne, H.-J., Fanning, C.M., Fadel Cury, L., Schwanethal, J., Fonseca, P.E., Galaz, G., Gaytán, D., Hervé, F., 2012. The low-grade Canal de las Montañas Shear Zone and its role on the tectonic emplacement of the Sarmiento Ophiolitic Complex and Late Cretaceous Patagonian Andes orogeny, Chile. Tectonophysics 524–525, 165–185. https://doi.org/10.1016/j.tecto.2011.12.034

Campion, K.M., Dixon, B.T., Scott, E.D., 2011. Sediment waves and depositional implications for fine-grained rocks in the Cerro Toro Formation (upper Cretaceous), Silla Syncline, Chile. Mar. Pet. Geol. 28, 761–784. https://doi.org/10.1016/j.marpetgeo.2010.07.002

Cartwright, J., Bouroullec, R., James, D., Johnson, H., 1998. Polycyclic motion history of some Gulf Coast growth faults from high-resolution displacement analysis. Geology 26, 819–822. https://doi.org/10.1130/0091-7613(1998)026<0819:PMHOSG>2.3.CO;2

Cartwright, J., James, D., Bolton, A., 2003. The genesis of polygonal fault systems: A review. Geol. Soc. Spec. Publ. 216, 223–234. https://doi.org/10.1144/GSL.SP.2003.216.01.15

Cecioni, G.O., 1957. Cretaceous Flysch and Molasse in Departamento Ultima Esperanza, Magallanes Province, Chile. Am. Assoc. Pet. Geol. Bull. 41, 538–564. https://doi.org/10.1306/0BDA5837-16BD-11D7-8645000102C1865D

Clark, J.D., Pickering, K.T., 1996. Architectural elements and growth patterns of submarine channels: Application to hydrocarbon exploration. Am. Assoc. Pet. Geol. Bull. 80, 194–221. https://doi.org/10.1306/64ed878c-1724-11d7-8645000102c1865d

Cobain, S.L., Peakall, J., Hodgson, D.M., 2015. Indicators of propagation direction and relative depth in clastic injectites: Implications for laminar versus turbulent flow processes. Bull. Geol. Soc. Am. 127, 1816–1830. https://doi.org/10.1130/B31209.1

Coleman, J.L., 2000. Reassessment of the Cerro Toro (Chile) Sandstones in View of Channel-Levee-Overbank Reservoir Continuity Issues. Deep. Reserv. World 20th Annu. 252–262.

https://doi.org/10.5724/gcs.00.15.0252

Covault, J.A., Romans, B.W., Graham, S.A., 2009. Outcrop expression of a continental-margin-scale shelf-edge delta from the cretaceous magallanes basin, chile. J. Sediment. Res. 79, 523–539. https://doi.org/10.2110/jsr.2009.053

Crane, W.H., Lowe, D.R., 2008. Architecture and evolution of the Paine channel complex, Cerro Toro Formation (Upper Cretaceous), Silla Syncline, Magallanes Basin, Chile. Sedimentology 55, 979–1009. https://doi.org/10.1111/j.1365-3091.2007.00933.x

Cronin, B.T., Hurst, A., Celik, H., Türkmen, I., 2000. Superb exposure of a channel, levee and overbank complex in an ancient deep-water slope environment. Sediment. Geol. 132, 205–216. https://doi.org/10.1016/S0037-0738(00)00008-7

Dalziel, I., 1981. Back-arc extension in the southern Andes: a review and critical reappraisal. Philos. Trans. R. Soc. London. Ser. A, Math. Phys. Sci. 300, 319–335. https://doi.org/10.1098/rsta.1981.0067

Damuth, J.E., 1994. Neogene gravity tectonics and depositional processes on the deep Niger Delta continental margin. Mar. Pet. Geol. 11, 320–346. https://doi.org/10.1016/0264-8172(94)90053-1

Daniels, B.G., Auchter, N.C., Hubbard, S.M., Romans, B.W., Matthews, W.A., Stright, L., 2018. Timing of deep-water slope evolution constrained by large-n detrital and volcanic ash zircon geochronology, Cretaceous Magallanes Basin, Chile. GSA Bull. 130, 438–454. https://doi.org/10.1130/B31757.1

Deptuck, M.E., Steffens, G.S., Barton, M., Pirmez, C., 2003. Architecture and evolution of upper fan channel-belts on the Niger Delta slope and in the Arabian Sea. Mar. Pet. Geol. 20, 649–676. https://doi.org/10.1016/j.marpetgeo.2003.01.004

Deptuck, M.E., Sylvester, Z., 2018. Submarine Fans and their Channels, Levees, and Lobes. in: Micallef, A., *et al.*, Submarine Geomorphology. 13–25. https://doi.org/10.1007/978-3-319-57852-1

Di Celma, C.N., Brunt, R.L., Hodgson, D.M., Flint, S.S., Kavanagh, J.P., 2011. Spatial and temporal evolution of a permian submarine slope channel-levee system, Karoo Basin, South Africa. J. Sediment. Res. 81, 579–599. https://doi.org/10.2110/jsr.2011.49

Dott, R.H., Winn, R.D., Smith, C.H.L., 1982. Relationship of late Mesozoic and early Cenozoic sedimentation to the tectonic evolution of the southernmost Andes and Scotia Arc (South America, Antarctica). Antarct. Geosci. 3rd Symp. Antarct. Geol. Geophys. Madison, August 1977 193–202.

Edwards, D.A., Leeder, M.R., Best, J.L., Pantin, H.M., 1994. On experimental reflected density currents and the interpretation of certain turbidites. Sedimentology 41, 437–461. https://doi.org/10.1111/j.1365-3091.1994.tb02005.x

Elliott, R.E., 1965. A classification of subaqueous sedimentary structures based on rheological and kinematical parameters. Sedimentology 5, 193–209. https://doi.org/10.1111/J.1365-3091.1965.TB02112.X

Englert, R.G., Hubbard, S.M., Matthews, W.A., Coutts, D.S., Covault, J.A., 2020. The evolution of submarine slope-channel systems: Timing of incision, bypass, and aggradation in late cretaceous nanaimo group channel-system strata, British Columbia, Canada. Geosphere 16, 281–296. https://doi.org/10.1130/GES02091.1

Fogwill, C.J., Kubik, P.W., 2005. A glacial stage spanning the Antarctic Cold Reversal in Torres del Paine (51°S), Chile, based on preliminary cosmogenic exposure ages. Geogr. Ann. Ser. A Phys. Geogr. 87, 403–408. https://doi.org/10.1111/j.0435-3676.2005.00266.x

Fosdick, J.C., Grove, M., Graham, S.A., Hourigan, J.K., Lovera, O., Romans, B.W., 2015. Detrital thermochronologic record of burial heating and sediment recycling in the Magallanes foreland basin, Patagonian Andes. Basin Res. https://doi.org/10.1111/bre.12088

Fosdick, J.C., Romans, B.W., Fildani, A., Bernhardt, A., Calderón, M., Graham, S.A., 2011. Kinematic evolution of the Patagonian retroarc fold-and-thrust belt and Magallanes foreland basin, Chile and Argentina, 51°30's. Bull. Geol. Soc. Am. 123, 1679–1698. https://doi.org/10.1130/B30242.1

France-Lanord, C., Spiess, V., Klaus, A., Adhikari, R.R., Adhikari, S.K., Bahk, J.-J., Baxter, A.T., Cruz, J.W., Das, S.K., Dekens, P., Duleba, W., Fox, L.R., Galy, A., Galy, V., Ge, J., Gleason, J.D., Gyawali, B.R., Huyghe, P., Jia, G., Lantzsch, H., Manoj, M.C., Martos Martin, Y., Meynadier, L., Najman, Y.M.R., Nakajima, A., Ponton, C., Reilly, B.T., Rogers, K.G., Savian, J.F., Schwenk, T., Selkin, P.A., Weber, M.E., Williams, T., Yoshida, K., 2016. Expedition 354 summary. https://doi.org/10.14379/iodp.proc.354.101.2016

Galloway, W., 1986. Growth Faults and Fault-Related Structures of Prograding Terrigenous Clastic Continental Margins: ABSTRACT. Am. Assoc. Pet. Geol. Bull. 70. https://doi.org/10.1306/94886b0a-1704-11d7-8645000102c1865d

García, J.L., Hall, B.L., Kaplan, M.R., Vega, R.M., Strelin, J.A., 2014. Glacial geomorphology of the Torres del Paine region (southern Patagonia): Implications for glaciation, deglaciation and paleolake history. Geomorphology 204, 599–616. https://doi.org/10.1016/j.geomorph.2013.08.036

García, J.L., Hein, A.S., Binnie, S.A., Gómez, G.A., González, M.A., Dunai, T.J., 2018. The MIS 3 maximum of the Torres del Paine and Última Esperanza ice lobes in Patagonia and the pacing of southern mountain glaciation. Quat. Sci. Rev. 185, 9–26. https://doi.org/10.1016/j.quascirev.2018.01.013

García, J.L., Strelin, J.A., Vega, R.M., Hall, B.L., Stern, C.R., 2015. Deglacial ice-marginal glaciolacustrine environments and structural moraine building in torres del paine, chilean southern patagonia. Andean Geol. 42, 190–212. https://doi.org/10.5027/andgeoV42n2-a03

George, S.W.M., Davis, S.N., Fernández, R.A., Manríquez, L.M.E., Leppe, M.A., Horton, B.K., Clarke, J.A., 2020. Chronology of deposition and unconformity development across the Cretaceous–Paleogene boundary, Magallanes-Austral Basin, Patagonian Andes. J. South Am. Earth Sci. 97, 102237. https://doi.org/10.1016/j.jsames.2019.102237

Ghiglione, M.C., Suarez, F., Ambrosio, A., Poian, G.D. a, Cristallini, E.O., Pizzio, M.F., Reinoso, R.M., Andina, L.D.T., Geológicas, C., Universitaria, C., Ii, P., Aires, B., 2009. Fold-Thrust Belt , Southern Patagonian Andes. Structure 65, 215–226.

Hansen, L., Callow, R., Kane, I., Kneller, B., 2017. Differentiating submarine channel-related thin-bedded turbidite facies: Outcrop examples from the Rosario Formation, Mexico. Sediment. Geol. 358, 19–34. https://doi.org/10.1016/j.sedgeo.2017.06.009

Hansen, L.A.S., Callow, R.H.T., Kane, I.A., Gamberi, F., Rovere, M., Cronin, B.T., Kneller, B.C., 2015. Genesis and character of thin-bedded turbidites associated with submarine channels. Mar. Pet. Geol. 67, 852–879. https://doi.org/10.1016/j.marpetgeo.2015.06.007

Harambour, S.M., 2002. Deep-seated thrusts in the frontal part of the Magallanes fold and thrust belt, Ultima Esperanza, Chile. 15th Congr. Geol. Argentino 232.

Hiscott, R.N., Hall, F.R., Pirmez, C., 1997. Turbidity-current overspill from the Amazon Channel: texture of the silt/sand load, paleoflow from anisotropy of magnetic susceptibility, and implications for flow processes, in: Proceedings of the Ocean Drilling Program, 155 Scientific Results. pp. 53–78. https://doi.org/10.2973/odp.proc.sr.155.202.1997

Hubbard, S.M., Fildani, A., Romans, B.W., Covault, J.A., McHargue, T.R., 2010. High-relief slope clinoform development: Insights from outcrop, magallanes Basin, Chile. J. Sediment. Res. 80, 357–375. https://doi.org/10.2110/jsr.2010.042

Hubbard, S.M., Romans, B.W., Graham, S.A., 2008. Deep-water foreland basin deposits of the Cerro Toro Formation, Magallanes basin, Chile: Architectural elements of a sinuous basin axial channel belt. Sedimentology 55, 1333–1359. https://doi.org/10.1111/j.1365-3091.2007.00948.x

Hurst, A., Cartwright, J., Duranti, D., 2003. Fluidization structures produced by upward injection of sand through a sealing lithology. Geol. Soc. Spec. Publ. 216, 123–137. https://doi.org/10.1144/GSL.SP.2003.216.01.09

Jobe, Z.R., Bernhardt, A., Lowe, D.R., 2010. Facies and architectural asymmetry in a conglomerate-rich submarine channel fill, cerro toro formation, Sierra Del Toro, Magallanes Basin, Chile. J. Sediment. Res. 80, 1085–1108. https://doi.org/10.2110/jsr.2010.092

Kane, I.A., 2010. Development and flow structures of sand injectites: The Hind Sandstone Member injectite complex, Carboniferous, UK. Mar. Pet. Geol. 27, 1200–1215. https://doi.org/10.1016/j.marpetgeo.2010.02.009

Kane, I.A., Hodgson, D.M., 2011. Sedimentological criteria to differentiate submarine channel levee subenvironments: Exhumed examples from the Rosario Fm. (Upper Cretaceous) of Baja California, Mexico, and the Fort Brown Fm. (Permian), Karoo Basin, S. Africa. Mar. Pet. Geol. 28, 807–823. https://doi.org/10.1016/j.marpetgeo.2010.05.009

Kane, I.A., Kneller, B.C., Dykstra, M., Kassem, A., McCaffrey, W.D., 2007. Anatomy of a submarine channel-levee: An example from Upper Cretaceous slope sediments, Rosario Formation, Baja California, Mexico. Mar. Pet. Geol. 24, 540–563. https://doi.org/10.1016/j.marpetgeo.2007.01.003

Kane, I.A., McCaffrey, W.D., Peakall, J., 2010. On the origin of paleocurrent complexity within deep marine channel levees. J. Sediment. Res. 80, 54–66. https://doi.org/10.2110/jsr.2010.003

Katz, H., 1963. Revision of Cretaceous Stratigraphy in Patagonian Cordillera of Ultima Esperanza, Magallanes Province, Chile. Am. Assoc. Pet. Geol. Bull. 47. https://doi.org/10.1306/bc743a5d-16be-11d7-8645000102c1865d

Kevin M. Scott (2), 1966. Sedimentology and Dispersal pattern of a Cretaceous Flysch Sequence, Patagonian Andes, Southern Chile. Am. Assoc. Pet. Geol. Bull. 50, 72–107. https://doi.org/10.1306/a663389e-16c0-11d7-8645000102c1865d

Khan, Z.A., Arnott, R.W.C., 2011. Stratal attributes and evolution of asymmetric inner- and outer-bend levee deposits associated with an ancient deep-water channel-levee complex within the Isaac Formation, southern Canada. Mar. Pet. Geol. 28, 824–842. https://doi.org/10.1016/j.marpetgeo.2010.07.009

Khani, H.F., Back, S., 2012. Temporal and lateral variation in the development of growth faults and growth strata in western Niger Delta, Nigeria. Am. Assoc. Pet. Geol. Bull. 96, 595–614. https://doi.org/10.1306/08291111023

Kohl, B., Williams, D.F., Ledbetter, M.T., Constans, R.E., King, J.W., Heusser, L.E., Schroeder, C., Morley, J.J., n.d. 30. SUMMARY OF CHRONOSTRATIGRAPHIC STUDIES, DEEP SEA DRILLING PROJECT LEG 96 1 Barry Kohl, Douglas F. Williams, Michael T. Ledbetter, Richard E. Constans, John W. King, Linda E. Heusser, Claudia Schroeder, and Joseph J. Morley 2 589–593.

Li, P., Kneller, B., Thompson, P., Bozetti, G., dos Santos, T., 2018. Architectural and facies organisation of slope channel fills: Upper Cretaceous Rosario Formation, Baja California, Mexico. Mar. Pet. Geol. 92, 632–649. https://doi.org/10.1016/j.marpetgeo.2017.11.026

Lin, C., Liu, J., Eriksson, K., Yang, H., Cai, Z., Li, H., Yang, Z., Rui, Z., 2014. Late Ordovician, deep-water gravity-flow deposits, palaeogeography and tectonic setting, Tarim Basin, Northwest China. Basin Res. 26, 297–319. https://doi.org/10.1111/bre.12028

Macauley, R. V., Hubbard, S.M., 2013. Slope channel sedimentary processes and stratigraphic stacking, Cretaceous Tres Pasos Formation slope system, Chilean Patagonia. Mar. Pet. Geol. 41, 146–162. https://doi.org/10.1016/j.marpetgeo.2012.02.004

Macellari, C.E., Barrio, C.A., Manassero, M.J., 1989. Upper cretaceous to paleocene depositional sequences and sandstone petrography of southwestern Patagonia (Argentina and Chile). J. South Am. Earth Sci. 2, 223–239. https://doi.org/10.1016/0895-9811(89)90031-X

Malkowski, M.A., Jobe, Z.R., Sharman, G.R., Graham, S.A., 2018. Down-slope facies variability within deep-water channel systems: Insights from the Upper Cretaceous Cerro Toro Formation, southern Patagonia. Sedimentology 65, 1918–1946. https://doi.org/10.1111/sed.12452

McArthur, A., Kane, I., Bozetti, G., Hansen, L., Kneller, B.C., 2020. Supercritical flows overspilling from bypass-dominated submarine channels and the development of overbank bedforms. Depos. Rec. 6, 21–40. https://doi.org/10.1002/dep2.78

McAtamney, J., Klepeis, K., Mehrtens, C., Thomson, S., Betka, P., Rojas, L., Snyder, S., 2011. Along-strike variability of back-arc basin collapse and the initiation of sedimentation in the Magallanes foreland basin, southernmost Andes (53-54.5°S). Tectonics 30, 1–27. https://doi.org/10.1029/2010TC002826

McHargue, T., Pyrcz, M.J., Sullivan, M.D., Clark, J.D., Fildani, A., Romans, B.W., Covault, J.A., Levy, M., Posamentier, H.W., Drinkwater, N.J., 2011. Architecture of turbidite channel systems on the continental slope: Patterns and predictions. Mar. Pet. Geol. 28, 728–743. https://doi.org/10.1016/j.marpetgeo.2010.07.008

Meyer, L., Ross, G.M., 2008. Channelized Lobe and Sheet Sandstones of the Upper Kaza Group Basin-floor Turbidite System, Castle Creek South, Windermere Supergroup, British Columbia, Canada. Atlas Deep. Outcrops.

Mutti, E., Normark, W.R., 1987. Comparing Examples of Modern and Ancient Turbidite Systems: Problems and Concepts. Mar. Clastic Sedimentol. 1–38. https://doi.org/10.1007/978-94-009-3241-8_1

Nakajima, T., Kneller, B.C., 2013. Quantitative analysis of the geometry of submarine external levées. Sedimentology 60, 877–910. https://doi.org/10.1111/j.1365-3091.2012.01366.x

Natland, M.L., Eduardo, G.P., Cañon, A., 1974. Introduction. Mem. Geol. Soc. Am. 139, 1–117. https://doi.org/10.1130/MEM139-p1

Normark, W., 1978. Fan Valleys, Channels, and Depositional Lobes on Modern Submarine Fans: Characters for Recognition of Sandy Turbidite Environments. Am. Assoc. Pet. Geol. Bull. 62, 912–931. https://doi.org/10.1306/c1ea4f72-16c9-11d7-8645000102c1865d

Normark, W.R., 1970. Channel piracy on Monterey Deep-Sea Fan. Deep. Res. Oceanogr. Abstr. 17, 837–846. https://doi.org/10.1016/0011-7471(70)90001-X

Normark, W.R., Carlson, P.R., 2003. Giant submarine canyons: Is size any clue to their importance in the rock record? LK - https://virginiatech.on.worldcat.org/oclc/108593371. Spec. Pap. / TA - TT - 175–190.

Normark, W.R., Posamentier, H., Mutti, E., 1993. Turbidite systems: State of the art and future directions. Rev. Geophys. https://doi.org/10.1029/93RG02832

Owen, G., Moretti, M., Alfaro, P., 2011. Recognising triggers for soft-sediment deformation: Current understanding and future directions. Sediment. Geol. 235, 133–140. https://doi.org/10.1016/J.SEDGEO.2010.12.010

Pankhurst, R.J., Riley, T.R., Fanning, C.M., Kelley, S.P., 2000. Episodic silicic volcanism in Patagonia and the Antarctic Peninsula: Chronology of magmatism associated with the break-up of Gondwana. J. Petrol. 41, 605–625. https://doi.org/10.1093/petrology/41.5.605

Petit, J., Beauchamp, J., 1986. Synsedimentary faulting and palaeocurrent patterns in the Triassic sandstones of the High Atlas (Morocco). Sedimentology 33, 817–829. https://doi.org/10.1111/j.1365-3091.1986.tb00984.x

Piper, D.J.W., Normark, W.R., 1983. Turbidite depositional patterns and flow characteristics, Navy Submarine Fan, California Borderland. Sedimentology 30, 681–694. https://doi.org/10.1111/j.1365-3091.1983.tb00702.x

Popescu, I., Lericolais, G., Panin, N., Wong, H.K., Droz, L., 2001. Late Quaternary channel avulsions on the Danube deep-sea fan, Black Sea. Mar. Geol. 179, 25–37. https://doi.org/10.1016/S0025-3227(01)00197-9

Posamentier, H.W., 2003. Depositional elements associated with a basin floor channel-levee system: Case study from the Gulf of Mexico. Mar. Pet. Geol. 20, 677–690. https://doi.org/10.1016/j.marpetgeo.2003.01.002

Prestholm, E., Walderhaug, O., 2000. Synsedimentary faulting in a Mesozoic deltaic sequence, Svalbard, Arctic Norway-fault geometries, faulting mechanisms, and sealing properties. Am. Assoc. Pet. Geol. Bull. 84, 505–522. https://doi.org/10.1306/c9ebce37-1735-11d7-8645000102c1865d

Rider, M.H., 1978. Growth faults in Carboniferous of western Ireland. AAPG Bull. (American Assoc. Pet. Geol. 62, 2191–2213. https://doi.org/10.1306/c1ea53be-16c9-11d7-8645000102c1865d

Ramos, V.A., Aguirre-Urreta, M.B., 1994. Cretaceous evolution of the Magallanes basin. In: Salfity, J.A. (Ed.), Cretaceous Tectonics of the Andes, Earth Evolution Sciences. Vieweg+Teubner Verlag, Wiesbaden, pp. 316–345. https://doi.org/10.1007/978-3-322-85472-8_7

Romans, B.W., Fildani, A., Graham, S.A., Hubbard, S.M., Covault, J.A., 2010. Importance of predecessor basin history on sedimentary fill of a retroarc foreland basin: provenance analysis of the Cretaceous Magallanes basin, Chile (50-52°S). Basin Res. 22, 640–658. https://doi.org/10.1111/j.1365-2117.2009.00443.x

Romans, B.W., Fildani, A., Hubbard, S.M., Covault, J.A., Fosdick, J.C., Graham, S.A., 2011. Evolution of deep-

water stratigraphic architecture, Magallanes Basin, Chile. Mar. Pet. Geol. 28, 612–628. https://doi.org/10.1016/j.marpetgeo.2010.05.002

Romans, B.W., Hubbard, S.M., Graham, S.A., 2009. Stratigraphic evolution of an outcropping continental slope system, Tres Pasos Formation at Cerro Divisadero, Chile. Sedimentology 56, 737–764. https://doi.org/10.1111/j.1365-3091.2008.00995.x

Rouby, D., Raillard, S., Guillocheau, F., Bouroullec, R., Nalpas, T., 2002. Kinematics of a growth fault/raft system on the West African margin using 3-D restoration. J. Struct. Geol. 24, 783–796. https://doi.org/10.1016/S0191-8141(01)00108-0

Schwartz, T.M., Fosdick, J.C., Graham, S.A., 2017. Using detrital zircon U-Pb ages to calculate Late Cretaceous sedimentation rates in the Magallanes-Austral basin, Patagonia. Basin Res. 29, 725–746. https://doi.org/10.1111/bre.12198

Scott, K.M., 1966. Sedimentology and Dispersal pattern of a Cretaceous Flysch Sequence, Patagonian Andes, Southern Chile. Am. Assoc. Pet. Geol. Bull. 50, 72–107. https://doi.org/10.1306/A663389E-16C0-11D7-8645000102C1865D

Shew, R.D., Tiller, G.M., Hackbarth, C.J., Rollins, D.R., White, C.D., 1995. Characterization and modeling of channel and thin-bedded turbidite prospects in the Gulf of Mexico: integration of outcrops, modern analogs, and subsurface data, in: Proceedings - SPE Annual Technical Conference and Exhibition. OnePetro, pp. 51–57. https://doi.org/10.2118/30535-ms

Shultz, M.R., Fildani, A., Cope, T.D., Graham, S.A., 2005. Deposition and stratigraphic architecture of an outcropping ancient slope system: Tres Pasos Formation, Magallanes Basin, southern Chile. Geol. Soc. London, Spec. Publ. 244, 27–50. https://doi.org/10.1144/GSL.SP.2005.244.01.03

Shultz, M.R., Hubbard, S.M., 2005. Sedimentology, Stratigraphic Architecture, and Ichnology of Gravity-Flow Deposits Partially Ponded in a Growth-Fault-Controlled Slope Minibasin, Tres Pasos Formation (Cretaceous), Southern Chile. J. Sediment. Res. 75, 440–453. https://doi.org/10.2110/jsr.2005.034

Slatt, R.M., Browne, G.H., Davis, R.J., Clemenceau, G.R., Colbert, J., Young, R.A., Anxionnaz, H., Spang, R.J., 1998. Outcrop-behind outcrop characterization of thin-bedded turbidites for improved understanding of analog reservoirs: New Zealand and Gulf of Mexico, in: Proceedings - SPE Annual Technical Conference and Exhibition. European Association of Geoscientists and Engineers, p. cp-100-00041. https://doi.org/10.2118/49563-ms

Smith, C., 1977. Sedimentology of the Late Cretaceous (Santonian–Maastrichtian) Tres Pasos Formation, Ultima Esperanza District, southern Chile. M.Sc Thesis, University of Wisconsin, Madison, WI, 129 p.

Sohn, Y.K., Choe, M.Y., Jo, H.R., 2002. Transition from debris flow to hyperconcentrated flow in a submarine channel (the Cretaceous cerro toro formation, southern Chile). Terra Nov. 14, 405–415. https://doi.org/10.1046/j.1365-3121.2002.00440.x

Stern, C.R., De Wit, M.J., 2004. Rocas Verdes ophiolites, southernmost South America: Remnants of progressive stages of development of oceanic-type crust in a continental margin back-arc basin. Geol. Soc. Spec. Publ. 218, 665–683. https://doi.org/10.1144/GSL.SP.2003.218.01.32

Stevenson, C.J., Jackson, C.A.L., Hodgson, D.M., Hubbard, S.M., Eggenhuisen, J.T., 2015. Deep-Water Sediment Bypass. J. Sediment. Res. 85, 1058–1081. https://doi.org/10.2110/jsr.2015.63

Stevenson, C.J., Peakall, J., Hodgson, D.M., Bell, D., Privat, A., 2020. TB OR NOT TB: BANDING in TURBIDITE SANDSTONES. J. Sediment. Res. 90, 821–842. https://doi.org/10.2110/JSR.2020.43

Stright, L., Jobe, Z., Fosdick, J.C., Bernhardt, A., 2017. Modeling uncertainty in the three-dimensional structural deformation and stratigraphic evolution from outcrop data: Implications for submarine channel knickpoint recognition. Mar. Pet. Geol. 86, 79–94. https://doi.org/10.1016/j.marpetgeo.2017.05.004

Talling, P.J., Masson, D.G., Sumner, E.J., Malgesini, G., 2012. Subaqueous sediment density flows: Depositional processes and deposit types. Sedimentology 59, 1937–2003. https://doi.org/10.1111/j.1365-3091.2012.01353.x

Tinterri, R., Muzzi Magalhaes, P., Tagliaferri, A., Cunha, R.S., 2016. Convolute laminations and load structures in turbidites as indicators of flow reflections and decelerations against bounding slopes. Examples from the Marnoso-arenacea Formation (northern Italy) and Annot Sandstones (south eastern France). Sediment. Geol. 344, 382–407. https://doi.org/10.1016/j.sedgeo.2016.01.023

Walker, R.G., 1975. Nested submarine-fan channels in the capistrano formation, San Clemente, California. Bull. Geol. Soc. Am. 86, 915–924. https://doi.org/10.1130/0016-7606(1975)86<915:NSCITC>2.0.CO;2

Wilson, T.J., 1991. Transition from back-arc to foreland basin development in the southernmost Andes: stratigraphic record from the Ultima Esperanza District, Chile. Geol. Soc. Am. Bull. 103, 98–111. https://doi.org/10.1130/0016-7606(1991)103<0098:TFBATF>2.3.CO;2

Winn, R.D., Dott, R.H., 1979. Deep-water fan-channel conglomerates of Late Cretaceous age, southern Chile. Sedimentology 26, 203–228. https://doi.org/10.1111/j.1365-3091.1979.tb00351.x

4 | DECIPHERING THE DEPOSITIONAL AGE OF COARSE-GRAINED DEEP-MARINE SEDIMENTATION IN A PREVIOUSLY UNDOCUMENTED LOCATION IN THE MAGALLANES FORELAND BASIN, SOUTHERN CHILE

Sebastian A. Kaempfe[1], Brian W. Romans[1], Stephen M. Hubbard[2] and Benjamin G. Daniels[3]

[1] Department of Geosciences, Virginia Tech, 926 West Campus Drive, Blacksburg, VA, 24061, USA

[2] Department of Geoscience, University of Calgary, 2500 University Drive NW, Calgary, AB, T2N1N4, Canada

[3] Department of Earth and Environmental Sciences, Mount Royal University, 4825 Mount Royal Gate SW, Calgary, AB, T3E 6K6, Canada.

ABSTRACT

Exposures of the Upper Cretaceous Magallanes-Austral Basin are part of a selected group of outcrops that are particularly useful as analogs for deep-marine sedimentary systems. As such, decades of sedimentologic and stratigraphic studies have resulted in a comprehensive characterization of the processes and depositional architecture associated with its evolution. Nonetheless, these studies have historically been focused in the Última Esperanza Province, with only a handful of studies carried out in isolated field sites south of the 51°30'S, in the Magallanes and Tierra del Fuego Provinces. The result is a disconnected chronostratigraphic framework between northern and southern exposures.

In this study we integrate nine new U-Pb zircon maximum depositional ages (MDA) into the Upper Cretaceous chronostratigraphic framework developed by Daniels *et al.* (2019), of which two come from an already constrained area at Cerro Jorge Montt and seven from three new locations south of the city of Puerto Natales (Cerro Aleta de Tiburón, Monte Rotunda and Cerro Pelario), thus, extend the chronostratigraphic framework another 55 km southward of previous studies. To calculate the MDAs we prioritized the weighted mean age of the youngest grain cluster (YGC) employing only grains ablated for 35s that overlap in age at 2σ to reduce the uncertainty and, for one sample, the youngest multiple ablated grain (YMAG) when the MDA uncertainties between both methods didn't overlap. Our results show that the Cerro Toro Formation equivalent succession at Cerro Aleta de Tiburón and Monte Rotunda span between 80.2±1.2 Ma and 78.7±1.1, whereas Dorotea Formation equivalent deposits exposed in Cerro Pelario range between 71.7±1.4 Ma and 66.0±1.13 Ma. We suggest that Cerro Toro Formation equivalent conglomeratic-rich deposits at this location are unlikely to represent the southward extension of the deep-marine axial-channel belt described in northern locations, and therefore they would potentially represent their own sediment routing system emanating from erosional catchments in the fold-thrust belt to the west.

In addition, our maximum depositional ages from the overlying Dorotea Formation show that these shallow-marine units are generally coeval to similar deposits to the north..

Keywords: Magallanes Basin, Cerro Toro Formation, axial channel-belt, detrital zircon geochronology, Monte Rotunda

4.1 | INTRODUCTION

Decades of extensive sedimentologic and stratigraphic studies on the superbly exposed Upper Cretaceous deposits of the Magallanes-Austral Basin (MAB) in the Ultima Esperanza Province (southern Chile) have resulted in a comprehensive understanding of the evolution of the sedimentary successions that comprise it (**Figure 4.1**) (Katz, 1963; Scott, 1966; Dalziel *et al.*, 1974; Natland *et al.*, 1975; Biddle *et al.*, 1986; Wilson, 1991; Shultz *et al.*, 2005; Fildani and Hessler, 2005; Romans *et al.*, 2011; Macauley and Hubbard, 2013; Bauer *et al.*, 2020). However, the temporal and large-scale spatial relationships of these units were not well understood until geochronological techniques developed in the past several years were applied, revealing aspects about timing and correlation previously unknown (Bernhardt *et al.*, 2011; Daniels *et al.*, 2018, 2019; Malkowski *et al.*, 2017a; 2018).

In contrast, a significantly lower number of studies have taken place south of Puerto Natales (in the Magallanes and Tierra del Fuego Provinces, between 52° and 55°S). The result is an overall disconnected stratigraphic framework where potential correlations between sedimentary successions in the Última Esperanza Province and southern field sites are hindered or made without geochronologic constraints in intermediate locations (Charrier and Lahsen, 1969; McAtamney *et al.*. 2011; Rivera *et al.*, 2020). A first step to address this uncertainty is to fill the geochronologic gap between outcrops. Here, we present new detrital zircon MDAs for two samples at an already constrained location and seven samples from three locations south of the city of Puerto Natales, which extend the chronostratigraphic framework of the Upper Cretaceous strata southward, thus reducing the gap between the Ultima Esperanza and the Magallanes Province. This study builds upon the Upper Cretaceous chronostratigraphic framework developed by Daniels *et al.* (2019) and adds geochronologic constraint to this area for the first time, setting up the framework for future studies. Additionally, it aims to address paleogeographic questions that have remained unanswered for many years: Are the prominent conglomeratic units exposed on Monte Rotunda correlative to the well-studied Cerro Toro Formation to the north? What does the temporal relationship of

these units indicate about basin-scale paleogeography and depositional system development in response to Andean tectonic evolution?

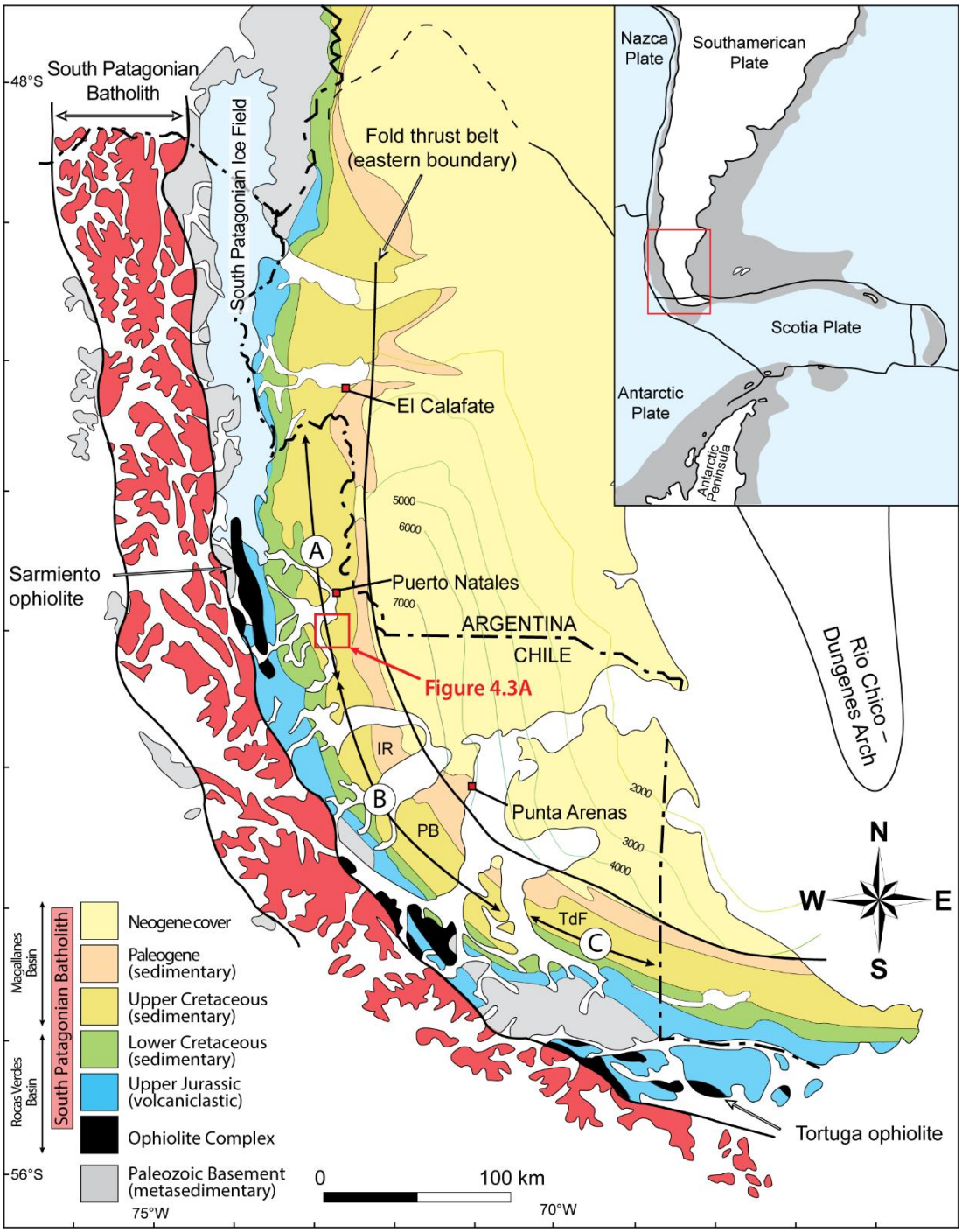

Figure 4.1: Geologic map of modern Patagonian fold-thrust belt and Magallanes-Austral foreland basin (based on Wilson *et al.*, 1991; modified from Romans *et al.*, 2010; Malkowski *et al.*, 2017b). Geopolitical administration: **(A)** Última Esperanza Province, **(B)** Magallanes Province and **(C)** Tierra del Fuego Province. Geographic locations: IR – Isla Riesco; PB – Peninsula de Brunswick; TdF – Tierra del Fuego.

4.2 | GEOLOGIC SETTING AND LOCATION

Mesozoic sedimentation in southern Patagonia is a twofold history that involves an early backarc-rift basin, the Rocas Verdes Basin (RVB) and a successor retroarc foreland basin, the Magallanes-Austral Basin (MAB) (Dalziel *et al.*, 1974; Wilson, 1991; Malkowski *et al.*, 2017a). The RVB records the extension associated with the breakup of Gondwana during the Mid-Late Jurassic to Early Cretaceous through bimodal volcanism represented by the extensive subaerial and marine silicic rift-related volcanism of the Tobifera, El Quemado and Ibañez Formations across Patagonia and ophiolitic outcrops of the Sarmiento and Tortuga Complexes in the Ultima Esperanza and Tierra del Fuego Provinces (Bruhn *et al.*, 1978; Wilson, 1991; Feraud *et al.*, 1999; Pankhurst *et al.*, 2000; Fildani and Hessler, 2005; Calderón *et al.*, 2007). Shallow to deeper marine conditions in this basin are represented by the quartz-rich sandstones of the Springhill Formation and black shales of the Zapata Formation (Cecioni, 1955; Katz, 1963; Fildani and Hessler, 2005).

In the Early Cretaceous, an increase in the spreading rate of the proto–Atlantic Ocean and subduction initiation along the Pacific margin initiated the closure of the RVB, and following transition to a compressional setting, resulted in the inception of the Andean orogeny and the development of a linked fold-thrust belt and foreland basin during the Turonian (Wilson, 1991; Fildani *et al.*, 2003; Romans *et al.*, 2010; Mpodozis *et al.*, 2011; Calderón *et al.*, 2012; Fosdick *et al.*, 2015).

The onset of deep-water sedimentation in the MAB is defined by laterally extensive tabular sand-rich turbidites of the Punta Barrosa Formation (~100-90 Ma; <1000 m), deposited in unconfined to weakly confined submarine fan systems (Fildani *et al.*, 2003; Romans *et al.*, 2011, Daniels *et al.*, 2019). Ongoing convergence and subsidence resulted in the transition to the fine-grained deposits of the Cerro Toro Formation (~90-80 Ma; ~2000 m), which in its upper section is characterized by a 100s m thick conglomeratic-rich interval, informally called the “Lago Sofia Member”, interpreted to be part of an axial channel-belt system (Katz, 1963; Winn and Dott; 1979; Hubbard *et al.*, 2008; Romans *et al.*, 2011; Bernhardt *et al.*, 2012; Malkowski *et al.*, 2018). As basin subsidence diminished, accommodation was eventually outpaced by sediment deposition, beginning the filling stage of the deep-marine phase of the MAB, recorded by the Tres Pasos (~81-72 Ma; 1200 – 1500 m) and the shallow-water Dorotea Formations (~73-63 Ma; ~1250 m thick) (Katz, 1963; Natland *et al.*, 1974; Smith, 1977; Romans *et al.*, 2010; Hubbard *et al.*, 2010; Daniels *et al.*, 2018, 2019; George *et al.*, 2020) (**Figures 4.2A**).

4.2.2 | Cerro Toro Formation

In the Última Esperanza Province, the Cerro Toro Formation comprises a >2,000 m thick succession of rhythmic alternation of mudstone and very fine-grained, thin-bedded sandstone that includes 100s of meters of thick conglomeratic-rich intervals in its upper section (Cecioni, 1957; Katz, 1963; Scott, 1966; Winn and Dott, 1979). The well-documented conglomeratic strata, mapped for more than 100 km along a north-south belt from Laguna Tres de Abril (Argentina), Laguna Azul, Sierra del Toro and Cordillera Manuel Señoret to the south, have been attributed to a 400 to 1,000 m thick, 4 to 8 km wide, low-sinuosity, axial channel-belt fed from the north and composed of at least three channel complexes in Sierra del Toro that occupied the foredeep of the Late Cretaceous MAB (Barton *et al.*, 2007; Hubbard *et al.*, 2007; 2008; Jobe *et al.*, 2010; Romans *et al.*, 2011; Malkowski *et al.*, 2018) (**Figure 4.2B**). Westward exposures of conglomeratic facies at La Silla Syncline in the Torres del Paine National Park and Cerro Ballena have been interpreted to represent tributary channel complexes systems in part coeval to the main channel-belt (Coleman, 2000; Sohn *et al.*, 2002; Crane and Lowe, 2008; Campion *et al.*, 2011; Bernhardt *et al.*, 2011, 2012). Whereas its relationship to southern outcrops with equivalent lithofacies at Monte Rotunda (Southern Ultima Esperanza) and as far south as Isla Riesco and Tierra del Fuego under the names of Escarpada and Cerro Matrero formations (Magallanes and Tierra del Fuego Provinces) remain poorly understood (Katz, 1963; Dott *et al.*, 1982; McAtamney *et al.*, 2011).

4.2.3 | Tres Pasos Formation

The lithostratigraphic transition to the Tres Pasos Formation is defined by the first significant sandstone succession overlying fine-grained deposits of the Cerro Toro Formation (Katz, 1963; Smith, 1977; Macellari *et al.*, 1989; Shultz *et al.*, 2005; Covault *et al.*, 2009; Romans *et al.*, 2009). Similarly, the Tres Pasos Formation is exposed for >100 km along a north-south, east-dipping monocline that crops out intermittently from the town of El Calafate (Argentina) to the North, to the town of Puerto Natales (Chile) to the South. A series of resistant ridges of turbiditic sandstones or conglomeratic sandstone interpreted as submarine channels record the axial filling of the Magallanes-Austral Basin through high-relief southward prograding clinoforms with paleo-bathymetric reliefs as much as >1,000 m in paleo-water depths that reach >1500 m during the early fill of the basin (Natland, *et al.*, 1974; Covault *et al.*, 2009; Romans *et al.*, 2009; Hubbard *et al.*, 2010; Macauley and Hubbard, 2013; Bauer *et al.*, 2020). The onset of the slope system is characterized by massive (up to 800 m thick) chaotically bedded siltstone-prone

deposits containing onlapping sandstone-prone deposits interpreted as amalgamated mass-transport deposits (Armitage *et al.*, 2009; Auchter *et al.*, 2016; Daniels *et al.*, 2018; Romans *et al.*, 2009; Shultz *et al.*, 2005; Shultz and Hubbard, 2005) (**Figure 4.2C**). In the southern portion of the Última Esperanza Province the slope channel system is glacially eroded and hasn't been documented. In the Magallanes Province, an apparently coeval succession of glauconitic sandstones and siltstones of the Fuentes Formation have been interpreted as a shallow shelf environment affected by storms (Charrier and Lahsen, 1969; Covacevich, 1991; Castelli *et al.*, 1992); however, its chronostratigraphic relationship with the Última Esperanza successions hasn't been established.

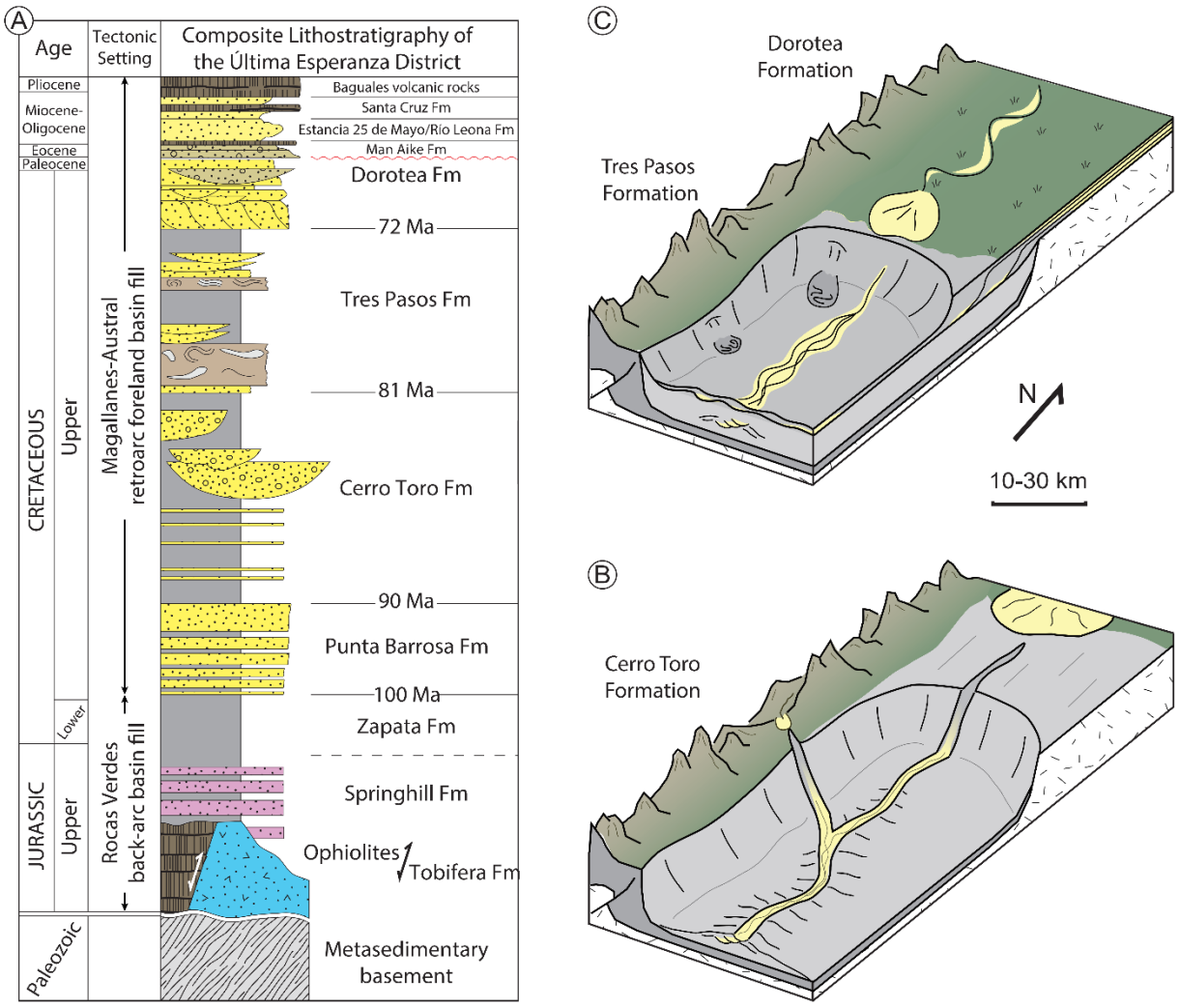

Figure 4.2: Lithostratigraphic context. **(A)** Generalized lithostratigraphic column for the Magallanes-Austral Basin in the Última Esperanza Province (modified from Wilson, 1991; Fildani *et al.*, 2003; Fosdick *et al.*, 2011; Schwartz *et al.*, 2017; George *et al.*, 2020). Age control from Daniels *et al.* (2019). **(B)** Schematic block diagram of the Cerro Toro Formation depicting a submarine tributary and axial channel belt flanked by levees. **(C)** Schematic block

diagram of the Tres Pasos (slope) and Dorotea (deltaic/shelfal) Formations. Part B and C modified from Romans *et al.* (2011).

4.2.4 | Dorotea Formation

Genetically linked to the Tres Pasos Formation as a shelf-slope system is the Upper Cretaceous – Danian Dorotea Formation (Katz, 1963; Macellari *et al.*, 1989; Shultz *et al.*, 2005; Covault *et al.*, 2009). The up to a ~1000 m thick Dorotea Formation records the transition from outer shelf shallow-marine to continental fluvial environments as sediment supply from nearby hinterland source areas overcomes basin accommodation and is interpreted to constitute the initiation point for sediment gravity flows deposited in the Tres Pasos slope system (Macellari *et al.*, 1989; Covault *et al.*, 2009; Hubbard *et al.*, 2010; Schwartz *et al.*, 2015; Bauer *et al.*, 2020). Like the underlying units, the Dorotea Formation also shows an overall diachronous evolution southward (Schwartz *et al.*, 2015; Daniels *et al.*, 2019; George *et al.*, 2020); which has been broadly used to reproduce a sequential stratigraphy model to explain internal environmental variations (Manríquez *et al.*, 2019; Rivera *et al.*, 2020). In the Magallanes Province, time equivalent deposits are attributed to the Rocallosa Formation (Charrier and Lahsen, 1969), nevertheless, a lack in chronostratigraphic constraints hinders its relationship with deposits in the Ultima Esperanza Province (**Figure 4.2C**).

4.3 | LOCATION

4.3.1 | Lago Aníbal Pinto transect

The Lago Aníbal Pinto transect is located near the southern end of the Última Esperanza Province (southern Chile). It encompasses the outcrops located between the Hollemberg River (51°54'24.81"S / 72°27'8.27"W) and the southern end of Monte Pelario (52°8'29.28"S / 72°23'2.81"W) (**Figure 4.3A**). Due to Pleistocene glaciations (Sagredo *et al.*, 2011; Solari *et al.*, 2012; Davies *et al.*, 2020), most of the area was affected by extensive erosion, leaving a 10 km wide NS valley with the Aníbal Pinto lake at its center and a widespread fluvioglacial sedimentary cover. Outcrops within this transect are restricted to coastal exposures where wave action have washed away some of the fluvioglacial cover and to the erosion-resistant topographic heights that make up the margins of this valley: Cerro Heede (referred as Aleta de Tiburón by the locals and in this study) and Monte Rotunda-Cerro Palladium to the west and Cerro Pelario to the east. The samples on which this study is focused were collected from these mountains (**Figures 4.3A**).

The ~950 m high Monte Rotunda (52°0'6.40"S / 72°37'4.84"W) is easily seen from the town of Puerto Natales (~25 km north) on a clear day and constitutes the most prominent topographic feature of this transect. Its shape is the result of a NS trending syncline formed by at least 8, up to ~100 m thick, conglomeratic levels that crop out in between forest covered intervals. Preliminary estimations suggest that the sedimentary succession exposed at this location might be at least 700 m thick (**Figure 4.3C**). The coarse-grained nature of these deposits has led previous authors to consider it the southward extension of the Sofia Member axial channel-belt of Upper Cretaceous the Cerro Toro Formation (Hubbard *et al.*, 2008; Jobe *et al.*, 2010; Bernhardt *et al.*, 2012; Malkowski *et al.*, 2018).

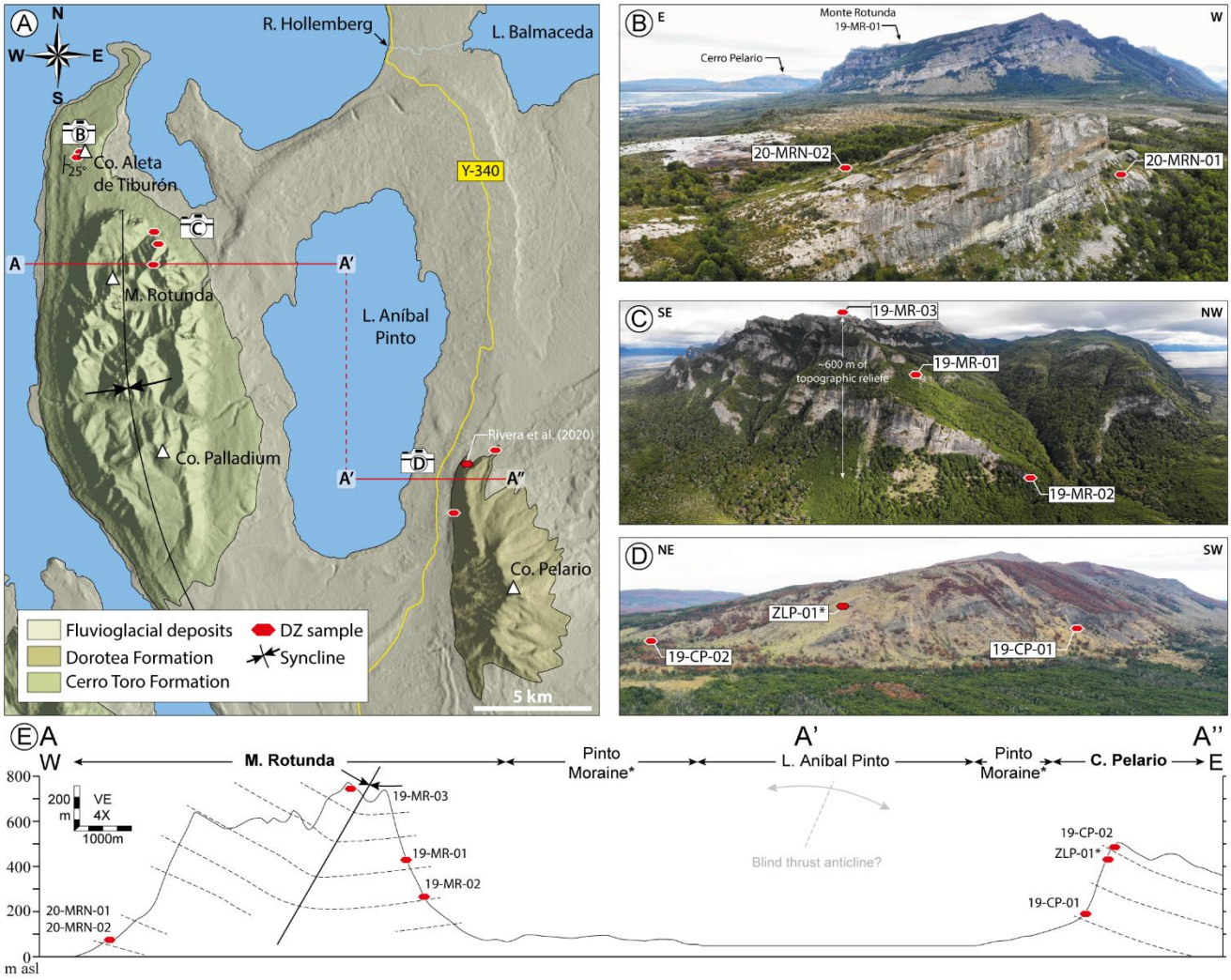

Figure 4.3: Lago Aníbal Pinto transect. **(A)** Geologic map elaborated from field observations with the general location of the samples. **(B)** Location of the samples at Cerro Aleta de Tiburon. (C) Location of the samples at Monte Rotunda. **(D)** Location of the samples at Cerro Pelario (*sample from Rivera *et al.*, 2020). **(E)** Structural cross-section depicting the general location of the samples in their stratigraphic context and the interpreted fold geometry.

Approximately 2 km north of Monte Rotunda, a comparatively small promontory crops out in between the forest, Cerro Aleta de Tiburón (51°57'4.37"S / 72°38'14.17"W; 204 m a.s.l.) (**Figure 4.3B**). The east-dipping, ~30-40 m thick outcropping sedimentary succession consists mainly of conglomeratic-rich strata with tabular fine-grained sandstones at its base. Structurally, this outcrop is associated with the west flank of the Rotunda Syncline and is slightly equivalent to the stratigraphically lowest portion of this succession.

On the other side of the glacial valley, towards the southern end of Aníbal Pinto lake, is Cerro Pelario (52°6'42.63"S / 72°22'4.07"W; ~1,100 m a.s.l.) (**Figure 4.3D**). This NS oriented mountain constitutes an east-dipping monocline that roughly represents 250 to 300 m of sandstone-dominated stratigraphy in its northern end.

4.4 | DATA AND METHODS

This study relies on detrital zircon U-Pb geochronology to constrain the depositional age of the sedimentary succession along the Lago Aníbal Pinto transect. Zircon crystals were obtained from seven, 3 to 5 kg, fine- to medium-grained sandstones samples at different stratigraphic intervals within Cerro Toro and Dorotea formation equivalent deposits. The samples were collected at Cerro Aleta de Tiburon (N = 2), Monte Rotunda (N = 3) and Cerro Pelario (N = 2). Additional samples (N = 2) collected at an already constrained location ~70 km north, Cerro Jorge Montt (51°23'4.21"S / 72°29'32.44"W), within Tres Pasos Formation, were also included in the chronostratigraphic analysis and added to this study (Laguna Figueroa transect; sector 3 in Daniels *et al.*, 2019) (**Table 4.1**).

Table 4.1: Sandstone sample information. Samples in the table are stratigraphically organized according to their overall stratigraphic position within the MAB (*new Lago Aníbal Pinto transect).

Code	Latitude (°S)	Longitude (°W)	Stratigraphic interval (or equivalent)	Location
19-CP-02	52° 3'42.36"S	72°23'18.28"W	Dorotea Fm	Cerro Pelario (up section)*
19-CP-01	52° 4'22.79"S	72°24'13.50"W	Dorotea Fm	Cerro Pelario (down section)*
19-JM-02	51°23'30.28"S	72°29'12.88"W	Tres Pasos Fm	Cerro Jorge Montt (top of MTC)
19-JM-01	51°22'55.23"S	72°30'38.36"W	Tres Pasos Fm	Cerro Jorge Montt (base of MTC)
19-MR-03	51°59'35.95"S	72°35'39.40"W	Cerro Toro Fm	Monte Rotunda (up section)*
19-MR-01	51°59'6.71"S	72°35'32.84"W	Cerro Toro Fm	Monte Rotunda (middle section)*
19-MR-02	51°58'50.45"S	72°35'35.71"W	Cerro Toro Fm	Monte Rotunda (down section)*
20-MRN-02	51°57'2.47"S	72°38'11.86"W	Cerro Toro Fm	Cerro Aleta de tiburón (up section)*
20-MRN-01	51°57'7.82"S	72°38'16.92"W	Cerro Toro Fm	Cerro Aleta de tiburón (down section)*

The use of detrital zircon has proved to be an effective tool to calculate the maximum depositional age (MDA) of sedimentary units where biostratigraphic markers or other datable materials such as volcanic ash beds are limited (Dickinson and Gehrels, 2009; Gehrels *et al.*, 2011; Daniels *et al.*, 2018; Malkowski *et al.*, 2017a; Coutts *et al.*, 2019). Because a sedimentary rock cannot be older than the particles they host, they are particularly useful in arc-adjacent basins, where a consistent supply of zircons is more likely to result in a reduced time interval between zircon crystallization and final deposition, thus, detrital zircon would potentially provide a MDA that is closer to the true depositional age (TDA) (Gehrels, 2014; Cawood *et al.*, 2012, Sharman and Malkowski, 2020). Because of its geologic history, the use of detrital zircons to calculate MDA has been particularly successful and valuable in the MAB (Malkowski *et al.*, 2017b; Schwartz *et al.*, 2017; Daniels *et al.*, 2018; 2019; Sickmann *et al.*, 2019; George *et al.*, 2020)

Crystal separation and analysis were conducted at the University of Calgary Geo- and Thermochronology Laboratory. Each sample was prepared using standard mineral separation techniques thoroughly described in Matthews and Guest (2016). U-Pb isotopic measurement and grain ages were acquired using laser-ablation inductively coupled plasma mass spectrometry (LA-IC-MS) optimized for large datasets ($n > 300$ per sample, where n is the number of dated grains). This process consists of two stages: (i) first a large number of individual grains is measured using short ablation periods (*i.e.*, screening ablations) (t = 5s per grain) to reproduce a reliable representation of the age populations within each sample and increase the likelihood of finding young zircons that approach the TDA, and (ii) after the youngest grain population has been identified, the sample is repolished and a second, longer ablation period (t = 35s per grain) is carried out multiple times in the youngest grains to enhance the age constrain (Spencer *et al.*, 2016; Daniels *et al.*, 2018; Coutts *et al.*, 2019).

To determine MDA of each sample we prioritized the use of the weighted mean age of the youngest grain cluster over other methods, that is, using ≥ 3 reablated grains that overlap in age at 2σ (*i.e.*, YGC2σ). This allows us to obtain a statistically robust and conservative measure of the youngest detrital zircon ages with low uncertainty that tends to approximate the TDA (*e.g.*, near deposition detrital zircons) (Dickinson and Gehrels, 2009; Englert *et al.*, 2018; Coutts *et al.*, 2019; Sharman and Malkowski, 2020). We also include the weighted mean age of the youngest multiple ablated grain (YMAG) to provide another MDA derived from a different method for reference. Both methods tend to provide consistent MDAs, that is, within uncertainty of one another, when the population of the youngest grains has been effectively identified (Daniels *et al.*, 2019). However, a large difference between the YGC2σ and the YMAG MDA

(beyond uncertainty of one another) may suggest a low concentration of near depositional age grains. Therefore the YMAG can be considered as the MDA if additional geochronological data supports it (**Table 4.2**).

4.5 | RESULTS

4.5.1 | New Late Cretaceous U-Pb detrital zircon age

This study reports nine new U-Pb detrital zircon MDAs from sandstone samples collected in Upper Cretaceous units within the MAB (**Table 4.1**). A total of *n* = 5,172 single grains were dated, of which n = 119 were reablated and used to calculate the MDA using the YGC2σ and YMAG (**Table 4.2**). The results are summarized in weighted mean age plots that show the youngest cluster of low uncertainty, 35s reablated grains (**Figure 4.4**). We used the same method as Daniels *et al.* (2019) to integrate our results into their chronostratigraphic framework, and therefore, to extend the Upper Cretaceous correlations 55 km south into a poorly understood area of the MAB (**Figure 4.5**).

Table 4.2: Summary of the MDAs. MDAs derived from the youngest grain cluster composed of three or more grains overlapping in age at 2σ (YGC2σ) and the youngest multiple ablated grain (YMAG) for reference. Samples in the table are stratigraphically organized from lower at the base to upper at the top. Ages in **bold** used as MDA.

Sample	# of ablated grains (5s)	YGC2		YMAG	
		# of reablated grains	MDA	# of measurements	MDA
19-CP-02	594	23	**66.0±1.3 Ma**	3	64.9±2.4 Ma
19-CP-01	528	6	**71.7±1.4 Ma**	3	69.5±1.3 Ma
19-JM-02	558	9	**78.2±1.2 Ma**	3	77.4±1.7 Ma
19-JM-01	593	14	**78.2±1.3 Ma**	3	76.5±2.3 Ma
19-MR-03	558	21	**78.7±1.2 Ma**	3	76.0±2.6 Ma
19-MR-01	587	20	**80.2±1.2 Ma**	4	78.1±2.6 Ma
19-MR-02	597	19	**80.2±1.2 Ma**	2	77.6±2.8 Ma^{+}
20-MRN-02	565	3	92.3±1.5 Ma	3	92.0±1.9 Ma
20-MRN-01	592	3	89.6±1.6 Ma	3	**79.4±1.7 Ma**

Cerro Aleta de Tiburón

Sandstone samples from Cerro Aleta de Tiburón were collected at the base (20-MRN-01) and top (20-MRN-02) of the conglomeratic-rich succession exposed at this location (**Table 4.1**). Detrital zircon dates from these samples range from 2866.4±60.7 Ma to 77.5±6.0 Ma. MDAs estimated from YGC2σ weighted mean age resulted in 92.3±1.5 Ma (20-MRN-02) and 89.6±1.6 Ma (20-MRN-01) and the

youngest multiple ablated grain (YMAG) yielded an age of 79.4±1.7 Ma (20-MRN-01). The ~10 My MDA difference between the YGC2σ and the YMAG in sample 20-MRN-01 and the fact that the latter is within the uncertainty of the YGC2σ MDA determined in sample 19-MR-02 at the base of Monte Rotunda suggest a low concentration of near depositional age grains in sample 20-MRN-01. Furthermore, because near depositional age zircons were not found in the overlying sample 20-MRN-02, we used the YMAG as the MDA for the succession at this location (**Figure 4.4**).

Monte Rotunda

We collected three sandstone samples from the ~600 m thick conglomeratic-rich succession exposed at Monte Rotunda. The samples were roughly located at the base (19-MR-02), middle (19-MR-01) and top (19-MR-03) of the mountain, encompassing most of its stratigraphy (**Table 4.1**). Detrital zircon dates span 3469.7±24.4 Ma to 68.0±6.0 Ma. YGC2σ MDAs from this location range between 80.2±1.2 Ma (19-MR-02 and 19-MR-01) and 78.7±1.2 Ma (19-MR-03), whereas the YMAG was dated at 76.0±2.6 Ma (19-MR-03) (**Figure 4.4**).

Cerro Pelario

Sandstone samples were collected at the base (19-CP-01) and the top (19-CP-02) of the ~300 m thick sandstone-dominated succession exposed in the northern end of Cerro Pelario (**Table 4.1**). The age of single detrital zircon grains fluctuates between 3246.7±31.4 Ma and 57.1±7.0 Ma. YGC2σ MDAs derived from this interval span 71.7±1.4 Ma to 66.0±1.3 Ma and the YMAG produced an age of 64.9±2.4 Ma in sample 19-CP-02 (**Figure 4.4**).

Cerro Jorge Montt

Cerro Jorge Montt samples were collected from lenticular sandstones located at the base (19-JM-01) and top (19-JM-02) of a ~500 m thick mass transport complex (**Table 4.1**) interpreted as the base of the Tres Pasos Formation (Daniels *et al.*, 2017). The age of individual detrital zircon grains obtained from these samples ranges from 3369.1±23.3 Ma to 73.4±4.9 Ma. YGC2σ MDA for both samples was estimated in 78.2 Ma with an uncertainty of ±1.2-1.3 Ma. The YMAG yielded an age of 76.5±2.3 Ma (19-JM-01) (**Figure 4.4**).

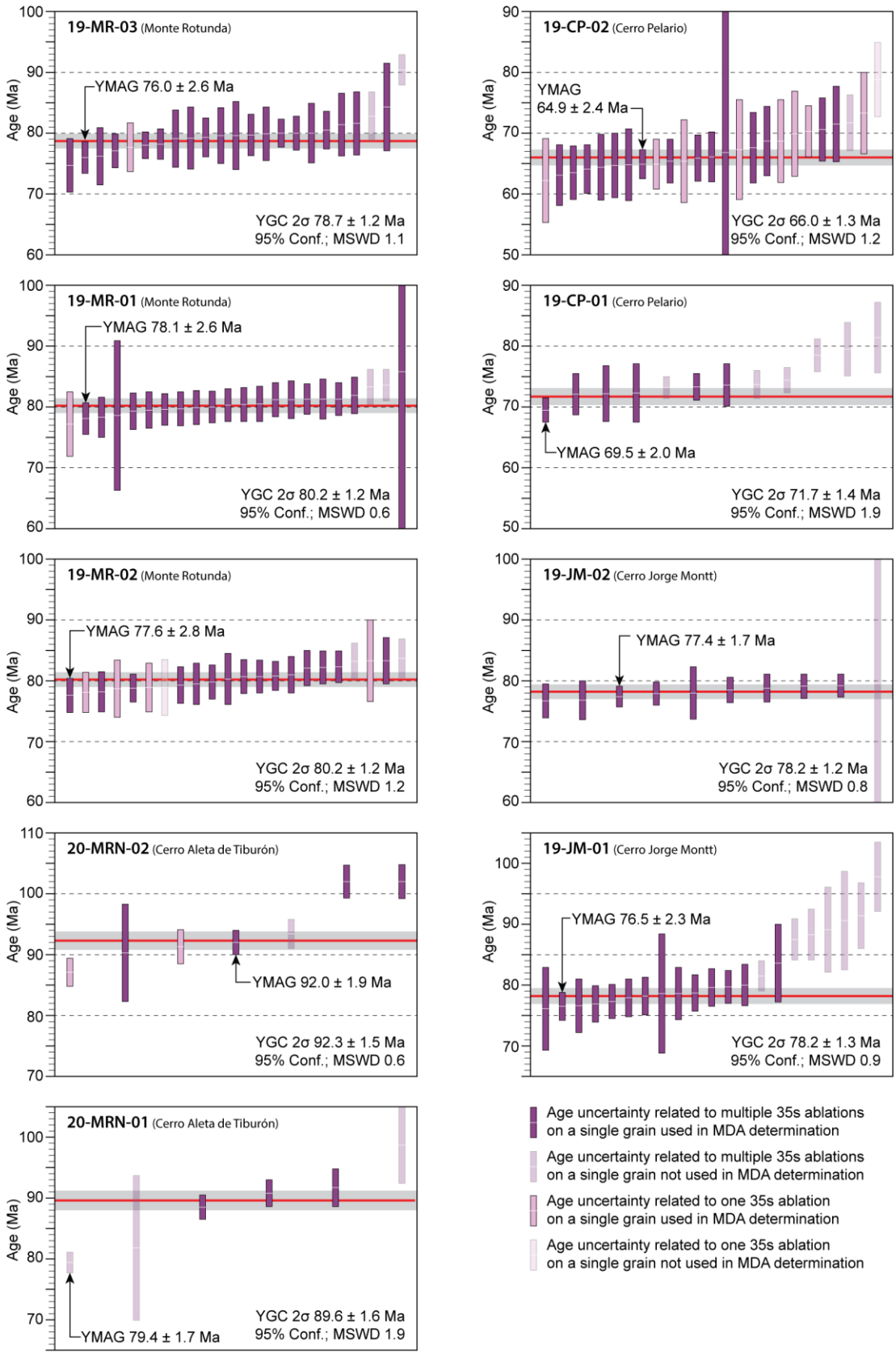
19-MR-03 (Monte Rotunda)
YMAG 76.0 ± 2.6 Ma
YGC 2σ 78.7 ± 1.2 Ma
95% Conf.; MSWD 1.1
19-CP-02 (Cerro Pelario)
YMAG
64.9 ± 2.4 Ma
YGC 2σ 66.0 ± 1.3 Ma
95% Conf.; MSWD 1.2
19-MR-01 (Monte Rotunda)
YMAG 78.1 ± 2.6 Ma
YGC 2σ 80.2 ± 1.2 Ma
95% Conf.; MSWD 0.6
19-CP-01 (Cerro Pelario)
YMAG 69.5 ± 2.0 Ma
YGC 2σ 71.7 ± 1.4 Ma
95% Conf.; MSWD 1.9
19-MR-02 (Monte Rotunda)
YMAG 77.6 ± 2.8 Ma
YGC 2σ 80.2 ± 1.2 Ma
95% Conf.; MSWD 1.2
19-JM-02 (Cerro Jorge Montt)
YMAG 77.4 ± 1.7 Ma
YGC 2σ 78.2 ± 1.2 Ma
95% Conf.; MSWD 0.8
20-MRN-02 (Cerro Aleta de Tiburón)
YMAG 92.0 ± 1.9 Ma
YGC 2σ 92.3 ± 1.5 Ma
95% Conf.; MSWD 0.6
19-JM-01 (Cerro Jorge Montt)
YMAG 76.5 ± 2.3 Ma
YGC 2σ 78.2 ± 1.3 Ma
95% Conf.; MSWD 0.9
20-MRN-01 (Cerro Aleta de Tiburón)
YMAG 79.4 ± 1.7 Ma
YGC 2σ 89.6 ± 1.6 Ma
95% Conf.; MSWD 1.9
Age (Ma)
Age uncertainty related to multiple 35s ablations on a single grain used in MDA determination
Age uncertainty related to multiple 35s ablations on a single grain not used in MDA determination
Age uncertainty related to one 35s ablation on a single grain used in MDA determination
Age uncertainty related to one 35s ablation on a single grain not used in MDA determination

Figure 4.4: Weighted mean age plots with the new detrital zircon MDA reported in this study. MDA obtained from the weighted mean of the youngest cluster of reablated grains that overlap in age at 2σ (*i.e.*, YGC2σ). The total number of ablated grains used to determine the youngest population and the number of reablated grains to obtain the MDA is provided in Table 4.2.

4.6 | INTERPRETATION AND DISCUSSION

The new MDAs reported in this study extend the chronostratigraphic framework for Upper Cretaceous units found in the Última Esperanza Province of the MAB basin 55 km south of previous studies and allow us to establish a framework upon which future stratigraphic, palaeontologic and/or geochronologic studies may rely on in this unexplored area. Our data shows that the Cerro Toro Formation equivalent, conglomeratic-rich succession outcropping at Cerro Aleta de Tiburón and Monte Rotunda is as old as 80.2±1.2 Ma and as young as 78.7±1.2 Ma, whereas deposits attributed to the Dorotea Formation are as old as 71.7±1.4 Ma (top of the formation was not identified). These ages allow us to also infer an age range for the Tres Pasos Formation, which does not seem to crop out due to glacial erosion, of at least between 78.7±1.2 Ma and 71.7±1.4 Ma (**Figure 4.5**).

4.6.1 | Chronostratigraphic relationship with other locations

Previous studies on the Cerro Toro Formation carried out north of Monte Rotunda have suggested its conglomeratic-rich deposits to be the southward extension of the Laguna Sofia channel axial belt based on the similarity of the observed lithofacies (Hubbard *et al.*, 2008; Jobe *et al.*, 2010; Bernhardt *et al.*, 2012; Malkowski *et al.*, 2018). However, new detrital zircon geochronology presented in this study show that coarse-grained deep-marine deposition within the Lago Aníbal Pinto transect (**Figure 4.3**) yield a statistical different age distribution in comparison to northern locations, suggesting that deposition occurred: (i) partially coeval to the upper part of the Lago Sofia axial channel belt (Hubbard *et al.*, 2008; Bernhardt *et al.*, 2012; Malkowksi *et al.*, 2017a, 2018; Daniels *et al.*, 2019) and to phase I mass-transport deposits that mark the onset of the Tres Pasos Formation slope system (between ~81 and 78 Ma) (Daniels *et al.*, 2018, 2019), and (ii) mostly before the development of the hypothesized Cerro Ballena tributary system (76.6±2.0 Ma) reported by Bernhardt *et al.* (2012)(**Figure 4.5**).

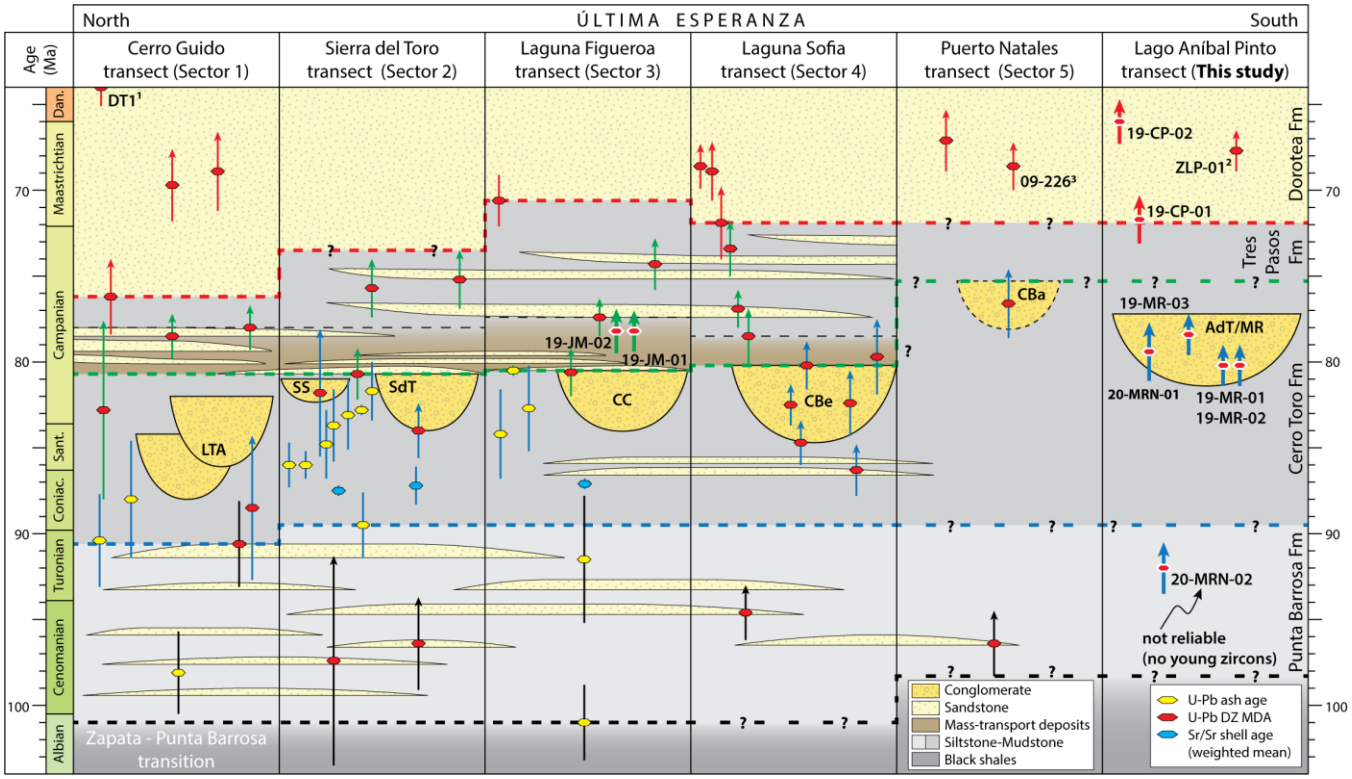

Figure 4.5: Chronostratigraphic framework of the Magallanes-Austral Basin in the Última Esperanza Province modified from Daniels *et al.* (2019) including the new detrital zircon ages reported in this study (white outlined diamonds) and extend it southward (Lago Aníbal Pinto transect). The sectors defined by Daniels *et al.* (2019) were associated with the names of well-known localities to facilitate their identification. We have also included relevant detrital zircon ages from: [1]George *et al.* (2020) (calculated from the weighted mean age of the youngest two grains that overlap at 1σ), [2]Rivera *et al.* (2020) (calculated from the weighted mean age of the youngest peak at 2σ), [3]Fosdick *et al.* (2015). Uncertainty is colored to represent its sample's stratigraphic unit provenance (black: Punta Barrosa Formation; blue: Cerro Toro Formation; green: Tres Pasos Formation; red: Dorotea Formation). Transitional boundaries between formations are shown with dashed lines, whereas speculative boundaries include question marks. LTA: Laguna Tres de Abril (Argentina); SS: Silla Syncline; SdT: Sierra del Toro; CC: Cerro Castillo; CBe: Cerro Benitez; Cba: Cerro Ballena; MR: Monte Rotunda; AdT: Aleta de Tiburón.

On the contrary, the calculated MDA of samples collected from deposits attributed to the Dorotea Formation in Cerro Pelario mostly overlap with ages calculated immediately north, in the Puerto Natales and Laguna Sofia transect (between ~72 and 67 Ma) (Fosdick *et al.*, 2015; Daniels *et al.*, 2019 and references therein) and in the same location (67.7±1.2 Ma) (Rivera *et al.*, 2020). These observations have implications for the Tres Pasos Formation, even though we did not identify any outcrop attributed to it, as they suggest that deposition associated to its slope system was temporarily restricted in this area to no more than 5 My (**Figure 4.5**).

4.6.2 | Implications for paleogeographic reconstructions

During the Late Cretaceous, the MAB reached its maximum subsidence coupled with high rates of accommodation, providing the conditions for the development of a >150 km long, NS oriented longitudinal channel belt in a deep-marine setting (Céspedes, 1971; Winn and Dott, 1979; Dott *et al.*, 1982; Rojas *et al.*, 1993; McAtamney *et al.*, 2011). This depositional system is represented in the Última Esperanza Province by the Cerro Toro Formation, a ~2,000 m thick mudstone-dominated sedimentary succession containing a distinctive 400 to 1,000 m thick interval of coarse-grained sediments informally called Laguna Sofia Conglomerates (Cecioni, 1957; Zeil, 1958; Katz, 1963; Scott, 1966, Natland *et al.*, 1974). Combined detrital and volcanic zircon geochronology reveals an overall diachronous filling of the basin during the Late Cretaceous, marked by a southward youngling trend of the sedimentary systems, which is also supported by southward paleocurrent data in the Ultima Esperanza Province and later deposition of the equivalent Escarpada and Cerro Matrero Formation in the Magallanes and Tierra del Fuego Provinces (McAtamney *et al.*, 2010; Bernhardt *et al.*, 2012; Malkowski *et al.*, 2018; Daniels *et al.*, 2019).

In contrast to the well-known chronostratigraphic framework of northern Última Esperanza, rough geography, difficult access and tectonic complexity has limited the amount of public research carried out on Upper Cretaceous units in the Magallanes and Tierra del Fuego Provinces (*i.e.*, south of 51°30'S). In the locations of Isla Riesco, Peninsula de Brunswick and Isla Tierra del Fuego the Latorre/Escarpada (McAtamney *et al.*, 2011) and Cerro Matrero Formations (Cortés and Valenzuela, 1960; Harambour *et al.*, 1989; Alvarez-Marrón *et al.*, 1993; Klepeis, 1994; Klepeis *et al.*, 2010; McAtamney *et al.*, 2011) have been correlated with the Cerro Toro Formation; however, their chronostratigraphic framework is still poorly constrained, as these units have been studied mostly as isolated field sites. Currently, the only chronostratigraphic constraint is provided by McAtamney *et al.* (2011), who mapped and dated the sedimentary successions that mark the initiation of the foreland regime at these locations. Their results show that the Escarpada and Cerro Matrero conglomerates were deposited around 81.0±1.2 Ma and 82.7±1.5 Ma, respectively, which is comparable to other ages north of Monte Rotunda. Nonetheless, the same authors also report paleoflows from a westward source and a depositional architecture comparable to submarine fans rather than submarine channels.

Despite the similarities in sedimentary facies, the MDAs reported in this study suggest that Cerro Toro Formation equivalent conglomeratic-rich deposits at Cerro Aleta de Tiburón and Monte Rotunda are

unlikely to represent the southward extension of the axial-channel belt described in northern locations (Hubbard *et al.*, 2008; Jobe *et al.*, 2010; Bernhardt *et al.*, 2012; Malkowski *et al.*, 2018) (**Figure 4.5**) or proximal deposits from southern units (Escarpada and Cerro Matrero Formations). Additionally, despite being partially coeval to phase I mass-transport deposits of the Tres Pasos Formation (Daniels *et al.*, 2018), strong lithofacies dissimilarities (*i.e.*, lack of massive conglomeratic-rich deposits) in this formation also make it an improbable link with Monte Rotunda and Cerro Aleta de Tiburón deposits.

We hypothesized that coarse-grained deposits at Cerro Aleta de Tiburón and Monte Rotunda may represent their own sedimentary routing system, disconnected from north and south equivalent deposits (**Figure 4.6**). However, whether this is the result of the natural southward diachronic evolution of the MAB (McAtamney *et al.*, 2011; Bernhardt *et al.*, 2012; Malkowsky *et al.*, 2017b) or of a tectonic control (Fosdick *et al.*, 2011) cannot be established with the current data. Moreover, we cannot fully discard the possibility that Monte Rotunda deposits were connected to the Cerro Ballena tributary system if YMAG ages are considered as MDAs. Thus, the importance of processing and collecting additional data that may help define the provenance of the successions found at Cerro Aleta de Tiburon and Monte Rotunda.

4.7 | FUTURE WORK

The majority of published Upper Cretaceous stratigraphic data of the MAB comes from decades of research in the Última Esperanza Province (Chile) (see references in this study). In contrast, a significantly lower number of studies have taken place south of Puerto Natales (in Magallanes and Tierra del Fuego Provinces, between 52° and 55°S). The result is an overall disconnected stratigraphic framework where potential correlations between individual field sites are hindered or made without geochronologic constraints in intermediate locations (McAtamney *et al.*, 2011; Rivera *et al.*, 2020).

Constraining the depositional age is the first step to reconstruct the paleogeographic distribution of Upper Cretaceous foreland basin units within the Lago Aníbal Pinto transect and to establish a more continuous stratigraphic framework along the basin. However, future work should be accompanied by the following tasks: (i) field mapping oriented to find new sampling sites for further detrital mineral analysis, including but not limited to, geochronology, provenance, rates of burial and exhumation, among others; (ii) detailed description of the stratigraphy and depositional architecture of undocumented outcrops enhanced by unmanned aerial vehicles (drones); and (iii) structural mapping.

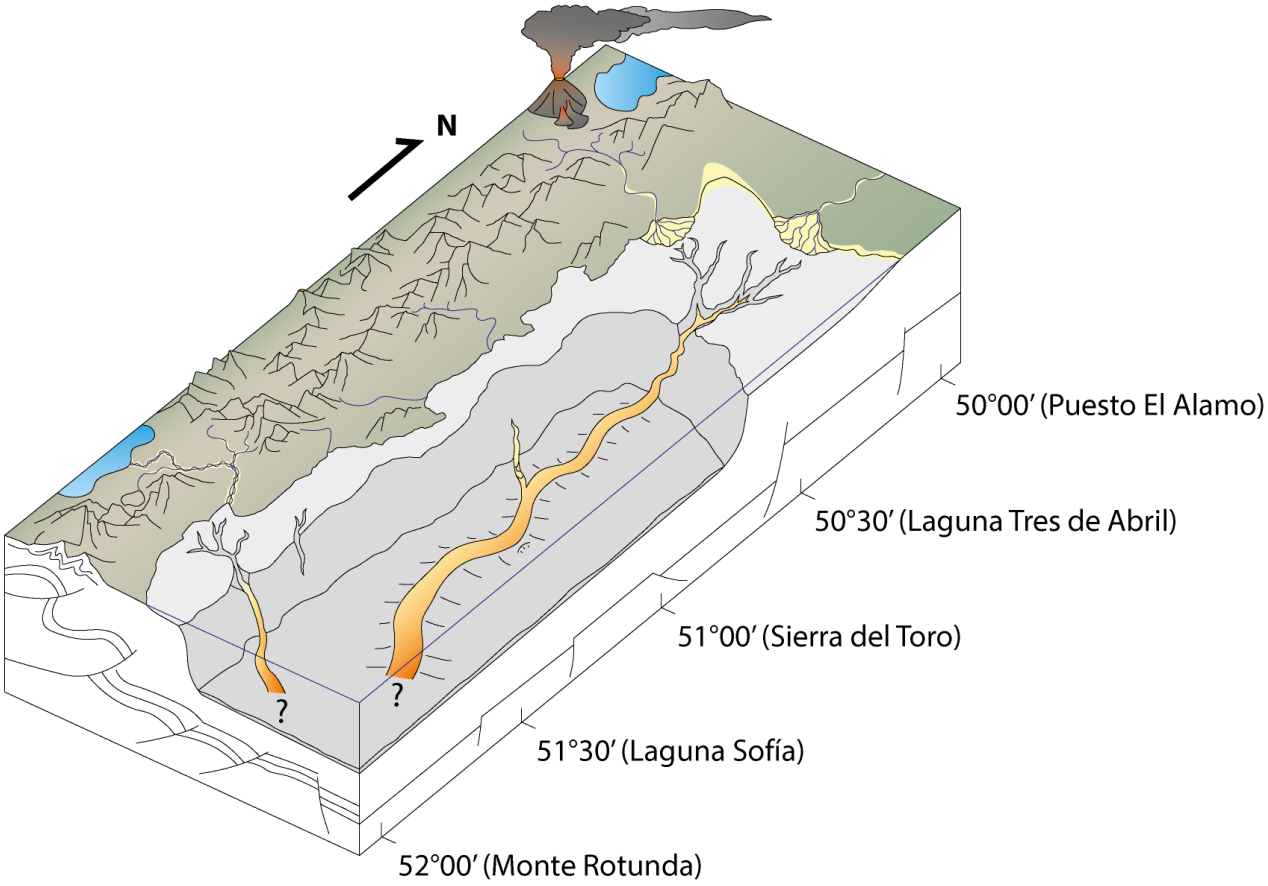

Figure 4.6: Interpreted paleogeographic reconstruction of the MAB throughout the extent of the Última Esperanza Province between 85 and 80 Ma based on the chronostratigraphic framework presented in figure 4.5 (based on Romans *et al.*, 2011).

4.8 | CONCLUSIONS

This study reports nine new U-Pb detrital zircon MDAs from sandstone samples collected in Upper Cretaceous units within the MAB. Two samples were collected from the already constrained Cerro Jorge Montt (Laguna Figueroa transect), outside the focus of this study, and seven from the area surrounding the Aníbal Pinto lake (Lago Aníbal Pinto transect), which makes the focus of this study.

MDAs were obtained from the weighted mean age of the youngest grain cluster (YGC) employing only grains ablated for 35s that overlap in age at 2σ; this method follows the one used in Daniels *et al.* (2019), and thus, allow us to integrate our results seamlessly. Our results show that the Cerro Toro Formation equivalent succession at Cerro Aleta de Tiburón and Monte Rotunda span between 80.2±1.2 Ma and 78.7±1.1, whereas Dorotea Formation equivalent deposits exposed in Cerro Pelario range between 71.7±1.4 Ma and 66.0±1.13 Ma. We suggest that Cerro Toro Formation equivalent conglomeratic-rich

deposits at this location are unlikely to represent the southward extension of the deep-marine axial-channel belt described in northern locations, and therefore they would potentially represent their own sediment routing system, emanating from erosional catchments in the fold-thrust belt to the west. For Dorotea equivalent deposits, MDAs overlap with other locations northward, suggesting a continuous routing system in shallow marine environments by the end of the Cretaceous.

Our results highlight the diachronous evolution of the MAB reported by previous authors and the value to increase the efforts to generate a consistent chronostratigraphic framework to properly reconstruct the paleogeography of the basin further south.

REFERENCES

Alvarez-Marron, J., McClay, K.R., Harambour, S., Rojas, L., Skarmeta, J., 1993. Geometry and evolution of the frontal part of the Magallanes Foreland Thrust and Fold Belt (Vicuna area), Tierra del Fuego, southern Chile. Am. Assoc. Pet. Geol. Bull. https://doi.org/10.1306/bdff8f74-1718-11d7-8645000102c1865d

Armitage, D.A., Romans, B.W., Covault, J.A., Graham, S.A., 2009. The influence of mass-transport-deposit surface topography on the evolution of turbidite architecture: The sierra contreras, tres pasos formation (Cretaceous), Southern Chile. J. Sediment. Res. 79, 287–301. https://doi.org/10.2110/jsr.2009.035

Auchter, N.C., Romans, B.W., Hubbard, S.M., 2016. Influence of deposit architecture on intrastratal deformation, slope deposits of the Tres Pasos Formation, Chile. Sediment. Geol. 341, 13–26. https://doi.org/10.1016/j.sedgeo.2016.05.005

Barton, M.D., Steffens, G.S., And O'byrne, C.J., 2007. Facies architecture of a submarine-slope channel complex, Condor West channel, Cerro Toro Formation, Chile, in Nilsen, T., Shew, R., Steffens, G., and Studlick, J., eds., Atlas of Deep-Water Outcrops, American Association of Petroleum Geologists, Studies in Geology 56, p. 149–153.

Bauer, D.B., Hubbard, S.M., Covault, J.A., Romans, B.W., 2020. Inherited Depositional Topography Control on Shelf-Margin Oversteepening, Readjustment, and Coarse-Grained Sediment Delivery to Deep Water, Magallanes Basin, Chile. Front. Earth Sci. 7. https://doi.org/10.3389/feart.2019.00358

Bernhardt, A., Jobe, Z.R., Grove, M., Lowe, D.R., 2012. Palaeogeography and diachronous infill of an ancient deep-marine foreland basin, Upper Cretaceous Cerro Toro Formation, Magallanes Basin. Basin Res. 24, 269–294. https://doi.org/10.1111/j.1365-2117.2011.00528.x

Bernhardt, A., Jobe, Z.R., Lowe, D.R., 2011. Stratigraphic evolution of a submarine channel–lobe complex system in a narrow fairway within the Magallanes foreland basin, Cerro Toro Formation, southern Chile. Mar. Pet. Geol. 28, 785–806. https://doi.org/10.1016/j.marpetgeo.2010.05.013

Biddle, K.T., Uliana, M.A., Mitchum, R.M., Fitzgerald, M.G., Wright, R.C., 1986. The stratigraphic and structural evolution of the central and eastern Magallanes Basin, southern South America. Forel. basins 41–61. https://doi.org/10.1002/9781444303810.ch2

Bruhn, R.L., Stern, C.R., De Wit, M.J., 1978. Field and geochemical data bearing on the development of a mesozoic volcano-tectonic rift zone and back-arc basin in southernmost South America. Earth Planet. Sci. Lett. 41, 32–46. https://doi.org/10.1016/0012-821X(78)90039-0

Calderón, M., Fildani, A., Hervé, F., Fanning, C.M., Weislogel, A., Cordani, U., 2007. Late Jurassic bimodal magmatism in the northern sea-floor remnant of the Rocas Verdes basin, southern Patagonian Andes. J. Geol. Soc. London. 164, 1011–1022. https://doi.org/10.1144/0016-76492006-102

Calderón, M., Fosdick, J.C., Warren, C., Massonne, H.J., Fanning, C.M., Cury, L.F., Schwanethal, J., Fonseca, P.E., Galaz, G., Gaytán, D., Hervé, F., 2012. The low-grade Canal de las Montañas Shear Zone and its role in the tectonic emplacement of the Sarmiento Ophiolitic Complex and Late Cretaceous Patagonian Andes orogeny, Chile. Tectonophysics 524–525, 165–185. https://doi.org/10.1016/J.TECTO.2011.12.034

Campion, K.M., Dixon, B.T., Scott, E.D., 2011. Sediment waves and depositional implications for fine-grained rocks in the Cerro Toro Formation (upper Cretaceous), Silla Syncline, Chile. Mar. Pet. Geol. 28, 761–784. https://doi.org/10.1016/j.marpetgeo.2010.07.002

Castelli, J. C., Robertson, R., Harambour, S., 1992. Evaluación Geológica y Petrolera, bloques Ultima Esperanza Sur e Isla Riesco: Informe Técnico ENAP (inédito), Santiago.

Cawood, P.A., Hawkesworth, C.J., Dhuime, B., 2012. Detrital zircon record and tectonic setting. Geology 40, 875–878. https://doi.org/10.1130/G32945.1

Cecioni, G., 1955, Distribuzione verticale di alcune Kossmaticertatidae nella Patagonia Chilena: Bulletino Societa Geológica d'Italia, v.74, p. 141-149

Cecioni, G.O., 1957. Cretaceous Flysch and Molasse in Departamento Ultima Esperanza, Magallanes Province, Chile. Am. Assoc. Pet. Geol. Bull. 41, 538–564. https://doi.org/10.1306/0BDA5837-16BD-11D7-8645000102C1865D

Céspedes, S., 1971. Estudio geológico de la zona de Cabo Nariz y Tierra del Fuego. Informe técnico, ENAP.

Charrier , R. and Lahsen, A., 1969. Stratigraphy of Late Cretaceous-Early Eocene, Seno Skyring-Strait of Magellan area, Magllanes province, Chile. American Association of Petroleum Geologist Bulletin, v. 53(3), p. 568-590.

Coleman, J.L., 2000. Reassessment of the Cerro Toro (Chile) Sandstones in View of Channel-Levee-Overbank Reservoir Continuity Issues. Deep. Reserv. World 20th Annu. 252–262. https://doi.org/10.5724/gcs.00.15.0252

Cortés , R., Valenzuela,H., 1960. Estudio geológico del área lago Blanco-Monte Hope, porción central de Tierra del Fuego: Informe Técnico ENAP (inédito) Santiago.

Coutts, D.S., Matthews, W.A., Hubbard, S.M., 2019. Assessment of widely used methods to derive depositional ages from detrital zircon populations. Geosci. Front. 10, 1421–1435. https://doi.org/10.1016/j.gsf.2018.11.002

Covacevich, V., 1991. Estudio paleontológicos y biostratigráficos en la costa norte de Isla Riesco e interior de Seno Skyring, Región de Magallanes: Informe Técnico ENAP (inédito) Santiago.

Covault, J.A., Romans, B.W., Graham, S.A., 2009. Outcrop Expression of a Continental-Margin-Scale Shelf-Edge Delta from the Cretaceous Magallanes Basin, Chile. J. Sediment. Res. 79, 523–539. https://doi.org/10.2110/jsr.2009.053

Crane, W.H., Lowe, D.R., 2008. Architecture and evolution of the Paine channel complex, Cerro Toro Formation (Upper Cretaceous), Silla Syncline, Magallanes Basin, Chile. Sedimentology 55, 979–1009. https://doi.org/10.1111/j.1365-3091.2007.00933.x

Dalziel, I., De Wit, M., Palmer, K., 1974, Fossil marginal basin in the southern Andes: Nature, v. 5464, p. 291-294.

Daniels, B.G., Auchter, N.C., Hubbard, S.M., Romans, B.W., Matthews, W.A., Stright, L., 2018. Timing of deep-water slope evolution constrained by large-n detrital and volcanic ash zircon geochronology, Cretaceous Magallanes Basin, Chile. Bull. Geol. Soc. Am. 130, 438–454. https://doi.org/10.1130/B31757.1

Daniels, B.G., Hubbard, S.M., Romans, B.W., Malkowski, M.A., Matthews, W.A., Bernhardt, A., Kaempfe, S.A., Jobe, Z.R., Fosdick, J.C., Schwartz, T.M., Fildani, A., Graham, S.A., 2019. Revised chronostratigraphic framework for the Cretaceous Magallanes-Austral Basin, Última Esperanza Province, Chile. J. South Am. Earth Sci. 94, 102209. https://doi.org/10.1016/j.jsames.2019.05.025

Davies, B.J., Darvill, C.M., Lovell, H., Bendle, J.M., Dowdeswell, J.A., Fabel, D., García, J.L., Geiger, A., Glasser, N.F., Gheorghiu, D.M., Harrison, S., Hein, A.S., Kaplan, M.R., Martin, J.R.V., Mendelova, M., Palmer, A., Pelto, M., Rodés, Á., Sagredo, E.A., Smedley, R.K., Smellie, J.L., Thorndycraft, V.R., 2020. The evolution of the Patagonian Ice Sheet from 35 ka to the present day (PATICE). Earth-Science Rev. 204, 103152. https://doi.org/10.1016/j.earscirev.2020.103152

Dickinson, W.R., Gehrels, G.E., 2009. Use of U-Pb ages of detrital zircons to infer maximum depositional ages of strata: A test against a Colorado Plateau Mesozoic database. Earth Planet. Sci. Lett. 288, 115–125. https://doi.org/10.1016/j.epsl.2009.09.013

Dott, R.H., Winn, R.D., Smith, C.H.L., 1982. Relationship of late Mesozoic and early Cenozoic sedimentation to the tectonic evolution of the southernmost Andes and Scotia Arc (South America, Antarctica). Antarct. Geosci. 3rd Symp. Antarct. Geol. Geophys. Madison, August 1977 193–202.

Englert, R.G., Hubbard, S.M., Coutts, D.S., Matthews, W.A., 2018. Tectonically controlled initiation of contemporaneous deep-water channel systems along a Late Cretaceous continental margin, western British Columbia, Canada. Sedimentology 65, 2404–2438. https://doi.org/10.1111/sed.12472

Féraud, G., Alric, V., Fornari, M., Bertrand, H., Haller, M., 1999. 40Ar/39Ar dating of the Jurassic volcanic province of Patagonia: migrating magmatism related to Gondwana break-up and subduction. Earth Planet. Sci. Lett. 172, 83–96. https://doi.org/10.1016/S0012-821X(99)00190-9

Fildani, A., Cope, T.D., Graham, S.A., Wooden, J.L., 2003. Initiation of the Magallanes foreland basin: Timing of the southernmost Patagonian Andes orogeny revised by detrital zircon provenance analysis. Geology 31, 1081–1084. https://doi.org/10.1130/G20016.1

Fildani, A., Hessler, A.M., 2005. Stratigraphic record across a retroarc basin inversion: Rocas Verdes-Magallanes Basin, Patagonian Andes, Chile. Bull. Geol. Soc. Am. 117, 1596–1614. https://doi.org/10.1130/B25708.1

Fosdick, J.C., Grove, M., Graham, S.A., Hourigan, J.K., Lovera, O., Romans, B.W., 2015. Detrital thermochronologic record of burial heating and sediment recycling in the Magallanes foreland basin, Patagonian Andes. Basin Res. https://doi.org/10.1111/bre.12088

Fosdick, J.C., Romans, B.W., Fildani, A., Bernhardt, A., Calderón, M., Graham, S.A., 2011. Kinematic evolution of the Patagonian retroarc fold-and-thrust belt and Magallanes foreland basin, Chile and Argentina, 51°30's. Bull. Geol. Soc. Am. 123, 1679–1698. https://doi.org/10.1130/B30242.1

Gehrels, G., 2014. Detrital zircon U-Pb geochronology applied to tectonics. Annu. Rev. Earth Planet. Sci. https://doi.org/10.1146/annurev-earth-050212-124012

George, S.W.M., Davis, S.N., Fernández, R.A., Manríquez, L.M.E., Leppe, M.A., Horton, B.K., Clarke, J.A., 2020. Chronology of deposition and unconformity development across the Cretaceous–Paleogene boundary, Magallanes-Austral Basin, Patagonian Andes. J. South Am. Earth Sci. 97, 102237. https://doi.org/10.1016/j.jsames.2019.102237

Harambour, S., Aguirre, G., Urzúa, F., 1989. Evaluación geológica y petrolera, Bloque Nº 7 Tierra del Fuego: IRD, Paris, Harambour, S., Soffia, J. M., 1988, Trancisión de margen pasivo a cuenca de antepaís: síntesis evolutiva para el extremo norte de Última Esperanza: Congreso Geológico Chileno Nº 5, Actas, v. 2 p. A385-A402, Santiago.

Hervé, F., Goday, E., Mpodozis, C., Fanning, M., 2004. Monitoring magmatism of the Patagonian Batholith through

the U-Pb SHRIMP dating of detrital zircons in sedimentary units of the Magallanes Basin., in: GEOSUR, UInternational Symposium on the Geology and Geophysics of the Southernmost Andes, the Scotia Arc and the Antartic Peninsula. pp. 4–06.

Hubbard, S.M., Fildani, A., Romans, B.W., Covault, J.A., McHargue, T.R., 2010. High-relief slope clinoform development: Insights from outcrop, magallanes Basin, Chile. J. Sediment. Res. 80, 357–375. https://doi.org/10.2110/jsr.2010.042

Hubbard, S.M., Romans, B.W., Graham, S.A., 2008. Deep-water foreland basin deposits of the Cerro Toro Formation, Magallanes basin, Chile: Architectural elements of a sinuous basin axial channel belt. Sedimentology 55, 1333–1359. https://doi.org/10.1111/j.1365-3091.2007.00948.x

Jobe, Z.R., Bernhardt, A., Lowe, D.R., 2010. Facies and architectural asymmetry in a conglomerate-rich submarine channel fill, cerro toro formation, Sierra Del Toro, Magallanes Basin, Chile. J. Sediment. Res. 80, 1085–1108. https://doi.org/10.2110/jsr.2010.092

Katz, H., 1963. Revision of Cretaceous Stratigraphy in Patagonian Cordillera of Ultima Esperanza, Magallanes Province, Chile. Am. Assoc. Pet. Geol. Bull. 47. https://doi.org/10.1306/bc743a5d-16be-11d7-8645000102c1865d

Klepeis, K., Betka, P., Clarke, G., Fanning, M., Hervé, F., Rojas, L., Mpodozis, C., Thomson, S., 2010. Continental underthrusting and obduction during the Cretaceous closure of the Rocas Verdes rift basin, Cordillera Darwin, Patagonian Andes. Tectonics 29, 1–24. https://doi.org/10.1029/2009TC002610

Klepeis, K.A., 1994. Relationship between uplift of the metamorphic core of the southernmost Andes and shortening in the Magallanes foreland fold and thrust belt, Tierra del Fuego, Chile. Tectonics 13, 882–904. https://doi.org/10.1029/94TC00628

Macauley, R. V., Hubbard, S.M., 2013. Slope channel sedimentary processes and stratigraphic stacking, Cretaceous Tres Pasos Formation slope system, Chilean Patagonia. Mar. Pet. Geol. 41, 146–162. https://doi.org/10.1016/j.marpetgeo.2012.02.004

Macellari, C.E., Barrio, C.A., Manassero, M.J., 1989. Upper cretaceous to paleocene depositional sequences and sandstone petrography of southwestern Patagonia (Argentina and Chile). J. South Am. Earth Sci. 2, 223–239. https://doi.org/10.1016/0895-9811(89)90031-X

Malkowski, M.A., Jobe, Z.R., Sharman, G.R., Graham, S.A., 2018. Down-slope facies variability within deep-water channel systems: Insights from the Upper Cretaceous Cerro Toro Formation, southern Patagonia. Sedimentology 65, 1918–1946. https://doi.org/10.1111/sed.12452

Malkowski, M.A., Schwartz, T.M., Sharman, G.R., Sickmann, Z.T., Graham, S.A., 2017a. Stratigraphic and provenance variations in the early evolution of the magallanes-austral foreland basin: Implications for the role of longitudinal versus transverse sediment dispersal during arc-continent collision. Bull. Geol. Soc. Am. 129, 349–371. https://doi.org/10.1130/B31549.1

Malkowski, M.A., Sharman, G.R., Graham, S.A., Fildani, A., 2017b. Characterisation and diachronous initiation of coarse clastic deposition in the Magallanes–Austral foreland basin, Patagonian Andes. Basin Res. 29, 298–326. https://doi.org/10.1111/bre.12150

Manríquez, L.M.E., Lavina, E.L.C., Fernández, R.A., Trevisan, C., Leppe, M.A., 2019. Campanian-Maastrichtian and Eocene stratigraphic architecture, facies analysis, and paleoenvironmental evolution of the northern

Magallanes Basin (Chilean Patagonia). J. South Am. Earth Sci. 93, 102–118. https://doi.org/10.1016/J.JSAMES.2019.04.010

Matthews, W.A., Guest, B., 2017. A Practical Approach for Collecting Large-n Detrital Zircon U-Pb Data sets by Quadrupole LA-ICP-MS. Geostand. Geoanalytical Res. 41, 161–180. https://doi.org/10.1111/ggr.12146

McAtamney, J., Klepeis, K., Mehrtens, C., Thomson, S., Betka, P., Rojas, L., Snyder, S., 2011. Along-strike variability of back-arc basin collapse and the initiation of sedimentation in the Magallanes foreland basin, southernmost Andes (53-54.5°S). Tectonics 30, 1–27. https://doi.org/10.1029/2010TC002826

Mpodozis, C., Mella, P., Padva, D., 2011. Estratigrafía y megasecuencias sedimentarias en la cuenca Austral – Magallanes , Argentina y Chile. VIII Congr. Explor. y Desarro. Hidrocarburos 97–138.

Natland, M.L., Eduardo, G.P., Cañon, A., 1974. Introduction. Mem. Geol. Soc. Am. 139, 1–117. https://doi.org/10.1130/MEM139-p1

Pankhurst, R.J., Riley, T.R., Fanning, C.M., Kelley, S.P., 2000. Episodic Silicic Volcanism in Patagonia and the Antarctic Peninsula: Chronology of Magmatism Associated with the Break-up of Gondwana. J. Petrol. 41, 605–625.

Rivera, H.A., Le Roux, J.P., Farías, M., Gutiérrez, N.M., Sánchez, A., Palma-Heldt, S., 2020. Tectonic controls on the Maastrichtian-Danian transgression in the Magallanes-Austral foreland basin (Chile): Implications for the growth of the Southern Patagonian Andes. Sediment. Geol. 403. https://doi.org/10.1016/j.sedgeo.2020.105645

Rojas, L., Harambour, S., Robertson, R. and Castelli, J. C. 1993. Geología, geofísica y delimitación de prospectos Bloque Lago Blanco. Archivo Técnico, ENAP.

Romans, B.W., Fildani, A., Graham, S.A., Hubbard, S.M., Covault, J.A., 2010. Importance of predecessor basin history on sedimentary fill of a retroarc foreland basin: provenance analysis of the Cretaceous Magallanes basin, Chile (50-52°S). Basin Res. 22, 640–658. https://doi.org/10.1111/j.1365-2117.2009.00443.x

Romans, B.W., Fildani, A., Hubbard, S.M., Covault, J.A., Fosdick, J.C., Graham, S.A., 2011. Evolution of deep-water stratigraphic architecture, Magallanes Basin, Chile. Mar. Pet. Geol. 28, 612–628. https://doi.org/10.1016/j.marpetgeo.2010.05.002

Romans, B.W., Hubbard, S.M., Graham, S.A., 2009. Stratigraphic evolution of an outcropping continental slope system, Tres Pasos Formation at Cerro Divisadero, Chile. Sedimentology 56, 737–764. https://doi.org/10.1111/j.1365-3091.2008.00995.x

Sagredo, E.A., Moreno, P.I., Villa-Martínez, R., Kaplan, M.R., Kubik, P.W., Stern, C.R., 2011. Fluctuations of the Última Esperanza ice lobe (52°S), Chilean Patagonia, during the last glacial maximum and termination 1. Geomorphology 125, 92–108. https://doi.org/10.1016/j.geomorph.2010.09.007

Schwartz, T.M., Fosdick, J.C., Graham, S.A., 2017. Using detrital zircon U-Pb ages to calculate Late Cretaceous sedimentation rates in the Magallanes-Austral basin, Patagonia. Basin Res. 29, 725–746. https://doi.org/10.1111/bre.12198

Schwartz, T.M., Graham, S.A., 2015. Stratigraphic architecture of a tide-influenced shelf-edge delta, Upper Cretaceous Dorotea Formation, Magallanes-Austral Basin, Patagonia. Sedimentology 62, 1039–1077. https://doi.org/10.1111/sed.12176

Scott, K.M., 1966. Sedimentology and Dispersal pattern of a Cretaceous Flysch Sequence, Patagonian Andes, Southern Chile. Am. Assoc. Pet. Geol. Bull. 50, 72–107. https://doi.org/10.1306/A663389E-16C0-11D7-8645000102C1865D

Sharman, G.R., Malkowski, M.A., 2020. Needles in a haystack: Detrital zircon U[sbnd]Pb ages and the maximum depositional age of modern global sediment. Earth-Science Rev. 203. https://doi.org/10.1016/j.earscirev.2020.103109

Shultz, M.R., Fildani, A., Cope, T.D., Graham, S.A., 2005. Deposition and stratigraphic architecture of an outcropping ancient slope system: Tres Pasos Formation, Magallanes Basin, southern Chile. Geol. Soc. London, Spec. Publ. 244, 27–50. https://doi.org/10.1144/GSL.SP.2005.244.01.03

Shultz, M.R., Hubbard, S.M., 2005. Sedimentology, Stratigraphic Architecture, and Ichnology of Gravity-Flow Deposits Partially Ponded in a Growth-Fault-Controlled Slope Minibasin, Tres Pasos Formation (Cretaceous), Southern Chile. J. Sediment. Res. 75, 440–453. https://doi.org/10.2110/jsr.2005.034

Smith, C., 1977. Sedimentology of the Late Cretaceous (Santonian–Maastrichtian) Tres Pasos Formation, Ultima Esperanza District, southern Chile. M.Sc Thesis, University of Wisconsin, Madison, WI, 129 p.

Sohn, Y.K., Choe, M.Y., Jo, H.R., 2002. Transition from debris flow to hyperconcentrated flow in a submarine channel (the Cretaceous cerro toro formation, southern Chile). Terra Nov. 14, 405–415. https://doi.org/10.1046/j.1365-3121.2002.00440.x

Solari, M.A., Le Roux, J.P., Herve, F., Airo, A., Calderon, M., 2012. Evolution of the Great Tehuelche Paleolake in the Torres del Paine National Park of Chilean Patagonia during the Last Glacial Maximum and Holocene. Andean Geol. 39, 1–21. https://doi.org/10.5027/andgeov39n1-a01

Spencer, C.J., Kirkland, C.L., Taylor, R.J.M., 2016. Strategies towards statistically robust interpretations of in situ U-Pb zircon geochronology. Geosci. Front. 7, 581–589. https://doi.org/10.1016/j.gsf.2015.11.006

Wilson, T.J., 1991. Transition from back-arc to foreland basin development in the southernmost Andes: stratigraphic record from the Ultima Esperanza District, Chile. Geol. Soc. Am. Bull. 103, 98–111. https://doi.org/10.1130/0016-7606(1991)103<0098:TFBATF>2.3.CO;2

Winn, R.D., Dott, R.H., 1979. Deep-water fan-channel conglomerates of Late Cretaceous age, southern Chile. Sedimentology 26, 203–228. https://doi.org/10.1111/j.1365-3091.1979.tb00351.x

Zeil, W., 1958. Sedimentation in der Magallanes-Geosynklinale mit besonderer Berucksichtigung des flysch. Geol. Rundsch., 47,425–443.

APPENDICES

APPENDIX A | SUPPLEMENTARY DATA FOR CHAPTER 2

Appendix A.1 | Compilation of measures sections

All measured stratigraphic sections that were used in Chapter 2 have been included in a separate PDF document compatible with Adobe Acrobat software or any other PDF viewer. Researchers who wish to view these measured sections should examine the supporting documents that were uploaded alongside this dissertation at https://vtechworks.lib.vt.edu/handle/10919/11041. The file that corresponds to this appendix is titled *Appendix_A.1_Kaempfe_SA_D_2022_Strat_Columns*.

Appendix A.2 | Compilation of paleoflow measurements

All measured paleoflow indicators that were used in Chapter 2 have been included in the following table:

Used magnetic declination = 13°

Section	Stratigraphic position (m)	Control point	East (UTM)	South (UTM)	Type	Dip_Dir	Dip
1	168	-	-	-	Flute	134	-
1	168	-	-	-	Flute	145	-
1	168	-	-	-	Tools	132	-
1	168	-	-	-	Tools	127	-
1	168	-	-	-	Tools	141	-
1	168	-	-	-	Tools	139	-
1	168	-	-	-	Tools	120	-
1	168	-	-	-	Tools	126	-
1	168	-	-	-	Grooves	136	-
1	193	-	-	-	Flutes	180	-
1	193	-	-	-	Flutes	178	-
1	193	-	-	-	Flutes	182	-
1	193	-	-	-	Flutes	186	-
1	193	-	-	-	Flutes	182	-
1	193	-	-	-	Tools	190	-
1	195	-	-	-	Tools	136	-
1	195	-	-	-	Tools	132	-
1	195	-	-	-	Tools	136	-
1	200	-	-	-	Tools	218	-
1	200	-	-	-	Tools	223	-
1	200	-	-	-	Tools	215	-
1	200	-	-	-	Tools	227	-
1	200	-	-	-	Tools	226	-
1	206	-	-	-	Tools	143	-
1	206	-	-	-	Tools	152	-
1	206	-	-	-	Tools	136	-
1	206	-	-	-	Tools	161	-
1	206	-	-	-	Tools	142	-
1	206	-	-	-	Tools	132	-
1	206	-	-	-	Tools	139	-
1	206	-	-	-	Tools	134	-
1	206	-	-	-	Flutes	145	-
1	206	-	-	-	Flutes	119	-
1	206	-	-	-	Flutes	146	-
1	206	-	-	-	Flutes	143	-
1	206	-	-	-	Flutes	138	-
1	206	-	-	-	Flutes	164	-
1	206	-	-	-	Flutes	118	-
1	206	-	-	-	Flutes	115	-
1	206	-	-	-	Flutes	122	-
1	206	-	-	-	Flutes	126	-

1	206	-	-	-	Flutes	156	-
1	206	-	-	-	Flutes	161	-
1	206	-	-	-	Flutes	155	-
1	206	-	-	-	Flutes	152	-
1	206	-	-	-	Flutes	154	-
1	206	-	-	-	Flutes	146	-
1	206	-	-	-	Flutes	126	-
1	206	-	-	-	Flutes	112	-
1	206	-	-	-	Flutes	132	-
1	206	-	-	-	Flutes	152	-
1	206	-	-	-	Flutes	164	-
1	206	-	-	-	Flutes	168	-
1	206	-	-	-	Flutes	135	-
1	206	-	-	-	Flutes	128	-
1	206	-	-	-	Flutes	130	-
1	206	-	-	-	Flutes	120	-
1	206	-	-	-	Flutes	146	-
1	206	-	-	-	Flutes	140	-
1	206	-	-	-	Flutes	160	-
1	206	-	-	-	Flutes	122	-
1	206	-	-	-	Flutes	145	-
1	206	-	-	-	Flutes	135	-
1	206	-	-	-	Flutes	138	-
1	206	-	-	-	Flutes	134	-
1	206	-	-	-	Flutes	146	-
1	206	-	-	-	Flutes	158	-
1	206	-	-	-	Flutes	160	-
1	206	-	-	-	Flutes	125	-
1	206	-	-	-	Flutes	130	-
1	255	-	-	-	Flutes	141	-
1	255	-	-	-	Flutes	150	-
1	255	-	-	-	Flutes	136	-
1	255	-	-	-	Tools	164	-
1	255	-	-	-	Tools	174	-
1	255	-	-	-	Tools	166	-
1	255	-	-	-	Tools	161	-
18B	74	-	-	-	Flutes	225	-
18B	74	-	-	-	Flutes	204	-
18B	74	-	-	-	Flutes	226	-
20	15	-	-	-	Tools	215	-
20	15	-	-	-	Tools	213	-
20	15	-	-	-	Tools	220	-
20	15	-	-	-	Flutes	195	-

20	15	-	-	-	Flutes	206	-
20	15	-	-	-	Flutes	194	-
20	15	-	-	-	Flutes	176	-
20	15	-	-	-	Flutes	212	-
20	15	-	-	-	Flutes	220	-
20	15	-	-	-	Flutes	197	-
20	15	-	-	-	Flutes	191	-
20	15	-	-	-	Flutes	200	-
20	15	-	-	-	Flutes	199	-
20	24	-	-	-	Flutes	184	-
20	24	-	-	-	Flutes	216	-
20	24	-	-	-	Flutes	198	-
20	24	-	-	-	Tools	191	-
20	24	-	-	-	Tools	164	-
20	24	-	-	-	Tools	184	-
20	24	-	-	-	Tools	165	-
20	24	-	-	-	Tools	170	-
20	24	-	-	-	Tools	165	-
20	24	-	-	-	Tools	175	-
20	24	-	-	-	Tools	180	-
20	24	-	-	-	Tools	184	-
20	40	-	-	-	Tools	150	-
20	40	-	-	-	Tools	157	-
20	40	-	-	-	Tools	145	-
20	40	-	-	-	Tools	144	-
20	40	-	-	-	Tools	146	-
20	40	-	-	-	Tools	143	-
20	40	-	-	-	Tools	138	-
20	40	-	-	-	Tools	130	-
20	40	-	-	-	Tools	152	-
20	40	-	-	-	Tools	155	-
20	40	-	-	-	Tools	142	-
20	40	-	-	-	Tools	156	-
20	40	-	-	-	Tools	148	-
20	40	-	-	-	Tools	175	-
20	40	-	-	-	Tools	162	-
20	40	-	-	-	Tools	180	-
20	40	-	-	-	Tools	176	-
20	40	-	-	-	Flutes	165	-
20	40	-	-	-	Flutes	170	-
20	40	-	-	-	Flutes	151	-
20	40	-	-	-	Flutes	143	-
20	40	-	-	-	Flutes	156	-

20	40	-	-	-	Flutes	158	-
20	40	-	-	-	Flutes	152	-
20	40	-	-	-	Flutes	152	-
20	40	-	-	-	Flutes	156	-
20	43	-	-	-	Tools	128	-
20	43	-	-	-	Tools	130	-
20	43	-	-	-	Flutes	123	-
22	12	-	-	-	Flutes	156	-
22	12	-	-	-	Flutes	143	-
22	12	-	-	-	Flutes	146	-
22	12	-	-	-	Flutes	137	-
22	37	-	-	-	Tools	158	-
22	37	-	-	-	Tools	182	-
22	37	-	-	-	Tools	200	-
22	73	-	-	-	Tools	155	-
22	73	-	-	-	Tools	154	-
22	73	-	-	-	Tools	154	-
22	73	-	-	-	Tools	160	-
22	128	-	-	-	Flutes	182	-
22	128	-	-	-	Flutes	168	-
22	128	-	-	-	Flutes	164	-
22	128	-	-	-	Flutes	209	-
22	128	-	-	-	Flutes	188	-
22	128	-	-	-	Flutes	210	-
22	128	-	-	-	Flutes	161	-
25F	1	-	-	-	Flutes	154	-
25F	1	-	-	-	Flutes	171	-
25F	1	-	-	-	Flutes	183	-
25F	1	-	-	-	Flutes	179	-
25F	1	-	-	-	Flutes	176	-
25F	1	-	-	-	Flutes	170	-
25F	1	-	-	-	Flutes	173	-
25F	1	-	-	-	Flutes	166	-
25F	1	-	-	-	Tools	174	-
25F	1	-	-	-	Tools	172	-
25F	1	-	-	-	Tools	183	-
25F	1	-	-	-	Tools	182	-
Kn1	4	I	675411	4293223	Ripples	175	25
Kn1	4	I	675411	4293223	Ripples	190	25
Kn1	4	I	675411	4293223	Ripples	154	29
Kn1	4	I	675411	4293223	Ripples	162	29
Kn1	4	I	675411	4293223	Ripples	164	21
Kn1	4	I	675411	4293223	Ripples	152	25

Kn1	4	I	675411	4293223	Ripples	122	21
Kn1	4	I	675411	4293223	Ripples	139	16
Kn1	4	I	675411	4293223	Ripples	144	16
Kn1	4	I	675411	4293223	Ripples	133	26
Kn1	4	I	675411	4293223	Ripples	157	22
Kn1	4	I	675411	4293223	Ripples	157	28
Kn1	4	I	675411	4293223	Ripples	155	16
Kn1	4	I	675411	4293223	Ripples	122	20
Kn1	4	I	675411	4293223	Ripples	133	32
Kn1	4	I	675411	4293223	Ripples	127	35
31A	4	-	-	-	Flutes	161	-
31A	4	-	-	-	Flutes	156	-
31A	4	-	-	-	Flutes	160	-
31A	4	-	-	-	Tools	168	-
31A	4	-	-	-	Tools	170	-
31C	15	-	-	-	Flutes	175	-
31C	15	-	-	-	Flutes	193	-
31C	15	-	-	-	Flutes	157	-
32A	14	-	-	-	Flutes	186	-
32A	14	-	-	-	Flutes	175	-
32A	14	-	-	-	Flutes	201	-
32A	29	-	-	-	Tools	170	-
32A	29	-	-	-	Tools	162	-
32A	29	-	-	-	Tools	176	-
32A	29	-	-	-	Tools	157	-
32A	29	-	-	-	Tools	163	-
32A	29	-	-	-	Tools	156	-
32A	29	-	-	-	Tools	161	-
32A	29	-	-	-	Tools	164	-
32A	29	-	-	-	Tools	176	-
32A	29	-	-	-	Tools	167	-
32A	29	-	-	-	Tools	172	-
32A	29	-	-	-	Tools	173	-
32A	29	-	-	-	Tools	181	-
32A	29	-	-	-	Flutes	150	-
32A	29	-	-	-	Flutes	158	-
32A	29	-	-	-	Flutes	146	-
32A	29	-	-	-	Flutes	142	-
32A	29	-	-	-	Flutes	126	-
32A	29	-	-	-	Flutes	161	-
32A	29	-	-	-	Flutes	160	-
32A	29	-	-	-	Flutes	148	-
32A	29	-	-	-	Flutes	156	-

32A	29	-	-	-	Flutes	168	-
32A	29	-	-	-	Flutes	150	-
32A	29	-	-	-	Flutes	142	-
32A	29	-	-	-	Flutes	149	-
32A	29	-	-	-	Flutes	152	-
32A	29	-	-	-	Flutes	151	-
32A	29	-	-	-	Flutes	161	-
32A	29	-	-	-	Flutes	133	-
32A	29	-	-	-	Flutes	154	-
32A	29	-	-	-	Flutes	166	-
32A	29	-	-	-	Flutes	169	-
32A	29	-	-	-	Flutes	149	-
32A	29	-	-	-	Flutes	126	-
32A	29	-	-	-	Flutes	147	-
32A	29	-	-	-	Flutes	145	-
32A	29	-	-	-	Flutes	128	-
-	-	A	675068	4293220	ImbricatedMudC	262	-
-	-	A	675068	4293220	ImbricatedMudC	270	-
-	-	A	675068	4293220	ImbricatedMudC	191	-
-	-	A	675068	4293220	ImbricatedMudC	223	-
-	-	A	675068	4293220	ImbricatedMudC	238	-
-	-	A	675068	4293220	ImbricatedMudC	234	-
-	-	A	675068	4293220	ImbricatedMudC	284	-
-	-	A	675068	4293220	ImbricatedMudC	253	-
-	-	A	675068	4293220	ImbricatedMudC	236	-
-	-	A	675068	4293220	ImbricatedMudC	262	-
-	-	A	675068	4293220	ImbricatedMudC	212	-
-	-	A	675068	4293220	ImbricatedMudC	131	-
-	-	A	675068	4293220	ImbricatedMudC	272	-
-	-	A	675068	4293220	ImbricatedMudC	183	-
-	-	A	675068	4293220	ImbricatedMudC	219	-
-	-	A	675068	4293220	ImbricatedMudC	228	-
-	-	A	675068	4293220	ImbricatedMudC	151	-
-	-	A	675068	4293220	ImbricatedMudC	197	-
-	-	A	675068	4293220	ImbricatedMudC	243	-
-	-	A	675068	4293220	ImbricatedMudC	258	-
-	-	A	675068	4293220	ImbricatedMudC	213	-
-	-	A	675068	4293220	ImbricatedMudC	218	-
-	-	A	675068	4293220	ImbricatedMudC	246	-
-	-	A	675068	4293220	ImbricatedMudC	231	-
-	-	A	675068	4293220	ImbricatedMudC	229	-
-	-	A	675068	4293220	ImbricatedMudC	283	-
-	-	A	675068	4293220	ImbricatedMudC	218	-

-	-	A	675068	4293220	ImbricatedMudC	212	-
-	-	A	675068	4293220	ImbricatedMudC	233	-
-	-	A	675068	4293220	ImbricatedMudC	239	-
-	-	A	675068	4293220	ImbricatedMudC	258	-
-	-	A	675068	4293220	ImbricatedMudC	260	-
-	-	A	675068	4293220	ImbricatedMudC	228	-
-	-	A	675068	4293220	ImbricatedMudC	283	-
-	-	A	675068	4293220	ImbricatedMudC	243	-
-	-	A	675068	4293220	ImbricatedMudC	255	-
-	-	A	675068	4293220	ImbricatedMudC	272	-
-	-	A	675068	4293220	ImbricatedMudC	192	-
-	-	A	675068	4293220	ImbricatedMudC	236	-
-	-	A	675068	4293220	ImbricatedMudC	227	-
-	-	A	675068	4293220	ImbricatedMudC	216	-
-	-	A	675068	4293220	ImbricatedMudC	249	-
-	-	A	675068	4293220	ImbricatedMudC	239	-
-	-	A	675068	4293220	ImbricatedMudC	272	-
-	-	A	675068	4293220	ImbricatedMudC	217	-
-	-	A	675068	4293220	ImbricatedMudC	243	-
-	-	A	675068	4293220	ImbricatedMudC	219	-
-	-	A	675068	4293220	ImbricatedMudC	245	-
-	-	A	675068	4293220	ImbricatedMudC	205	-
-	-	A	675068	4293220	ImbricatedMudC	254	-
-	-	A	675068	4293220	ImbricatedMudC	250	-
-	-	A	675068	4293220	ImbricatedMudC	225	-
-	-	A	675068	4293220	ImbricatedMudC	273	-
-	-	A	675068	4293220	ImbricatedMudC	283	-
-	-	A	675068	4293220	ImbricatedMudC	239	-
-	-	A	675068	4293220	ImbricatedMudC	242	-
-	-	A	675068	4293220	ImbricatedMudC	252	-
-	-	A	675068	4293220	ImbricatedMudC	276	-
-	-	B1	675140	4293240	Scour Edges	192	-
-	-	B1	675140	4293240	Scour Edges	192	-
-	-	B1	675140	4293240	ImbricatedMudC	243	-
-	-	B1	675140	4293240	ImbricatedMudC	220	-
-	-	B1	675140	4293240	ImbricatedMudC	239	-
-	-	B1	675140	4293240	ImbricatedMudC	270	-
-	-	B1	675140	4293240	ImbricatedMudC	232	-
-	-	B1	675140	4293240	ImbricatedMudC	231	-
-	-	B1	675140	4293240	ImbricatedMudC	229	-
-	-	B1	675140	4293240	ImbricatedMudC	239	-
-	-	B1	675140	4293240	ImbricatedMudC	219	-
-	-	B1	675140	4293240	ImbricatedMudC	178	-

-	-	B1	675140	4293240	ImbricatedMudC	182	-
-	-	B1	675140	4293240	ImbricatedMudC	186	-
-	-	B1	675140	4293240	ImbricatedMudC	141	-
-	-	B1	675140	4293240	ImbricatedMudC	268	-
-	-	B1	675140	4293240	ImbricatedMudC	252	-
-	-	B1	675140	4293240	ImbricatedMudC	222	-
-	-	B1	675140	4293240	ImbricatedMudC	220	-
-	-	B1	675140	4293240	ImbricatedMudC	223	-
-	-	B1	675140	4293240	ImbricatedMudC	194	-
-	-	B1	675140	4293240	ImbricatedMudC	252	-
-	-	B1	675140	4293240	ImbricatedMudC	270	-
-	-	B1	675140	4293240	ImbricatedMudC	254	-
-	-	B1	675140	4293240	ImbricatedMudC	169	-
-	-	B1	675140	4293240	ImbricatedMudC	266	-
-	-	B1	675140	4293240	ImbricatedMudC	232	-
-	-	B1	675140	4293240	ImbricatedMudC	278	-
-	-	B1	675140	4293240	ImbricatedMudC	241	-
-	-	B1	675140	4293240	ImbricatedMudC	294	-
-	-	B1	675140	4293240	ImbricatedMudC	203	-
-	-	B1	675140	4293240	ImbricatedMudC	243	-
-	-	B1	675140	4293240	ImbricatedMudC	235	-
-	-	B1	675140	4293240	ImbricatedMudC	228	-
-	-	B1	675140	4293240	ImbricatedMudC	230	-
-	-	B1	675140	4293240	ImbricatedMudC	190	-
-	-	B1	675140	4293240	ImbricatedMudC	226	-
-	-	B1	675140	4293240	ImbricatedMudC	159	-
-	-	B1	675140	4293240	ImbricatedMudC	250	-
-	-	B2	675179	4293254	ImbricatedMudC	203	-
-	-	B2	675179	4293254	ImbricatedMudC	269	-
-	-	B2	675179	4293254	ImbricatedMudC	231	-
-	-	B2	675179	4293254	ImbricatedMudC	222	-
-	-	B2	675179	4293254	ImbricatedMudC	219	-
-	-	B2	675179	4293254	ImbricatedMudC	231	-
-	-	B2	675179	4293254	ImbricatedMudC	238	-
-	-	B2	675179	4293254	ImbricatedMudC	227	-
-	-	B2	675179	4293254	ImbricatedMudC	271	-
-	-	B2	675179	4293254	ImbricatedMudC	265	-
-	-	C	675021	4293158	Scour Edges	265	-
-	-	C	675021	4293158	Scour Edges	267	-
-	-	C	675021	4293158	Scour Edges	308	-
-	-	C	675021	4293158	Scour Edges	261	-
-	-	C	675021	4293158	Scour Edges	275	-
-	-	C	675021	4293158	Scour Edges	272	-

-	-	C	675021	4293158	ImbricatedMudC	200	-
-	-	C	675021	4293158	ImbricatedMudC	259	-
-	-	C	675021	4293158	ImbricatedMudC	143	-
-	-	C	675021	4293158	ImbricatedMudC	207	-
-	-	C	675021	4293158	ImbricatedMudC	202	-
-	-	C	675021	4293158	ImbricatedMudC	164	-
-	-	C	675021	4293158	ImbricatedMudC	237	-
-	-	C	675021	4293158	ImbricatedMudC	242	-
-	-	D	675025	4293147	Tools	258	-
-	-	D	675025	4293147	Tools	257	-
-	-	E	675030	4293141	Ripples	137	-
-	-	E	675030	4293141	Ripples	152	-
-	-	E	675030	4293141	Ripples	156	-
-	-	E	675030	4293141	Ripples	149	-
-	-	E	675030	4293141	Ripples	147	-
-	-	E	675030	4293141	Ripples	205	-
-	-	E	675030	4293141	Ripples	118	-
-	-	E	675030	4293141	Ripples	129	-
-	-	E	675030	4293141	Ripples	115	-
-	-	E	675030	4293141	Ripples	108	-
-	-	E	675030	4293141	Ripples	110	-
-	-	E	675030	4293141	Ripples	159	-
-	-	E	675030	4293141	Ripples	93	-
-	-	E	675030	4293141	Ripples	120	-
-	-	E	675030	4293141	Ripples	162	-
-	-	F	675034	4293139	Ripples	147	-
-	-	F	675034	4293139	Ripples	133	-
-	-	F	675034	4293139	Ripples	132	-
-	-	F	675034	4293139	Ripples	102	-
-	-	F	675034	4293139	Ripples	135	-
-	-	F	675034	4293139	Ripples	164	-
-	-	F	675034	4293139	Ripples	143	-
-	-	F	675034	4293139	Ripples	137	-
-	-	F	675034	4293139	Ripples	172	-
-	-	F	675034	4293139	Ripples	176	-
-	-	F	675034	4293139	Ripples	156	-
-	-	F	675034	4293139	Ripples	129	-
-	-	F	675034	4293139	Ripples	164	-
-	-	F	675034	4293139	Ripples	146	-
-	-	F	675034	4293139	Ripples	127	-
-	-	F	675034	4293139	Ripples	172	-
-	-	F	675034	4293139	Ripples	122	-
-	-	F	675034	4293139	Ripples	127	-

-	-	F	675034	4293139	Ripples	154	-
-	-	F	675034	4293139	Scour Edges	167	-
-	-	F	675034	4293139	Scour Edges	152	-
-	-	F	675034	4293139	Scour Edges	168	-
-	-	F	675034	4293139	Tools	169	-
-	-	F	675034	4293139	Tools	189	-
-	-	F	675034	4293139	Tools	188	-
-	-	F	675034	4293139	Tools	183	-
-	-	F	675034	4293139	Tools	166	-
-	-	F	675034	4293139	Flutes	145	-
-	-	F	675034	4293139	Flutes	152	-
-	-	F	675034	4293139	Flutes	154	-
-	-	G1	675139	4293176	Flutes	194	-
-	-	G1	675139	4293176	Flutes	182	-
-	-	G1	675139	4293176	Flutes	200	-
-	-	G1	675139	4293176	Flutes	151	-
-	-	G1	675139	4293176	Scour Edges	153	-
-	-	G1	675139	4293176	Scour Edges	157	-
-	-	G1	675139	4293176	Scour Edges	198	-
-	-	G1	675139	4293176	Scour Edges	154	-
-	-	G1	675139	4293176	Scour Edges	174	-
-	-	G1	675139	4293176	Ripples	104	-
-	-	G1	675139	4293176	Ripples	112	-
-	-	G1	675139	4293176	Ripples	114	-
-	-	G1	675139	4293176	Ripples	105	-
-	-	G1	675139	4293176	Ripples	114	-
-	-	G1	675139	4293176	Ripples	158	-
-	-	G1	675139	4293176	Ripples	156	-
-	-	G2	675203	4293213	Scour Edges	151	-
-	-	G2	675203	4293213	Scour Edges	142	-
-	-	G2	675203	4293213	Scour Edges	146	-
21	4	H	-	-	Ripples	83	-
21	4	H	-	-	Ripples	55	-
21	4	H	-	-	Ripples	86	-
21	4	H	-	-	Ripples	69	-
21	4	H	-	-	Ripples	87	-
21	4	H	-	-	Ripples	49	-
21	4	H	-	-	Ripples	71	-
21	4	H	-	-	Ripples	78	-
21	4	H	-	-	Ripples	82	-
21	4	H	-	-	Ripples	77	-
-	-	J	675204	4293000	Tools	162	-
-	-	J	675204	4293000	Tools	174	-

-	-	J	675204	4293000	Tools	176	-
-	-	J	675204	4293000	Tools	168	-
-	-	J	675204	4293000	Tools	164	-
-	-	K	675168	4292913	Flutes	168	-
-	-	L	675040	4292890	Flutes	132	-
-	-	L	675040	4292890	Flutes	174	-
-	-	L	675040	4292890	Flutes	156	-
-	-	L	675040	4292890	Flutes	121	-
-	-	L	675040	4292890	Flutes	168	-
-	-	L	675040	4292890	Flutes	176	-
-	-	L	675040	4292890	Flutes	161	-
-	-	L	675040	4292890	Flutes	174	-
-	-	L	675040	4292890	Flutes	165	-
-	-	L	675040	4292890	Flutes	172	-
-	-	L	675040	4292890	Tools	172	-
-	-	L	675040	4292890	Tools	168	-
-	-	L	675040	4292890	Tools	161	-
-	-	L	675040	4292890	Tools	175	-
-	-	L	675040	4292890	Tools	165	-
-	-	L	675040	4292890	Tools	178	-
-	-	L	675040	4292890	Tools	168	-
-	-	L	675040	4292890	Grooves	174	-
-	-	L	675040	4292890	Grooves	178	-
-	-	M	674985	4292770	Tools	178	-
-	-	M	674985	4292770	Tools	176	-
-	-	M	674985	4292770	Tools	181	-
-	-	M	674985	4292770	Tools	171	-
-	-	M	674985	4292770	Tools	178	-
-	-	M	674985	4292770	Tools	185	-
-	-	M	674985	4292770	Tools	191	-
-	-	M	674985	4292770	Tools	173	-
-	-	M	674985	4292770	Tools	168	-
-	-	M	674985	4292770	Tools	191	-
-	-	M	674985	4292770	Tools	172	-
-	-	M	674985	4292770	Tools	168	-
-	-	M	674985	4292770	Tools	162	-
-	-	M	674985	4292770	Tools	163	-
-	-	M	674985	4292770	Tools	132	-
-	-	M	674985	4292770	Flutes	162	-
-	-	M	674985	4292770	Flutes	151	-
-	-	M	674985	4292770	Flutes	168	-
-	-	M	674985	4292770	Flutes	148	-
-	-	M	674985	4292770	Flutes	142	-

-	-	M	674985	4292770	Flutes	138	-
-	-	M	674985	4292770	Flutes	146	-
-	-	M	674985	4292770	Flutes	145	-
-	-	M	674985	4292770	Flutes	126	-
-	-	N	675016	4292908	Flutes	152	-
-	-	N	675016	4292908	Flutes	154	-
-	-	N	675016	4292908	Flutes	163	-
-	-	N	675016	4292908	Flutes	157	-
-	-	N	675016	4292908	Flutes	159	-
-	-	N	675016	4292908	Flutes	160	-
-	-	N	675016	4292908	Flutes	164	-
-	-	N	675016	4292908	Flutes	152	-
-	-	N	675016	4292908	Flutes	156	-
-	-	N	675016	4292908	Flutes	158	-
-	-	N	675016	4292908	Flutes	161	-
-	-	N	675016	4292908	Flutes	164	-
-	-	N	675016	4292908	Flutes	146	-
-	-	N	675016	4292908	Flutes	155	-
-	-	N	675016	4292908	Flutes	157	-
-	-	N	675016	4292908	Flutes	152	-
-	-	N	675016	4292908	Flutes	157	-
-	-	N	675016	4292908	Flutes	158	-
-	-	N	675016	4292908	Flutes	155	-
-	-	N	675016	4292908	Flutes	171	-
-	-	N	675016	4292908	Flutes	175	-
-	-	O	674919	4292472	Flutes	148	-
-	-	O	674919	4292472	Flutes	141	-
-	-	O	674919	4292472	Flutes	154	-

APPENDIX B | SUPPLEMENTARY DATA FOR CHAPTER 3

Appendix B.1 | Compilation of measures sections

All measured stratigraphic sections that were used in Chapter 3 have been included in a separate PDF document compatible with Adobe Acrobat software or any other PDF viewer. Researchers who wish to view these measured sections should examine the supporting documents that were uploaded alongside this dissertation at https://vtechworks.lib.vt.edu/handle/10919/11041. The file that corresponds to this appendix is titled *Appendix_B.1_Kaempfe_SA_D_2022_Strat_Columns*.

Appendix B.2 | Compilation of paleoflow measurements

All measured paleoflow indicators used in Chapter 3 have been included in the following table:

Used magnetic declination = 13°

Section	Stratigraphic position (m)	Control point	East (UTM)	South (UTM)	Type	Dip_Dir
ECB_1	7	-	-	-	flutes	155
ECB_1	7	-	-	-	flutes	146
ECB_1	7	-	-	-	flutes	152
ECB_1	7	-	-	-	flutes	150
ECB_1	7	-	-	-	flutes	140
ECB_1	7	-	-	-	flutes	143
ECB_1	7	-	-	-	flutes	139
ECB_1	7	-	-	-	flutes	128
ECB_1	41	-	-	-	flutes	160
ECB_1	41	-	-	-	flutes	153
ECB_1	41	-	-	-	flutes	140
ECB_1	41	-	-	-	flutes	142
ECB_1	41	-	-	-	flutes	159
ECB_1	124	-	-	-	tools	104
ECB_1	124	-	-	-	tools	96
ECB_1	124	-	-	-	tools	93
ECB_1	124	-	-	-	tools	100
ECB_1	336	-	-	-	Flute	122
ECB_1	336	-	-	-	Flute	112
ECB_1	336	-	-	-	Flute	150
ECB_1	336	-	-	-	Flute	110
ECB_1	336	-	-	-	Flute	116
ECB_1	336	-	-	-	Flute	102
ECB_1	336	-	-	-	Flute	106
ECB_1	336	-	-	-	Flute	115
ECB_1	336	-	-	-	Flute	104
ECB_1	336	-	-	-	Flute	110
ECB_1	336	-	-	-	Flute	113
ECB_1	336	-	-	-	Flute	105
ECB_1	337	-	-	-	Tool	114
ECB_1	337	-	-	-	Tool	119
ECB_1	337	-	-	-	Tool	122
ECB_1	339	-	-	-	Flute	107
ECB_1	339	-	-	-	Flute	112
ECB_1	339	-	-	-	Flute	95

ECB_1	339	-	-	-	Flute	105
ECB_1	339	-	-	-	Flute	134
ECB_1	339	-	-	-	Flute	114
ECB_1	339	-	-	-	Tool	108
ECB_1	339	-	-	-	Tool	107
ECB_1	339	-	-	-	Tool	112
ECB_1	339	-	-	-	Tool	118
ECB_1	339	-	-	-	Tool	111
ECB_1	339	-	-	-	Tool	110
ECB_1	339	-	-	-	Tool	112
ECB_1	339	-	-	-	Tool	82
ECB_1	339	-	-	-	Tool	90
ECB_1	340-343	-	-	-	Flute	109
ECB_1	340-343	-	-	-	Flute	110
ECB_1	340-343	-	-	-	Flute	122
ECB_1	340-343	-	-	-	Flute	111
ECB_1	340-343	-	-	-	Flute	114
ECB_1	340-343	-	-	-	Flute	105
ECB_1	340-343	-	-	-	Flute	124
ECB_1	340-343	-	-	-	Flute	129
ECB_1	340-343	-	-	-	Flute	121
ECB_1	340-343	-	-	-	Flute	111
ECB_1	340-343	-	-	-	Flute	120
ECB_1	340-343	-	-	-	Flute	118
ECB_1	340-343	-	-	-	Flute	121
ECB_1	340-343	-	-	-	Flute	116
ECB_1	340-343	-	-	-	Flute	119
ECB_1	340-343	-	-	-	Flute	124
ECB_1	340-343	-	-	-	Flute	110
ECB_1	340-343	-	-	-	Flute	119
ECB_1	340-343	-	-	-	Flute	111
ECB_1	340-343	-	-	-	Flute	114
ECB_1	340-343	-	-	-	Flute	119
ECB_1	340-343	-	-	-	Tool	89
ECB_1	340-343	-	-	-	Tool	85
ECB_1	345-350	-	-	-	Flute	110
ECB_1	345-350	-	-	-	Flute	114
ECB_1	345-350	-	-	-	Flute	119
ECB_1	345-350	-	-	-	Flute	106
ECB_1	345-350	-	-	-	Flute	118
ECB_1	345-350	-	-	-	Flute	132
ECB_1	345-350	-	-	-	Flute	136
ECB_1	345-350	-	-	-	Flute	141

ECB_1	345-350	-	-	-	Flute	128
ECB_1	345-350	-	-	-	Flute	138
ECB_1	345-350	-	-	-	Tool	154
ECB_1	345-350	-	-	-	Tool	126
ECB_1	345-350	-	-	-	Tool	144
ECB_1	345-350	-	-	-	Flutes	115
ECB_1	345-350	-	-	-	Flutes	111
ECB_1	345-350	-	-	-	Flutes	118
ECB_1	345-350	-	-	-	Flutes	106
ECB_1	345-350	-	-	-	Flutes	126
ECB_1	345-350	-	-	-	Flutes	121
ECB_1	345-350	-	-	-	Flutes	116
ECB_1	345-350	-	-	-	Tool	115
ECB_1	345-350	-	-	-	Tool	102
ECB_1	345-350	-	-	-	Tool	109
ECB_1	345-350	-	-	-	Flutes	115
ECB_1	345-350	-	-	-	Flutes	106
ECB_1	345-350	-	-	-	Flutes	115
ECB_1	353-356	-	-	-	Flutes	105
ECB_1	353-356	-	-	-	Flutes	114
ECB_1	353-356	-	-	-	Flutes	115
ECB_1	353-356	-	-	-	Flutes	120
ECB_1	353-356	-	-	-	Flutes	109
ECB_1	353-356	-	-	-	Flutes	104
ECB_1	353-356	-	-	-	Flutes	110
ECB_1	353-356	-	-	-	Flutes	106
ECB_1	353-356	-	-	-	Flutes	84
ECB_1	353-356	-	-	-	Tool	116
ECB_1	353-356	-	-	-	Tool	120
ECB_1	353-356	-	-	-	Tool	113
ECB_1	353-356	-	-	-	Tool	118
ECB_1	353-356	-	-	-	Flutes	140
ECB_1	353-356	-	-	-	Flutes	131
ECB_1	353-356	-	-	-	Flutes	136
ECB_1	353-356	-	-	-	Flutes	125
ECB_1	353-356	-	-	-	Flutes	131
ECB_1	353-356	-	-	-	Tool	146
ECB_1	353-356	-	-	-	Tool	133
ECB_1	353-356	-	-	-	Flutes	123
ECB_1	353-356	-	-	-	Flutes	141
ECB_1	353-356	-	-	-	Tool	144
ECB_1	353-356	-	-	-	Tool	149
ECB_1	353-356	-	-	-	Tool	159

ECB_1	353-356	-	-	-	Tool	190
ECB_1	353-356	-	-	-	Tool	150
ECB_1	353-356	-	-	-	Tool	132
ECB_1	359	-	-	-	Flutes	159
ECB_1	359	-	-	-	Flutes	155
ECB_1	359	-	-	-	Flutes	170
ECB_1	359	-	-	-	Flutes	176
ECB_1	359	-	-	-	Flutes	154
ECB_1	359	-	-	-	Flutes	162
ECB_1	359	-	-	-	Flutes	160
ECB_1	359	-	-	-	Tool	169
ECB_4	18	-	-	-	Flutes	140
ECB_4	18	-	-	-	Flutes	133
ECB_4	18	-	-	-	Flutes	130
ECB_4	18	-	-	-	Flutes	135
ECB_4	34	-	-	-	Flutes	139
ECB_4	34	-	-	-	Flutes	145
ECB_4	34	-	-	-	Flutes	146
ECB_4	34	-	-	-	Flutes	142
ECB_4	34	-	-	-	Flutes	145
ECB_5	30	-	-	-	Flutes	147
ECB_5	30	-	-	-	Flutes	134
ECB_5	30	-	-	-	Flutes	135
ECB_5	30	-	-	-	Flutes	139
ECB_5	30	-	-	-	Flutes	140
ECB_5	30	-	-	-	Flutes	133
ECB_5	30	-	-	-	Flutes	142
ECB_5	30	-	-	-	Flutes	145
ECB_5	30	-	-	-	Flutes	136
ECB_5	30	-	-	-	Flutes	131
ECB_5	30	-	-	-	Flutes	141
ECB_5	30	-	-	-	Flutes	121
ECB_5	30	-	-	-	Flutes	129
ECB_5	30	-	-	-	Flutes	133
ECB_5	30	-	-	-	Flutes	129
ECB_5	30	-	-	-	Flutes	134
ECB_8	16-18	-	-	-	Flutes	134
ECB_8	16-18	-	-	-	Flutes	134
ECB_8	16-18	-	-	-	Flutes	136
ECB_8	16-18	-	-	-	Flutes	114
ECB_8	16-18	-	-	-	Flutes	135
ECB_8	16-18	-	-	-	Flutes	134
ECB_8	16-18	-	-	-	Flutes	127

ECB_8	16-18	-	-	-	Flutes	131
ECB_8	16-18	-	-	-	Flutes	135
ECB_8	16-18	-	-	-	Flutes	119
ECB_8	16-18	-	-	-	Flutes	134
ECB_8	16-18	-	-	-	Flutes	121
-	-	PF1	676750	4331146	Flute	125
-	-	PF1	676750	4331146	Flute	118
-	-	PF1	676750	4331146	Flute	129
-	-	PF1	676750	4331146	Flute	108
-	-	PF1	676750	4331146	Flute	102
-	-	PF1	676750	4331146	Flute	125
-	-	PF1	676750	4331146	Flute	111
-	-	PF1	676750	4331146	Flute	109
-	-	PF1	676750	4331146	Flute	121
-	-	PF1	676750	4331146	Flute	108
-	-	PF1	676750	4331146	Flute	112
-	-	PF1	676750	4331146	Flute	115
-	-	PF1	676750	4331146	Flute	122
-	-	PF1	676750	4331146	Flute	115
-	-	PF2	676757	4331103	Flute	121
-	-	PF2	676757	4331103	Flute	105
-	-	PF2	676757	4331103	Flute	118
-	-	PF2	676757	4331103	Flute	111
-	-	PF2	676757	4331103	Tool	108
-	-	PF2	676757	4331103	Tool	111
-	-	PF2	676757	4331103	Tool	110
-	-	PF3	676754	4331118	Flute	116
-	-	PF3	676754	4331118	Flute	111
-	-	PF3	676754	4331118	Flute	110
-	-	PF3	676754	4331118	Flute	126
-	-	PF3	676754	4331118	Flute	113
-	-	PF3	676754	4331118	Flute	115
-	-	PF3	676754	4331118	Flute	100
-	-	PF3	676754	4331118	Flute	106
-	-	PF6	676765	4331036	Flute	109
-	-	PF6	676765	4331036	Flute	95
-	-	PF6	676765	4331036	Flute	104
-	-	PF6	676765	4331036	Flute	96
-	-	PF6	676765	4331036	Flute	110
-	-	PF6	676765	4331036	Flute	105
-	-	PF6	676765	4331036	Flute	101
-	-	PF7	676765	4331036	Flute	96
-	-	PF7	676765	4331036	Flute	111

-	-	PF7	676765	4331036	Flute	110
-	-	PF7	676765	4331036	Flute	100
-	-	PF7	676765	4331036	Flute	107
-	-	PF7	676765	4331036	Flute	108
-	-	PF7	676765	4331036	Flute	113
-	-	PF8	676768	4331019	Flute	110
-	-	PF8	676768	4331019	Flute	113
-	-	PF8	676768	4331019	Flute	108
-	-	PF8	676768	4331019	Flute	110
-	-	PF8	676768	4331019	Flute	98
-	-	PF8	676768	4331019	Flute	101
-	-	PF8	676768	4331019	Flute	102
-	-	PF8	676768	4331019	Flute	100
-	-	PF9	676772	4331021	Flute	128
-	-	PF9	676772	4331021	Flute	121
-	-	PF9	676772	4331021	Flute	122
-	-	PF9	676772	4331021	Flute	111
-	-	PF9	676772	4331021	Flute	140
-	-	PF10	676769	4331008	Flute	117
-	-	PF10	676769	4331008	Flute	117
-	-	PF10	676769	4331008	Flute	111
-	-	PF11	676769	4331008	Flute	99
-	-	PF11	676769	4331008	Flute	110
-	-	PF11	676769	4331008	Flute	111
-	-	PF11	676769	4331008	Flute	86
-	-	PF11	676769	4331008	Flute	96
-	-	PF11	676769	4331008	Flute	91
-	-	PF11	676769	4331008	Flute	97
-	-	PF11	676769	4331008	Flute	96
-	-	PF11	676769	4331008	Flute	97
-	-	PF11	676769	4331008	Flute	109
-	-	PF20	676776	4331000	Flute	112
-	-	PF20	676776	4331000	Flute	126
-	-	PF20	676776	4331000	Flute	123
-	-	PF20	676776	4331000	Flute	122
-	-	PF20	676776	4331000	Flute	118
-	-	PF20	676776	4331000	Flute	125
-	-	PF20	676776	4331000	Flute	120
-	-	PF20	676776	4331000	Flute	118
-	-	PF20	676776	4331000	Flute	119
-	-	PF20	676776	4331000	Flute	113
-	-	PF21	676759	4330952	Flute	111
-	-	PF21	676759	4330952	Flute	110

-	-	PF21	676759	4330952	Flute	99
-	-	PF22	676776	4330964	Flute	120
-	-	PF22	676776	4330964	Flute	116
-	-	PF22	676776	4330964	Flute	104
-	-	PF22	676776	4330964	Flute	111
-	-	PF22	676776	4330964	Flute	97
-	-	PF22	676776	4330964	Flute	119
-	-	PF22	676776	4330964	Tool	95
-	-	PF23	676786	4330963	Flute	160
-	-	PF23	676786	4330963	Flute	169
-	-	PF23	676786	4330963	Flute	171
-	-	PF23	676786	4330963	Flute	169
-	-	PF23	676786	4330963	Flute	163
-	-	PF23	676786	4330963	Flute	164
-	-	PF23	676786	4330963	Flute	170
-	-	PF23	676786	4330963	Flute	168
-	-	PF23	676786	4330963	Flute	172
-	-	PF23	676786	4330963	Flute	170
-	-	PF23	676786	4330963	Flute	161
-	-	PF23	676786	4330963	Flute	156
-	-	PF23	676786	4330963	Flute	147
-	-	PF23	676786	4330963	Flute	151
-	-	PF23	676786	4330963	Flute	164
-	-	PF23	676786	4330963	Flute	166
-	-	PF23	676786	4330963	Flute	176
-	-	PF23	676786	4330963	Flute	170
-	-	PF23	676786	4330963	Flute	180
-	-	PF23	676786	4330963	Flute	171
-	-	PF24	676786	4330963	Flute	163
-	-	PF25	676770	4330898	Flute	102
-	-	PF26	676770	4330898	Flute	120
-	-	PF26	676770	4330898	Flute	110
-	-	PF15	676815	4330831	Flute	128
-	-	PF15	676815	4330831	Flute	125
-	-	PF15	676815	4330831	Flute	121
-	-	PF15	676815	4330831	Flute	129
-	-	PF15	676815	4330831	Flute	111
-	-	PF15	676815	4330831	Flute	125
-	-	PF15	676815	4330831	Flute	120
-	-	PF15	676815	4330831	Flute	123
-	-	PF16	676815	4330831	Flute	141
-	-	PF16	676815	4330831	Flute	146
-	-	PF16	676815	4330831	Flute	155

-	-	PF16	676815	4330831	Flute	135
-	-	PF17	676815	4330831	Flute	149
-	-	PF17	676815	4330831	Flute	157
-	-	PF17	676815	4330831	Flute	146
-	-	PF17	676815	4330831	Flute	153
-	-	PF17	676815	4330831	Flute	145
-	-	PF17	676815	4330831	Flute	141
-	-	PF17	676815	4330831	Flute	151
-	-	PF17	676815	4330831	Flute	147
-	-	PF17	676815	4330831	Flute	140
-	-	PF17	676815	4330831	Flute	140
-	-	PF17	676815	4330831	Flute	157
-	-	PF17	676815	4330831	Flute	169
-	-	PF17	676815	4330831	Tool	153
-	-	PF17	676815	4330831	Tool	150
-	-	PF17	676815	4330831	Tool	144
-	-	PF17	676815	4330831	Tool	165
-	-	PF17	676815	4330831	Tool	138
-	-	PF17	676815	4330831	Tool	152
-	-	PF17	676815	4330831	Tool	161
-	-	PF17	676815	4330831	Tool	159
-	-	PF17	676815	4330831	Tool	144
-	-	PF17	676815	4330831	Tool	150
-	-	PF18	676807	4330759	Flute	99
-	-	PF18	676807	4330759	Flute	102
-	-	PF18	676807	4330759	Flute	107
-	-	PF18	676807	4330759	Flute	97
-	-	PF18	676807	4330759	Flute	110
-	-	PF19	676821	4330760	Flute	108
-	-	PF19	676821	4330760	Flute	111
-	-	PF19	676821	4330760	Flute	115
-	-	PF19	676821	4330760	Flute	108
-	-	PF19	676821	4330760	Flute	112
-	-	PF19	676821	4330760	Flute	104
-	-	PF19	676821	4330760	Flute	109
-	-	PF19	676821	4330760	Flute	114
-	-	PF46	676825	4330797	Flute	159
-	-	PF46	676825	4330797	Flute	168
-	-	PF46	676825	4330797	Flute	172
-	-	PF46	676825	4330797	Flute	175
-	-	PF46	676825	4330797	Flute	162
-	-	PF46	676825	4330797	Flute	160
-	-	PF46	676825	4330797	Flute	164

-	-	PF46	676825	4330797	Flute	168
-	-	PF46	676825	4330797	Flute	171
-	-	PF46	676825	4330797	Flute	150
-	-	PF46	676825	4330797	Flute	165
-	-	PF46	676825	4330797	Flute	155
-	-	PF46	676825	4330797	Flute	165
-	-	PF46	676825	4330797	Flute	161
-	-	PF46	676825	4330797	Tool	161
-	-	PF47	676825	4330797	Flute	171
-	-	PF47	676825	4330797	Flute	168
-	-	PF47	676825	4330797	Flute	166
-	-	PF47	676825	4330797	Flute	174
-	-	PF47	676825	4330797	Flute	162
-	-	PF47	676825	4330797	Flute	154
-	-	PF47	676825	4330797	Flute	141
-	-	PF47	676825	4330797	Flute	140
-	-	PF47	676825	4330797	Flute	155
-	-	PF47	676825	4330797	Flute	159
-	-	PF47	676825	4330797	Flute	139
-	-	PF47	676825	4330797	Flute	154
-	-	PF47	676825	4330797	Flute	162
-	-	PF47	676825	4330797	Flute	157
-	-	PF47	676825	4330797	Flute	166
-	-	PF47	676825	4330797	Tool	165
-	-	PF47	676825	4330797	Tool	167
-	-	PF47	676825	4330797	Tool	145
-	-	PF47	676825	4330797	Tool	150
-	-	PF47	676825	4330797	Tool	154
-	-	PF48	676825	4330797	Tool	126
-	-	PF48	676825	4330797	Tool	150
-	-	PF 49	676919	4330288	Tool	127
-	-	PF 49	676919	4330288	Flute	142
-	-	PF 49	676919	4330288	Flute	125
-	-	PF 49	676919	4330288	Flute	150
-	-	PF 49	676919	4330288	Flute	132
-	-	PF 49	676919	4330288	Flute	137
-	-	PF 49	676919	4330288	Flute	135
-	-	PF50	676919	4330288	Flute	124
-	-	PF50	676919	4330288	Flute	118
-	-	PF50	676919	4330288	Flute	136
-	-	PF51	676919	4330288	Flute	97
-	-	PF51	676919	4330288	Flute	94
-	-	PF51	676919	4330288	Flute	106

-	-	PF52	676919	4330288	Flute	106
-	-	PF52	676919	4330288	Flute	110
-	-	PF52	676919	4330288	Flute	107
-	-	PF52	676919	4330288	Flute	107
-	-	PF52	676919	4330288	Flute	121
-	-	PF52	676919	4330288	Flute	101
-	-	PF52	676919	4330288	Flute	104
-	-	PF53	676933	4330286	Flute	145
-	-	PF53	676933	4330286	Flute	142
-	-	PF53	676933	4330286	Flute	142
-	-	PF53	676933	4330286	Flute	150
-	-	PF53	676933	4330286	Flute	152
-	-	PF53	676933	4330286	Flute	155
-	-	PF53	676933	4330286	Flute	159
-	-	PF54	676933	4330286	Tool	148
-	-	PF54	676933	4330286	Flute	154
-	-	PF54	676933	4330286	Flute	150
-	-	PF54	676933	4330286	Flute	148
-	-	PF54	676933	4330286	Flute	146
-	-	PF55	676934	4330243	Flute	132
-	-	PF55	676934	4330243	Flute	123
-	-	PF55	676934	4330243	Flute	126
-	-	PF55	676934	4330243	Flute	130
-	-	PF55	676934	4330243	Flute	114
-	-	PF55	676934	4330243	Flute	117
-	-	PF55	676934	4330243	Flute	131
-	-	PF55	676934	4330243	Flute	126
-	-	PF55	676934	4330243	Flute	144
-	-	PF55	676934	4330243	Flute	139
-	-	PF55	676934	4330243	Flute	137
-	-	PF55	676934	4330243	Flute	133
-	-	PF55	676934	4330243	Flute	135
-	-	PF56	676934	4330243	Flute	130
-	-	PF56	676934	4330243	Flute	142
-	-	PF56	676934	4330243	Flute	124
-	-	PF57	676934	4330243	Flute	115
-	-	PF57	676934	4330243	Flute	111
-	-	PF59	676948	4330211	Flute	159
-	-	PF59	676948	4330211	Flute	160
-	-	PF59	676948	4330211	Flute	150
-	-	PF59	676948	4330211	Flute	152
-	-	PF59	676948	4330211	Flute	157
-	-	PF59	676948	4330211	Flute	149

-	-	PF60	676895	4330498	Flute	133
-	-	PF60	676895	4330498	Flute	131
-	-	PF60	676895	4330498	Flute	141
-	-	PF60	676895	4330498	Flute	136
-	-	PF60	676895	4330498	Flute	130
-	-	PF60	676895	4330498	Flute	132
-	-	PF60	676895	4330498	Flute	135
-	-	PF60	676895	4330498	Flute	129
-	-	PF60	676895	4330498	Flute	131
-	-	PF60	676895	4330498	Flute	128
-	-	PF61	676910	4330501	Flute	172
-	-	PF61	676910	4330501	Flute	161
-	-	PF61	676910	4330501	Flute	164
-	-	PF62	676910	4330501	Flute	171
-	-	PF62	676910	4330501	Flute	166
-	-	PF62	676910	4330501	Flute	176
-	-	PF62	676910	4330501	Flute	160
-	-	PF62	676910	4330501	Flute	149
-	-	PF62	676910	4330501	Flute	161
-	-	PF62	676910	4330501	Flute	153
-	-	PF62	676910	4330501	Flute	171
-	-	PF62	676910	4330501	Flute	190
-	-	PF63	676910	4330501	Flute	160
-	-	PF63	676910	4330501	Flute	151
-	-	PF63	676910	4330501	Flute	155
-	-	PF63	676910	4330501	Flute	156
-	-	PF63	676910	4330501	Flute	145
-	-	PF63	676910	4330501	Flute	157
-	-	PF63	676910	4330501	Flute	161
-	-	PF63	676910	4330501	Flute	160
-	-	PF63	676910	4330501	Flute	149
-	-	PF63	676910	4330501	Flute	156
-	-	PF63	676910	4330501	Flute	153
-	-	PF63	676910	4330501	Flute	154
-	-	PF63	676910	4330501	Flute	154
-	-	PF63	676910	4330501	Flute	155
-	-	PF63	676910	4330501	Flute	154
-	-	PF63	676910	4330501	Flute	151
-	-	PF63	676910	4330501	Flute	150
-	-	PF63	676910	4330501	Flute	151
-	-	PF63	676910	4330501	Flute	150
-	-	PF63	676910	4330501	Flute	150
-	-	PF63	676910	4330501	Flute	146

-	-	PF63	676910	4330501	Flute	155
-	-	PF63	676910	4330501	Flute	151
-	-	PF64	676910	4330501	Flute	140
-	-	PF64	676910	4330501	Flute	138
-	-	PF64	676910	4330501	Flute	151
-	-	PF64	676910	4330501	Flute	143
-	-	PF64	676910	4330501	Flute	149
-	-	PF64	676910	4330501	Tool	145

Appendix B.3 | Compilation of fault measurements

All measured faults used in Chapter 3 have been included in the following table:

Used magnetic declination = 13°

Location	Strike	Dip	Quad	Type
ECB-N	42	37	E	Normal
ECB-N	45	41	E	Normal
ECB-N	43	64	E	Normal
ECB-N	46	64	E	Normal
ECB-N	355	82	E	Normal
ECB-N	21	32	E	Normal
ECB-N	80	30	E	Normal
ECB-N	37	49	E	Normal
ECB-N	50	39	S	Normal
ECB-N	39	57	S	Normal
ECB-N	54	39	S	Normal
ECB-N	19	42	E	Normal
ECB-N	39	54	S	Normal
ECB-N	168	62	E	Normal
ECB-C	149	44	N	Normal
ECB-C	112	56	N	Normal
ECB-C	291	52	N	Normal
ECB-C	135	45	N	Normal
ECB-C	296	62	N	Normal
ECB-N	39	59	S	Normal
ECB-N	30	42	S	Normal
ECB-N	40	39	S	Normal
ECB-N	29	48	S	Normal
ECB-N	165	77	E	Normal
ECB-N	35	47	S	Normal
ECB-N	85	46	S	Normal
ECB-N	108	54	S	Normal
ECB-N	33	50	S	Normal
ECB-N	31	40	S	Normal
ECB-N	58	46	S	Normal
ECB-N	47	45	S	Normal
ECB-N	63	78	N	Normal
ECB-N	52	59	S	Normal
ECB-N	83	32	S	Normal
ECB-N	65	45	S	Normal
ECB-N	51	52	S	Normal

ECB-N	35	47	S	Normal
ECB-N	32	36	E	Normal
ECB-N	45	45	E	Normal
ECB-N	33	57	S	Normal
ECB-N	146	65	N	Normal
ECB-N	18	57	S	Normal
ECB-S	104	77	N	Normal
ECB-S	125	71	N	Normal
ECB-S	141	88	N	Normal
ECB-S	138	88	N	Normal
ECB-S	96	77	N	Normal
ECB-S	155	90	N	Normal
ECB-S	144	66	N	Normal
ECB-S	142	66	N	Normal
ECB-S	148	70	N	Normal
ECB-S	150	64	N	Normal

Appendix B.4 | Compilation of injectite measurements

All injectite measurements used in Chapter 3 have been included in the following table:

Used magnetic declination = 13°

Location	Strike	Dip	Quad	Type	Thickness
ECB-S	112	87	N	injectite	10
ECB-S	107	70	S	injectite	5
ECB-S	90	87	S	injectite	5
ECB-S	113	83	S	injectite	15
ECB-S	304	89	N	injectite	8
ECB-S	83	70	S	injectite	10
ECB-S	116	87	S	injectite	15
ECB-S	111	82	N	injectite	15
ECB-S	105	70	S	injectite	10
ECB-S	115	90		injectite	10
ECB-S	108	85	S	injectite	6
ECB-S	109	78	S	injectite	15
ECB-S	136	76	W	injectite	20
ECB-S	118	74	S	injectite	20
ECB-S	206	42	w	injectite	88
ECB-S	78	72	N	injectite	25
ECB-S	140	81	S	injectite	10
ECB-S	143	83	S	injectite	10
ECB-S	107	67	S	injectite	10
ECB-S	100	83	N	injectite	8
ECB-S	133	77	S	injectite	60
ECB-S	141	67	S	injectite	15
ECB-S	143	72	w	injectite	59
ECB-S	174	72	W	injectite	60
ECB-S	53	82	N	injectite	40
ECB-S	233	77	N	injectite	-
ECB-S	178	60	W	injectite	-
ECB-S	171	82	W	injectite	-
ECB-N	158	62	W	injectite	20
ECB-N	168	86	W	injectite	40
ECB-N	158	62	W	injectite	15
ECB-N	157	81	S	injectite	20
ECB-N	160	66	W	injectite	-
ECB-N	88	83	S	injectite	20
ECB-N	14	82	W	injectite	-
ECB-N	137	83	S	injectite	25

ECB-N	179	68	W	injectite	25
ECB-N	184	87	W	injectite	20
ECB-N	177	68	W	injectite	30
ECB-N	25	56	W	injectite	25
ECB-N	181	77	W	injectite	25
ECB-N	173	78	W	injectite	20
ECB-N	190	68	W	injectite	30
ECB-N	179	73	W	injectite	8
ECB-N	179	81	W	injectite	10
ECB-N	35	87	W	injectite	8
ECB-N	22	63	W	injectite	25
ECB-N	166	69	W	injectite	40
ECB-N	163	63	W	injectite	10
ECB-N	94	88	S	injectite	25
ECB-N	77	83	N	injectite	25
ECB-S	108	78	S	injectite	-
ECB-S	124	74	S	injectite	15
ECB-S	88	85	S	injectite	-
ECB-S	129	79	S	injectite	15
ECB-S	148	76	S	injectite	-
ECB-S	135	83	S	injectite	-
ECB-S	332	90		injectite	-
ECB-S	140	67	S	injectite	-
ECB-S	146	80	S	injectite	-
ECB-S	146	75	S	injectite	-
ECB-S	168	71	W	injectite	-
ECB-S	164	72	W	injectite	30
ECB-S	164	70	W	injectite	15
ECB-S	164	70	W	injectite	-
ECB-S	109	65	S	injectite	-
ECB-S	127	68	S	injectite	10
ECB-S	130	64	S	injectite	5
ECB-S	142	90		injectite	10
ECB-S	155	90		injectite	15
ECB-S	148	86	S	injectite	5
ECB-S	156	74	S	injectite	-
ECB-S	169	90		injectite	-
ECB-S	101	76	S	injectite	-
ECB-S	178	80	W	injectite	35
ECB-S	145	80	S	injectite	15
ECB-S	116	90		injectite	10
ECB-S	102	64	S	injectite	5
ECB-S	120	65	S	injectite	40

ECB-S	128	70	S	injectite	10
ECB-S	207	60	W	injectite	40
ECB-S	132	70	S	injectite	5
ECB-S	80	68	S	injectite	5
ECB-S	126	85	S	injectite	5
ECB-S	148	88	S	injectite	10
ECB-S	60	55	S	injectite	-
ECB-S	172	70	W	injectite	40
ECB-S	60	86	S	injectite	-
ECB-S	57	86	S	injectite	30
ECB-S	22	65	E	injectite	40
ECB-S	95	83	S	injectite	20
ECB-S	240	80	N	injectite	5
ECB-S	86	90		injectite	5
ECB-S	178	80	W	injectite	65
ECB-S	34	70	S	injectite	50
ECB-S	180	90		injectite	15
ECB-S	181	82	W	injectite	-
ECB-S	32	85	S	injectite	5
ECB-S	173	80	W	injectite	5
ECB-S	205	87	W	injectite	5
ECB-S	177	86	W	injectite	-
ECB-S	184	78	W	injectite	-
ECB-S	185	90		injectite	-
ECB-S	176	78	W	injectite	-
ECB-S	168	82	W	injectite	-
ECB-C	176	39	S	injectite	10
ECB-C	164	66	S	injectite	10
ECB-C	161	84	S	injectite	20
ECB-C	164	90		injectite	25
ECB-C	163	75	W	injectite	10
ECB-C	154	83	W	injectite	25
ECB-C	136	84	S	injectite	20
ECB-C	142	76	W	injectite	15
ECB-C	162	72	W	injectite	10
ECB-C	159	73	W	injectite	-
ECB-C	157	68	S	injectite	20
ECB-N	226	72	N	injectite	5
ECB-N	181	70	W	injectite	20
ECB-N	184	62	W	injectite	15
ECB-N	201	68	W	injectite	10
ECB-N	154	48	W	injectite	25
ECB-N	196	44	W	injectite	20

ECB-N	63	60	S	injectite	5
ECB-N	78	76	S	injectite	5
ECB-N	265	62	N	injectite	10
ECB-N	160	85	S	injectite	12
ECB-N	171	88	S	injectite	12
ECB-N	11	76	W	injectite	12
ECB-N	164	35	W	injectite	-
ECB-N	190	74	N	injectite	5
ECB-N	170	74	W	injectite	-
ECB-C	155	78	W	injectite	-
ECB-C	154	64	S	injectite	15
ECB-C	152	69	S	injectite	12
ECB-C	158	56	S	injectite	40
ECB-C	139	60	S	injectite	-
ECB-C	156	70	S	injectite	15
ECB-C	150	74	S	injectite	5
ECB-C	155	90		injectite	40
ECB-C	144	65	S	injectite	10
ECB-C	150	75	S	injectite	5
ECB-C	170	73	S	injectite	10
ECB-C	160	76	S	injectite	10
ECB-C	150	66	S	injectite	50

Appendix B.5 | Compilation of sedimentary parameters for quantitative analysis of sandstone beds

Measured sedimentary parameters used in figures 3.7 and 3.13 of Chapter 3 have been included in a separate text file. All text files are tab delimited. Researchers who wish to view these data should examine the supporting documents that were uploaded alongside this dissertation at https://vtechworks.lib.vt.edu/handle/10919/11041. The file that corresponds to this appendix is titled *Appendix_B.5_Kaempfe_SA_D_2022_Sandstones*.

Bed thickness	
Very thin bed	<3 cm
Thin bed	3-10 cm
Medium bed	10-30 cm
Thick bed	30-100 cm
Very thick bed	>100 cm

Maximum grain size (estimated in the field)	
Very fine lower	2
Very fine upper	3
Fine lower	4
Fine upper	5
Medium lower	6
Medium upper	7
Coarse lower	8
Coarse upper	9

Appendix B.6 | Script for computing boxcar filter sandstone percentage

Python (Jupyter notebook) script for calculating moving sandstone percentage (shown in Fig. 3.7 and 3.13); Based on Matt Hall's boxcar filter code:

https://gist.github.com/kwinkunks/ee4ca6a440b9b6f50c82dc0b36a9a4be

Cell 1:
```
import striplog
striplog.__version__
```

Cell 2:
```
from striplog import Striplog, Component
s = Striplog.from_csv(filename='XXXX.csv')    # put filename in place of XXXX
s.plot(aspect=3)
```

Cell 3:
```
# 0.02 step was used for ECB data
start, stop, step = 89, 124, 0.02
L = s.to_log(start=start, stop=stop, step=step)
```

Cell 4:
```
import matplotlib.pyplot as plt
plt.plot(L)
len(L)
```

Cell 5:
```
import numpy as np
# Define a window length in m
window_length = 5   # change this to desired length
# Compute the number of samples in the window
N = int(window_length / step)
# Make the boxcar filter: divide by N to get the mean,
# and multiply by 100 to get percentage not proportion
boxcar = 100 * np.ones(N) / N
# Make a linear 'space' (range of numbers) representing
# depth. (We only really need this for the plot.)
z = np.linspace(start, stop, L.size)
# Convolve the log with the boxcar. This computes the
# running mean. (Convolution does a running weighted sum
# in the window; the weights are the boxcar array.)
prop = np.convolve(L, boxcar, mode='same')
# Quick plot of results
plt.plot(z, prop)
plt.grid(c='k', alpha=0.2)
plt.ylim(-5, 105)
```

Cell 6:

```
# outputs the data that was then used to create plots in Fig. 7; replace XXXXXX with name for .csv file
z_prop = np.stack([z, prop], axis=1)
np.savetxt('XXXXXX.csv', z_prop, delimiter=',', header='elev, sand_perc', comments='', fmt='%1.2f')
```

Appendix B.7 | Script for computing boxcar filter for sandstone grainsize and bed thickness

The MatLab script for computing moving averages (used for grain size and bed thickness in figures 3.7 and 3.13) is the following:

```
%% This scripts does a moving average of field observations
%(e.g. grain size, organic matter, bed thickness) along a geologic log

%% usual commands at the start of a script to clear any previous work in Matlab
close all
clc
clear all

%% load data in Matlab workspace
load ('South_Chingue.mat')
load ('ECB1.mat')
load ('ECB2.mat')
load ('ECB3_B7.mat')
load ('ECB_3BDE.mat')
load ('ECB_5.mat')
load ('ECB_4.mat')
load ('ECB_7.mat')
load ('ECB_2L.mat')

%% chose data file we want to process
Data=ECB_5;
Y=Data(:,1); %Define Y axis (Stratigraphic position)
GS=Data(:,2); %Grain size data
BT=Data(:,3); %Bed thickness data

%% Moving average between observations - Grain size
GS_mean_5=movmean(GS,5); % average over 5 observations
GS_mean_10=movmean(GS,10); % average over 10 observations
GS_mean_15=movmean(GS,15); % average over 15 observations
GS_mean_20=movmean(GS,20); % average over 20 observations
GS_mean_25=movmean(GS,25); % average over 25 observations
GS_mean_30=movmean(GS,30); % average over 30 observations
GS_mean_40=movmean(GS,40); % average over 40 observations

%Moving average between observations - Bed thickness
BT_mean_5=movmean(BT,5); % average over 5 observations
BT_mean_10=movmean(BT,10); % average over 10 observations
BT_mean_15=movmean(BT,15); % average over 15 observations
BT_mean_20=movmean(BT,20); % average over 20 observations
BT_mean_25=movmean(BT,25); % average over 25 observations
BT_mean_30=movmean(BT,30); % average over 30 observations
```

```
BT_mean_40=movmean(BT,40); % average over 40 observations

%% save generated data in ascii files
save('ECB_3BDE_GS_5obs.txt','GS_mean_5','-ASCII');
save('ECB_3BDE_GS_40obs.txt','GS_mean_40','-ASCII');
save('ECB_3BDE_BT_5obs.txt','BT_mean_5','-ASCII');
save('ECB_3BDE_BT_40obs.txt','BT_mean_40','-ASCII');


%% Create 8 plots in 1 figure to display bed thickness data

f=figure

subplot (1,6,1)
plot (BT, Y,'Color',[0 0.5 0.1],'LineWidth',0.1)
xlabel (['Bed thickness (BT) raw'])
ylabel (['Stratigraphic position (m)'])

subplot (1,6,2)
plot (BT_mean_5, Y,'Color',[0 0.5 0.1],'LineWidth',0.1)
xlabel (['mean 5 obs'])

subplot (1,6,3)
plot (BT_mean_10, Y,'Color',[0 0.5 0.1],'LineWidth',0.1)
xlabel (['mean 10 obs'])

% subplot (1,8,4)
% plot (BT_mean_15, Y,'Color',[0 0.5 0.1],'LineWidth',0.1)
% xlabel (['mean 15 obs'])

subplot (1,6,4)
plot (BT_mean_20, Y,'Color',[0 0.5 0.1],'LineWidth',0.1)
xlabel (['mean 20 obs'])

subplot (1,6,5)
plot (BT_mean_25, Y,'Color',[0 0.5 0.1],'LineWidth',0.1)
xlabel (['mean 25 obs'])

% subplot (1,8,7)
% plot (BT_mean_30, Y,'Color',[0 0.5 0.1],'LineWidth',0.1)
% xlabel (['mean 30 obs'])

subplot (1,6,6)
plot (BT_mean_40, Y,'Color',[0 0.5 0.1],'LineWidth',0.1)
xlabel (['mean 40 obs'])
```

```
%%
h=gcf;
set(h,'PaperPositionMode','auto');
set(h,'PaperOrientation','landscape');
set(h,'Position',[50 50 1200 800]);
print(gcf, '-dpdf', 'ECB_5_BT.pdf')

%% Creat 8 plots in 1 figure to display Grain Size data

f=figure

subplot (1,8,1)
plot (GS, Y,'Color',[1 0.1 0.1],'LineWidth',0.1)
xlabel (['Grain size (GS) raw'])
ylabel (['Stratigraphic position (m)'])

subplot (1,8,2)
plot (GS_mean_5, Y,'Color',[1 0.1 0.1],'LineWidth',0.1)
xlabel (['mean 5 obs'])

subplot (1,8,3)
plot (GS_mean_10, Y,'Color',[1 0.1 0.1],'LineWidth',0.1)
xlabel (['mean 10 obs'])

subplot (1,8,4)
plot (GS_mean_15, Y,'Color',[1 0.1 0.1],'LineWidth',0.1)
xlabel (['mean 15 obs'])

subplot (1,8,5)
plot (GS_mean_20, Y,'Color',[1 0.1 0.1],'LineWidth',0.1)
xlabel (['mean 20 obs'])

subplot (1,8,6)
plot (GS_mean_25, Y,'Color',[1 0.1 0.1],'LineWidth',0.1)
xlabel (['mean 25 obs'])

subplot (1,8,7)
plot (GS_mean_30, Y,'Color',[1 0.1 0.1],'LineWidth',0.1)
xlabel (['mean 30 obs'])

subplot (1,8,8)
plot (GS_mean_40, Y,'Color',[1 0.1 0.1],'LineWidth',0.1)
xlabel (['mean 40 obs'])
%%
h=gcf;
set(h,'PaperPositionMode','auto');
```

```
set(h,'PaperOrientation','landscape');
set(h,'Position',[50 50 1200 800]);
print(gcf, '-dpdf', 'ECB5_GS.pdf')

%% save figure

set(f,'Units','Inches');
pos = get(f,'Position');
set(f,'PaperPositionMode','Auto','PaperUnits','Inches','PaperSize',[pos(3), pos(4)])
print(f,'ChingueSouth_ECB1_BT','-dpdf','-r0')
```

APPENDIX C | SUPPLEMENTARY DATA FOR CHAPTER 4

Appendix C.1 | Geochronologic data after 5s screening abalations

The raw data obtained from the screening ablations used to identify the youngest detrital zircon population of the samples used in Chapter 4 has been included in a separate text file. All text files are tab delimited. Researchers who wish to view these data should examine the supporting documents that were uploaded alongside this dissertation at https://vtechworks.lib.vt.edu/handle/10919/11041. The file that corresponds to this appendix is titled *Appendix_C.1_Kaempfe_SA_D_2022_Geochron_Screening_Ablations*.

Appendix C.2 | Geochronologic data after 35s reabalations

The raw data obtained from the reablations used to determine the maximum depositional age of the samples used in Chapter 4 has been included in a separate text file. All text files are tab delimited. Researchers who wish to view these data should examine the supporting documents that were uploaded alongside this dissertation at https://vtechworks.lib.vt.edu/handle/10919/11041. The file that corresponds to this appendix is titled *Appendix_C.2_Kaempfe_SA_D_2022_Geochron_Reablations*.